

Washington University in St. Louis

Washington University Open Scholarship

McKelvey School of Engineering Theses & Dissertations

McKelvey School of Engineering

Winter 12-15-2016

Applications of Aerosol Technologies in the Silicon Industry

Miguel Vazquez Pufleau

Washington University in St. Louis

Follow this and additional works at: https://openscholarship.wustl.edu/eng_etds



Part of the [Engineering Commons](#)

Recommended Citation

Vazquez Pufleau, Miguel, "Applications of Aerosol Technologies in the Silicon Industry" (2016). *McKelvey School of Engineering Theses & Dissertations*. 212.

https://openscholarship.wustl.edu/eng_etds/212

This Dissertation is brought to you for free and open access by the McKelvey School of Engineering at Washington University Open Scholarship. It has been accepted for inclusion in McKelvey School of Engineering Theses & Dissertations by an authorized administrator of Washington University Open Scholarship. For more information, please contact digital@wumail.wustl.edu.

WASHINGTON UNIVERSITY IN ST. LOUIS

School of Engineering and Applied Sciences
Department of Energy, Environmental and Chemical Engineering

Dissertation Examination Committee:

Pratim Biswas, Chair
Elijah Thimsen, Co-Chair
Richard Axelbaum
Marcus Foston
Alexis Grabbe
Gregory Yablonsky

Applications of Aerosol Technologies in the Silicon Industry

by

Miguel Vazquez Pufleau

A dissertation presented to
The Graduate School
of Washington University in
partial fulfillment of the
requirements for the degree
of Doctor of Philosophy

December 2016

Saint Louis, Missouri

© 2016, Miguel Vazquez Pufleau

Table of Contents

List of figures.....	v
List of tables.....	ix
Nomenclature.....	x
Acknowledgements.....	xii
CHAPTER 1: INTRODUCTION	2
1.1. Motivation for the research.....	3
1.2. Background.....	5
1.2.1. Silicon role in the current world	5
1.2.2. Silicon processing and cost overview	6
1.2.3. Silicon wafer based solar panels	7
1.2.4. Silicon based solar energy cost reduction efforts.....	8
1.2.5. Kerf	9
1.2.6. Silane Chemical vapor deposition (CVD) kinetics	11
1.2.7. Silicon aerosol formation.....	12
1.2.8. Fluidized Bed Reactors (FBR) and aerosol capture in beds.....	14
1.3. RESEARCH OBJECTIVES	18
1.4. STRUCTURE OF THESIS.....	22
CHAPTER 2: ELIMINATION OF CARBON CONTAMINATION FROM KERF USING A FURNACE AEROSOL REACTOR.....	25
2.1. Abstract.....	26
2.2. Introduction.....	27
2.3. Methods.....	30
2.3.1. Experimental setup.....	30
2.3.2. Test plan.....	31
2.3.3. Characterization tools	32
2.4. Model description	33
2.4.1. Aerosolization and in flight carbon elimination.....	34
2.5. Results and Discussion	35
2.5.1. Characterization of as received kerf.....	35
2.5.2. TGA results of carbon elimination kinetics	37
2.5.3. FuAR experimental runs and model validation	40
2.6. Conclusions.....	42

CHAPTER 3: ACTIVATION ENERGY DETERMINATION AND MECHANISTIC CONSIDERATIONS OF CARBON ELIMINATION IN KERF	44
3.1. Abstract.....	45
3.2. Introduction.....	46
3.3. Experimental methods.....	51
3.3.1. Sample characterization	51
3.3.2. Experimental setup.....	53
3.3.3. Test plan.....	53
3.4. Model description	54
3.5. Results and discussion	55
3.6. Conclusion and summary.....	75
CHAPTER 4: INSIGHTS INTO THE OXIDATION BEHAVIOR OF SILICON IN KERF USING SILICON POWDER FROM A FLUIDIZED BED	77
4.1. Abstract.....	78
4.2. Introduction.....	79
4.3. Experimental methods.....	86
4.3.1. Characterization tools	86
4.4. Results & discussion	87
4.5. Conclusion and summary.....	96
CHAPTER 5: MEASUREMENT OF A STABLE SILICON HYDRIDE CLUSTER FROM SILANE PYROLYSIS IN A HELIUM ATMOSPHERE THAT DOES NOT SEEM TO BEHAVE AS A STABLE NUCLEUS BUT RATHER AS A CONDENSABLE SPECIES	97
5.1. Abstract.....	98
5.2. Introduction.....	99
5.3. Experimental methods.....	102
5.3.1. Experimental setup.....	102
5.3.2. Characterization tools	103
5.4. Results and discussion	105
5.4.1. Interpretation of stable silicon hydride cluster as a condensable species and not as a stable nuclei 113	
5.5. Conclusion and summary.....	114
CHAPTER 6: DETERMINATION OF RELATIVE RATES OF CONDENSATION AND NUCLEATION IN SILICON NANOPARTICLE SYNTHESIS FROM SILANE PYROLYSIS	117
6.1. Abstract.....	118
6.2. Introduction.....	119
6.3. Experimental methods.....	123

6.3.1.	Experimental setup.....	123
6.3.2.	Characterization tools	124
6.3.3.	Model description	125
6.4.	Results.....	126
6.5.	Discussion.....	136
6.5.1.	Evidence that supports the no sintering assumption	143
6.5.2.	Discussion on assumption of 1 nucleus per primary particle.....	146
6.5.3.	Discussion of collision frequency effect.....	147
6.5.4.	Interpretation of 1.5 / 1 order for nucleation / condensation.....	150
6.5.5.	Comparison of various methods for determining aerosol size distributions	159
6.5.6.	Obtaining a size distribution from chemical reaction	163
6.6.	Conclusion and summary.....	166
CHAPTER 7: SUMMARY AND RECOMMENDATIONS.....		169
7.1.	Summary.....	170
7.2.	Future work recommendations.....	173
7.3.	Safety considerations	175
APPENDIX		178
A: Capture of aerosols by silicon beads and their saturation in an FBR.....		179
B: Silane pyrolysis literature review		203
C: Appendix silane setup diagram		211
D: References.....		213
E: Vita.....		229

List of figures

Figure 1-1 Cost overview for polysilicon solar panels. Data from Ranjan et al. ⁴	6
Figure 1-2 Silicon purity and cost during its processing data obtained from ibm.gov.in, www.alibaba.com, www.zauba.com, www.pv-tech.org, blog.securities.com, apcmag.com www.products.cvdequipment.com, siliconwaferprices.org, Williams, Eric D., Robert U. Ayres, and Miriam Heller, Environmental science & technology 36.24 (2002): 5504-5510.	7
Figure 1-3 Sketch of a typical monosilicon wafering rotary wire saw and detail of wafers being sliced and kerf produced as a result	10
Figure 1-4 Critical silane concentration for nucleation based on detection of particles using a condensation nucleus counter with detection limits of 10nm vs temperature for different dilution gases. (From Sloodman et al ³ , reproduced with permission).	13
Figure 1-5 Empirical Geldart's classification (D Geldart ² , reproduced with permission)	16
Figure 1-6 Hsu et al. ¹ setup and experimental results vs theoretical prediction. A large discrepancy can be seen. Reproduced with permission.....	17
Figure 2-1 FuAR Experimental setup. It consists of a controlled gas supply, a dust disperser mechanism, an electric furnace, and a filter for sample collection.	30
Figure 2-2 a) SEM image showing the flake structure of kerf. b) TEM image for kerf. Plastic deformation can be observed in the flake shaped powder. c) XRD spectra for kerf and the reference for polysilicon. After being cut the monocrystalline silicon becomes polycrystalline in kerf due to the intense shear forces	35
Figure 2-3 a) Size distribution function for number concentration using SMPS and APS b) size distribution for mass concentration determined by APS. The mass from the SMPS particles is negligible and therefore not included.	36
Figure 2-4 a) Normalized weight change as a function of temperature for linear heating rate at 20 °C per minute. It can be seen that first carbon is eliminated and then silicon is oxidized. Under nitrogen atmosphere almost no weight gain is observed. b) Remaining carbon fraction calculated from isothermal program in TGA versus prediction from equation 2-4 on the left y axis. On the right axis the TGA thermocouple temperature is displayed.....	37
Figure 2-5 a) Carbon elimination in FuAR versus model for kerf atomized under air atmosphere. b) And under nitrogen atmosphere. For the operating conditions in N ₂ , carbon was not completely eliminated at 900 °C.	40
Figure 3-1 Sketch of experimental plan for characterization of volatiles evolved from kerf thermal treatment using thermogravimetric analysis and its solid residue based on the indicated characterization methods	53
Figure 3-2 Volatiles evolution from kerf using a heating rate of 20 °C/min. Conversion is calculated by weight loss from TGA and total carbon (TC) of the remaining sample in air and in N ₂ atmospheres.	56
Figure 3-3 Elemental characterization of the volatiles using GCMS. Samples were extracted using a manual syringe at the indicated TGA temperatures and injected into the GCMS column. Plots (a) air and (b) N ₂ show the total signal measured from MS (upper) and the relative abundance for various groups of compounds (lower). On gray the TGA rate of weight loss as a function of temperature (lower).....	59
Figure 3-4 FTIR for kerf thermally treated at various temperatures (a) in air and (b) in N ₂ . Peaks are labeled based on the literature. A summary of the molecular motion assignment is presented in Table 3-3	61
Figure 3-5 Rate of volatiles elimination for kerf at various heating rates (a) in air and (b) in N ₂ . Insets show carbon elimination from kerf in the given atmosphere.....	64

Figure 3-6 Activation energy (E_A) for volatile elimination from kerf using OFW, KAS and Kissinger methods as a function of conversion (a) in air and (b) in N_2 . At low conversion both reactions display a similar behavior, but as reaction continues the N_2 case displays higher E_A compared to air.....	65
Figure 3-7 OFW method to calculate EA (a) in air and (b) in N_2 . High regression values are observed. .	66
Figure 3-8 KAS method to calculate E_A (a) in air and (b) in N_2 . The data quadruplet shows consistency and a high linear regression value indicating experimental data reliability.	66
Figure 3-9 Normalized reaction rate (a) in air and (b) in N_2 . The sharp slope indicates both reactions are predominantly exothermic.	67
Figure 3-10 SEM of dried kerf at (a) RT, (b) heated to 900 °C in air and (c) heated to 900 °C in N_2 . No significant differences are observed in the flake shape after thermal treatment.	68
Figure 3-11 Two-step mechanism for carbon elimination in kerf. Arrow thickness shows qualitative dominance for each parallel reaction pathway. At the end of the reaction in N_2 12% of carbon remains as tar.	73
Figure 4-1 TGA calculated conversion for heating rates at various temperatures for Sample 11m ² /g of fluidized bed reactor dust.	88
Figure 4-2 TGA weight gained derivatives for all silicon samples and kerf for a) 3m ² /g, b) 6m ² /g c) 11m ² /g d) 19m ² /g and e) kerf. Both the 3 m ² and the 11 m ² display two similar peaks, the first around 650 °C and the second around 750 °C. On the other hand the samples for 6 and 19 m ² /g display a less marked first peak. Also for the sample of 6m ² /g the first peak occurs around 550 °C, 100 °C before the first peak of the other silicon samples. Both of these trends are linked to the crystallite size rather than the surface area. We note that the 6m ² /g, with the smallest first peak of all has a crystallite size of only 50nm	89
Figure 4-3 Evaluation of various kinetic models for describing the oxidation of 11 m ² /g silicon. BET particle size based D-G underpredicts oxidation, whereas XRD crystallite size based D-G overpredicts oxidation. This might be the source of some contradiction in the literature, whether nanoparticles oxidize quicker or slower than predicted by the D-G model.	90
Figure 4-4 Normalized activation energy for all silicon samples. To obtain the real activation energy it is necessary to multiply the plotted value by the crystallite size of the sample.....	91
Figure 4-5 Experimentally calculated conversion from TGA data (symbols) for all samples at 1000 °C vs prediction from the function to calculate the parabolic factor as a function of surface area, crystallite size and roughness factor.	93
Figure 4-6 Effect of residence time on carbon elimination and silicon oxidation for various temperatures a) linear scale, b) log scale with details of relevant intersection for both elemental composition of carbon and oxygen curves.....	95
Figure 5-1 Silane reactor setup, including ancillary systems and connected online characterization instruments.....	102
Figure 5-2 Temperature profile of flow reactor inside the Lindbergh furnace. The highest temperature is located at the end of the first third of the furnace. At this point maximum reaction rates are expected... 106	106
Figure 5-3 Negatively charged clusters measured by the DMA in the temperature range of a) 25 °C to 550°C and b) 420 °C to 490 °C a) measurement including the nitrate ion with a peak around 0.65nm and b) The nitrate ion has been subtracted using a Gaussian regression.	107
Figure 5-4 Aerosols collected for 5 min from running 0.3% silane through the reactor at temperatures between 400 -600 °C and b) Relative mass gain in the filter compared to the 400 °C case deviations in the linearity are attributed to filter handling and weighing.....	109
Figure 5-5 a) TEM silicon nanoparticles synthesized at different temperatures b) Primary particle size distributions for various temperatures and c) Relative abundance of silicon aerosols based on the projected area from representative TEM images. It provides the same trend as the filter weight gain from Figure 5-4 but with more resolution and accuracy.....	111

Figure 5-6 Sub-3 nm particle size distributions measured under different SiH ₄ concentrations at 450 °C. The peak at 0.67 nm is generated by the neutralizer whereas the peak at around 0.75nm is attributed to the silicon hydride stable cluster. Detection of this cluster below 0.075% SiH ₄ was not possible.....	112
Figure 5-7 Neutralizer-generated positive ions measured in the temperature range of 25 °C to 550 °C. The decrease of the peak intensity at 550°C is attributed to ion scavenging by the large amount of aerosols formed at that temperature.	112
Figure 5-8 m/z spectra obtained via GCMS from an aliquot extracted manually from the reactor a) without silane and b) with 0.3% silane at 450 °C c) The spectra for the ion extraction plot for m/z 207 is displayed in c) for the blank reactor, and d) for the reactor with silane at 450°C. In the case of the blank reactor (c), a noisy signal at a time of around 6 min. is observed. It is attributed to traces of the cluster of interest from the reactor. In the case of the reactor with silane at 450°C (d), the plot indicates that the GC column used was not optimized for separating this compound. However, the presence of broad peaks is in agreement with a realistic signal and not to random noise. The signal suggests the presence of the 207m/z ion is real. Thus it is the best and most realistic candidate for assigning the identity of the 0.75 nm cluster measured using the half mini DMA.....	113
Figure 6-1 Experimental setup for silane pyrolysis and formation of silicon aerosols.....	123
Figure 6-2 a) TEM results showing temperature's effect on primary particle size distribution, b) Agglomerate size by SMPS where dp stands for particle diameter, c) Summary of agglomerate mean size and lognormal standard deviation, d) Primary particle size distribution, e) Summary of primary particle size distribution compared to crystallite size f) XRD pattern for silicon nanoparticles synthesized at various temperatures, g) Unfiltered silicon pattern from a crystalline silicon nanoparticle sample.	128
Figure 6-3 a) TEM images comparing the effect of residence time at 2 different temperatures b) agglomerate size distribution at 700 °C c) at 1000 °C d) primary particle size distribution at 700 °C and e) at 1000 °C f) summary of the agglomerate size distribution for both conditions where error bars represent the lognormal standard deviation and g) summary of the primary particle sizes for both temperatures. .	131
Figure 6-4 Run at 700 °C using different concentrations of silane in helium. a) Picture of the filters after collection of silicon nanoparticles, filters are arranged at progressively increasing concentrations where the lowest concentration is in the left side and the highest concentration in the right hand b) TEM images of silicon nanoparticles synthesized at different silane concentrations c) Agglomerate size distribution for various concentrations d) Primary particle size distribution for the different concentrations e) summary of agglomerate size. The dots represent the mean and the error bars are the lognormal standard deviation f) summary of primary particle size.....	133
Figure 6-5 Schematic mechanism for silane pyrolysis and particle evolution in a flow reactor.....	139
Figure 6-6 Condensed mass over nucleated mass for various concentrations	140
Figure 6-7 a) TEM images of four different residence times for the temperature of 800 °C. b) The summary of primary particle size distributions for the four residence times. The effect of size distribution broadening starts to take place suggesting that sintering becomes important above this temperature.	142
Figure 6-8 a) Two TEM images of silicon nanoparticles synthesized from silane pyrolysis in helium with a residence time of 51.2 s, and a concentration of 0.02% SiH ₄ . Nanoparticles as small as 2-3 nm are abundant and visible in contact with each other, yet they do not sinter. This is consistent with the assumption of no thermal sintering occurring at this temperature. b) Primary particle size distributions for a residence time run at 700°C. $\tau = 8 \times$ corresponds to the TEM images on a). The peak at around 14nm is larger than the other 3 peaks with lower residence times and is attributed to further condensation in the window that the aerosol passes through the reaction zone.	145
Figure 6-9 Simulated concentration profiles of ane from 1% silane in nitrogen at 890K Giunta et al. ⁵⁶ Reproduced with permission. n represents the number of silicon atoms within the polymeric unit.....	146

Figure 6-10 Observed agglomerate mean size (green) and predicted based on the monodisperse model (yellow) and measured primary particle size distribution (black) compared to predicted using the monodisperse model (red) and coagulation from the method of moments (blue) . The agglomerate behavior as a function of concentration is fairly well described by the model. On the other hand the mean primary particle size is not well described by either of the models. The predictions from the polydisperse and monodisperse models are close to each other but far from the experimental data, suggesting that the dominant mechanism for the formation of the primary particles is not dominated by collision of aerosols.

..... 149

Figure 6-11 Sequence of chemical reactions and aerosol processes 152

Figure 6-12 Number concentration of nuclei in number/m³ as a function of concentration. Black dots represent the data calculated from experimental results. The red line represents the fit provided in Eq. 6-31. 155

Figure 6-13 Proposed mechanism for nucleation quenching. Newly formed radicals are attracted by electrostatic forces between the dipoles of the formed radical and the charged surface of nuclei. In this way the radical undergoes surface reaction before it gets a chance to react with silane molecules and form new nuclei. 157

Figure 6-14 Color lines are the simulated size distributions for using equations 6-34 to 6-36. Symbols of the same color represent the lognormal fit of the experimental data presented in Figure 6-4d. The condensation constant used was $1.51 \cdot 10^{12} \text{ L}^{0.5}/(\text{mol}^{0.5}\text{s})$ and the nucleation rate was $1.2 \cdot 10^6 \text{ 1/s}$. These values are based on silylene formation and the relative rate expression developed previously in this chapter. The nucleation rate was corrected by a factor of 2.5 to account for the quenching effect. 159

Figure 6-15 Comparison of the experimental primary particle size distribution from the pyrolysis of 25 ppm silane in helium at 700°C vs. selected models for predicting the primary particle size distribution. The condensation with inhibited nucleation at higher conversion is capable of fitting the experimental size distribution well. On the other hand, the full reaction followed by coagulation model shows a broader geometric standard deviation (1.35), which is much higher than the experimental (1.17). Furthermore the time used to stop coagulation is rather arbitrary so accurately predicting the mean size of primary particles from this model is virtually impossible. 165

Figure A-1 Schematic of proposed mechanism for silicon bead growth in FBR..... 182

Figure A-2 Experimental setup 189

Figure A-3 a) The size distribution of the silicon beads b) A silicon bead at different levels of magnification under SEM, from 1 mm to 300 μm 190

Figure A-4 SEM images of various cleaning procedures before and after fluidization. The beads etched with 20% mass KOH for 1 min show significant fissures in the surface. The remaining material is still subject to abrasion through fluidization. 192

Figure A-5 Shows the bed expansion as a function of fluidization velocity. The error bars indicate the minimum and maximum height observed at the given flow rate conditions. 192

Figure A-6 Effect of different fluidization flow rates for a 30 mL bed of raw silicon beads 193

Figure A-7 Filtration efficiency (negative because it is produced by attrition) for various fluidization conditions without introducing aerosols in the inlet of the bed for raw (not-cleaned beads) and clean beads at 1.5 minimum fluidization velocity (u_{mf}). The cleaned beads had low attrition at the given conditions. The bed consisted on 30mL of silicon beads, with a bed height of 13 cm. The minimum fluidization velocity for the beads was 10 lpm. The experiment was carried out at room temperature. 194

Figure A-8 Saturation of a fluidized bed at 700 °C with an aerosol synthesized at 700 °C from a 0.072% silane in He in a total flow of 2.5lpm. The flow was merged then with 7 lpm of nitrogen. Moving

clockwise from the upper left, we see the aerosol collected in a filter, the filtration efficiency as a function of time, a clean bead in the initial condition, a saturated bead at the end of the run, and finally a TEM micrograph of the silicon introduced in the bottom of the fluidized bed.	196
Figure A-9 Saturation of fluidized bed at room temperature for an aerosol synthesized at 1000 °C 0.072% silane in He in a total flow of 2.5lpm. The bed was fluidized using 13 lpm of nitrogen, which provides for a total flow equivalent to 1.5 the minimum fluidization velocity (μ_{mf}) As before we see the aerosol collected in a filter, the filtration efficiency as a function of time, a clean bead at the initial condition, a saturated bead at the end of the run, and finally a TEM micrograph of the silicon produced.	197
Figure A-10 The scavenging rate k_{sc} experimental results for a fluidized bed at 700 °C receiving aerosols synthesized at 700 °C based on SMPS data. k_{sc} is not constant because as the bed gets saturated with aerosols, the filtration efficiency decreases.	199
Figure A-11 Gamma as a function of total silicon aerosol mass feed to the fluidized bed per unit of mass for beads. As the beads get saturated, their gamma decreases, indicating a lower capacity to filter/retain aerosols per unit of filtering media or silicon beads	200
Figure A-12 a) Sketch of the natural recirculation that occurs inside the FBR. Recirculation is a function of fluidization gas velocity, which also impacts the elutriation of fines and bead attrition. For that reason a compromise between both effects should be found and the reactor should be operated at such a condition, as sketched in b).....	201
Figure C-1. Silane setup and reactor diagram.....	211
Figure C-2. Picture of silane setup and reactor.....	212

List of tables

Table 2-1 Experiments list for carbon elimination kinetics determination and experimental runs in FuAR	31
Table 3-1 Kerf elemental analysis provided by SunEdison, Inc.	51
Table 3-2 Experimental plan for gaining kinetic information and mechanistic evidence on carbon elimination from kerf.	53
Table 3-3 FTIR peak assignment	62
Table 4-1 Summary of silicon nanoparticle samples, including TEM, BET surface area, calculated particle size according to BET, and calculated crystallite size from the Sherrer equation using XRD peaks. The first four columns are FBR silicon and the last column is kerf.....	87
Table 6-1 Relative condensed/nucleated mass effect of temperature.....	135
Table 6-2 Summary of conditions and synthesized aerosols characteristics. Residence time has been calculated based on the set point temperature.....	136
Table 6-3 Comparison of different models to describe aerosol dynamics for aerosol formation via chemical reaction. A sketch of dominant processes with qualitative times are shown. Also the assumption each model does is presented.	161
Table 6-4 Comparison of pros and cons of the various methods available for describing aerosol dynamics	162
Table A-1 Fluidized bed filtration efficiencies for various collection mechanisms, from Xiao et al. ²⁰⁸ ..	195

Nomenclature

- $A \rightarrow$ Linear constant for oxidation
 $A_0 \rightarrow$ Preexponential factor
 $\alpha \rightarrow$ Conversion
 $B \rightarrow$ Parabolic rate constant
 $\beta_{\text{coll}} \rightarrow$ Collision kernel
 $\beta \rightarrow$ Heating rate
 $C_{\text{cluster}} \rightarrow$ Concentration of aerosols [=] g/m^3
 $d \rightarrow$ Monomer diameter [=] nm
 $d_c \rightarrow$ Bed material parameter
 $D_{\text{fm}} \rightarrow$ Aggregate mass-mobility exponent [=] (-)
 $d_m \rightarrow$ Aggregate mobility diameter [=] nm
 $d_p \rightarrow$ Parameter for the particles to be removed
 $d_{\text{tube}} \rightarrow$ Dimensionless diameter of the tube
 $\bar{\varepsilon} \rightarrow$ Bed porosity
 $E_A \rightarrow$ Activation energy
 $E_{A,\alpha} \rightarrow$ Activation energy at conversion α
 $E_D \rightarrow$ Collection efficiency due to diffusion
 $E_G \rightarrow$ Collection efficiency due to gravitational settling
 $E_I \rightarrow$ Collection efficiency due to impaction
 $E_{EI} \rightarrow$ Collection efficiency due to electrostatic attraction
 $E_R \rightarrow$ Collection efficiency due to interception
 $\varepsilon_f \rightarrow$ Dielectric constant of the fluid
 $g \rightarrow$ Gravitational acceleration
 $Ga \rightarrow$ Galileo number
 $k_b \rightarrow$ Boltzmann constant
 $K \rightarrow$ Kinetic constant
 $K_c \rightarrow$ Dimensionless electrical constant
 $k_{\text{fm}} \rightarrow$ Aggregate mass-mobility prefactor [=] (-)
 $k_{\text{sc}} \rightarrow$ Rate constant for aerosol scavenging [=] m^3/s

$L \rightarrow$ Oxide thickness

$\lambda \rightarrow$ Mean free path of gas molecules

$M \rightarrow$ Aggregate mass [=] g

$n \rightarrow$ Power law exponent

$n(dp) \rightarrow$ Size distribution function [=] $\#/cm^3nm$

$n_{Si,cond} \rightarrow$ Number of silicon atoms in the predominant condensable species

$n_{Si,nuc1} \rightarrow$ Number of silicon atoms in the chemical formula of the predominant nucleus

$N \rightarrow$ Particle number concentration

$N_0 \rightarrow$ Initial concentration of monomers

$\eta \rightarrow$ Filtration efficiency [=] (-)

$\eta_{overall} \rightarrow$ Overall filtration efficiency [=] (-)

$Pe \rightarrow$ Péclet number

$\dot{Q} \rightarrow$ Flow rate [=] m^3/s

$Q_c \rightarrow$ Electrical charge density on the bed material

$Q_p \rightarrow$ Electrical charge density of the particles

$R \rightarrow$ Gas constant

$\bar{R} \rightarrow$ Interception parameter,

$r_A \rightarrow$ Reaction rate

$Re \rightarrow$ Reynolds number

$R_{sc} \rightarrow$ Aerosol scavenging rate [=] g/s

$\rho_p \rightarrow$ Density of the particles

$St \rightarrow$ Stokes number

$t \rightarrow$ Time

$\mu \rightarrow$ Dynamic viscosity of the gas

$\mu_f \rightarrow$ Superficial gas velocity

$T \rightarrow$ Absolute temperature unless otherwise indicated

$T_\alpha \rightarrow$ Temperature required to achieve conversion α

$\tau \rightarrow$ Time required for initial oxidation

$v_0 \rightarrow$ Initial monomer volume

$V_1 \rightarrow$ Volume of particle 1

Acknowledgements

I would like to thank my advisor Prof. Pratim Biswas and my co-advisor Prof. Elijah Thimsen for their support and mentorship being both endless sources of inspiration during my doctoral studies. I am thankful to Prof. Biswas for giving me the opportunity to join his lab as one of his students and for financing with his grants my research, also for very productive and inspirational discussions that taught me much more than what it means to be an aerosol scientist. For his continuous efforts to guide me and drive me towards high productivity and success through my doctoral studies, I am thankful to Prof. Thimsen for having accepted me as a co-advised student in the interface research lab and having offered me his mentorship, guidance and advice through the ups and downs of the doctoral studies, always eager to have lengthy and productive discussions on the science and hands on of my experiments and their results.

I am also thankful to Prof. Yablonsky, with whom very productive scientific discussions took place in the fields of kinetics and reaction engineering through my PhD, to Dr. Alexis Grabbe for providing me with hands on expertise and samples for executing a significant fraction of the silicon experiments from this work and for his endless advice and sharing his technical expertise regarding fluidized bed reactors and silicon refining in general. I also would like to thank Prof. Foston for very productive scientific discussions, and for his motivation and willingness to help me through my PhD, I am also indebted to Prof. Axelbaum for being a source of inspiration and providing me with great advice towards deciding my own path through my PhD.

I am grateful to all professors of the Energy, Environmental and Chemical Engineering Department who one way or the other helped me through this process. I would also like to thank Patty Wurm for her significant help in training and setting up measurements in numerous

instruments at the Jens Lab, also to Allen Kesselring for his help using GCMS, to Remya Nair for her help in using TEM and SEM, and to Sanmathi Chavalmane for her help as well.

I am also thankful to Henry Erk for providing me with the kerf samples and for being one of the minds that in conjunction with Prof. Biswas, outlined the kerf recycling need that was developed in the first sections of this work. Also many thanks to the various members from SunEdison that provided me useful feedback for all my projects.

I owe thanks to Sun Edison for supporting my funding source: the Solar Energy Research Institute for India and the United States (SERIUS) funded jointly by the US department of Energy under subcontract DE-AC36-08GO28308 and the government of India through the Department of Science and Technology under Subcontract IUSSTF/JCERDC-SERIUS/2012, and to the Nano Research Facility (NRF) at Washington University in St. Louis, a member of the National Nanotechnology Infrastructure Network (NNIN) for providing the resources and infrastructure without which this work would be unrealizable.

I am grateful to all my current and former lab mates at the AAQRL, with special thanks to Wei-NingWang for being my first mentor in the aerosol world, and to Tandeep Chadha for being my mentor afterwards. To Yang Wang, Nathan Reed, Xiaofei Wang, Yao Nie and Ramesh Raliya for the countless times that they helped me with theory, instruments and all sorts of life issues, and for motivating me in ups and downs. I am also thankful to all current and former members of the interface research lab: John Ephraim Necip B. Uner and Deanna Lanigan for their help in the lab.

I am also very thankful to my undergraduate mentees: Martin Yamane and Dany Sales for their significant help to build the silane reactor, for helping me characterizing samples and for motivating me with their vivid youth.

I am also thankful to my friends Juan Pablo Saa, Philipp Diebolder, Andrea Balassy, Dhruv Mitroo, Nathalia Vieira, Silvana del Valle, Fernando Hidalgo, Liz Perez, Mario Ortega, and all of the friends that I made in Saint Louis that provided me inspiration, motivation, advise and friendship through the ups and downs of this process.

I am indebted to James Ballard, Sandra Matteucci and Cindy Mittanck for their help reviewing the grammar correctness, cogency and scientific style in the present work. I am also grateful to Rose Baxter, Kim Coleman, Elizabeth Mehringer, Sutton Trisha, Christine Tilley for helping me through the process an uncountable amount of times and many thanks as well to Tim McHugh for significant help when my hard drive broke and for his assistance with computer issues.

Miguel Vazquez Pufleau

Washington University in St. Louis

December 2016

ABSTRACT OF THE DISSERTATION
APPLICATIONS OF AEROSOL TECHNOLOGIES IN THE SILICON INDUSTRY

By

Miguel Vazquez Pufleau

Doctor of Philosophy in Energy Environmental and Chemical Engineering

Washington University in St. Louis, December 2016

Professors: Pratim Biswas (Chair) and Elijah Thimsen (Co-chair)

Silicon is the main semiconductor component of the electronic and photovoltaic industries, accounting for about 400 billion dollars revenue per year for both industries or 0.5% of the gross world product in 2014. Despite being the second most abundant element in the earth crust, silicon is still very expensive to refine to the purity levels that both industries demand. The current refining steps include carbothermal reduction of silica (SiO_2) to form metallurgical silicon, which is later converted into silanes by hydrochlorination, and purified via distillation. To obtain solid polysilicon, silanes are later pyrolysed via chemical vapor deposition (CVD) using either the Siemens or the fluidized bed reactor (FBR) process. Polysilicon is then either casted via directional solidification in a crucible to obtain polysilicon ingots or pulled from a Czochralski crucible to produce monocrystalline ingots. Both products are then sliced using abrasive wire to obtain wafers.

In this dissertation, the focus was on two unit operations that have the potential to significantly lower the cost and energy required for refining silicon. First, the removal of carbon from silicon kerf (sawing dust from wafering) was examined to enable its recycling. Second, silane

pyrolysis was studied to better understand the dynamics of the initial stages of silicon aerosol formation and growth.

The first section of this work focuses on addressing the elimination of carbon contamination from kerf, which is one of the most difficult contaminants to remove. This is important because the wafering process wastes around 45% of the expensively purified silicon ingots in the form of kerf. A proof of concept for the use of a furnace aerosol reactor for carbon removal in kerf is presented. Then a mechanistic understanding of the process and the determination of its activation energy in air and nitrogen are determined. In addition, the oxidation of non-ideal silicon agglomerates at high temperatures is assessed. Finally, by combining the kinetics of both processes, optimal operating conditions for the removal of carbon at minimum silicon oxidation are revealed.

The second section of this work is dedicated to studying the initial stages of aerosol formation during silane pyrolysis. This knowledge is important for FBR technology, which requires 90% less energy for producing polysilicon compared to its counterpart, the Siemens process. For this purpose, a silicon hydride cluster from silane pyrolysis was measured using a half mini differential mobility analyzer. In addition, the relative kinetics of condensation/nucleation for silane pyrolysis were determined in a regime where both sintering and coalescence are negligible. The gained knowledge of relative rates for silicon nanoparticle formation helps to predict the aerosol behavior inside a fluidized bed reactor. This knowledge is also useful to engineer silicon nanoparticles and predict their morphology for several advanced applications.

In summary, the knowledge presented in this work has the potential to cut the energy required to refine silicon by more than 40%, with a corresponding reduction in cost to end users. Towards that end, the work developed in this dissertation is twofold. Firstly, it seeks to enable kerf

recycling technologies by optimizing the elimination of carbon from kerf in a furnace aerosol reactor. Secondly, it provides fundamental knowledge for better understanding the initial dynamics of aerosol formation in silane pyrolysis. This information is useful not only to optimize FBRs, but also to tune silicon nanoparticles properties by engineering their morphology.

Dedicated to Marlene, my parents and professors

CHAPTER 1:INTRODUCTION

1.1. Motivation for the research

Silicon, the most important and widely used semiconductor in the digital era finds wide applications in the electronic industry as the heart of electronic chips used in computers, tablets, cellphones, and most electronic devices. Silicon also finds wide applications in the photovoltaic (PV) industry, where silicon wafer based technology accounted for 90% of all solar panels manufactured in 2013.⁵

High purity silicon is an expensive commodity despite its abundance in the earth crust as silicon dioxide (SiO_2). The reasons for this stem from the wasteful silicon processing and the numerous energy intensive steps demanded by the silicon purification industries to reach high purity. More recently in the global markets, the renewable energies have been attracting increasing attention due to an increase in public awareness of global warming, a long term increase in the fossil fuels price, and energy supply insecurity due to political interests as well as energy-related conflicts in certain regions of the world. The photovoltaic industry, that decades ago had so heavily relied on rejects from the electronic industry as its main raw material source,⁶ has experienced severe shortages in silicon global supply yielding a dramatic increase in its price⁷. Contrary to the electronic chips, PV requires large amounts of silicon per unit and competes against widely used commodities such as petroleum, gas, and nuclear energy among others. The cost of silicon accounts for more than 30% of the solar panel price. For that reason, it becomes imperative to develop more efficient processes that permit a decrease in the cost of PV.

The processing of silicon (Si) is considerably wasteful in two areas: the ingot slicing into wafers using abrasive cutting techniques; and the Siemens process for silicon chemical vapor deposition (CVD). Both areas are developed in this work:

Silicon kerf on the one hand represents a huge problem in terms of material waste after the lengthy and expensive purification process. This waste accounts for more than 40% of the total material and despite efforts on using kerfless procedures such as ribbon technologies⁸, wafering from ingots continues to be the dominant industrial pathway. New Si ingot slicing techniques (e.g. using fixed abrasive and polymeric lubricants) developed in recent years are able to produce cleaner kerf that shows more promise of being cleaned and reutilized. Carbon is one of the most difficult contaminants to remove from kerf for various reasons: it belongs to the same group as silicon; non-organic solvents would not be able to remove the carbon contaminant whereas solvents that can dissolve the organic contaminant would leave another carbon containing residue. In this section, the idea is to study carbon elimination and Si oxidation to optimize a furnace aerosol method to purify silicon from kerf, maximizing carbon elimination, and minimizing silicon oxidation.

On the other hand, the demand of large temperature gradients between the interior of the reactor and the reactor walls represent a huge energy cost. Changing this kind of reactor to a fluidized bed reactor (FBR) is a desirable operation due to 90% energy savings that have already been suggested in the first boom of the renewable energies during the oil embargo crisis in the seventies. Despite awareness of process advantages of FBRs over Siemens reactors since the early ages of the semiconductor era, the transition was not accomplished due to low energy costs, high quality of Siemens polysilicon, and technological challenges of FBR implementation. In recent years, renewed interest from the PV industry has been focusing on developing Si-FBR processes for PV manufacturing. However, an overall lack of understanding in the simultaneous silane CVD chemistry, aerosol formation, and fluid dynamics demand the usage of expensive pilot plants that not necessarily guarantee the success of large scale plants. After undergoing the scaling process,

typical material waste due to fine losses is in the range of 10% of the total inlet material. In this part of the work, the objective is to identify, measure, and quantify kinetic parameters that are relevant for describing the initial stages of silicon aerosol formation during silane pyrolysis and that determine the nanoparticle properties. The focus is primarily the determination of the relative rates of silane condensation/nucleation and secondly, the measurement of a silicon hydride stable cluster to better understand the process of nucleation.

1.2. Background

1.2.1. Silicon role in the current world

Silicon is a metalloid,⁹ the second most abundant element in the earth's crust¹⁰ following oxygen.¹¹ After refining silicon to metallurgical grade, most of it is used as an alloy to produce silicon steel¹² or aluminum,¹³ followed by usage in polymeric form as silicones.¹⁴ To a lesser extent it is reacted with nitrogen to form silicon nitride or with carbon to form silicon carbide for high performance ceramic applications.¹⁵ Although only a small fraction (less than 4%) of the total silicon produced is processed to high purity,¹⁶ this refined silicon plays a central role in the daily lives of contemporary societies of the digital age.¹⁷ This refined silicon is used mainly in integrated circuits,¹⁸ and in solar panels.¹⁹

Energy, environmental, political, and sustainability concerns have popularized solar panels in recent years. Silicon (Si) is the preferred material for its construction (currently 90% of the world market share)^{5,20} due to its reliability, high efficiency, and non-toxicity. Despite being more expensive than fossil fuels, some governments, especially Spain and Germany, started aggressive subsidy plans for domestic PV implementation in 2005.²¹ However, worldwide large scale implementation is only viable if the technology itself becomes economically competitive. Solar panels are still more expensive than fossil fuels because the silicon wafers required account for a

significant fraction of a solar panel total cost. High purity silicon is currently a very expensive commodity due to the energy intensive and wasteful processing. Reducing solar panel cost requires improving several of the extensive Si purification and processing operations.

1.2.2. Silicon processing and cost overview

Currently solar energy is more expensive than fossil fuels. Figure 1-1 shows the percentile cost of polysilicon solar wafers and modules. It can be seen that the raw material represents a significant fraction of the total cost.

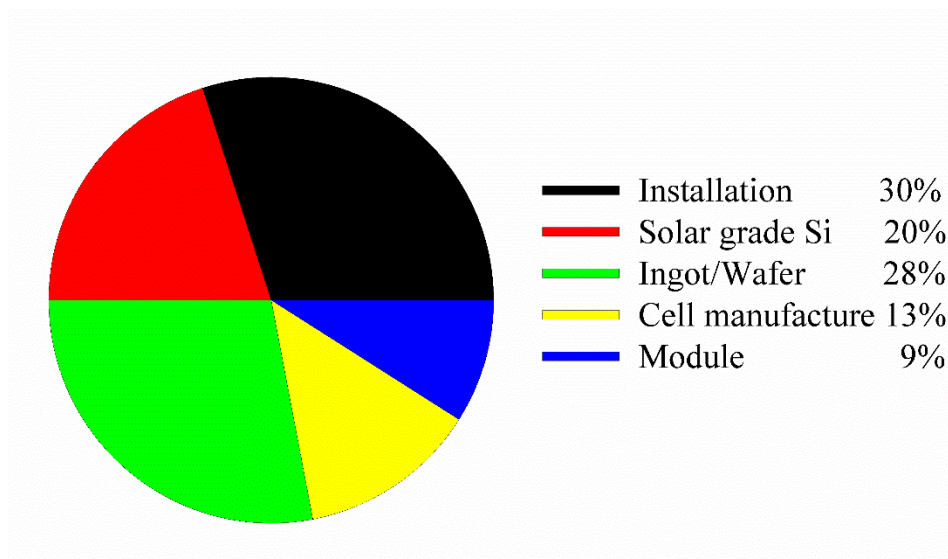


Figure 1-1 Cost overview for polysilicon solar panels. Data from Ranjan et al.⁴

Silicon purification is performed following a complex series of processes. Figure 1-2 shows an overview of intermediate products in the silicon refining industry with the energy cost, the process typically used for refining from one step to the other, the purity level, and the approximate costs in 2014 USD. An overview of silicon processing follows: Quartzite (a SiO_2 mineral) is reduced with graphite in an electric arc furnace forming metallurgical silicon and CO_2 . Metallurgical silicon is then reacted with HCl to produce trichlorosilane (HSiCl_3), which is then

passed through a metal halide catalyst bed and by disproportionation yields silane (SiH_4), which is then purified using triple distillation.^{6a} Traditionally, SiHCl_3 is subjected to CVD at high temperatures in a Siemens reactor to produce polysilicon (FBRs use silane). Polysilicon is further processed to manufacture ingots of higher purity using block casting, directional solidification, Czochralsky method, etc. Finally, the ingots are sliced using an abrasive sawing technique and the wafers are ready for further cell processing.



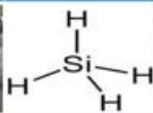




<div> <div>Silicon</div> <div>14</div> <div>Si</div> <div>28.086</div> </div>	Quartzite	Metallurgical	Silane	Polysilicon	Czochralski	Kerf	Si wafers
							
Price (USD/kg)	0.005	1.5 – 2	6	20– 40	50 – 200	0	100 – 400
Purity	99% SiO_2 46%Si	95 - 98 % Si	99.99999999% (10N)	99.999% (5N)	(9N)	85% Si	(9N)
Process	→	Arc Furnace	Chlorination & distillation	Siemens reactor	Czochralski crucible	Slicing	Polishing →
Electrical input (kWh/kg of product)		13	50	250	250	240	13

Figure 1-2 Silicon purity and cost during its processing data obtained from ibm.gov.in, www.alibaba.com, www.zauba.com, www.pv-tech.org, blog.securities.com, apcmag.com, www.products.cvdequipment.com, siliconwaferprices.org, Williams, Eric D., Robert U. Ayres, and Miriam Heller, Environmental science & technology 36.24 (2002): 5504-5510.

1.2.3. Silicon wafer based solar panels

The first step after slicing is to remove imperfections caused by sawing. This can be achieved by different etching processes. One of the most common in the industry is to etch using KOH diluted in water to remove saw damage. Further processing of the cell varies depending on the manufacturer. For monocrystalline cells, a slower secondary etching preferential to crystal orientation is performed to provide a differentiated surface, including a smooth area for the

contacts and a section with a pyramidal surface to avoid light reflection. In the case of polycrystalline cells, this approach is not effective hence a thin antireflection coating must be applied at the end of the cell processing.²²

The p-n junction is formed on the following way. Typically ingots are already doped with boron making them p-type. After being etched, wafers receive a thin n type layer by exposing the wafer to a phosphorous source and heating. Later, the contacts are printed into the cell using silver paste. After fabrication, typically 36 cells are soldered together and introduced into a weatherproof module. More details on converting Si wafers into electronic chips or solar panels are beyond the scope of this work and can be found elsewhere.²³

1.2.4. Silicon based solar energy cost reduction efforts

Various different approaches have been suggested to reduce the price of solar energy. Some authors have proposed implementing different PV systems that rely on cheaper materials. Others recommend different improvements in the traditional Si processing in areas ranging from the substitution or removal of the Siemens reactor or even the whole CVD process²⁴ to improve the wafering technologies and recycle the kerf produced during sawing.²⁵

Alternative PV technologies such as perovskites²⁶, amorphous,²² thin film polycrystalline semiconductors (e.g. CdTe²⁷ and CuInS₂²⁸) have been claimed in later years to be promising alternatives for PV. However, they are still in early stages of technical development and do not comprise a significant fraction of the global solar panel market. Moreover these technologies face additional problems such as low efficiency, degradability, toxicity, scarcity of constituents, and high cost.

Some techniques have been developed to avoid CVD processing in the traditional Si refining and rather employ solely metallurgical techniques like upgraded metallurgical grade (UMG) silicon production, which relies mainly on methods as pre-purification pre-solidification, chemical cleaning, or reactive gas blowing.^{6a} However, these techniques have not yet commercially succeeded due to the superior semiconductor quality of CVD silicon.²⁴

Other alternatives to reduce polysilicon cost focus on replacing Siemens reactors with fluidized bed reactors (FBRs). FBRs are promising reactors (90% energy savings compared to Siemens) but technologically a challenging endeavor due to fine formation and turbulent interaction between beads, aerosols, and inert and reactive gases.

Strategies to reduce or recycle sawing wastes have also been proposed. Ribbon technologies²⁹ have been developed to avoid the need of slicing ingots. Nevertheless, the solar panel market is still highly dominated by ingot based monocrystalline (MC) and polycrystalline (PC) wafers^{6a} due to higher efficiencies,^{29,30} more reliability,²² and better return on investment.³¹ Wafers are sliced from ingots using fixed abrasive or slurry methods³², that unavoidably produce kerf. The present work focuses on the study of kerf recycling and better understanding silane pyrolysis in order to make feasible the substitution of Siemens reactors with FBRs.

1.2.5. Kerf

In the slicing process more than 40% of the MC or PC ingot initial material becomes silicon sawdust (kerf) waste.³¹ Figure 1-3 illustrates the sawing of wafers from a monocrystalline silicon ingot and the production of kerf as a result. Even more dramatic is the overall material balance in

PV production where 68% silicon is wasted through the different production steps.^{6a} Kerf is a complex industrial residue involving numerous metallic contaminants,³³ and organics coming mainly from the polymeric lubricant used during the cutting process. Despite the technical difficulties imposed by abundant contaminants, the economic potential of kerf recycling has encouraged various researchers to find viable ways to approach these challenges. Previous studies focused primarily on separating silicon carbide (SiC) abrasives from kerf using various techniques.^{25, 34} Nevertheless, thanks to a better understanding on the ductile behavior of silicon in a narrow range of cutting speeds,³⁵ the previously common slurry sawing for silicon has been upgraded to a fixed-abrasive diamond sawing technique, mainly because diamond sawing causes less surface damage to the wafers, provides better thickness consistency, and results in lower concentrations of metal impurities derived from the slicing wire on the wafer surface.³⁶

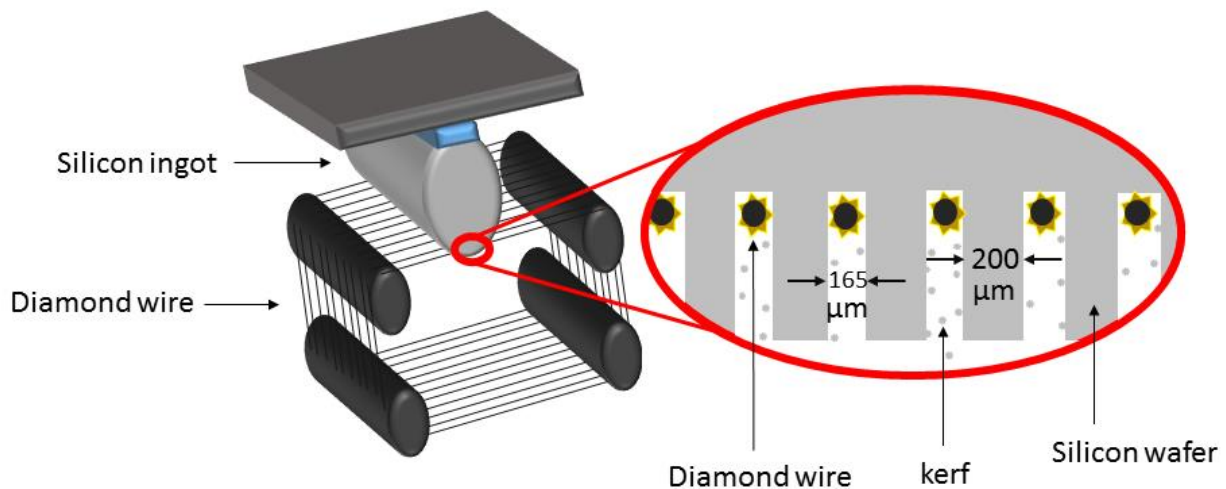


Figure 1-3 Sketch of a typical monosilicon wafering rotary wire saw and detail of wafers being sliced and kerf produced as a result

Few studies have been published on purification of kerf produced by diamond wire slicing. Maeda et al.,³⁷ after milling and etching kerf, fused it to build solar cells. Tomono et al.³⁸ explored

generating bromosilanes from kerf and then distilling them. They reported carbon removal as a remaining problem. Dhamrin et al.³⁹ also stated that carbon contamination on their silicon wafers from recycled kerf severely impacted cell efficiency.

1.2.6. Silane Chemical vapor deposition (CVD) kinetics

Several approaches have been taken including the search for a process that improves the Siemens reactor for wiser energy usage for silane or trichlorosilane pyrolysis. To lower energy demands in high purity Si purification, a fluidized bed reactor (FBR) technology was proposed more than 50 years ago but its implementation awaited some more decades until companies such as Ethyl corporation, MEMC/SunEdison, and REC implemented it commercially. Using FBR to produce polysilicon was regarded as being too complex and produced lower quality product than when using the Siemens process. At that time, two factors prevented the need of using FBR CVD. First, most of the silicon was intended for electronic applications, where the implementation of energy efficient processing of materials was not a paragon for success. Secondly the cheap cost of energy at that time did not constitute enough pressure to push the process into higher energy usage efficiency.

Reaction kinetics are fundamental for reactor design and operation. FBRs are not the exception. The challenge here is that the kinetics of silane are complex and still have not been fully elucidated.⁴⁰ Numerous papers have been published on proposed reaction mechanisms such as Jasinski et al.⁴¹, White et al.⁴², Ring et al.⁴³, Hashimoto et al.⁴⁴, Purnell et al.⁴⁵, Filtvedt et al.⁴⁶ among others. These mechanisms range from a few species (Five by Kleijn et al.⁴⁷) to several hundred reactions (400 by Girschick et al.⁴⁸). Other authors propose intermediates that are not

always physical such as Si atom formation in the gas phase.⁴⁹ Most of the up to date scientific efforts have been focused on understanding silicon growth in wall CVD mainly for applications on electronic chip processing systems.⁵⁰ However, despite all efforts to determine the kinetics of silane decomposition, the proposed mechanisms have not yet been capable of describing the behavior of silicon formation beyond a limited range of operating conditions. The fundamental problem of silicon CVD remains the competition between free atomic diffusion and heat transport.

Full scale CVD systems are far more complicated than a reaction mechanism that for the case of silane pyrolysis is itself not completely understood. They also comprise fluid dynamics, heat, and mass transport limitations and a multicomponent and multiscale factor that combined are very hard to study and predict.⁵¹ For that reason, the proposed study needs to be done in a simplistic reactor where less unknowns are present.

1.2.7. Silicon aerosol formation

A key concept to understand aerosol formation from silane is the critical silane concentration: This is the minimum concentration required to start nucleating silane and forming stable silicon clusters that can be detected by an analytical instrument.³ Sloodman et Parent³ studied the decomposition of silane in the range of 100 ppm to 10% by volume using different dilution gases in a tube reactor. The critical temperature and concentration for SiH_4 homogeneous nucleation was determined in inert gases and hydrogen, and it was observed that hydrogen causes a retardation in particle formation. Results of critical silane concentrations are presented in Figure 1-4.

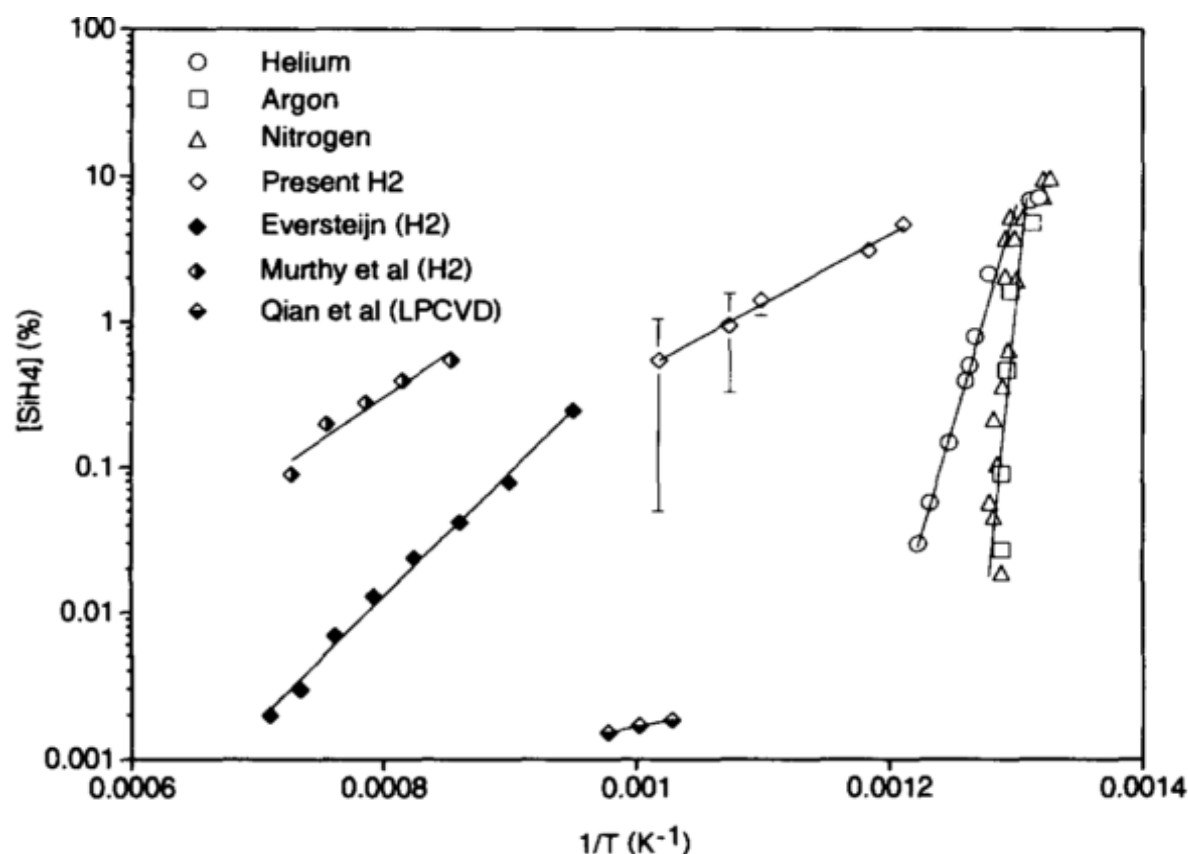


Figure 1-4 Critical silane concentration for nucleation based on detection of particles using a condensation nucleus counter with detection limits of 10nm vs temperature for different dilution gases. (From Sloodman et al³, reproduced with permission).

In the electronic industry, low pressure chemical vapor deposition (LPCVD) has been used to manufacture integrated circuits. Especially in this cases it is important to avoid aerosol formation to stay below the critical silane concentration as a prerequisite. However, this precise control on deposition morphology has the disadvantage of low deposition rates. From a silicon utility manufacturing point of view, this low rates are not economical and therefore reactor operation at conditions above the critical silane concentration are used.

Si aerosol formation has been studied by some authors, most of them at low pressures: Qian et al.⁵² studied silane CVD homogeneous nucleation just above the critical concentration.

Nijhawan et al.⁵³ showed some experimental data on particle nucleation and growth of silicon at pressure lower than 2.5 torr. Van Den Brekel et al.⁵⁴ found the critical silane pressure from Si_2H_2 to be 0.1 torr silane at 725 °C. Other authors have studied silicon aerosol formation using inert gases such as Wiggers et al.⁵⁵, who investigated the formation of silicon powder by pyrolysis of 10 and 40% volume silane diluted in argon. They characterized the samples with TEM, BET, XRD, FTIR, and IR-Spectroscopy. Other authors that studied the same problem are Giunta et al.,⁵⁶ who synthesized particles using N_2 . High pressure homogeneous nucleation has been studied by Odden et al.⁵⁷ using monosilane at temperatures from 690 to 830 °C and pressures from 0.1 to 6.6 MPa employing a free space reactor.

In SiH_4 based fluidized bed reactors (FBR), commercial reactors use SiH_4/H_2 mixtures, where H_2 is recycled and recirculated as the fluidization gas. The reason for using H_2 instead of inert gas atmospheres is to reduce the formation of fines based on Le Châtelier's principle. The presence of H_2 as a product of silicon nuclei formation drives backwards the polymerization reaction and favors CVD compared to nucleation. This is the reason why H_2 is preferred compared to inert gases in the industrial reactors. In addition, pressurized fluidized bed reactors (pFBR) are used to enhance the mass yield per volume of reactor and/or to minimize aerosol formation based on Le Châtelier's principle. Here, the enhancement obtained depends on the fraction of SiH_4 to H_2 used.

1.2.8. Fluidized Bed Reactors (FBR) and aerosol capture in beds

Utilization of gas solid FBR for chemical vapor deposition (CVD) is a promising and versatile tool⁵⁸ but also complex and challenging to model,⁵⁹ and operate²¹ due to the formation of fines. Several authors have studied FBRs for silane decomposition: Reuge et al.⁶⁰ executed simulation work using a multifluid Eulerian model, Filtvedt et al.²⁰ reviewed different FBRs that can be used for Si CVD, Zbib et al.⁶¹ studied characterization of granules from FBRs, Dahl et al.⁶² studied the porosity of polycrystalline silicon grown in FBRs, Caussat et al. studied silicon deposition on FBR both experimentally⁶³ and presented some modelling work⁶⁴ using computational fluid dynamics (CFD). Most of them have proposed empirical correlations to explain the relation of dependent and independent variables.

One important parameter in understanding FBRs is the empirical Geldarts classification for bead size within a fluidized bed. Most of the FBR processes are used employing Group B As shown in Figure 1-5 (density dependent but $\sim 100\mu\text{m}$ to $\sim 1\text{mm}$).⁶⁵ However as particles grow larger and approach the borderline of B-D particles, fluidization becomes more difficult to achieve.

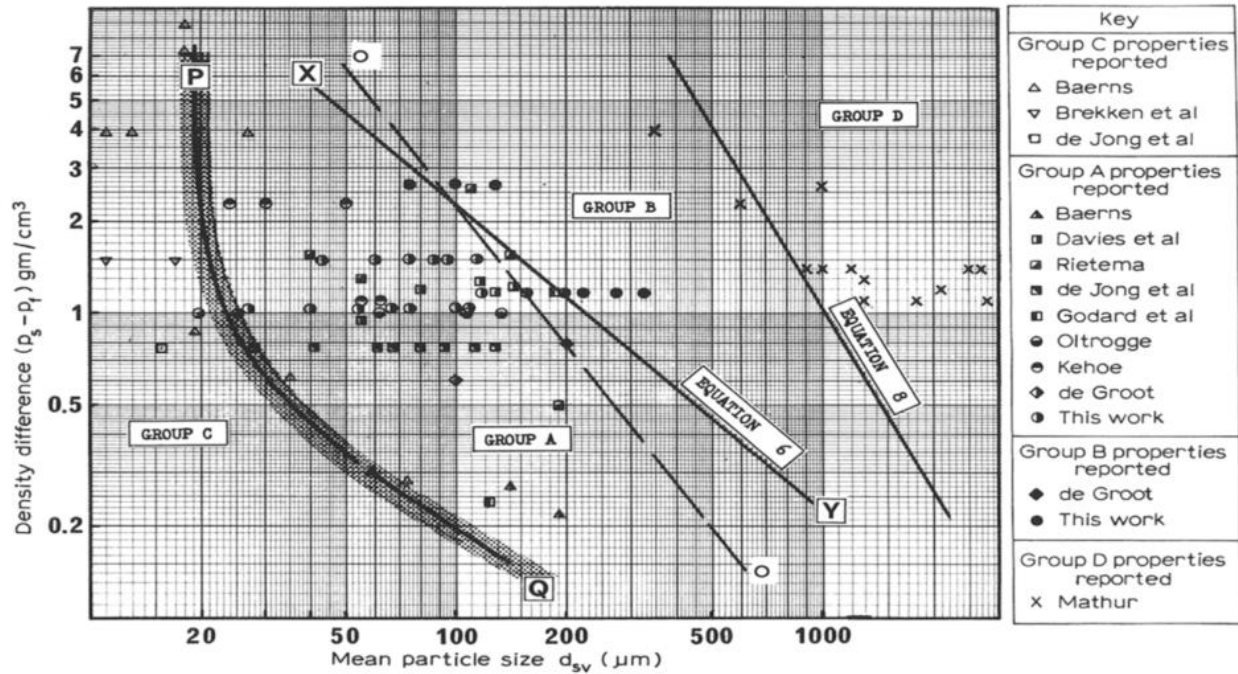


Figure 1-5 Empirical Geldart's classification (D Geldart², reproduced with permission)

Lai, Dudukovic, and Ramachandran⁶⁶ were the first to develop a model for CVD silicon deposition in FBR. Using a modified version of the Kato and Wen⁶⁷ model and a kinetic law from Hogness et al.⁶⁸ and Iya et al.⁶⁹ One of the problems to implement a CVD FBR is the expensive and time consuming requirement to utilize a pilot plant for more certainty during reactor scale up. This prevents the widespread use of this technology.⁷⁰

Hsu et al.¹ studied fines formation in a FBR using the independent variables of bed temperature, silane concentration, and fluidization velocity. They found the best operating conditions were between 600 and 800 °C and a fluidization velocity between 3 and 8 times higher than the minimum. The optimum conditions that they recommend are 700 °C and 5 times higher fluidization velocity than the minimum. They employ summarized kinetics for homogeneous and

heterogeneous reactions and obtained a huge discrepancy between predicted and measured fines elutriated (see Figure 1-6).

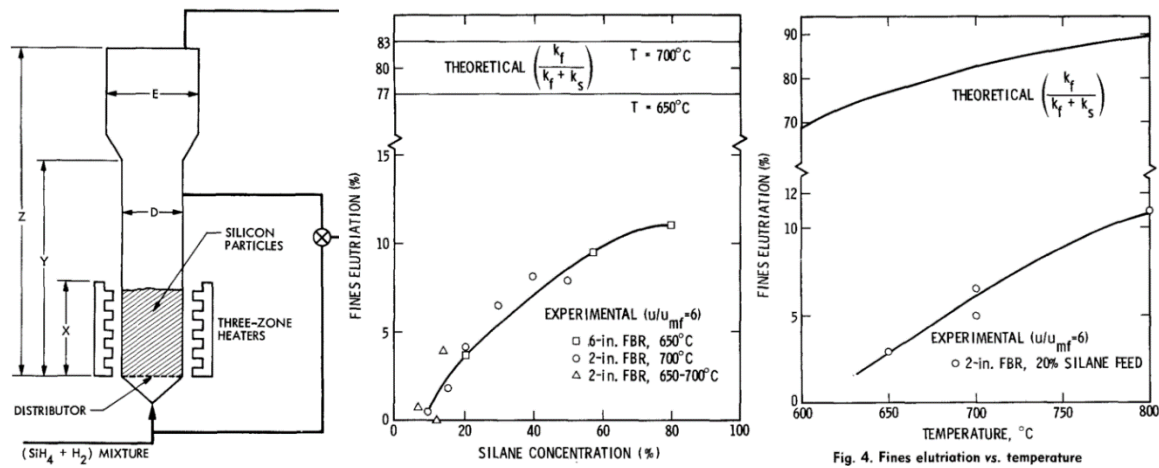


Figure 1-6 Hsu et al.¹ setup and experimental results vs theoretical prediction. A large discrepancy can be seen. Reproduced with permission.

Rohatgi et al.⁷¹ performed a study at the Jet Propulsion Laboratory and reported the successful production of polysilicon from silane in a 6 inch diameter fluidized bed reactor. A proof of concept was provided for using different silane concentrations and continuous operation was achieved for up to 4 hrs. A 90% of deposition of the total silicon injected in the reactor was achieved. The remaining 10% of the inlet silicon mass was found to be elutriated as fines.

1.3. RESEARCH OBJECTIVES

The main objectives of this work are to contribute to the theoretical understanding of silicon processing, and to provide experimental support for material usage optimization alternatives in the wafering technologies. All of these represent echelons in the effort of four interrelated long term goals:

1. Developing cost effective renewable energies
2. Reducing the price of the high purity silicon commodity
3. Minimizing carbon footprint in the manufacturing of silicon
4. Abating global warming

More concisely, the objectives of this work are divided into two sections, each divided into subsections:

1) Optimize carbon elimination in kerf while limiting its oxidation to enable its recycling

This section consists of three parts: the proof of concept for the elimination of carbon from kerf using a furnace aerosol reactor, the determination of the kinetics and reaction mechanism for the carbon elimination through thermal treatment in air and nitrogen, and finally the determination of kinetics of silicon nanoparticles and kerf oxidation. All together this section provides the kinetic information required to design a carbon elimination furnace aerosol reactor that makes kerf recycling more feasible. A description of each subtask follows.

a) Validate an aerosol method of carbon elimination in kerf

Kerf purification involves the elimination of numerous contaminants, metals can generally be washed out by using acid leaching. However, carbon and organic compounds are more difficult to remove because of their hydrophobic properties and similarities with silicon as

both elements are in the same group of the periodic table. Conventional burning of carbon is undesirable because excessive silicon oxidation occurs. Inert gas pyrolysis on the other hand is insufficient for full carbon elimination. Under these premises, a method that maximizes carbon removal and minimizes silicon oxidation is required. Aerosol methods are good candidates for the task as they can reduce diffusion constraints by allowing intimate contact of powder and the process gas, thus boosting the overall rate of carbon elimination. The proposed Furnace Aerosol Reactor (FuAR) needs to demonstrate its capability to reduce total carbon content in kerf while keeping silicon oxidation at low levels.

b) Determine the kinetics of carbon elimination in air and inert gas atmosphere

The kinetics and mechanism of carbon elimination in kerf are necessary to understand the combustion/pyrolysis phenomena in air and nitrogen respectively, and to assess their viability for implementation in an industrial reactor. Therefore, the kinetic expressions for the removal of carbon from kerf needs to be studied under both atmospheres. The model should have applicability in a wide range of reactor conditions in order to provide flexibility for finding optimal operating conditions in the reactor. A mechanism of the process needs to be obtained, and it should be simple and describe the process qualitatively.

c) Develop the kinetics of silicon oxidation in nanoparticles and kerf

While carbon is eliminated from kerf in an air atmosphere, silicon gets oxidized. This also occurs in inert gas atmospheres because trace amounts of oxygen react with the high surface area of kerf ($\sim 10 \text{ m}^2/\text{g}$). However, different slicing methods or cut velocities could produce kerf with different surface areas. Thus, it is important for process optimization to understand silicon nanoparticles oxidation kinetics in air atmosphere employing standards

of comparable size as kerf. This is necessary because the kinetics of silicon oxidation is different for nanoparticles than for a wafer.⁷² The kinetics should be provided as a function of measurable parameters.

2) Understand the initial stages of silicon aerosols formation during silane pyrolysis

a) Build a setup for silane pyrolysis

A silane reactor with accurate control of process parameters such as mass flow rate of reagents, temperature control, pressure control, and capability to pressurize and purge needs to be built. The reactor should be solid rock, but also sufficiently modular for allowing to change reactor parameters without significant setup modification. The reactor should allow for online characterization of produced aerosols and, at the same time, should permit offline characterizations by means of sample collection through a filter holder. The outlet should also be equipped with a pump to purge the system at startup and end of the experimental runs.

b) Measure a stable silicon hydride cluster from silane pyrolysis

It is important to identify stable silicon hydride cluster formation from silane pyrolysis for several reasons including to determine the kinetics of its formation and the subsequent formation of silicon powder. By better understanding the process for nuclei formation, kinetic mechanistic computational models can be validated so low pressure chemical vapor deposition (LPCVD) processes used in the semiconductor industry can be optimized to the maximum rate without risking nucleation of silicon nanoparticles.

c) Understand the mechanisms determining the morphology of silicon aerosols formed in a tubular reactor

Numerous studies have been performed to understand silane pyrolysis kinetics. Most of them are descriptive on the formation process and do not fully show the mechanisms of CVD synthesized silicon aerosols and their morphology. In this subtask, the target is to obtain a kinetic model to predict the behavior of nucleation and condensation. Towards that goal, the change of aerosol morphological parameters such as primary particle size, aerodynamic size distribution agglomerate size and crystallite size should be measured and analyzed.

1.4. STRUCTURE OF THESIS

This work begins with an introductory chapter that provides an overview of the silicon market, current refining processes, and a literature review of the full thesis. The body of this thesis is subdivided in two sections. Section one refers to kerf recycling efforts and comprise three chapters. Section two is devoted to silane pyrolysis and it is made up of two chapters which focus on gaining a better understanding of the process of silane pyrolysis and the initial stages of aerosol formation.

A more detailed overview of each chapter is given below:

- Chapter 1 is the introduction of this dissertation

Section One Chapters include material relevant for kerf recycling

- In Chapter 2, a proof of concept for the application of furnace aerosol reactor (FUAR) is executed and achieved. The FUAR demonstrates good capabilities of eliminating carbon and is tested in two atmospheres, nitrogen, and air. Both cases show a decrease in the total content of carbon, but only the air case achieves elimination below detection limits of the instrument.
- Chapter 3 is dedicated to the development of a mechanistic understanding of the process of carbon elimination in kerf for both inert (nitrogen) and oxidizing (air) atmospheres. Carbon in kerf comes from polyethylene/polypropylene glycol from the slicing lubricant and epoxy. The activation energy for the complex process is determined by using the kinetic methods of KAS, OFW, and Kissinger methods. More techniques are used including GCMS, FTIR, SEM, TC, and in conjunction with the literature review of poly-

ethylene glycol and polypropylene glycol (related compounds) a two stage mechanism is proposed. At the end of the thermal treatment all carbon is eliminated in the air atmosphere but 12% total carbon remains in the nitrogen atmosphere.

- Chapter 4 is dedicated to the oxidation of high surface area polycrystalline silicon agglomerates with BET surface areas in the range of 3-19 m²/g, and XRD determined crystallite sizes around 50-80 nm. The nanoparticles behave in a different manner than the monocrystalline wafer oxidation of the Deal and Grove model. The activation energy for the process of oxidation is obtained and it is found to correlate with the mean crystallite size. A single expression for the parabolic rate constant that contains the BET surface area, crystallite size, and surface roughness is developed for all samples and is shown that it can predict the 1000 °C oxidation of all silicon and kerf samples.

Section Two of this dissertation is focused on better understanding silane pyrolysis and the initial stages of aerosol formation.

- Chapter 5 describes the measurement of a stable high molecular weight (Si_nH_m with $n>5$) silicon hydride from silane pyrolysis using a half mini differential mobility analyzer (DMA). The mean size for the cluster measured is found to be 0.75 nm. The maximum concentration detected was at 440 °C for a concentration of 0.3 % SiH_4 in helium.
- Chapter 6 focuses on the synthesis of silicon aerosols and their differences based on the reactor conditions implemented such as silane initial concentration, residence time, and reactor temperature. A model is proposed for the initial nucleation and subsequent condensation of polymerized silane into particles after finding a condition where sintering does not occur regardless of the dynamic range of residence times in the reactor. A full

range of measurements are performed to test the effect of concentration on the primary particle size distribution within the agglomerates using TEM. Kinetic information is inferred based on primary particle size change as concentration increases. With this information a relative rate description is proposed in which condensation/nucleation is well correlated with a 1.5/1 relative orders. This value is useful for determining the rate limiting process during aerosol formation from silane, either the chemical kinetics or the aerosol dynamics.

- Chapter 7 summarizes the mean results for all chapters and suggests future research directions.

The document ends with various annexes including fluidized bed reactor silicon powder and silicon beads grown in its interior. In addition, the curriculum vitae of the author of the present work is also listed.

CHAPTER 2:ELIMINATION OF CARBON CONTAMINATION FROM KERF USING A FURNACE AEROSOL REACTOR

Results of this chapter have been published:

Vazquez-Pufleau, M., Chadha, T. Yablonsky G. Erk, H. and Biswas, P., Elimination of Carbon Contamination from Silicon Kerf using a Furnace Aerosol Reactor (FuAR) Methodology; Ind. Eng. Chem. Res., 2015, 54 (22), pp 5914–5920, DOI: 10.1021/acs.iecr.5b0057

2.1. Abstract

Approximately 40% of the refined silicon is lost as sawdust (kerf) during the cutting process while producing wafers. Attempts have been made to recycle this kerf, but abundant impurities such as carbon (~13000 ppm) burden its recovery. Using conventional bulk heating methods to remove carbon requires long residence time and inevitably causes silicon oxidation. This makes the treated kerf unsuitable for further processing and re-use. A novel aerosol method that is effective for selective carbon removal from silicon kerf at low residence times is described. The design of the aerosol process is supported by thermogravimetric analysis of kerf that provides insights into kinetics of the carbon removal process. At 900 °C in an air atmosphere carbon was removed below detection levels at a residence time of 6 seconds. Under the same conditions in a nitrogen atmosphere, 90% elimination of carbon was measured. Minimal oxidation of the Si sample was observed under these conditions.

2.2. Introduction

Silicon is a metalloid,⁹ the second most abundant element in the earth's crust¹⁰ after oxygen.¹¹ After refining silicon to metallurgical grade, most of it is used as an alloy to produce silicon steel¹² or aluminum,¹³ followed by usage in polymeric form as silicones.¹⁴ To lesser extents it is reacted with nitrogen to form silicon nitride or with carbon to form silicon carbide for high performance ceramic applications.¹⁵ Although only a small fraction (less than 4%) of the total silicon produced is processed to high purity,¹⁶ this refined silicon plays a central role in the daily lives of contemporary societies of the digital age.¹⁷ This refined silicon is used mainly in the electronics industry for integrated circuits¹⁸, and in solar panels¹⁹.

For material usage optimization both electronic and solar panel industries require silicon to be supplied as thin wafers mainly produced by slicing ingots with an abrasive wire. Other methods to produce wafers such as ribbon technologies²⁹ have been developed. Nevertheless, one hundred percent of the electronic grade silicon (99.9999999% purity)⁷³ is manufactured using Czochralski monocrystalline silicon to avoid interference of impurities or grain boundaries within the minute electronic transistors in an integrated circuit.⁷⁴ In the solar panel industry; the current silicon market is still highly dominated by monocrystalline (MC) and polycrystalline (PC) wafers due to higher efficiencies,^{29,30} more reliability²² and better return on investment.³¹ Wafers are sliced from ingots using fixed abrasive or slurry methods,³² with the former method offering better wafer quality and reduced rejections.³⁶ However both methods result in significant waste from the ultrapure material being sliced.

In the slicing process more than 40% of the MC or PC ingot initial material becomes silicon sawdust (kerf) waste.³¹ Kerf is a complex industrial residue involving numerous metallic contaminants,³³ and organics coming mainly from the polymeric lubricant used during the cutting process, epoxy resin and glue of the ingot mount. Despite the technical difficulties imposed by abundant contaminants, the economic potential of kerf recycling has encouraged various researchers to find viable ways to approach these challenges. Previous studies focused primarily on separating silicon carbide (SiC) abrasives from kerf using various techniques.^{25, 34} Nevertheless, the previously common slurry sawing technique for silicon has been upgraded to a fixed-abrasive diamond sawing technique, mainly because diamond sawing causes less surface damage to the wafers, provides better thickness consistency and results in lower concentrations of metal impurities derived from the slicing wire on the wafer surface.³⁶

Few studies have been conducted on purification of kerf produced by diamond wire slicing. Maeda et al.,³⁷ after milling and etching kerf, fused it to build solar cells. Tomono et al.³⁸ explored generating bromosilanes from kerf and then distilling them. They reported carbon removal as a key problem. Dhamrin et al.³⁹ also stated that carbon contamination on their silicon wafers from recycled kerf severely negatively impacted cell efficiency.

Carbon in kerf can be eliminated by increasing the temperature to permit its oxidation. Currently available methods to oxidize carbonaceous compounds include bulk heating in a furnace,⁷⁵ rotary kiln⁷⁶, or fluidized bed.⁷⁷ These methods successfully lower the total carbon (TC) content, but due to large diffusion timescales, require long residence times to permit intimate contact of the carbonaceous species with oxygen. Long residence times bring silicon oxidation to

levels that prevent kerf from further processing and reuse. The reason is the higher fusion point of SiO_2 compared to Si. If a highly oxidized kerf were introduced into a silicon crucible at normal operating conditions, the presence of a SiO_2 surface layer would prevent kerf melting. On the other hand, inert atmospheres limit the degree of silicon oxidation but do not permit lubricant oxidation, which undergoes a different volatilization mechanism that might not yield full elimination of carbon from kerf. Thus it is important to develop a process that selectively eliminates carbonaceous compounds without oxidizing silicon. Additionally, an understanding of silicon oxidation kinetics is essential. However, despite being extensively studied, kinetic data reported for silicon oxidation show large discrepancies. Ranges of activation energy are reported from 113 kJ/mol to 418 kJ/mol for single crystal oxidation, with kinetics being a complex function of temperature, oxygen partial pressure, and formed oxide thickness.⁷⁸

Many studies have been done to elucidate pyrolysis and combustion kinetics for different materials containing complex carbonaceous species.⁷⁹ In addition, the concept of optimizing conditions to favor kinetics of reaction for metal recycling technologies has also been studied. Some researchers have applied kinetic principles to develop recycling techniques for different residual metals,⁸⁰ however none of the researchers have approached the removal of carbon from kerf and performed a kinetic study to predict and optimize removal under different conditions. This necessity motivates us to study complex kinetics of carbon removal in kerf.

The objective of this work is to establish the furnace aerosol reactor (FuAR) as an effective method to eliminate the carbon contamination from kerf. Kerf samples were characterized using x-ray diffraction (XRD), scanning electron microscopy (SEM), transmission electron microscopy

(TEM), Brunauer-Emmett-Teller surface area measurement (BET), total carbon (TC), scanning mobility particle sizer (SMPS) and aerodynamic particle sizer (APS). Thermogravimetric analysis (TGA) was used to study the kinetics of carbon oxidation/volatilization. This novel technique was assayed to selectively eliminate carbonaceous compounds, while limiting the extent of silicon oxidation. Finally, a phenomenological model was developed to predict the elimination of carbonaceous compounds at 300 °C and extended to the whole range of experimental temperatures using activation energies from the Kissinger method.⁸¹ Further, the experimental results were compared with FuAR experimental values.

2.3. Methods

2.3.1. Experimental setup

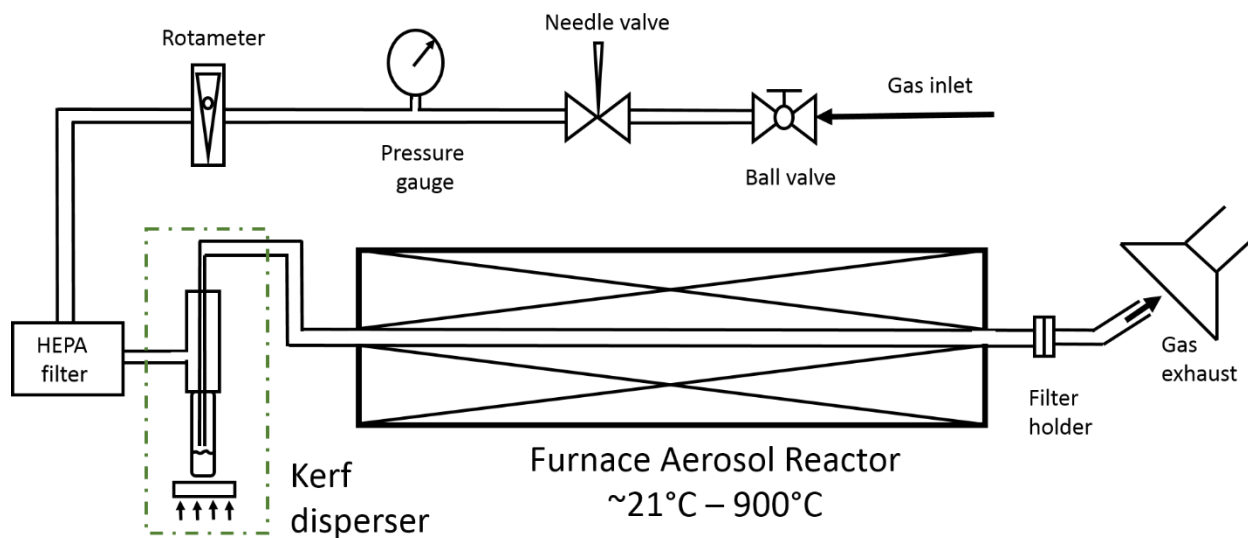


Figure 2-1 FuAR Experimental setup. It consists of a controlled gas supply, a dust disperser mechanism, an electric furnace, and a filter for sample collection.

The experimental setup used for the elimination of carbon from kerf is shown in Figure 2-1. The setup is made of a furnace equipped with a PID temperature controller. The inlet gas used

was either air or nitrogen and a dry homemade powder disperser was used for aerosolizing kerf. A 1” stainless steel tubing was used to direct the gas into the 1/16” interior tubing where shear forces disperse the kerf. Dispersion rate is controlled by a syringe pump moving plate that lifts the sample to close proximity of the smaller tube to allow its dispersion. After passing through the furnace, the sample is collected in a quartz fiber filter for further analysis

2.3.2. Test plan

The starting material used for the experiments was kerf powder provided by SunEdison Inc. in dry form from fixed abrasive silicon sawing residue. The dust was filtered out, then washed and dried to 24% moisture content. The reported carbon concentration was 13000 ppm in the sample received. An overall list of experiments performed is provided in Table 2-1.

Table 2-1 Experiments list for carbon elimination kinetics determination and experimental runs in FuAR

Test #	Test	Technique	Description	Objective	Atmosphere	Range of temperature	Figure
1	20 °C/min kerf air	TGA	linear heating program (LHP)	Observe carbon elimination for different atmospheres	air	20 °C - 1000 °C	2-4a
2	20 °C/min kerf N ₂				N ₂		
3	Kerf air isothermal		isothermal at 300 °C for 1 hr.	Single temperature kinetic determination	air		2-4b
4	Kerf N ₂ isothermal				N ₂		
5	FuAR kerf air	FuAR & Total Carbon	single temperature per reading	Testing of carbon elimination on reactor	air	20 °C, 300 °C, 500 °C, 700 °C, 900 °C	2-5a
6	FuAR kerf N ₂				N ₂		2-5b

2.3.3. Characterization tools

Kerf characterization and preparation

The crystallographic structure of kerf was measured using XRD (Rigaku D-MAX/A Diffractometer, Japan) with Cu-K α radiation (wavelength= 1.5406 Å) at 35 kV and 35mA. The surface area was determined by using a BET instrument (Nova 2000e BET, Quantachrome instruments, Boynton Beach, FL). Pore volume and diameter were measured using Barrett—Joyner—Halenda (BJH) desorption isotherms in the same instrument. TOC was measured using a Shimadzu SSM-5000 (Schimadzu, Columbia, MD) with a solid sample module. Surface morphology and structural analysis was obtained by TEM in a FEI Spirit TEM and SEM in a FEI Nova 2300 SEM (FEI, Hillsboro, OR).

Before introducing kerf into the FuAR, it was dried to permit more efficient de-agglomeration and thus a higher atomization efficiency and better mass transfer for the elimination of carbonaceous compounds. Therefore, kerf was ground with a clean ceramic mortar and pestle, and dried at 120 °C for 24 hours while it was regularly mixed to ensure uniform and complete moisture removal.

Experimental determination of carbon removal kinetics

TGA was performed using a Q5000 IR Thermogravimetric Analyzer (TA Instruments, New Castle, DE). Several constant heating and isothermal programs were used in the TGA to develop kinetic estimations for the elimination of carbonaceous compounds in the FuAR. The mass (20 to 30 mg) of kerf sample used was small enough to ensure that there was no heat or mass transfer limitations. The constant heating ramps for both air and nitrogen were done at 20 °C/min with 1 hour isothermal at 120 °C for moisture removal. In the case of nitrogen, the furnace was

purged for 10 min before heating. Isothermal determinations were done at 300 °C. This temperature was chosen above the maximum decomposition rate temperature but not too high to permit good data resolution. The TGA furnace tightness to air leaks and the absence of oxygen in the N₂ tank were verified by employing a standard procedure using copper oxalate and testing the weight difference after 30 min at 400 °C. The experimental plan is presented in Table 1.

2.4. Model description

According to Vyazovkin et al.,⁸² and to Zhou et al.⁸³ a simple TGA reaction model is presented to be a function of temperature, T and conversion, α . This can be represented as

$$\frac{d\alpha}{dt} = kf(\alpha) \quad (2-1)$$

where k is the apparent kinetic constant at a given temperature and it is assumed to follow Arrhenius behavior:

$$k = A_0 \exp(-E_A/RT) \quad (2-2)$$

where A_0 is a preexponential factor and E_A the activation energy. In typical experimental data, the measured values are conversion temperature dependent. Generally, they can exhibit different features, i.e. accelerating, decelerating and sigmoidal. The phenomenological model to fit these three different types of conversion dependencies is:

$$f(\alpha) = \alpha^m (1 - \alpha)^n [-\ln(1 - \alpha)]^p \quad (2-3)$$

where m , n and p are phenomenological parameters. In this case each of the three phenomenological terms can be used to reflect different trends observed experimentally. The first term implies an accelerating dependence, the second relates to a decelerating one, and the third to

a sigmoidal relationship.⁸² The normal practice to determine the dominant reaction trend is to plot conversion versus time. This provides a clear reaction trend. The other two mechanisms are then assumed to be negligible. Interestingly, most of the reactions in nature are decelerating (m and p are set equal to zero).⁸²

2.4.1. Aerosolization and in flight carbon elimination

The furnace aerosol reactor (FuAR) setup is illustrated in Figure 2-1. The setup consists of the following parts from top right onwards: The stream starts with a compressed gas source: ultrapure nitrogen gas, (Airgas 99.999%) or compressed air depending on the test. The flow rate of the stream is controlled using a needle valve. All incoming aerosols are eliminated using a high efficiency particulate air (HEPA) filter. The particle free gas is then introduced into a homemade dust disperser where particulates are carried and fed to the FuAR; a SS 316 pipe in the interior of an efficiently temperature controlled 6kW Lindberg/Blue Electric Furnace (Thermo Scientific, Waltham, MA). From there the sample is carried by the gas into a Quartz filter on which the sample is collected and later extracted and analyzed.

All runs in the FuAR were fixed at constant values: The gas flow rate was 5 liter per minute. The mean residence time in the furnace was 0.09 minutes. The moving part of the disperser had a displacement of 4 cm per hour. The carbon elimination was tested by changing the furnace temperature from room temperature (RT) to 300 °C, 500 °C, 700 °C and 900 °C. Particle size distributions were measured using a 3321 APS spectrometer (TSI Inc, Shoreview, MN) and a 3080 SMPS from the same company. (TSI Inc).

2.5. Results and Discussion

The microscopic properties and composition of kerf is presented first. Results of TGA are presented to establish the carbon removal kinetics during heating. Knowing this, a series of operating conditions were tested in the FuAR to demonstrate carbon removal from kerf.

2.5.1. Characterization of as received kerf

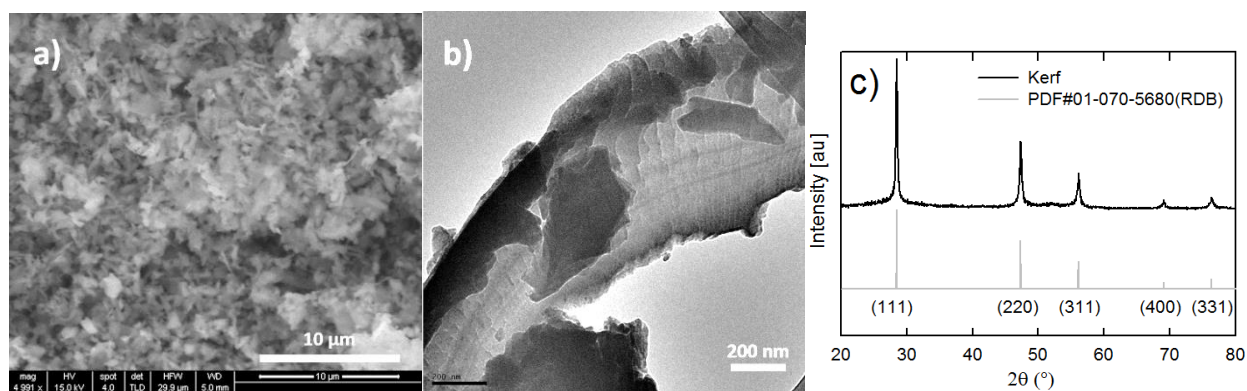


Figure 2-2 a) SEM image showing the flake structure of kerf. b) TEM image for kerf. Plastic deformation can be observed in the flake shaped powder. c) XRD spectra for kerf and the reference for polysilicon. After being cut the monocrystalline silicon becomes polycrystalline in kerf due to the intense shear forces

Kerf was characterized by numerous techniques. SEM and TEM characterization indicated it to be a highly aggregated material made of thin flake-layers about 100 nm each (Figure 2-2a and 2b). This makes the material prone to easy oxidation and hard to handle due to its high surface area.

XRD was performed to prove the presence of silicon carbide (SiC) in the kerf sample (Figure 2-2c). First, the kerf sample contained no significant amounts of crystalline silicon carbide, as the SiC pattern was not found. XRD typical detection limits are in the order of 1% for mixed powders. Second, kerf was found to be made of polycrystalline silicon. This is an interesting

observation that describes the mechanism of diamond wire sawing that generated a plastic deformation in the kerf flakes as visible in Figure 2-2b changing the structure from monocrystalline to polycrystalline. This observation is in good agreement with the work of Chao et al.,³⁵ where ductile behavior of silicon under optimized diamond cutting conditions was studied.

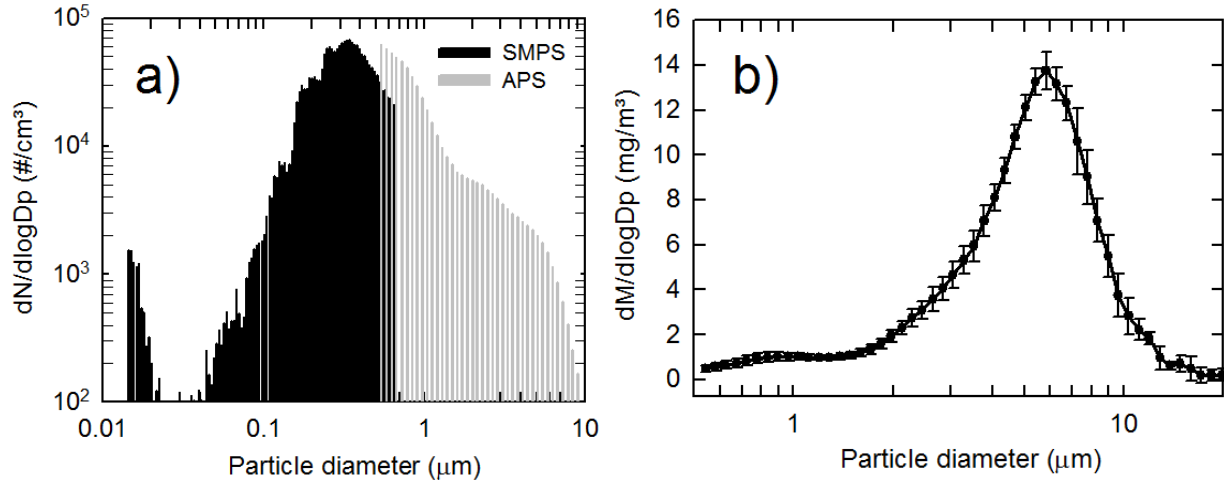


Figure 2-3 a) Size distribution function for number concentration using SMPS and APS b) size distribution for mass concentration determined by APS. The mass from the SMPS particles is negligible and therefore not included.

Surface area determined using a BET isotherm was estimated to be: $10 \text{ m}^2/\text{g}$. Using the same instrument, kerf was determined to have a pore volume of $0.05 \text{ cm}^3/\text{g}$ and a pore radius of 15.6 \AA . TC indicated that carbon (1.3%) is the main contaminant after oxygen in this type of kerf. Inorganic carbon was not found in the kerf, indicating that diamond particles are not present above 50ppm, which is the instrument detection limit. The results of kerf size distribution characterization performed by APS and SMPS can be seen for number concentration in Figure 2-3a and for mass concentration in Figure 2-3b. These size distributions were determined using the setup shown in Figure 2-1. It can be observed that the kerf has unimodal distribution with a particle mass mode at $5.5 \mu\text{m}$ and a particle number concentration mode at 330 nm . The differences

between SMPS and APS determinations are attributed to intrinsic dissimilarities in measurement principles, the former being based on electrical mobility and the latter on optical methods. The rate of carbon elimination is expected to be much slower for bigger particles or bulk material, due to additional diffusion resistance. In this study, the particles are sufficiently small so that diffusion resistances can be neglected.

2.5.2. TGA results of carbon elimination kinetics

In Figure 2-4 a), TGA results for silicon and kerf in different atmospheres are presented. It is evident that some silicon oxidizes. In the case of air, the reason for oxidation is its 21% oxygen content. This causes a significant increase in the normalized weight at high temperatures, accounting for more than 6% oxygen gain for the described conditions. In the case of the silicon standard employed, the rate of silicon oxidation at moderate temperatures is low but it becomes important above 500 °C as seen in Figure 2-4 a).

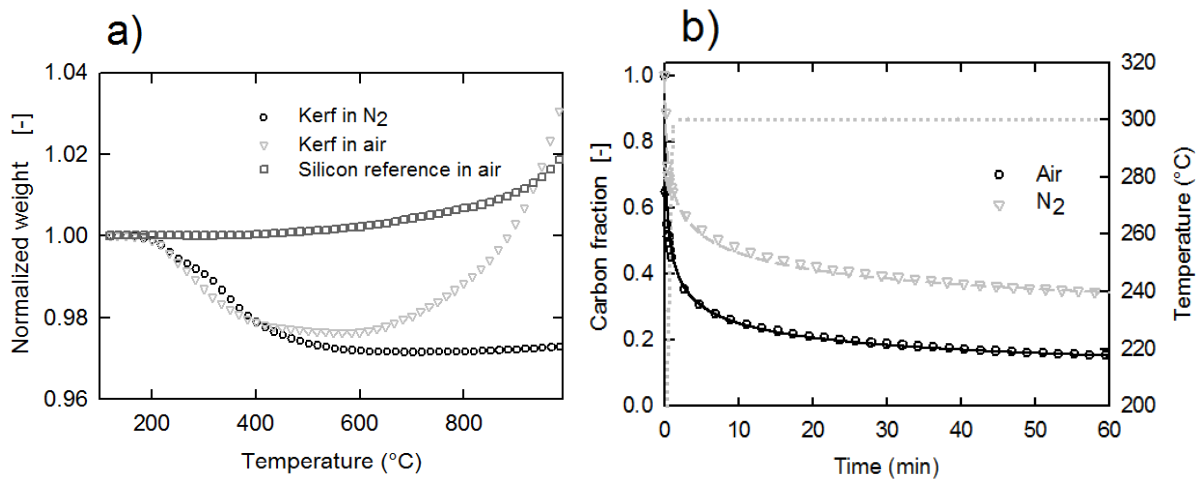


Figure 2-4 a) Normalized weight change as a function of temperature for linear heating rate at 20 °C per minute. It can be seen that first carbon is eliminated and then silicon is oxidized. Under nitrogen atmosphere almost no weight gain is observed. b) Remaining carbon fraction calculated from isothermal program in TGA versus prediction from equation 2-4 on the left y axis. On the right axis the TGA thermocouple temperature is displayed

Commercial nitrogen atmospheres contain oxygen traces that may result in silicon oxidation although at a low rate. Comparing the minimum and final weight measurements of kerf under N₂ at 1000 °C, a weight increase of 0.5% can be seen (Figure 2-4 a). Silicon nitride formation could be a reason, however this reaction is known to be negligible up to 1200 °C due to the formation of an initial nitride surface layer that restricts the access of nitrogen to lower layers.⁸⁴ Thus the minor weight increase in Figure 2-4 (a) is considered to be caused by trace amounts of oxygen (up to 0.001%) contained in ultrapure nitrogen that flows continuously. Any trace oxygen will be very reactive at temperatures above 500 °C and thus will oxidize the silicon. This shows that strict pyrolysis is hard to accomplish in practical conditions and there is always some oxidation occurring in parallel. This phenomenon is particularly a concern for bulk carbon elimination procedures, where high residence times, even under inert atmospheres, cause the silicon in the treated kerf to oxidize. Thus this demonstrates the great advantage of using aerosol techniques that require low residence time, and hence, result in minimum silicon oxidation while maximizing carbon elimination.

In order to determine if we have accelerating, decelerating or sigmoidal kinetics (Vyazovkin et al.⁸²), preliminary runs were conducted and the conversion versus time plotted. Based on the decelerating nature of the reactions, several models are possible. Kinetic dependences were determined to be decelerating with no specific features. Thus, we used the power law model for its advantages as a simple and precise model. Furthermore, it is known that the complex mixture of organic contaminants do not decompose in a single step, and a mechanistic approach would involve a high degree of mathematical complexity without guaranty of accuracy. Therefore, for

providing the simplicity and better accuracy desirable in the industry, the most suitable model was used:

$$-r_A = k[1 - \alpha]^N \quad (2-4)$$

This equation is also known as the power law phenomenological model where k and N are factors obtained by fitting the experimental data. The values for the apparent reaction constants at 300 °C are $k = 4.077\text{min}^{-1}$, $N=4.607$ for air and $k=1.681\text{min}^{-1}$, $N=6.995$ for nitrogen. The physical meaning of the high value for the exponents in the phenomenological models can be attributed to the complexity of the mechanism for the long series of reactions, analogous to polymerization phenomena, that carbonaceous compounds pass through for removal in kerf. This sequence may include synthesis of macromolecules followed by its decomposition. The overall reaction is irreversible but the high order of reaction is an indication of a series of fast equilibrium processes that comprise the overall reaction. The fitted equations are plotted versus the experimental data for isothermal TGA measurements and are presented in Figure 2-4 b). They are in good agreement with the experimental data.

2.5.3. FuAR experimental runs and model validation

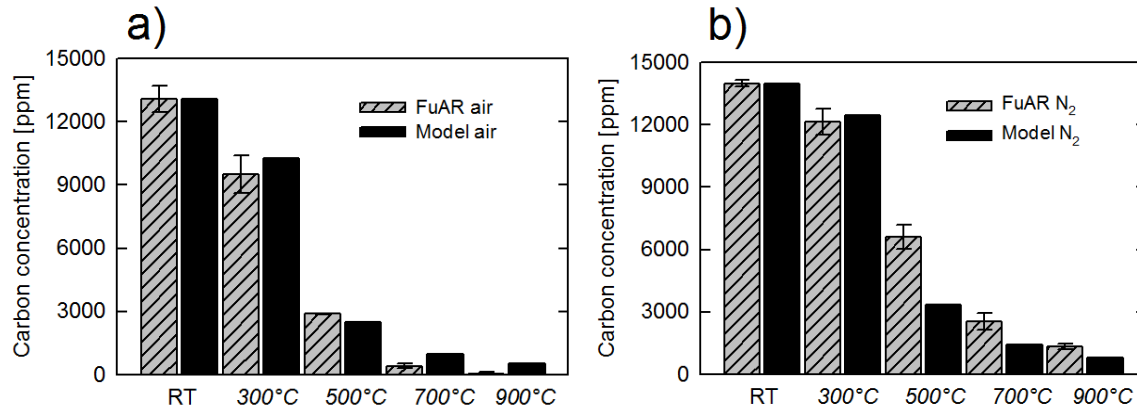


Figure 2-5 a) Carbon elimination in FuAR versus model for kerf atomized under air atmosphere. b) And under nitrogen atmosphere. For the operating conditions in N₂, carbon was not completely eliminated at 900 °C.

Consistent with predictions of the TGA, a reduction in carbon content in kerf was achieved in short time for different FuAR processing temperatures and gases (Figure 2-5 a for air and Figure 2-5 b for nitrogen). Both the FuAR and TGA experiments are reaction limited and have no mass or heat transfer limitations. This is verified by estimation of the Weisz modulus criterion⁸⁵, and the modulus is less than 0.15 for our system.

By comparing these graphs, it can be observed that the rate of carbonaceous compounds elimination is faster in an oxidizing atmosphere (air) than in an inert atmosphere (N₂). Quicker mass elimination of organic carbon in oxygen than in nitrogen is consistent with previous observations of polymer thermal and thermo-oxidative decomposition kinetics.⁸⁶ In Figure 2-4a) it can be observed that for kerf, the maximum weight loss occurs at around 600 °C. In the case of an air atmosphere, as temperature rises beyond this point, the weight grows rapidly indicating that the kinetics of silicon oxidation begin to become important. The same effect is observed for the nitrogen atmosphere but the rate of weight increase is to a lesser extent. The total mass loss

attributed to carbonaceous compounds is 27000 ppm, from this only 13000 ppm is elemental carbon and the rest can be attributed to covalently bound H and OH radicals in the polymeric chain contained in the lubricant.

The FuAR can be treated as an isothermal plug flow reactor (PFR). With an ideal differential equation:

$$\frac{d\alpha}{d\tau} = -r_A \quad (2-5)$$

where τ is residence time = 0.09 min in the furnace. Coupling it with the power law kinetics and solving for the conversion, α :

$$\alpha = 1 - \left\{ \left[\frac{1}{N-1} + k\tau \right] (N-1) \right\}^{\left(\frac{1}{1-N} \right)} \quad (2-6)$$

In Figure 2-5 the measured carbon elimination is compared to the prediction of equation 6 for the 300 °C run. As it can be seen, the kinetic model derived from the TGA shows good consistency with the experimental data from the FuAR. Additionally, based on the Arrhenius equation, kinetic constants for the temperatures evaluated in the FuAR were computed using activation energies obtained by the Kissinger method; 105kJ/mol for air and 160kJ/mol for nitrogen atmospheres.⁸¹ Certainly these activation energies should be considered to be approximate overall values. A prediction was made for each of the run temperatures and was plotted in Figure 2-5a) for air and Figure 2-5 b) for N₂. Most of the results show good agreement. However, some discrepancy exists for the run at 500 °C for both nitrogen and air. The higher measurement of carbon in FuAR compared to the model is attributed to recaptured organic volatiles. These organic fragments volatilize from the solid phase and do not have enough time to decompose in the gas phase, being re-adsorbed by the product in the filter cake at the outlet. This

is the main difference between the TGA reactor used for the modeling and the FuAR. The first is a batch reactor where kerf remains separated from the gas outlet. Conversely the second is a continuous PFR in which both kerf and the evolved gases get transported in the same stream.

Silicon oxidation preliminary work using a standard with the same surface area as kerf has shown that for 6 seconds residence time, less than 0.1% of silicon gets oxidized at 1000 °C. More research is required to develop kinetic expressions for silicon oxidation in kerf.

2.6. Conclusions

A novel approach for carbon elimination in silicon kerf has been demonstrated. Kerf was atomized in the FuAR setup and carbon elimination was determined at different temperatures for different gases. The removal of carbonaceous compounds from kerf was faster in oxygen than in inert atmospheres. These results were also confirmed by exploratory TGA measurements where weight reduction for kerf under both nitrogen and air atmospheres was measured. The silicon oxidation rate is highly correlated to temperature, hence a balance needs to be achieved between temperature and residence time in the reactor. Based on the intricate nature of the contaminants, it is clear that complex reactions take place and a simple mechanistic model might not be achievable. In this work a single temperature power law phenomenological model was obtained at 300 °C for carbonaceous compounds elimination for both air and N₂. Finally, the phenomenological model generated was tested against the FuAR kerf carbon output for temperatures ranging from room temperature to 900 °C. Using activation energy values gained by the Kissinger method, the conversion in the full range of experimental conditions in the FuAR was evaluated against the model showing good agreement.

More extensive kinetic determinations for kerf and silicon are required to provide a model that can predict both oxidation of silicon and elimination of carbonaceous compounds of kerf in the FuAR. Differences between using other concentrations of oxygen is an interesting path for further research and improvement on carbon elimination from kerf. Based on both models, an industrial scale reactor can be optimized over a wider temperature range to ensure complete carbon removal while limiting to minimum silicon oxidation.

CHAPTER 3: ACTIVATION ENERGY DETERMINATION AND MECHANISTIC CONSIDERATIONS OF CARBON ELIMINATION IN KERF

Results of this chapter have been submitted to a peer review journal:

Vazquez-Pufleau, M., Chadha, T. Yablonsky, G. and Biswas, P., Kinetics of Carbon elimination from Kerf by Thermogravimetric Analysis with mechanistic insights (2016), Nature Scientific Reports, Submitted

3.1. Abstract

Ultrapure silicon, widely used in the electronic and solar industry, is expensive despite the element's abundance in the earth's crust. After purification and crystal ingot formation, 40% of the ultrapure material is lost as kerf during slicing to produce wafers. Kerf is currently not being recycled due to engineering challenges and costs associated with removing its abundant impurities. Carbon left behind from the lubricant used for slicing is an important contaminant in kerf and its removal is difficult and complex, yet essential to reuse kerf. Pyrolysis does not fully eliminate carbon, and thermal oxidation treatment using conventional procedures oxidizes the silicon. In this paper, we studied the kinetics of carbon elimination in the no-diffusion-limitation regime using thermogravimetric analysis (TGA) in two atmospheres: air and N_2 . We report the activation energy in both atmospheres using three methods: Kissinger, and two isoconversional methodologies. Based on total carbon analysis, scanning electron microscopy, gas chromatography mass spectroscopy, and Fourier transformed infrared spectroscopy, a reaction mechanism is proposed in which C-C and C-O bond cleavage reactions occur in parallel with polymer formation that, at higher temperatures, fully degrades in air but leaves a tarry residue in N_2 .

3.2. Introduction

Silicon (Si) is the main semiconductor used in electronic and solar industries. Despite Si abundance in the earth's crust, ultrapure silicon production is expensive as it goes through a myriad of industrial refining processes. These well-established processes⁴, developed and optimized for microchip needs, provide superior quality and purity at the cost of being highly energy intensive and wasteful, in that 68% of the initial silicon is converted to waste during the refining steps^{6a}. Microchips need only a few grams of silicon per chip, which comprise less than 1% of the final microchip cost. However, producing a solar module requires more than 400g of silicon per m², and silicon wafers add up to more than 45% of the total cost for installed modules⁴. This shows how silicon refining inefficiencies directly translate into high cost of solar modules, hindering its large scale implementation. Therefore, efficiency improvements in silicon manufacture are highly relevant.

A key point for improvement in ultrapure silicon processing is the production of wafers, consisting of slicing silicon ingots, which wastes 45% of the ultrapure material. Efforts such as ribbon technologies to avoid the need of axial slicing have been suggested²⁹. Nevertheless, traditional wafer slicing techniques have shown higher efficiencies^{29,30}, more reliability²² and better return on investment of the final solar panel³¹ compared to ribbon wafers. Thus, abrasive slicing from mono and polycrystalline ingots is still the dominant technology^{6a}. Wafers so produced are sliced from ingots using fixed abrasive or slurry methods³² that unavoidably produce silicon sawing dust (kerf) impregnated in lubricant.

Silicon carbide (SiC) was traditionally used in slurry slicing techniques, and its removal was the main concern in previous studies of kerf recycling^{25, 34}. However, recent advances in understanding of silicon ductile behavior in a narrow range of cutting speeds³⁵ have enabled

diamond wire sawing to produce better results than slurry slicing³⁶. Further optimization of diamond wire slicing is still an ongoing effort⁸⁷. Diamond wire kerf is a complex industrial residue containing numerous metallic contaminants³³ and organics mainly from the polymeric lubricant used during slicing, and also trace amounts of polymers used for sticking the silicon ingot to the aluminum supporting beam. The exact composition of this lubricant is protected by proprietary rights. However, it is known to be mainly composed of polyethylene glycol (PEG)³⁸ mass average molar mass (M_w) around 400-500 or combinations of PEG with diethylene glycol (DEG)³⁹, polypropylene glycol (PPG). To date, a few authors have reported methodologies for recycling kerf produced during diamond wire slicing. Their results point to the need for efficient removal of carbon. Tomono et al.³⁸ reacted kerf with bromine forming bromosilanes for further distillation. Unfortunately, the carbon content in kerf reacted to form brominated organic compounds that behaved azeotropically and could not be separated via distillation. Dhamrin et al.³⁹, on the other hand, melted kerf to make solar panels and showed the devastating effect that carbon contamination has on the efficiency of the so formed devices. Finally, Maeda et al.³⁷ reported improvements in solar panel efficiency from recycled kerf by milling kerf and heating it in inert gas to remove carbon.

Previous efforts by Vazquez-Pufleau et al.⁸⁸ demonstrated that carbon elimination from kerf was feasible using a furnace aerosol reactor (FuAR). In air, at high temperatures and low residence times, total carbon (TC) measurements below detection limits were achieved. To design an industrial reactor with more certainty, it is important to better understand the process and the kinetics of carbon elimination in a FuAR, including accurate activation energy (E_A) values for the full range of conversion. To the best of our knowledge, the kinetics for the removal of organics for a metal recycling and particularly for silicon kerf, as well as the mechanistic understanding of the

reaction paths, have not been systematically studied. Both will be required for industrial scale up of kerf recycling processes.

The most important parameter for determining the kinetic behavior of a reacting system with Arrhenius behavior is the E_A ⁸⁶. The k parameter, or pre-exponential factor, can then be determined via compensation effect⁸⁹, which depends on the reaction model employed. However, the reaction's E_A remains unaffected even if the kinetic model employed is incorrectly chosen. Therefore, the focus of kinetics has historically been E_A determinations⁸⁶. The Kissinger method is a simple and well known technique to obtain E_A , but this value is determined based on limited information, i.e. the peak values of the reaction rate. The values obtained are more meaningful after comparing and contrasting with isoconversional analysis, which provides reliable E_A values for the entire range of conversion⁸². Reliable E_A for the entire range of conversion is needed because a single value of E_A is not enough to describe the full process for polymeric decomposition, as the apparent E_A might be different from the intrinsic E_A due to competition among radical polymerization, homolysis and volatilization⁹⁰.

In general, the elimination of residual polymer contamination from powders has not been widely studied, even less so in the case of kerf. Nevertheless, kinetic studies for pure PEG have been executed experimentally⁹⁰⁻⁹¹ and theoretically⁹². A detailed discussion on the PEG literature is provided in the following section. The reported PEG literature needs to be analyzed carefully to extrapolate the findings under ideal conditions to conditions of real kerf recycling systems full of other contaminants. As Lin et al.⁹³ have observed, the presence of nanoparticles significantly alters the degradation kinetics for PEG which follows a different degradation process when combined with Ni and Al nanoparticles. Ni accelerated the decomposition whereas Al was a retardant at the beginning but accelerated the decomposition at a later stage. This indicates that the kinetics and

mechanism of removal of slicing lubricant (composed of PEG, epoxy and additives) from kerf (made of silicon nanoparticles and metallic contaminants) might differ compared to pure PEG degradation.

In this work, based on thermogravimetric analysis (TGA) results, we determine the activation energy (E_A) of carbon removal in kerf using the Kissinger method and Ozawa-Flynn-Wall (OFW) and Kissinger-Akahira-Sunose (KAS) isoconversional analysis. Additionally, we present characterization results from samples thermally treated by TGA in either air or N_2 using Fourier transformed infrared (FTIR) spectroscopy, gas chromatography mass spectroscopy (GCMS), total carbon (TC) determination, Brunauer–Emmett–Teller (BET) surface area measurement and scanning electron microscopy (SEM). At the end, we provide an overall reaction mechanism for the elimination of carbon from kerf based on the instrumental evidence.

PEG literature discussion

The degradation mechanism of PEG is complex. It decomposes endothermically under pyrolytic conditions according to Arisawa et al.^{91c} but exothermically in oxidative processes according to Lin et al.⁹³ In addition, even under oxygenic conditions, the degradation inside a thick sample would still be a pyrolysis process. Several authors have reported E_A ranging from 129 to 209 KJ/mol for the decomposition of PEG with MW from around 10^3 to 10^5 g/mol at temperatures of 315 °C – 410 °C as summarized by Arisawa et al.⁹⁰ The degradation temperature of PEG rises as the MW increases, but after about 1000 Da the maximum degradation temperature is rather constant at about 350 °C according to Voorhees et al.^{91c} The primary degradation is above 325 °C while the secondary is after 450 °C. They also suggest that PEG undergoes a series of

homolytic cleavages between the C-C and the C-O bonds followed by disproportionation and reactions of hydrogen abstraction. Arisawa et al.^{91e} report that C-O and C-C homolysis occur approximately at the same rate between 370 and 550 °C. Saint de Claire et al.⁹² suggest that the reaction mechanism initiates by hydroperoxide dissociation, propagates by alkoxy radicals and chain growth, and terminates when two radicals neutralize each other. However, this last step is heavily diffusion dependent.

According to Han et al.⁹⁴, one of the specific degradation mechanisms for PEG is the volatile formation from random chain scission phenomena, in which PEG reacts with oxygen to form thermally sensitive peroxides that decompose via a radical mechanism to produce formic esters. Regarding the random chain scission phenomena, there seems to be dispute about which bond breaks at the initial stage of polymeric pyrolysis. Fares et al.⁹⁵ indicate that C-O homolysis dominates over C-C homolysis in the first stages of pyrolysis. Lattimer et al.^{91d} also report that at relatively low temperatures (150 °C) homolytic cleavage of C-O bonds is the most important degradation step. Arisawa et al.^{91e} on the other hand suggest that the rates of both cleavages are comparable.

Pielichowski et al.^{91b} found that PEG non oxidative decomposition yielded an apparent E_A of 145-180 kJ/mol, in agreement with our own results for N₂ decomposition (120-170 kJ/mol). Kitahara et al.^{91f} on the other hand reported E_A for three PEG pyrolysis products ranging from 155 to 214 kJ/mol and a reaction rate peak at 470 °C instead of our observed 350 °C. Kitahara's higher reaction rate peak compared to ours can be explained by the MW of their PEG being 2 million atomic units, whereas ours is below a few thousand. This is consistent with the requirement of more bond ruptures to form volatiles in the high MW compared to the low MW polymer. The expected C-O bond strength is around 335 kJ/mol, much higher than the measured value. This is

due to several reactions with differing E_A occurring in parallel. The complex reaction likely includes hydrogen abstraction reactions that display negative E_A ⁹². As a result, the apparent E_A of the global reaction is significantly changed.

3.3. Experimental methods

3.3.1. Sample characterization

Table 3-1 Kerf elemental analysis provided by SunEdison, Inc.

Element	Composition (%)
Silicon	> 84
Oxygen	13
Carbon	1.3
Aluminum	0.3
Nickel	0.015
Iron	0.0035

Kerf was provided by SunEdison, Inc. (Saint Louis, MO) along with its elemental analysis determined by combustion infrared, inert gas fusion non dispersive infrared, and glow discharge mass spectrometry shown in Table 3-1. The surface area determination was performed using a Nova 200e BET instrument (Quantachrome Instruments, Boynton Beach, FL). Surface morphology and structural analysis were obtained by SEM in a FEI Nova 2300 SEM (FEI, Hillsboro, OR). Dried kerf was heated to various temperatures using TGA in a Q5000 IR thermogravimetric analyzer (TA Instruments, New Castle, DE) using a heating rate of 20 °C/min up to various temperatures at intervals of around 200 °C in either air (Airgas, St. Louis, MO) or ultra-high purity (99.999%) N₂ (Airgas, St. Louis, MO). Samples were then quickly cooled down by shutting off the TGA furnace and characterized using TC determinations (Shimadzu SSM-5000, Shimadzu, Columbia, MD) with a solid sample module and FTIR spectroscopy (Nicolette Nexus

470 GMI, Ramsey, MN). The volatiles, evolved from kerf at different temperatures and atmospheres, were extracted from the TGA exhaust at the desired temperature using a gas tight 0.5 mL Luer syringe (Restek, Bellefonte, PA) and were immediately injected into a RTX 50 gas chromatography (GC) column equipped with mass spectroscopy (MS) (Agilent 5975C Series GC/MSD, Santa Clara, CA). Peaks were integrated using Agilent Mass Hunter Quantitative Analysis Software and identified using the NIST library.

TGA for kinetic analysis

TGA was used to determine the kinetics of carbon elimination in kerf. Each kerf sample was heated up to 120°C and kept at that temperature for 60 min. to remove water and volatiles from the sample. DEG as a component of the lubricant has a vapor pressure of 5.6 Torr at 120°C⁹⁶ and would be removed from the sample within this time (1hr). TGA was used to determine the kinetics of carbon elimination in kerf. Dried kerf samples were subjected to four heating rates: 2, 5, 10 and 20 °C/min. under combustion (air) or pyrolysis (ultrapure N₂, 99.999%). The experiments were run in triplicate. A detailed discussion of the thermal analysis methods to determine E_A is provided in Section 3.4 Model description.

3.3.2. Experimental setup

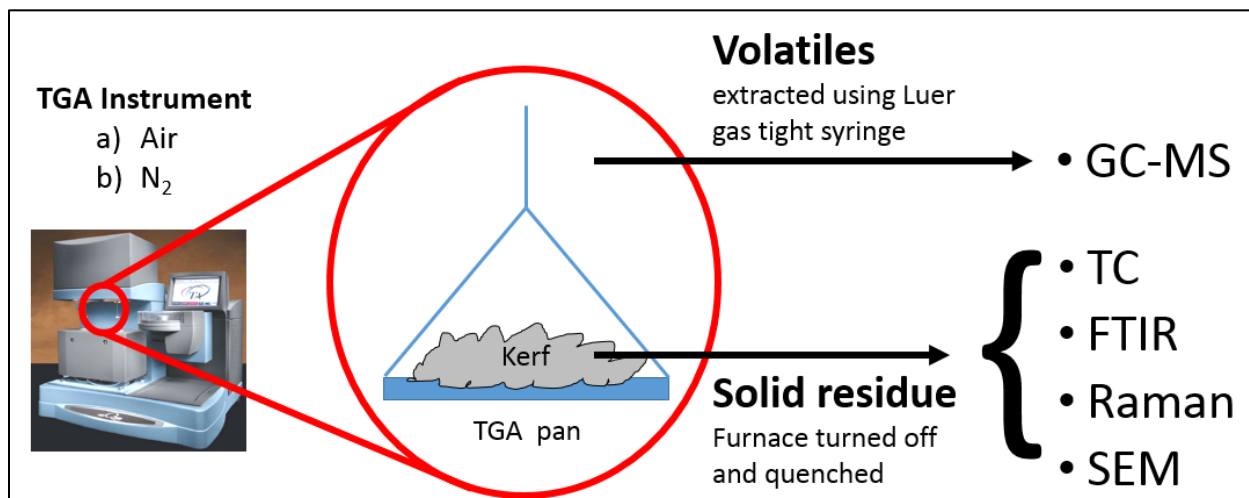


Figure 3-1 Sketch of experimental plan for characterization of volatiles evolved from kerf thermal treatment using thermogravimetric analysis and its solid residue based on the indicated characterization methods

The thermogravimetric analyzer instrument and the summary of the techniques that were used for both volatiles and solid residue from kerf heated up to various temperatures is shown in Figure 3-1.

3.3.3. Test plan

Table 3-2 Experimental plan for gaining kinetic information and mechanistic evidence on carbon elimination from kerf.

	Instrument	TGA Program	Sample	Information Obtained
1	TGA	Different heating rates (2, 5, 10 & 20 °C/min) up to 900 °C	Dried kerf	Activation energy (E_A)
2	TC	20 °C/min up to desired temperature	TGA treated kerf	Total remaining carbon
3	GCMS	20 °C/min up to 900 °C	Kerf volatiles from TGA	Evolved gas composition
4	FTIR	20 °C/min up to desired temperature	Residue kerf from TGA	Species remaining in kerf
5	SEM	20 °C/min up to 900 °C	Kerf after TGA	Sample morphology

3.4. Model description

Determination of E_A

Most of the kinetic methods used in thermal analysis consider the reaction rate to be a function of only two variables⁸²:

$$\frac{d\alpha}{dt} = k(T)f(\alpha) \quad (3-1)$$

where k is the reaction rate constant, α the conversion, and T the temperature. Since isoconversional methods are based on the idea that the reaction rate at a constant conversion is only a function of temperature, we compared four sets of data using different heating rates, defined by:

$$\beta = \frac{dT}{dt} = \text{constant} \quad (3-2)$$

, where β is the heating rate, T is the temperature and t is time.

Since the Kissinger method uses only the peak rates providing single point values for E_A , we extend our analysis to include two isoconversional methods: the Kissinger-Akahira-Sunose (KAS) method and the Ozawa-Flynn-Wall (OFW) method used to obtain E_A as a function of temperature.

Kissinger Method

Under the condition of maximum reaction rate:

$$\frac{d^2\alpha}{dt^2} = \left[\frac{E_A\beta}{RT_m^2} + Af'(\alpha_m)e^{\left(-\frac{E_A}{RT_m}\right)} \right] \left(\frac{d\alpha}{dt} \right)_m = 0 \quad (3-3)$$

rearranging

$$\ln\left(\frac{\beta}{T_m^2}\right) = \ln\left(-\frac{AR}{E_A}f'(\alpha_m)\right) - \frac{E_A}{RT_m} \quad (3-4)$$

where β is the heating rate in °C/min, R is the gas constant (8.314 J/molK) and E_A the activation energy (J/mol), m indicates values corresponding to maximum rate, The assumption for the Kissinger method⁸² is that $f(\alpha)_m$ is independent of the heating rate so the term f' is constant. This assumption is valid for n-th order kinetics and Avrami-Erofeev models.⁸²

Ozawa-Flynn-Wall Method

$$\ln(\beta) = Const - 1.052 \left(\frac{E_{A,\alpha}}{RT_\alpha}\right) \quad (3-5)$$

The value of the coefficient equal to 1.052 is known as the Doyle approximation⁹⁷.

Kissinger-Akahira-Sunose Method

$$\ln\left(\frac{\beta}{T_\alpha^{1.92}}\right) = Const - 1.0008 \left(\frac{E_{A,\alpha}}{RT_\alpha}\right) \quad (3-6)$$

Where T_α is the temperature required to achieve a given conversion for a specific linear heating rate program. The coefficient 1.0008 represents the Starink et al. approximation⁹⁸.

3.5. Results and discussion

Kerf was initially characterized by BET, and had a surface area of 9.6 m²/g, a pore volume of 0.052 cm³/g and a pore radius of 15.6 Å, proving its large surface area and flake-like morphology. In this section the results of each technique are presented separately followed by a brief discussion of direct implications for the individual instrumental observations summarized in

Table 2. Finally, in the mechanism section, the implications for all results and individual instrument discussions are combined and given the complexity of kerf composition and carbon elimination kinetics, a qualitative reaction mechanism is provided.

Total carbon content

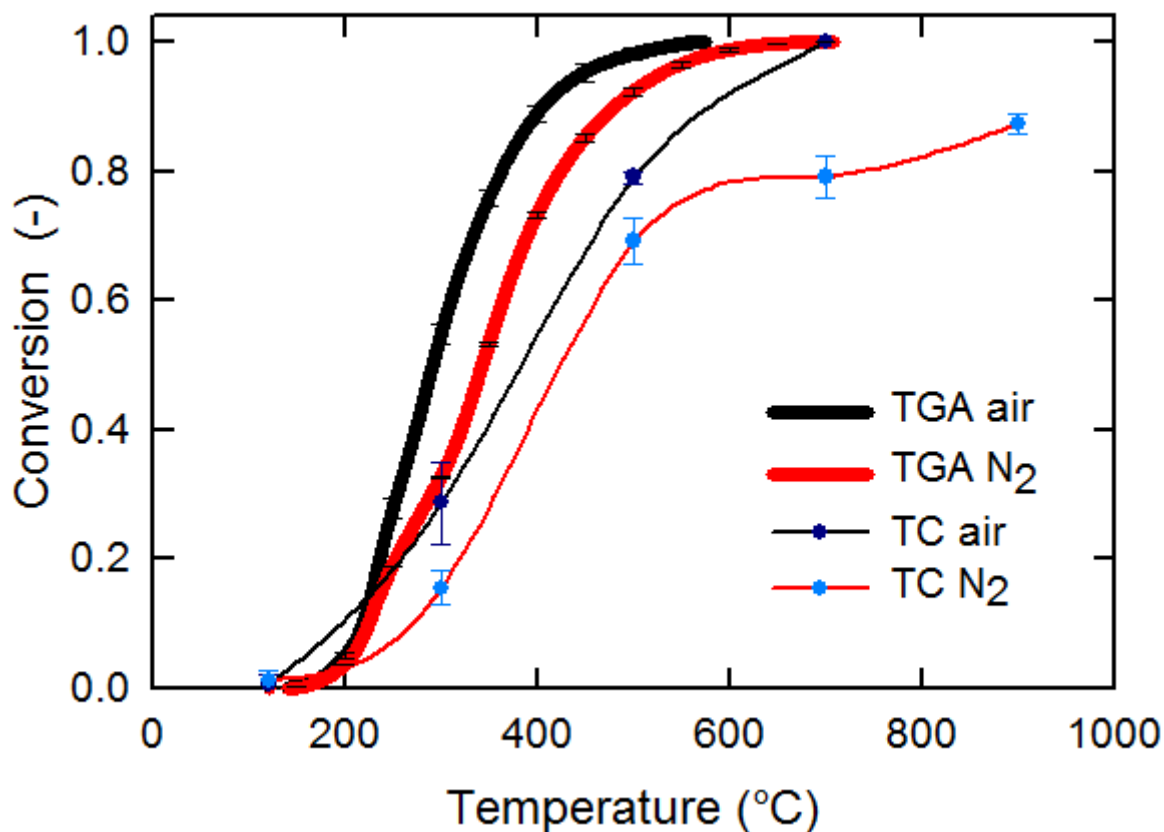


Figure 3-2 Volatiles evolution from kerf using a heating rate of 20 °C/min. Conversion is calculated by weight loss from TGA and total carbon (TC) of the remaining sample in air and in N₂ atmospheres.

The conversion of carbon calculated using traditional TGA weight loss method was compared with a TGA-TC method (using TGA and stopping the run to determine its remaining total carbon (TC) content at various temperatures). The heating rate chosen of 20 °C/min is

sufficiently high to emulate real aerosol reactor conditions and at the same time, low enough to guarantee mass and heat transfer. Thus, providing an accurate thermogravimetric reading. Figure 3-2 shows that the conversion using the two methods differs.

TGA vs TC conversion

TC is considered to be a less biased instrument to determine the total amount of carbon present in the sample. This becomes evident in the case of samples treated in air, where carbon is eliminated at a slightly lower rate than predicted by TGA, reaching full conversion with a small delay. In the case of samples treated in N₂, a similar delay in conversion is observed but full carbon removal is not achieved under the examined conditions (up to 900 °C). Conversion is calculated using the classical definition (1- reactant current concentration/ reactant initial concentration). The discrepancy in the values between TGA and TC for the N₂ atmosphere is due to the different bases used for each. On one hand TGA conversion is based on the minimum of the weight measured. On the other hand TC conversion is based on the absolute value reported by the instrument.

Gas chromatography mass spectroscopy

Based on their chemical composition, detected peaks were classified into different categories as: saturated C_nH_m (aliphatic compounds containing only carbon and hydrogen), unsaturated C_nH_m, C_nH_mN_l, C_nH_mO_l and C_nH_mO_lSi_k. The chromatogram area corresponding to all components assigned to each category were summed and normalized with respect to the total area, a relative abundance value was assigned for each category. See Figure 3-3 (a) for samples treated in air and Figure 3-3 (b) for samples treated in N₂. A discussion follows for each atmosphere

based on observations for each category except for $C_nH_mO_lSi_k$, whose consistent presence in most samples is explained in a separate paragraph.

In Figure 3-3 (a), for samples treated in air, GCMS shows that the highest rate of all volatiles formation occurs around 300 °C and no unsaturated C_nH_m compounds are observed at any temperature. $C_nH_mO_l$ compounds seem to be present in the same ratio (around 20%) at all temperatures except at the peak of volatile formation where its presence becomes more abundant. Elimination of nitrogenated compounds peak at 450 °C, showing that they are more difficult to remove than oxygenated compounds or aliphatic compounds that have an absolute peak at 300 °C.

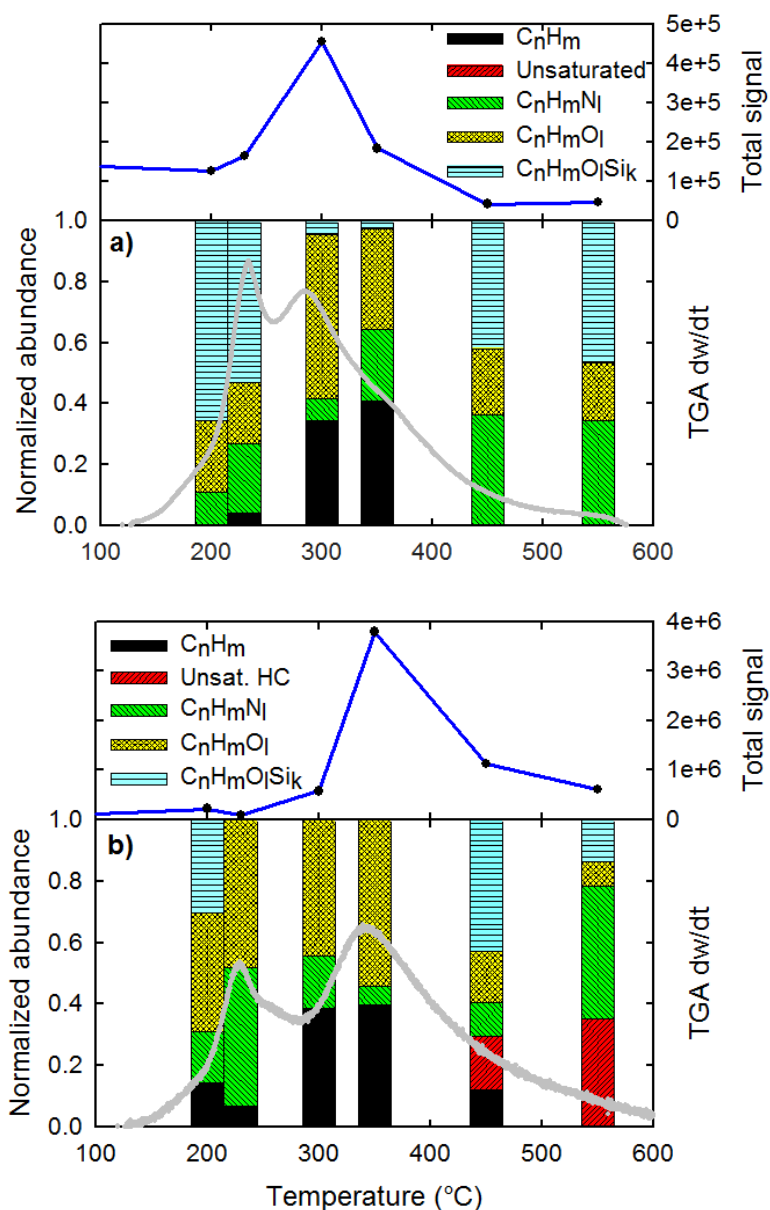


Figure 3-3 Elemental characterization of the volatiles using GCMS. Samples were extracted using a manual syringe at the indicated TGA temperatures and injected into the GCMS column. Plots (a) air and (b) N₂ show the total signal measured from MS (upper) and the relative abundance for various groups of compounds (lower). On gray the TGA rate of weight loss as a function of temperature (lower)

Figure 3-3 (b) summarizes the GCMS data for samples treated in N₂ atmosphere. There, the peak of volatiles formation occurs at a higher temperature than in air; at about 350 °C and,

beyond this temperature, a significant fraction of unsaturated compounds gets released. C_nH_mO compounds are copious at the beginning, but their abundance drops after 350 °C. A significant fraction of saturated compounds is visible at 450 °C, and at 550 °C all of the C_nH_m compounds are already saturated. This can be interpreted as the lack of available O_2 causes any remaining polymer in the kerf to undergo saturation reactions, leaving a carbonaceous residue that is hard to pyrolyze (tar). This agrees with the TC results from Figure 3-2, where not all the carbon can be eliminated. In contrast, in the air atmosphere, the availability of O_2 permits virtually full polymer decomposition into volatiles and thus no saturated C_nH_m compounds are formed. Nitrogenated compounds in N_2 atmosphere become more abundant in terms of total signal as temperatures rise, XPS preliminary results indicate that the source of nitrogen are the organic compounds themselves. Finally, the total GCMS signal for the pyrolysis is six times more intense than the one for air atmosphere (combustion) indicating that, during the combustion process, a significant fraction of volatiles fully reacts into CO_2 .

During TGA thermal operations, siloxanes seem always to be present in trace amounts. This is due to the presence of silicon nanoparticles in contact with the lubricant. Its total abundance seems to be constant, but due to large differences in the abundance of other compounds, its fraction is highly diluted on the peaks of signal and conversely overshadows other components especially at the beginning of the TGA thermal run and at the end when most of the organics have already been released.

Fourier transformed infrared spectroscopy

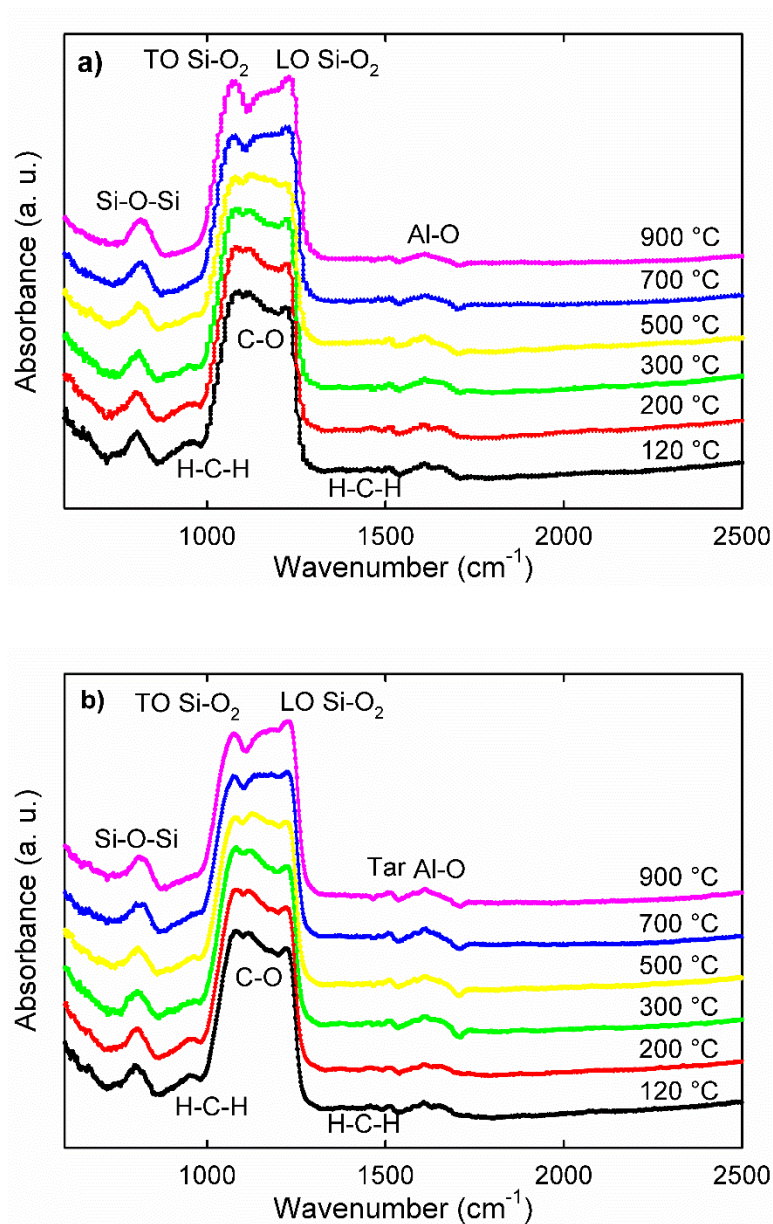


Figure 3-4 FTIR for kerf thermally treated at various temperatures (a) in air and (b) in N₂. Peaks are labeled based on the literature. A summary of the molecular motion assignment is presented in Table 3-3

The results of FTIR for different temperatures are displayed in Figure 3-4 (a) for kerf treated in air atmosphere and Figure 3-4 (b) for kerf treated in N₂ atmosphere. The peak assignment

with references is presented in Supplementary Table 1. The peaks can be classified into three groups: silicon and SiO_x, organics, and Al. Insights into sample composition are gained through analyzing the characteristics of the most important peaks.

The assignments of chemical bonding identity for peaks used in Figure 3-4 were based on the references summarized in Table 3-3.

Table 3-3 FTIR peak assignment

Molecular motion	Peaks FTIR	
	this study (cm ⁻¹)	Other studies (cm ⁻¹)
Si-O-Si bending vibration	805	800 ⁹⁹
CH ₂ bending, rocking and twisting	960	964 ^{93,91b}
Transverse optic (TO) SiO ₂	1070	1074 ¹⁰⁰ 1050 ¹⁰¹ 1060 ¹⁰² 1070 ¹⁰³
C-O stretching	1149	1149 Wang et al. 1153 ^{91b}
Longitudinal optic (LO) SiO ₂	1230	1235 ¹⁰² 1250 ¹⁰³ 1230 ¹⁰¹
CH ₂ scissoring	1460	1470 ^{91b}
Stretching and bending modes of aromatic hydrocarbon tar, soot or coke	1510	1500 ¹⁰⁴ 1300-1600 ¹⁰⁵
Al-O vibration	1615	1612 ¹⁰⁶

Regarding silicon, the peak at ~1230 cm⁻¹ is attributed to the silicon longitudinal optical (LO) mode. The peak at ~1050 cm⁻¹ is attributed to transverse optical (TO) mode of the silicon asymmetric stretching vibrations¹⁰¹. It is well known that the exact peak of TO in cm⁻¹ is proportional to the thickness of the alpha-SiO₂ layer with an interface region of about 1.6 nm and shows a simplified chemical formula of SiO¹⁰³. Both the outer layer of SiO₂ and the interface with Si include effects such as compressive stress and roughness that change the LO and TO mode. Furthermore, the peak intensity of TO and LO is directly correlated with the degree of silicon

oxidation¹⁰². In our case TO for air is evidently larger than the one for N₂, evidencing a higher degree of oxidation in the first scenario.

Organic peaks are small due to their low mass fraction in the sample. Before thermal treatment, total organics account for 4% of the sample, TC is 1.3%. After thermal treatment, TC approaches 0% for air and 0.15% in N₂, imposing instrumental detection challenges. The peak at 960 cm⁻¹ corresponds to hydrocarbon CH₂ motion in the C axis.^{91b} A C-O stretching characteristic peak^{91b} appears at 1149 cm⁻¹ in the region between TO and LO altering its shape. CH₂ scissoring is attributed to the peak at 1460 cm⁻¹^{91b}. Depending on the molecular weight (MW) of PEG, a difference of up to 10 cm⁻¹ in the peaks of characteristic bonds can be expected¹⁰⁷. Finally, in the region between 1300 and 1600 cm⁻¹ several peaks are observed at low temperatures. These peaks are attributed to aromatic hydrocarbons¹⁰⁵. Most of these peaks disappear, indicating decomposition. However, above 700 °C in N₂ atmosphere, a small differentiated peak can be observed that does not appear in air atmosphere. This peak is attributed to aromatic hydrocarbons¹⁰⁴ that are believed to be the tarry residue following pyrolysis of the polymer mixture. This is in agreement with TC measurements.

The third most abundant contaminant in kerf after oxygen and carbon, see Table 1, is aluminum (0.3%). The peak at 1612 cm⁻¹ of the kerf sample is similar for both atmospheres and is assigned to be due to the molecular motion of Al-O corresponding to Al₂O₃¹⁰⁶. It originates from the beam supporting the ingot during slicing.

TGA kinetics

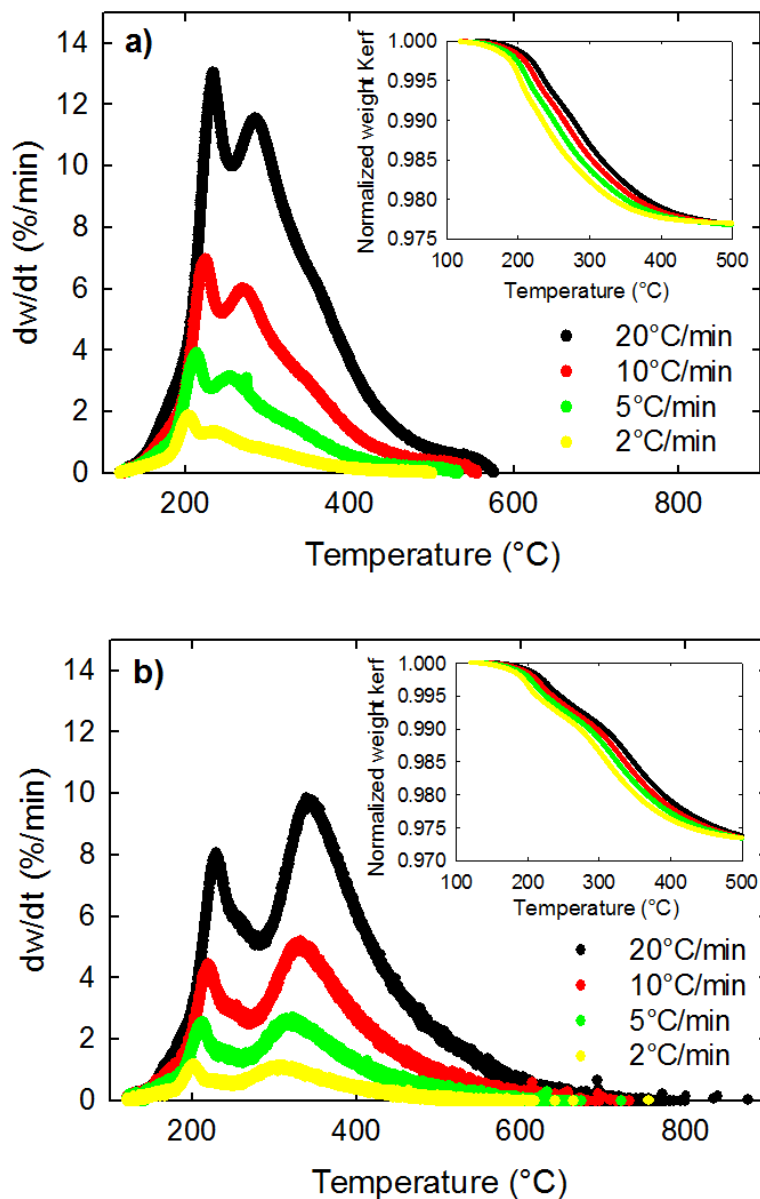


Figure 3-5 Rate of volatiles elimination for kerf at various heating rates (a) in air and (b) in N₂. Insets show carbon elimination from kerf in the given atmosphere.

Kinetics of carbon elimination in kerf were evaluated using three thermogravimetric analysis methods: OFW, KAS and Kissinger. The three methods are used in conjunction as their combined results provide more certainty on the accuracy of the obtained activation energy⁸². The

raw quadruplet data at four different heating rates and its derivatives are shown for air in Figure 3-5 (a) and for N₂ in Figure 3-5 (b). For information on determination of OFW and KAS E_A refer to the supplementary section. The E_A determined with the Kissinger method was obtained by computing the peak values of the derivatives from insets of Figure 3-5 (a) and Figure 3-5 (b). The apparent E_A determination results from the three methods are compared in Figure 3-6 (a) for air and Figure 3-6 (b) for N₂. The OFW and KAS methods provide a similar plot as they are both isoconversional methods, yet the KAS determined E_A is considered to be a more accurate method⁸². The first peak for both gases shows a rather similar behavior even though in air the E_A is about 10 kJ/mol lower than in N₂. However, the second peak for E_A is significantly more elevated in N₂ than in air, suggesting a radically different mechanism for this second stage.

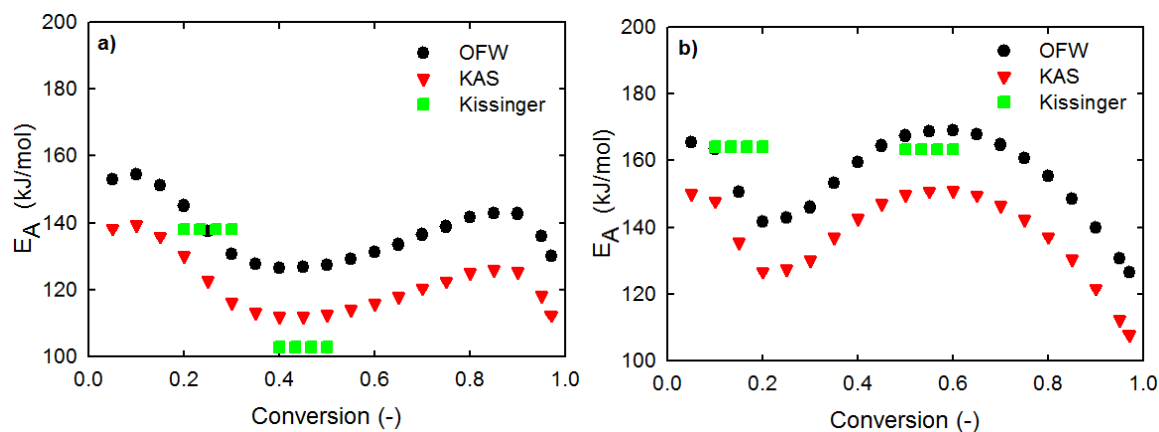


Figure 3-6 Activation energy (E_A) for volatile elimination from kerf using OFW, KAS and Kissinger methods as a function of conversion (a) in air and (b) in N₂. At low conversion both reactions display a similar behavior, but as reaction continues the N₂ case displays higher E_A compared to air.

Figure 3-7 (a) and Figure 3-7 (b) show the OFW method plots for obtaining the activation energy. Similarly, for the KAS method Figure 3-8 (a) and Figure 3-8 (b) were used. The Kissinger

method produces only one E_A per the given peak whereas isoconversional models provide E_A for all the range of reaction temperatures which make it more suitable for describing the whole process. However, a combination of both gives more certainty in the accuracy of the E_A determination.

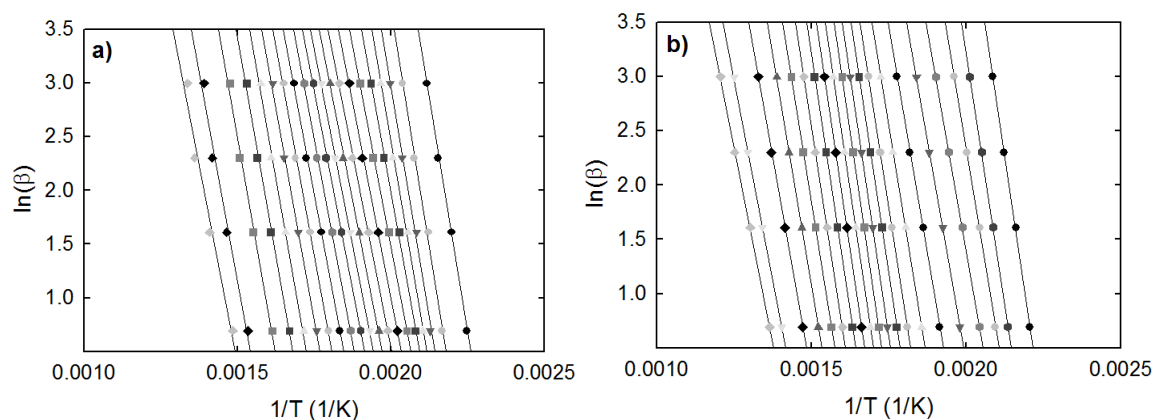


Figure 3-7 OFW method to calculate E_A (a) in air and (b) in N_2 . High regression values are observed.

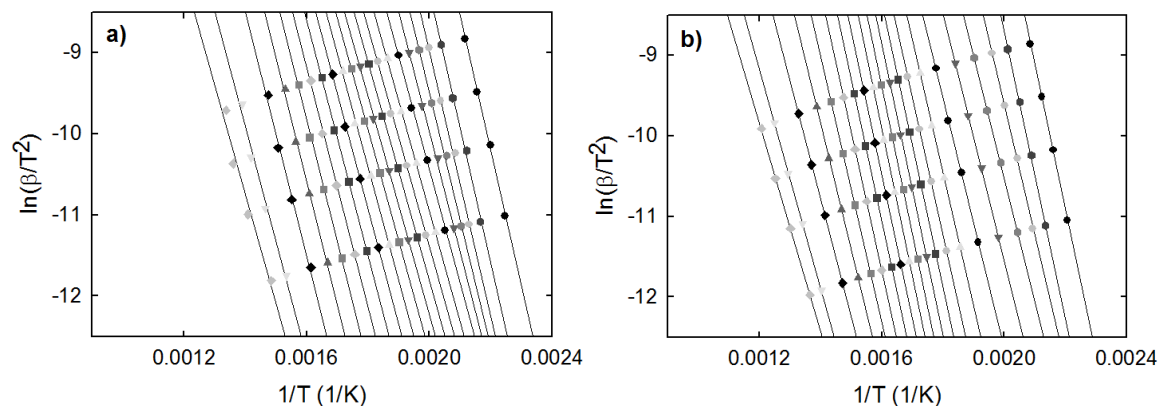


Figure 3-8 KAS method to calculate E_A (a) in air and (b) in N_2 . The data quadruplet shows consistency and a high linear regression value indicating experimental data reliability.

Figure 3-9 compares the reaction rate with the values of the normalized rate by dividing it by the concentration to the power of either one or the phenomenological reaction order determined from via the power law model. The objective of this is to show the behavior of rate when the

concentration effect is eliminated, as if the reaction rate proceeded without conversion. A sharp slope indicates exothermicity whereas a less steep or even a change in the slope sign is an indication of endothermicity.

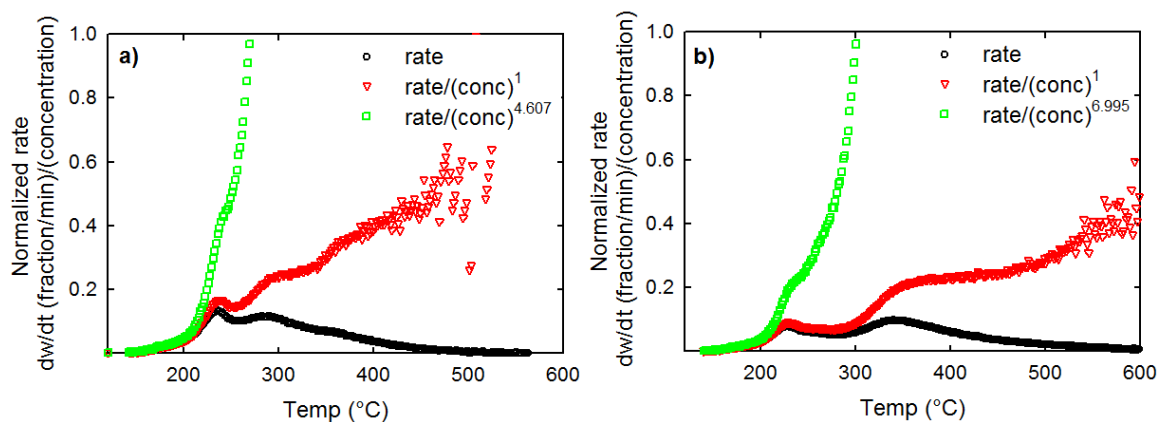


Figure 3-9 Normalized reaction rate (a) in air and (b) in N₂. The sharp slope indicates both reactions are predominantly exothermic.

SEM characterization

To observe the effect of thermal treatment on morphology, SEM characterization was performed. Figure 3-10 (a) shows dried kerf, Figure 3-10 (b) displays kerf processed in air atmosphere at 900 °C and Figure 3-10 (c) presents kerf after exposure in N₂ atmosphere at 900 °C. No evident morphological changes are visible for the different processes. This supports the idea that the particle size does not change and introduce modifications into the silicon peaks.

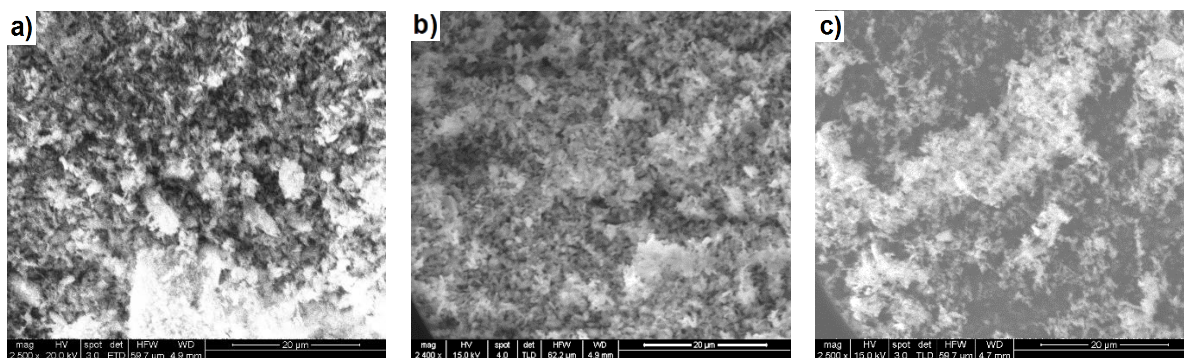


Figure 3-10 SEM of dried kerf at (a) RT, (b) heated to 900 °C in air and (c) heated to 900 °C in N₂. No significant differences are observed in the flake shape after thermal treatment.

XPS preliminary results

Nitrogenated compounds evolved as volatiles were observed to occur both in air and N₂. Preliminary results using XPS (not reported) show that the nitrogen level decreases for a sample treated at a higher temperature suggesting that nitrogen is part of the lubricant formulation and is located inside the polymeric chains rather than either adsorbed on the surface or extracted from the inert atmosphere or air. These nitrogenated compounds might be incorporated into the PEG as antioxidants in the form of aromatic aminated additives since their properties against polymer free radical oxidative degradation¹⁰⁸ would extend the lubricant life span. The nitrogenated species might also originate from proprietary post-processing operations to recover the lubricant from the kerf slurry for its reuse.

Stages of the process.

Carbon elimination in kerf is a two stage process

The rate of weight loss as a function of temperature exhibits two peaks, both in air, and in N₂ (Figure 3-5). The similar two-peak dependence is observed for the apparent activation energy as a function of conversion. Two peak phenomenon is the first fingerprint that our process is characterized by two stages. These stages are well distinguished by the products which are observed within the different temperature domains. (See Figure 3-3 with the elemental characterization of corresponding volatiles).

GCMS for both air atmospheres and N₂ shows two differentiated processes. In air, C_nH_m compounds are observed up to 350 °C and not above this temperature. In the case of N₂, saturated C_nH_m compounds at temperatures above 450 °C, become less abundant, and unsaturated C_nH_m compounds become more dominant. This comes in accordance with Arisawa et al.⁹⁰, who reported that below this temperature, PEG forms both volatiles and a higher MW residue. Above this temperature, both PEG and its higher MW residue begin to decompose. Similar observations have been made for PEG decompositions at low pressure^{91e}. All of these facts provide evidence that carbon elimination in kerf is a two stage process.

Apparent activation energy and stages of the process.

Apparent activation energies, both for air and N₂ atmospheres, as a function of temperature (and conversion as well) are not constant. Moreover, they are not constant even within the stages selected. This is consistent with observations of E_A behavior on PEG at comparable conditions by Arisawa et al.⁹⁰. The two-peak apparent energy dependence is observed for the N₂ atmosphere. Also the similar dependence is presented for the air atmosphere. For both cases, one can distinguish the clear ‘volcano-shape’ peculiarities of these dependences.

In the kinetic and catalytic literature, the observed increase in the apparent activation energy is typically attributed to the endothermic reactions, while the decrease is attributed to exothermic reactions¹⁰⁹. The decrease in E_A between the two peaks for either air or N_2 shows the point where the exothermic process (likely, polymerization) provides energy for volatiles to evolve but also diminishes the rate of total volatiles being released at that particular temperature. Then, in the second stage, the endothermic process (cleavage of molecules) produces the increase in E_A and releases more mass in the gas phase. Generally, two stages of our process present an interplay between the endothermic and exothermic factors.

All these facts provide evidence that our process is complex, displays at least two stages, and every stage is not an elementary reaction.

Chemical reactions. Preliminary considerations.

Two differentiated stages of reaction are observed in both atmospheres. A description of each follows.

First stage

Both atmospheres display a qualitatively analogous first stage, yet with different magnitudes. Based on GCMS (Figure 3-3), oxygenated compounds, released as volatiles in the N_2 atmosphere are abundant at the beginning of the 1st peak (Figure 3-5), but become scarce after 350 °C. On the other hand, in air for the same temperature domains, the oxygenated compounds ratio remains constant. This suggests that for the first stage, volatiles are evolving from comparably

analogous mechanisms where the polymer cleaves itself using its own oxygen atoms to favor bond rupture. This holds true for both atmospheres (air and N₂), although the magnitude of the effect is different. Moisture and low MW volatiles can be ruled out as the kerf sample is heated up to 120 °C for 1 hr. and TGA shows a plateau in weight loss.

Furthermore, the results for the formation of C_nH_m aliphatic compounds for pyrolysis (N₂ atmosphere) conditions qualitatively suggest firstly an increasing degree of polymerization with progressively increasing chain length. At temperatures below 350 °C, highly saturated linear chains form and volatilize, and above that temperature more unsaturated compounds become prevalent. This is in agreement with PEG degradation studies by Lattimer et al.^{91d} who report that up to their tested temperature of 325 °C, in pyrolysis, no unsaturated compounds were found on volatilized products.

Second stage

In the second stage domain, a larger fraction of oxygenated compounds are found via GCMS in air rather than in N₂. This suggests that in the air atmosphere, either oxygen reacts with the polymer and gets incorporated into the volatile chains as part of the reaction mechanism or the evolved gases oxidize in the gas phase. For N₂, a relative lower abundance of oxygenated compounds indicates that as oxygen becomes less abundant in the remaining polymeric chain, C-C cleavage turns more dominant, yet not the sole reaction pathway. In the case of air atmosphere, C_nH_m saturated compounds are not detected beyond 350 °C, and unsaturated C_nH_m compounds were not found at any temperature.

Higher MW polymer formation

Based on the FTIR results in N₂, as shown in Figure 3-4 (a) and 3-4(b), a small peak visible above 700 °C, is attributable to tar. Additionally, 12% of the original TC cannot be removed. This proves that pyrolysis is not enough for full carbon elimination of kerf lubricant. Lattimer et al.^{91d} similarly observed a dark colored PEG residue attributable to highly unsaturated organics. In the case of N₂, this higher MW PEG residue strongly influences the second peak decomposition features. Furthermore C-O and C-C bond cleavage (volatile formation) competes with radical recombination generating an even higher MW residue (tar), in agreement with previous studies^{90, 94, 110}.

Analysis of apparent E_A dependences

As indicated, the apparent E_A dependence on temperature is characterized by two peaks similar to the rate of volatiles elimination. We considered it as a fingerprint of the two stage process. However even within one stage this apparent energy is not constant. Obviously it is the strong kinetic fingerprint that each stage is not an elementary reaction. Moreover, the maximum of the apparent energy for each stage can be interpreted as a result of the complicated interplay between at least two reactions, endothermic for decomposition reactions and exothermic for polymerization reactions. This interplay can be attributed both to the first and second stage.

Detailed mechanism.

Based on the presented composition and kinetic data and supported by the literature for PEG, a mechanism for the elimination of carbon from kerf is presented graphically in Figure 3-11.

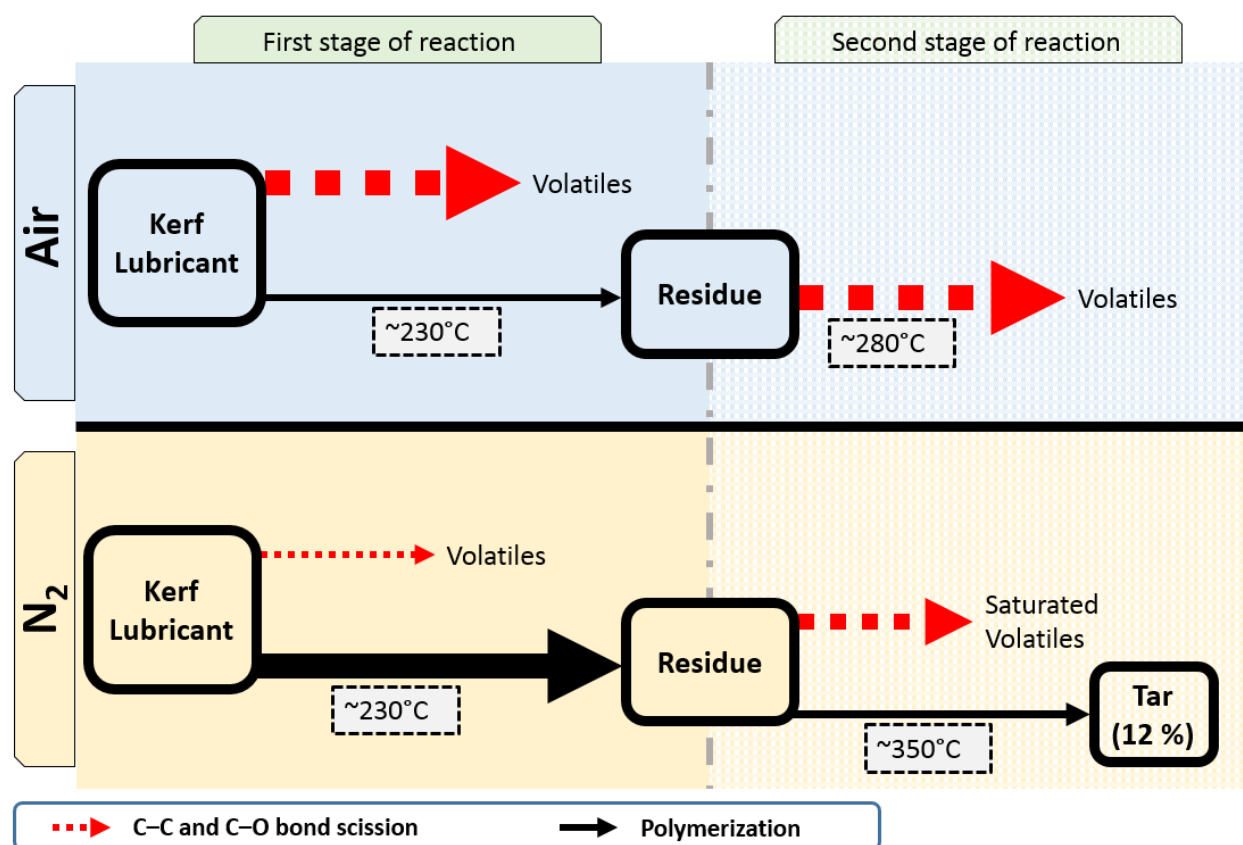


Figure 3-11 Two-step mechanism for carbon elimination in kerf. Arrow thickness shows qualitative dominance for each parallel reaction pathway. At the end of the reaction in N₂ 12% of carbon remains as tar.

In air

The reduction of mass during TGA in air can be explained by the formation of species with lower MW due to thermal degradation released to the gas phase upon formation. For the first stage, there are two competing types of reactions during thermal oxidation of PEG: oxidative degradation of PEG by a chain scission mechanism, and polymerization of PEG by loose crosslinking. The process of degradation consists primarily of competing C-C and C-O bond cleavage occurring in parallel at arguably comparable rates^{91e}. This is not different for the decomposition of polypropylene Glycol (PPG) or its related compounds^{91a}. During TGA in air, PEG undergoes

thermal degradation forming lower MW species which are released into the gas phase, causing weight loss.

The second stage consists of the higher MW PEG undergoing full degradation into volatiles, with a peak in the formation of volatiles around 280 °C. No remaining carbon could be measured after exposing the sample up to 900 °C using a heating rate of 20 °C/min.

In N₂

The proposed mechanism for kerf lubricant degradation in N₂ involves also two types of reaction as in air, each comprising different mechanisms. In the first stage, the two overall processes occur in parallel. Competing C–C and C–O scissions take place to form volatiles, while at the same time, a higher MW polymer is formed at the same temperature as in the case of air (230 °C) hinting that the process might be the same in both atmospheres. Whereas in air the formation of volatiles dominates, in N₂, the conditions favor the formation of high MW residue.

In the second stage in N₂, the same two processes occur as in the first stage, C–O and C–C bond scissions compete to form volatiles. Those volatiles include a large fraction of saturated hydrocarbons in the gas phase that are not seen in the corresponding second stage in air. In N₂, similar to the first stage, the polymerization continues and forms a tarry residue. This residue accounts for about 12% of the original TC content even after heating up to 900 °C using a heating rate of 20 °C/min. and shows that C elimination is not achievable under inert atmospheres. Tar was not observed in air.

Interpretation of ‘volcano-shape’ energetic dependences.

Our activation energy curves are similar to volcano-shape energetic dependences (volcano curves) which have been found in many heterogeneous chemical systems, particularly in gas-solid

catalytic systems Typically, the interpretation of these interesting effects is presented based on linear correlations between the activation energy and the reaction enthalpy, Broensted-Evans-Polyani correlations, with the different sign, positive or negative, for endothermic and exothermic reactions, respectively¹¹¹. In a simple way, the volcano curve can be explained by the compromise between endothermic and exothermic reactions.

3.6. Conclusion and summary

In summary, we studied the carbon elimination from kerf and defined it as a two stage process based on TGA analysis. The activation energy for carbon elimination from kerf and its evolution was obtained in air and N₂ atmospheres from room temperature to 900 °C. We developed a mechanistic model based on characterization tools including TC, FTIR, and GCMS and supported the model by the PEG decomposition literature, which is believed to be the main source of carbon content in kerf. This mechanism is proposed as the skeleton of the actual reaction mechanism for the thermal decomposition of slicing lubricant in kerf in air and N₂. In the first stage of our proposed model, the reaction rate is dominated by long hydrocarbon chains undergoing depolymerization by rupture of C-C and C-O bonds in competition with further polymerization. This happens in both atmospheres, but with different output ratios. The second stage is radically different for each atmosphere. In the case of air, this second stage is less energy demanding and the carbonaceous compounds polymerize to a lesser extent facilitating the removal of organics during the second stage. Complete carbon elimination in N₂ atmosphere was not achieved under the temperatures and heating rates tested. The reaction rate is slower compared to air and yields a tarry byproduct (12% of original TC content) that cannot be easily eliminated by further heating.

We observe a higher rate of carbonaceous compound removal from kerf in air than in N₂ atmosphere; however, this comes at the cost of oxidizing the silicon which is undesirable for kerf purification. More work is required to link the kinetics of carbon elimination with a reliable model for silicon oxidation from kerf. Further research on different concentrations of O₂ and N₂ could provide optimum conditions to maximize carbonaceous compound elimination while minimizing silicon oxidation. Such models will help to design processes to more effectively recycle and re-use kerf so as to bring down costs of Si wafers.

CHAPTER 4:INSIGHTS INTO THE OXIDATION BEHAVIOR OF SILICON IN KERF USING SILICON POWDER FROM A FLUIDIZED BED

This chapter is intended to be submitted to a peer reviewed journal

Vazquez Pufleau M., Cui, J., Hayes, S. & Biswas, P. A simple model for the high temperature oxidation of non-ideal silicon agglomerates, (2016) Silicon journal, to be submitted

4.1. Abstract

Silicon nanoparticles are a promising material in fields such as electronics, catalysis, and biomaterial engineering, among other applications. Synthesis in the gas phase and in aerosol processes allows us to engineer and tune several material properties, such as the primary particle size distribution, agglomerate size distribution, crystallite size, and morphology. Proper control of these features is desirable for these nanomaterials and their applications. A common application involves oxidizing the nanomaterials either totally or in a core-shell fashion. For that an accurate understanding of the kinetics of the silicon oxidation process is highly desired. Significant work has been devoted to understanding the kinetics of monocrystalline silicon, and generally accepted models such as the one by Deal and Grove provide an accurate description of the bulk oxidation of silicon. However, these models provide an inaccurate description of the first hundreds of angstroms of the oxidation. While this inaccuracy is acceptable for bulk wafers, it has critical results for silicon nanoparticles, which are not much larger than that size. For that reason, a model that reasonably describes silicon oxidation of agglomerates is required. In this work, we propose an equation for the parabolic kinetics of high temperature oxidation of polycrystalline silicon with a surface area in the range of 3 to 19 m²/g. and crystallite sizes from 50 to 70 nm. The activation energy of the process is also reported to be linked to the crystallite size.

4.2. Introduction

A critical process in the semiconductor industry is the formation of an oxide layer on top of monocrystalline silicon for passivation and protection. Therefore, the oxidation kinetics of monocrystalline silicon have received significant attention in the last several decades. Most of the literature on silicon oxidation is based on bulk silicon oxidation of wafers. A summary can be found elsewhere.¹¹² A general relationship for the complex process of the thermal oxidation of silicon has been proposed by Deal and Grove (D-G):⁷⁸

$$L^2 + AL = B(t + \tau) \quad (4-1)$$

where L is the oxide thickness, A is the linear parameter, t is time, and τ is the time needed to achieve an initial oxidation thickness. B is the parabolic rate constant, defined as¹¹³

$$B = 2c_L \frac{D}{\rho} \quad (4-2)$$

where ρ is the density of the oxide, c_L is the concentration of molecular oxygen in the silica gas interface, and D is the parabolic diffusion coefficient; hence, B/A would express the linear rate constant. The D-G expression is satisfactory for flat pristine and crystalline surfaces beneath a layer of dozens of nanometers where silicon oxidation occurs more rapidly. The D-G model is described by two regions, a linear oxidation region and a parabolic oxidation region which is diffusion controlled¹¹⁴. The linear parameter has been related to microchannels that open due to stress in the silicon.¹¹⁵ It has been proposed by Irene et al.¹¹⁵ that during dry oxidation of silicon, micropores that create a linear region for oxidation might arise. Doremus¹¹³ reported that variations in A from the D-G model can be expected due to strains on the silica layers. The reason for the

anomalously slower rate of oxidation on the edge of walls is attributed to compressive stress within the oxide, reducing diffusivity and inducing parabolic oxidation at an earlier stage.¹¹⁶

More recently, improved D-G based models have been proposed. Fargeix et al.¹¹⁷ developed a model that implements a lower diffusivity in the surface due to compressive effects. This model incorporates the fact that the oxidation of silicon is fast in the first nanometers of oxidation of flat single crystalline silicon, but then the rate decreases rapidly until a critical thickness is reached and the rate becomes dominated by diffusion. The decrease in diffusivity is explained by the presence of compressive stress formed by silicon oxidation.¹¹⁸ Beneath the critical thickness, a viscous flow of silica is believed to take place and relax the stresses.¹¹⁹ Jimin et al.¹²⁰ added an additional logarithmic term to better explain the silicon oxidation of monocrystalline wafers, where the model still fails to accurately predict the first nm of oxidation. Other improvements of the D-G model account for the effect of the stress profile in the oxide layer that has an effect on the effective oxygen diffusivity.¹²¹ Additionally, Irene et al.¹²² proposed a model of micropores to better explain the high and low temperature behaviors. Their model is a revised linear parabolic D-G model. It predicts that at 1000 °C transport is Fickian because viscous flow destroys the micropores, whereas at lower temperatures the transport is believed to occur due to diffusion of oxidant into the pores bypassing the SiO₂ layer. The Deal and Grove model is not fully satisfactory in describing either the initial oxidation period (τ), oxidation at the edge of walls¹¹⁶ or the oxidation of polycrystalline silicon.¹²³ The same difficulties in accurately predicting silicon oxidation arise for silicon nanoparticles, because of their small size and quasi-spherical morphology. The stress evolution behavior during the oxidation of silicon nanowires also faces these difficulties.¹²⁴

Silicon nanoparticle oxidation

Wafers are thick substrates where the small layer of inaccurately predicted initial oxidation by the D-G model is acceptable. However, for nanoparticles, a significant fraction of their entire mass lies in this poorly understood regime. Various systems of silicon nanoparticle oxidation have been studied, using a variety of instruments. Liao et al.¹²⁵ studied the thermal oxidation of silicon nanoparticles using a tandem DMA setup. They observed two regimes at 800 °C, a fast and a slow oxidation regime. They found the transition to occur at a shell oxide thickness of 0.3 nm and to be independent of the furnace setting. They propose that silicon oxidation becomes diffusion limited after the formation of a silicon dioxide or suboxide monolayer on the surface of the nanoparticles. They mention that oxidation of silicon nanoparticles at low temperatures results in suboxide formation, with an oxygen to silicon ratio lower than SiO₂. Das et al.¹²⁶ reported that at low temperatures, the oxidation of silicon nanoparticles is not diffusion controlled. Winters et al.¹²⁷ found that the hydrogen coverage on a silicon nanoparticle affects the oxidation kinetics in a complex way, so that freshly generated particles with a higher hydrogen content oxidize more rapidly than particles partially covered by hydrogen. They explain this by stating that intermediate coverage reduces the energy of bonding configurations and steric interferences, lowering the oxidation rate. Also, the presence of hydrogen in the surface might affect the formation of a well-ordered crystalline surface. Yang et al.¹²⁸ measured the kinetics of ~5 nm silicon nanoparticles and found that their oxidation rate is slower than predicted by bulk silicon oxidation. Pereira et al.¹²⁹ proposed a mechanism for the initial oxidation through dangling bonds of silicon hydride nanocrystals. Their main finding was that the D-G model overpredicts silicon oxidation in nanoparticles in the long term.¹³⁰ An improved understanding of silicon nanoparticle oxidation

kinetics is relevant for several reasons. We have already mentioned the importance of kinetics in forming an oxide layer for passivation and stability and in synthesizing nanoparticles for electronic applications¹³¹. In addition, oxidation kinetics are important for passivation of photoluminescent devices¹³², for engineering nanoparticles for biomedical research,^{129, 133} to enable large scale production of silicon nanopowders in aerosol reactors,⁵⁵ and for optimizing carbon removal from kerf to improve its recyclability in furnace aerosol reactors.⁸⁸

Regimes of oxidation

Liao et al.¹²⁵ have proposed two regimes for silicon oxidation. In the first, oxygen has direct access to the silicon surface; in the second, oxygen needs to diffuse through the shell of oxide, so oxidation is slower than in the first regime. Das et al.¹²⁶ reported that below 500 °C the oxidation of silicon nanoparticles has little effect on oxygen partial pressure. Measurements by electron paramagnetic resonance techniques have shown that the maximum concentration of unsatisfied silicon bonds occurs at 500 °C.¹³⁴ Yu et al.¹³⁵ found that fully hydrogenated Si nanocrystals form the most stable clusters and that removing 50% of H atoms causes lattice distortions, but tetrahedral structures are retained. On the other hand, removing more than 70 to 80% of the total terminating H atoms produces more compact structures in the silicon clusters. Holm and Roberts¹³⁶ reported that the presence of hydrogen on nanoparticle surfaces inhibits their oxidation below 500 °C. Above that temperature, hydrogen desorption occurs. They explain the inhibited oxidation as a result of compressive stress in the core as it shrinks due to oxide formation and the slowing of oxide growth because oxygen diffusion through the oxide shell is suppressed. This is particularly important below the viscoelastic transition temperature of SiO₂.

Activation energy

Despite being extensively studied, kinetic data reported for silicon oxidation show large discrepancies. Ranges of activation energy are reported from 113 kJ/mol to 418 kJ/mol for single crystal oxidation, with kinetics being a complex function of temperature, oxygen partial pressure, and formed oxide thickness.⁷⁸ Due to these discrepancies, it becomes important to determine the silicon oxidation activation energy and kinetics for nanoparticles with surface areas in the range of kerf.

Amorphous vs. crystalline silicon

The difference in oxidation rates between amorphous silicon and crystalline silicon was studied by Fritzsche et al.¹³⁷, who found that crystalline silicon oxidized more rapidly than amorphous silicon. Mills et al.¹³⁸ reported the same trend in an amorphous layer of silicon hydride that was remarkably stable against surface oxidation. Agnello et al.¹³² suggested that interstitial oxygen distribution in amorphous SiO₂ nanoparticles decreased with nanoparticle radius. They determined that O₂ cannot remain on the surface of an exterior shell of about 1 nm, regardless of the nanoparticle size. The oxidation of amorphous silicon nanoparticles at low temperatures in dry air depends significantly on the hydrogen content on its surface.¹²⁶ The disorganized outer shell has been proven to not be largely composed of stoichiometric or substoichiometric silicon oxide; rather it is likely to be amorphous silicon. This effect has been observed also by Yu et al.¹³⁵

Knowledge gaps

In a study focused on silicon nanoparticles deposited in a substrate or thin films, Okada et al.⁷² observed that small nanoparticles are oxidized more slowly than larger nanoparticles (opposed to the D-G theory). They attribute that phenomenon to stress in the exterior oxide layer that suppresses oxidation inside the nanoparticle. Okada et al.⁷² did not provide a kinetic model but rather observed thickness growth after 3 hours. For particles between 20 and 500 nm at four temperatures between 850 and 1000 °C. They observed a lower oxidation rate for nanoparticles than for wafers, a behavior that could not be explained by the D-G model. Yang et al.¹²⁸ and Lu et al.¹³⁹ indicated the degree of oxidation after a certain time and only at room temperature. Yang et al.¹³⁰ in 2005 noted that the slope of oxide thickness formation (equivalent to the reaction rate) for particles between 20 and 500 nm was not available even for room temperature.

Okada et al.⁷² found that because of the stress on the surface, silicon nanoparticles actually oxidize at a slower rate than predicted by the D-G model.⁷⁸ Nevertheless, for nanoparticles between 20 and 500 nm, to the best of our knowledge no kinetic information has been presented to describe their oxidation rate. In addition to finding the transition regime for silicon nanoparticles, it is also highly desirable to understand the nanoparticle oxidation kinetics, because Vazquez-Pufleau et al.¹⁴⁰ have proven that only under oxygenic atmospheres can a significant amount of carbon be eliminated from kerf. To optimize kerf recycling under atmospheres that contain oxygen, ideally we should be able to predict the kinetics based on an inexpensively measurable parameter such as surface area and crystallite size. Licciardello et al.¹⁴¹ reported that the oxidation kinetics of silicon are retarded by organic contaminants, which produce hydrophobic surfaces on top of the silicon. Chuanqiang et al.¹⁴² studied the oxidation behavior of kerf in aqueous media. They found that PEG in the slicing lubricant protects kerf from oxidation.

This work

Good models for crystalline silicon oxidation exist. These models rely on accurate values of, for example, thickness of the oxide layer. This value has been proposed also for nanoparticles, assuming that they are perfect spheres. However most of the nanoparticles synthesized via furnace reactors or fluidized bed reactors are rather agglomerates, whose morphology is ill defined by purely spherical models. Applications of silicon synthesized via FBRs or furnace reactors require a more precise knowledge of silicon oxidation for particles, with an easy to measure parameter such as surface area or crystallite size. Furthermore we consider the possibility of having different crystallite sizes. In this work we present a parabolic rate constant that predicts the oxidation kinetics for silicon agglomerates synthesized in a FBR that are non-uniform, non-unimodal, and non-ideal in general for various BET determined surface areas and that are constituted by various crystallite sizes. This approach to generalize the oxidation of silicon agglomerates has, to the best of our knowledge, not yet been reported in the literature. In this work, we employ thermogravimetric analysis (TGA) to study the activation energy of four silicon samples composed of silicon nanoparticles agglomerates with surface areas of 3, 6, 11 and 19 m²/g respectively and different crystallite sizes. We analyze the data using the Ozawa-Flynn-Wall (OFW) and Kissinger-Akahira-Sunose (KAS) methods to determine their overall activation energy and normalize their value by dividing it by the sample crystallite size. Values for samples with different surface areas (an indirect measure of particle size) were determined using BET.

4.3. Experimental methods

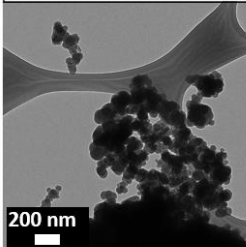
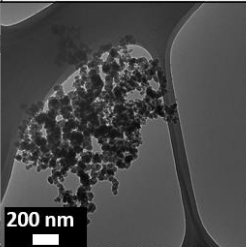
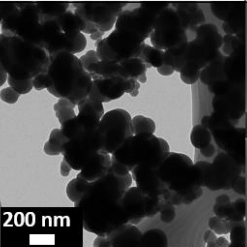
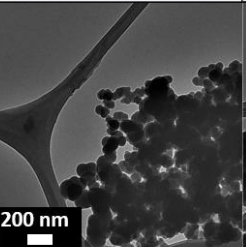
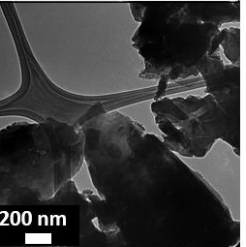
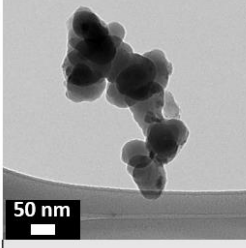
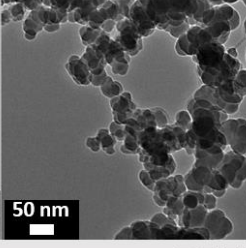
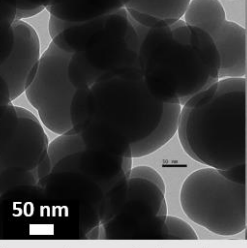
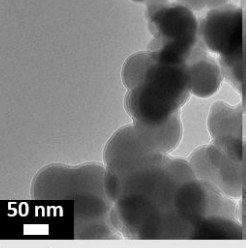
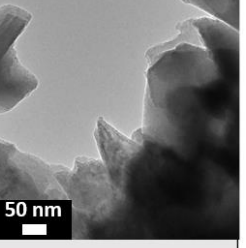
4.3.1. Characterization tools

Silicon powder from a pilot plant fluidized bed reactor (FBR) and kerf from sawing monocrystalline silicon ingots were provided by SunEdison Inc. (Saint Louis, MO). Kerf was processed using a furnace aerosol reactor (FUAR) to lower the carbon contamination to negligible levels.¹⁴⁰ Thermogravimetric analysis (TGA) was executed in platinum and ceramic pans in a Q5000 IR thermogravimetric analyzer (TA Instruments, New Castle, DE, USA) using heating rates of 20, 10, 5 and 2 °C/min and also at isotherms at 1000 °C in dry air (Airgas, St. Louis, MO). Transmission electron microscopy (TEM) characterizations were performed on all silicon samples. They were prepared by suspending 2-5 mg of the powder in deionized water and then sonicating for a few seconds. Then 20-40 µl of the colloid were pipetted onto a TEM copper grid. The grid was then allowed to air dry and observed in a FEI Spirit TEM (Fei, Hillsboro, OR, USA). Surface area was determined using the Brunauer-Emmett-Teller theory (BET) based on adsorption and desorption at cryogenic isotherms, in a Nova 200e BET instrument (Quantachrome Instruments, Boynton Beach, FL). The initial thickness of oxidation was assumed to be 2 nm. The BET-based particle diameter was used to calculate the oxidation layer thickness and extent of conversion according to the formula: $\text{surface area} = \text{Area}_{\text{sphere}} / (\text{vol}_{\text{sphere}} * \text{density}_{\text{material}})$. The diameter of the particle (d_p) was $= 6 / (\text{surface area} * \text{density}_{\text{material}})$. Then the parabolic rate constant (B) value was corrected using the crystallite size determined by the Sherrer equation from the X-Ray diffraction (XRD) patterns. The patterns were measured using a Bruker D8 Advance powder diffractometer (Bruker Corporation, Billerica, MA, USA) with a 3.0 kW generator, a Cu K α X-ray source, and a LynxEye XE energy-dispersive strip detector. The method of least squares was used to fit the data of the experimentally determined conversion to the parabolic constant model. The conversion

extent (α), was calculated from the predicted thickness of the oxide layer. Assuming that the outer shell of a sphere up to the oxide thickness was the reacted material, the volume inside that threshold was considered unreacted silicon.

4.4. Results & discussion

Table 4-1 Summary of silicon nanoparticle samples, including TEM, BET surface area, calculated particle size according to BET, and calculated crystallite size from the Sherrer equation using XRD peaks. The first four columns are FBR silicon and the last column is kerf

Silicon				Kerf
BET surface area (m ² /g)				
3	6	11	19	9
				
				
BET based particle size (nm)				
860	430	235	135	269
XRD crystallite size (nm)				
68	50	73	60	83

The results for the silicon samples from various characterization techniques, including TEM, BET, and crystallite size from XRD, are summarized in Table 4-1. It is interesting to note

that the crystallite size does not seem to be associated with BET surface area, but it can be qualitatively inferred from TEM micrographs.

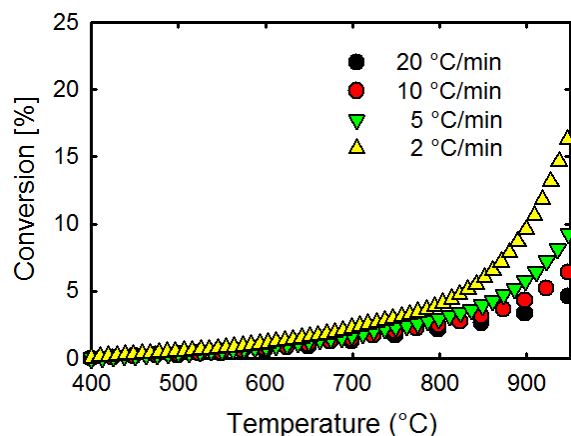
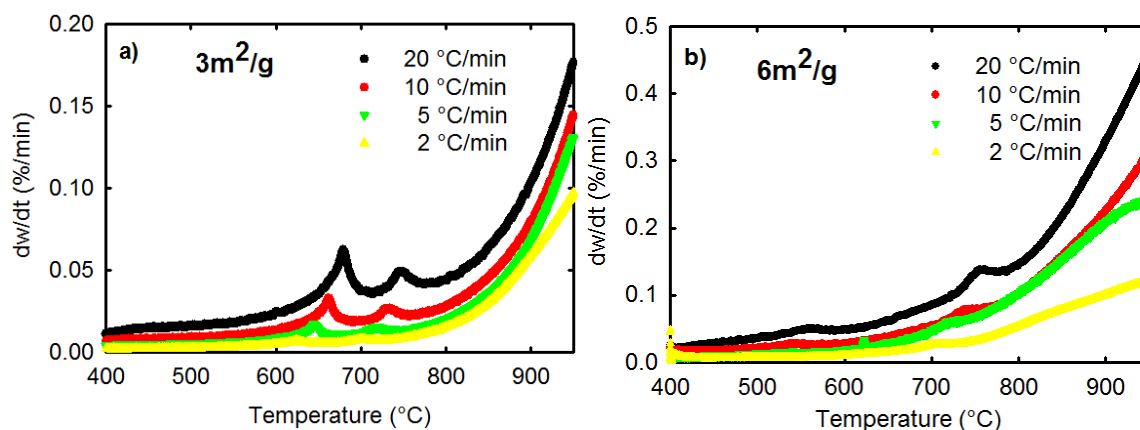


Figure 4-1 TGA calculated conversion for heating rates at various temperatures for Sample 11 m²/g of fluidized bed reactor dust.

Figure 4-1 shows the representative weight gain vs time or temperature for various heating rates, β (20, 10, 5 and 2 °C/min) of the 11 m²/g sample. The gain weight of other samples seems to correlate to BET surface area, the more surface area: the higher the oxidation rate at a given heating rate β .



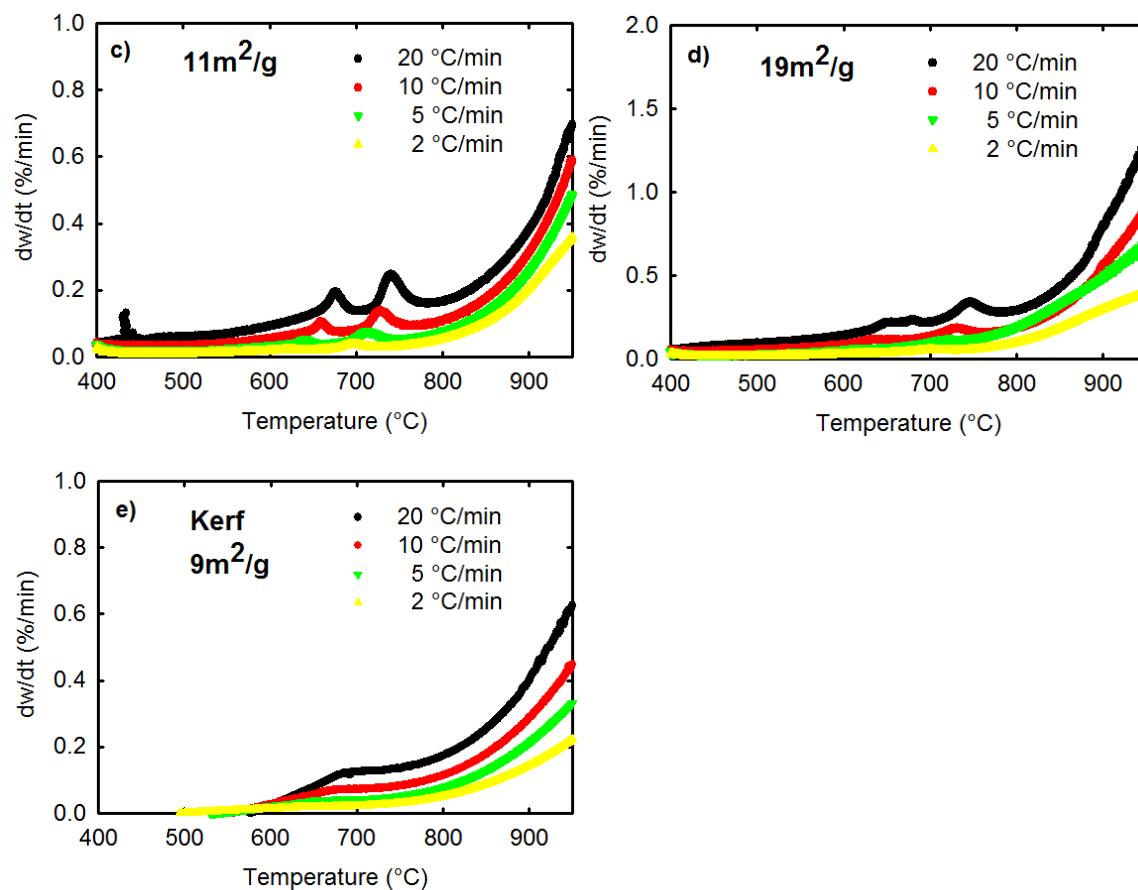


Figure 4-2 TGA weight gained derivatives for all silicon samples and kerf for a) 3m²/g, b) 6m²/g c) 11m²/g d) 19m²/g and e) kerf. Both the 3 m² and the 11 m² display two similar peaks, the first around 650 °C and the second around 750 °C. On the other hand the samples for 6 and 19 m²/g display a less marked first peak. Also for the sample of 6m²/g the first peak occurs around 550 °C, 100 °C before the first peak of the other silicon samples. Both of these trends are linked to the crystallite size rather than the surface area. We note that the 6m²/g, with the smallest first peak of all has a crystallite size of only 50nm

The derivative of the TGA weight gain as a function of time is shown in Figure 4-2. In this case, there are two peaks for all four silicon samples. Interestingly, the shape of these two peaks and the ratio of them within each sample seem to be correlated to the crystallite size. In the larger crystallite size cases (3 and 11 m²/g), both the first and second peak are of comparable sizes. However in the case of the 6 and 19 m²/g samples, which have the smaller crystallite sizes, the

first peak is significantly smaller, suggesting a slightly different oxidation mechanism that is crystallite size dependent.

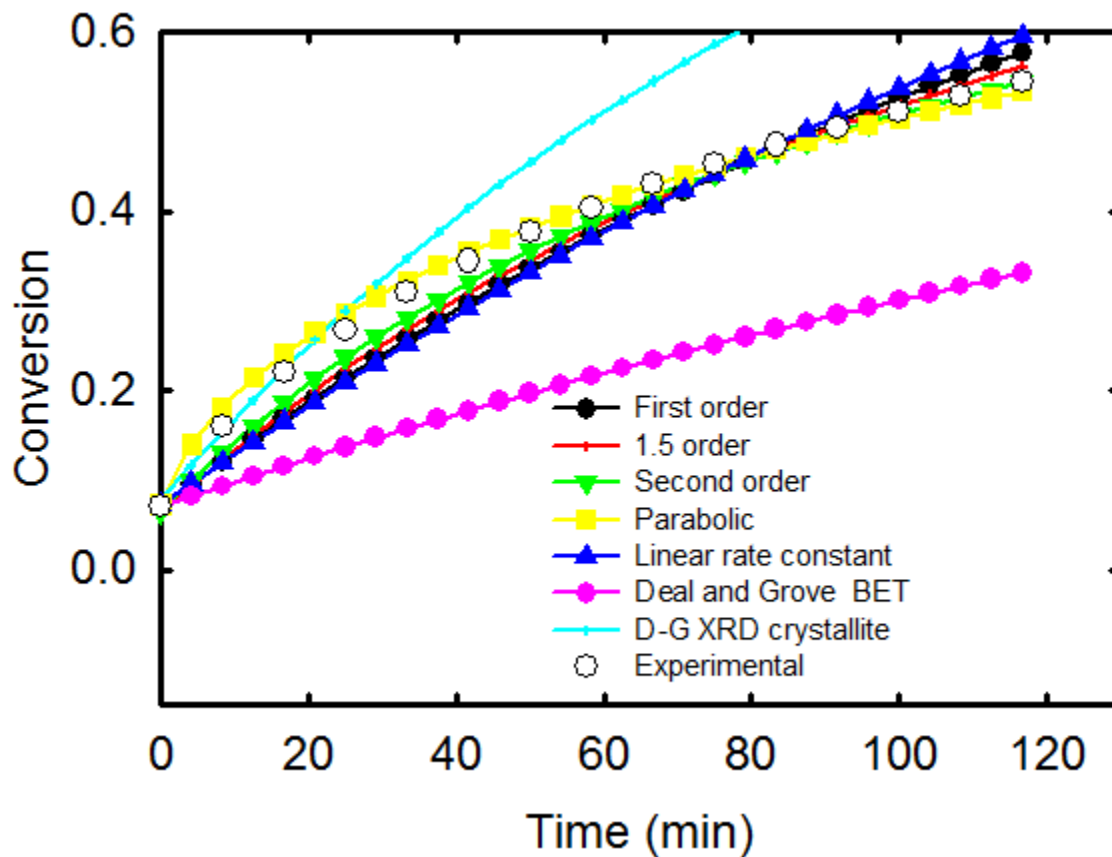


Figure 4-3 Evaluation of various kinetic models for describing the oxidation of 11 m²/g silicon. BET particle size based D-G underpredicts oxidation, whereas XRD crystallite size based D-G overpredicts oxidation. This might be the source of some contradiction in the literature, whether nanoparticles oxidize quicker or slower than predicted by the D-G model.

An example of fitting the experimentally measured conversion for an isothermal at 1000 °C is shown in Figure 4-3 for the 11 m²/g case. It can be observed that the only tested model that seems to fit well with the experimental data is the parabolic reaction model. For this case, the D-G model obtained from the BET based average particle size underpredicts the oxidation behavior.

On the other hand, if only crystallite size is used in the D-G model, it overpredicts the extent of oxidation of the silicon nanoparticles.

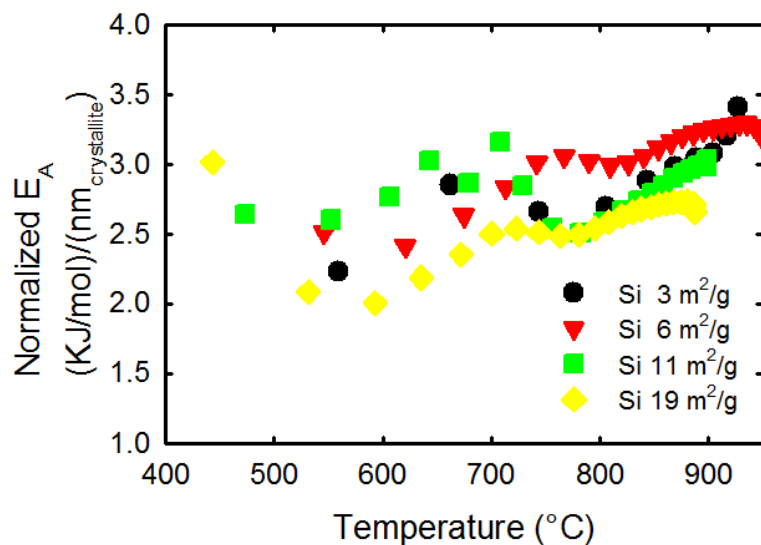


Figure 4-4 Normalized activation energy for all silicon samples. To obtain the real activation energy it is necessary to multiply the plotted value by the crystallite size of the sample.

The activation energies that we measured is shown in Figure 4-4, which indicates that lower activation energy is a function of both crystallite size and surface area. A reduction in either of these parameters is linked with a reduction in the activation energy of the oxidation reaction. This trend is in agreement with the observation of Liao et al.¹²⁵, who found an activation energy of 106 kJ/mol for nanoparticles of about 10 nm.¹²⁵ The activation energy can now be used to calculate the parabolic kinetic constant using the Arrhenius dependence, because it has been experimentally confirmed that B follows an Arrhenius behavior.¹⁴³

The oxidation of silicon was done using a TGA instrument. Several isotherms and constant heating ramps were employed to determine the kinetics and activation energy of silicon samples obtained from the FBR pilot plant of SunEdison Inc. Pap et al.¹⁴⁴ report that neglecting the initial state of oxidation produces results with an accuracy of +/- 2% for porous silicon samples. In our

case, for more accuracy, we assume a 2 nm oxide shell on the silicon nanoparticles, in agreement with Bohling & Sigmund¹⁴⁵ who report native oxidation of silicon as limited to ~2 nm in air at room temperature. In addition, during the time necessary to reach the 1000 °C isotherm the sample oxidizes further. For that reason and according to EerNisse¹¹⁹, silicon flows viscously above 960 °C. Therefore for the conditions here tested a linear regime dominated by the linear parameter (A) is neither expected nor measurable, because TGA oxidizes silicon beyond the linear regime during rise to 1000 °C. In addition, it has been reported that the transition into viscous flow destroys the microchannels that cause the linear rate region to be dominant, and in this viscous flow the dominant mechanism is Fickian¹²², or dominantly parabolic in such a way that the anomalous high oxidation rate regime is minimized. Therefore our system does not allow calculating the linear reaction rate zone described in the Deal and Grove model, and the linear zone in our model.

The effect of organic contaminants in the surface of silicon on its oxidation has been studied by Licciardello et al.¹⁴¹ They also found that oxidation kinetics are slower in monocrystalline wafers than in a silicon sample from wafers fractured in air.¹⁴¹ For that reason, a factor needs to be included when considering silicon nanoparticles of different roughness. The determination of the roughness factor is not trivial and challenging to measure and is rarely reported in the models for crystalline silicon oxidation¹⁴⁶ For our model for spherical nanoparticles the roughness factor used is 1.0, whereas, based on the oxidation rate of silicon kerf, we determined the roughness factor for the kinetic oxidation of kerf in air at 1000 °C to be 2.6.

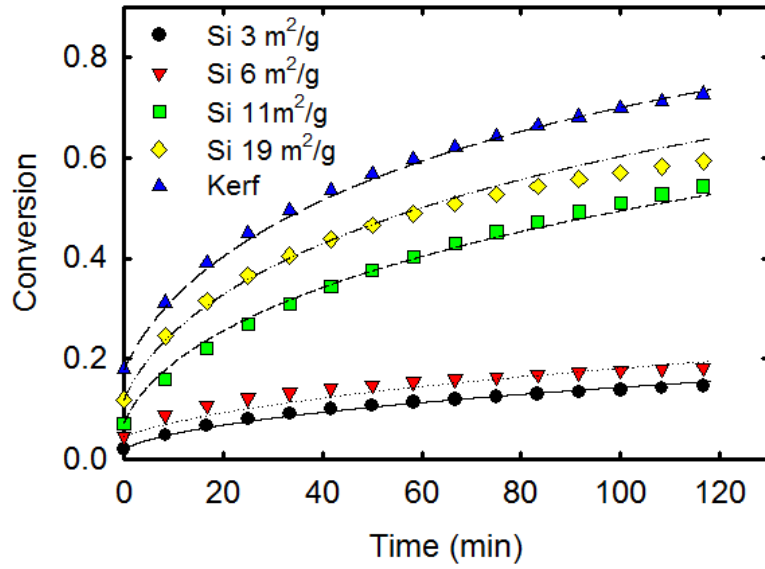


Figure 4-5 Experimentally calculated conversion from TGA data (symbols) for all samples at 1000 °C vs prediction from the function to calculate the parabolic factor as a function of surface area, crystallite size and roughness factor.

The isotherm of all four FBR silicon samples, the kerf sample and the parabolic model are displayed in Figure 4-5. The parabolic equation is defined by

$$L^2 = B(t + \tau) \quad (4-3)$$

The parabolic rate constant was determined based on the various silicon standards at 1000 °C in dry air. Its value is defined by

$$B = \left(5.87 * 10^{-5} \frac{\text{nm}^2}{(\text{min})(\text{nm}^3)} \right) (d_{\text{XRD}})^3 (R_a) \quad (4-4)$$

The equivalent initial oxide can be calculated from

$$\tau = \frac{L_0^2}{B} \quad (4.5)$$

where L_0 is the initial oxide thickness. By taking the mean particle size from BET, and assuming monodisperse and spherical particles, the conversion can be written as

$$d_{p,BET} = \frac{6}{S_A \rho} \quad (4-6)$$

where S_A is the surface area measured by BET, $d_{p,BET}$ is the mean particle diameter calculated based on the BET surface area, and ρ is the density of the silicon. Thus, conversion is given by

$$\alpha = 1 - \frac{\left(\frac{6}{S_A \rho} - (B(t+\tau))^{0.5}\right)^3}{\left(\frac{6}{S_A \rho}\right)^3} \quad (4-7)$$

substituting B , we derive the expression for conversion for polycrystalline agglomerate oxidation in air atmosphere at 1000°C.

$$\alpha = 1 - \frac{\left(\frac{6}{S_A \rho} - \left(5.87 \frac{nm^2}{min(nm^3)}\right) (d_{XRD})^3 (R_a) (t+\tau)\right)^{0.5}}{\left(\frac{6}{S_A \rho}\right)^3} \quad (4-8)$$

where L is the thickness of the oxide shell of a hypothetical sphere calculated using the BET surface area. d_{XRD} is the crystallite size determined by XRD using the Scherrer equation, and R_a is a roughness factor. R_a is 1.0 for agglomerates with smooth primary particles (quasispherical) and 2.6 for the kerf used in this study.

With the developed model, the kinetics of silicon oxidation in kerf can be compared with the kinetics of carbon elimination from Chapter 2. In Figure 4-6 the effect of residence time on both dynamic processes can be observed.

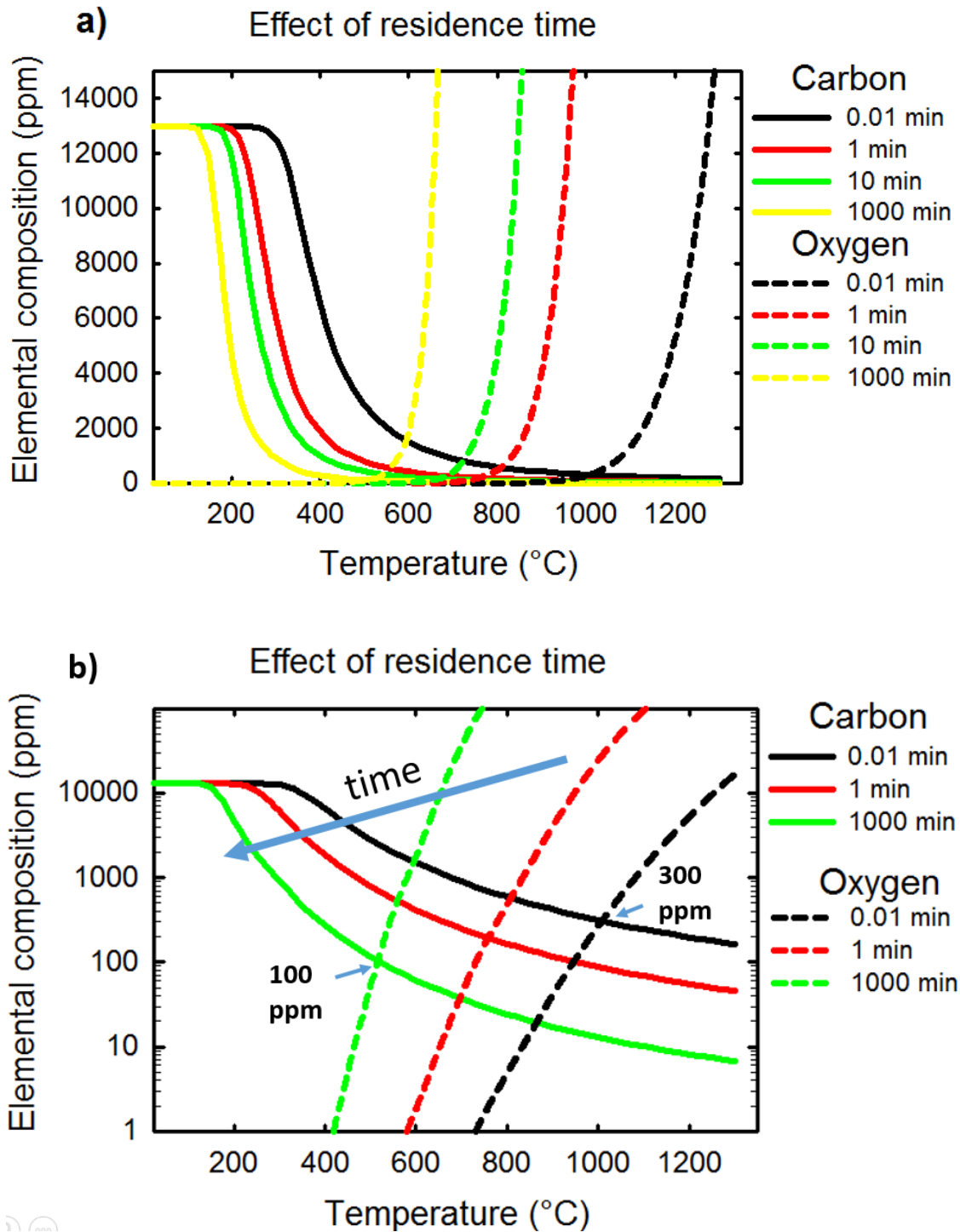


Figure 4-6 Effect of residence time on carbon elimination and silicon oxidation for various temperatures a) linear scale, b) log scale with details of relevant intersection for both elemental composition of carbon and oxygen curves.

4.5. Conclusion and summary

The parabolic constant of the D-G model is proposed as a function of crystallite size and BET surface area for polycrystalline silicon agglomerates with surface areas of 3-19m²/g. A factor to account for surface roughness is also proposed, and the single coefficient proposed is capable of satisfactorily fitting all five non-ideal samples, including kerf purified by a FuAR.

Primary particles from agglomerates do not seem to be the best source for assigning silicon oxidation kinetics, as there is not good correlation between them and surface area. This might be due to three reasons: Sintering significantly reduces surface area, mechanical sintering seems to be different from just physical agglomeration for the kinetics of oxidation and pore swelling could prevent exposure of oxygen into the silicon at the interior of the agglomerates.

For non-ideal conditions, such as kerf recycling at an industrial level, the best way to do kinetic estimations is to use the total surface area rather than an average mean particle size distribution, because the amount of sintering is typically not well reported in the literature on kinetic oxidation of silicon.

The silicon raw material is not pure, which could be due to oxidation in the surface and the presence of silicon hydrides. When heating to 700°C and 800°C, dehydration and de-hydrogenation occur at the same time, and, oxidation of silicon forms both silicon oxides and silicon suboxides.

CHAPTER 5: MEASUREMENT OF A STABLE SILICON HYDRIDE CLUSTER FROM SILANE PYROLYSIS IN A HELIUM ATMOSPHERE THAT DOES NOT SEEM TO BEHAVE AS A STABLE NUCLEUS BUT RATHER AS A CONDENSABLE SPECIES

Results from this chapter are intended for publication in a peer review journal

Vazquez-Pufleau, M[†], Wang, Y[†], Thimsen, E., & Biswas, P. Measurement of a silicon hydride cluster from silane pyrolysis in a helium atmosphere (2016), Journal of physical chemistry, [†] equal contribution authors, to be submitted.

5.1. Abstract

The formation of aerosols from silane pyrolysis is a delicate process in the semiconductor and photovoltaic industry. In semiconductor fabrication, it is seen as an undesirable process to be avoided at all costs, whereas in the photovoltaic field, its understanding and control is promising for the synthesis of cheap polysilicon through advanced reactors, whose widespread implementation can significantly lower PV costs. Due to its importance, efforts have been devoted to understanding the complex reactions and mechanisms of silane pyrolysis, in order for the aerosol simulation to accurately predict the properties and evolution of the aerosols formed. As a critical process in silane pyrolysis, nucleation has received attention in the form of simulations that have yielded proposed mechanisms with hundreds of reactions and critical nucleation sizes for Si_nH_m with $n>7$,⁵⁹ or $n>10$.^{48, 147} Where the capacity of a compound to act as a nucleus is based on the stability of the compound itself based on its ΔG of formation. In this work, we measured a stable silicon hydride cluster size distribution experimentally for 0.3% silane in a helium atmosphere using a high resolution half mini differential mobility analyzer. Our findings are also supported by transmission electron microscopy and gas chromatography mass spectrometry. The measured mobility diameter is approximately 0.75 nm, and the evidence is consistent with a formula of Si_7H_{11} in agreement with data reported by Wong et al.¹⁴⁸ However, even though the molecule is thermodynamically stable, it does not seem to behave as a critical nucleus in contrast to conventional theories of nucleation of liquid particles (where the requirement for a stable nuclei is that its $\Delta G<0$) that have been typically taken as granted for silane pyrolysis. The present work provides evidence of the contrary: It is suggested that not necessarily every stable high molecular weight silicon hydride molecule behaves as a critical nucleus, but can also be a condensable species.

5.2. Introduction

For more than half a century, silicon has been the most effective material (in terms of cost-performance) for both semiconductors and photovoltaics (PV).¹⁴⁹ In the semiconductor industry, it is desired to avoid aerosol formation due to the difficulty of accurately controlling their deposition in the nanometer range. The processing of electronic chips typically occurs under low pressure chemical vapor deposition (LPCVD) systems, at conditions below the nucleation regime. Due to fear of silicon aerosol contamination, and an incomplete understanding of their formation, LPCVD processes are normally operated in a suboptimal region with lower yield.¹⁵⁰ Improving our understanding of the silane nucleation mechanism and measuring intermediate compounds from silane pyrolysis as well as understanding if they behave as stable nuclei or condensable species can help to more accurately predict the rate at which nucleation occurs at various conditions^{147b}. Such knowledge allows the use of higher epitaxial deposition rates in the semiconductor industry, which would safely enhance the speed of chip processing under optimal conditions. Therefore it is important to understand and determine the critical nucleation size. On the other hand, for both industries, purification of silicon is complex and requires various energy intensive steps.¹⁵¹ One of the most demanding is the chemical vapor deposition required to obtain the stringent levels of purity demanded by such industries. Here, a better understanding of aerosol formation in its incipient phases is also highly relevant.²⁰ Here we focus on silane pyrolysis, which is important for both photovoltaics and semiconductors.

The kinetics of silane pyrolysis are highly relevant for understanding and predicting nucleation. Several kinetic models and mechanisms⁴³ have been predicted for the gross pyrolysis reaction of silane; $SiH_4 \rightarrow Si + 2H_2$. Girshick et al.⁴⁸ proposed 100 species and 400 reactions, Kremer et al.⁴⁷ 33 reactions, Giunta et al.⁵⁶ 18 reactions, and Kleijn et al.¹⁵² 10 reactions and five

species. Polymerization is believed to occur until a stable nucleus size is reached for molecules larger than the point where the forward reaction is orders of magnitude faster than the backward reaction. Experimental evidence supports the polymerization theory, such as the facts that the concentration of aerosol precursors is related to polysilane concentration and that aerosol formation occurs after the onset of pyrolysis¹⁵³. Nucleation of silicon has historically been explained using a polymerization approach, where silane reacts with itself to form dimers, trimers, tetramers, and so on. Once the series of reactions reaches a certain species or the silicon hydride polymer grows larger than a given molecular weight, it is assumed that the reversible reaction interplay ends and nucleation begins. Several borderlines have been proposed. On one hand, the silane polymerization reaction is assumed to form silicon atoms¹⁵⁴ that then physically evolve following classical aerosol dynamics. The process of nucleation and condensation occurs due to differences in stability between silicon hydrides that conform the polymer. As reaction progresses and silane pyrolyses and forms silicon hydride polymers, the stability of these molecules varies depending on how well satisfied the electronic charges of the atoms are based on the different chemical bonds. Wong et al.¹⁴⁸ proposed that the nuclei contains at least seven silicon atoms. On the other hand, studies by Girshick et al.⁴⁸, Swihart et al.^{147b} and Nijhawan et al.⁵³ suggest the number of silicon atoms must be at least ten in order to produce a stable nuclei. Above that number, higher silicon hydrides have been neglected from calculations for computational efficiency. Evenso, obtaining the corresponding size of stable silicon nuclei as a function of $\text{SiH}_4\text{:H}_2$ ratio, temperature and pressure has not been possible, due to limitations of computational resources¹⁴⁸. Furthermore, to the best of our knowledge, no experimental measurement of a silane nucleus has been reported, in part due to the difficulty of measuring such small, reactive, and low concentration particles in real time.

It has been reported that the mean size and number concentration of particulates formed during silane pyrolysis are dominated by coagulation, causing the mean particle size to be directly related to the precursor concentration¹⁵⁵. This is true for large scale aerosols. However, many of the properties of an aerosol are given not only by the size of their agglomerates, but also by the size of the primary particles that constitute them¹⁵⁶, and this determination cannot be done unless the reaction mechanism, including the nuclei sizes is determined. Talukdar et al.^{147a} have reported that for complex systems such as silane, considering the aerosol dynamics only is not sufficient for describing aerosol evolution in the initial stages of reaction. It is also important to consider the complexities in the chemical reaction by including the rate of nucleation.

Differential mobility analyzers (DMAs) have often been used to investigate the size distribution characteristics of airborne particles. DMAs classify particles as a function of their electrical mobility, and specific mobility sizes are measured with a particle counter, such as an electrometer or a condensation particle counter, downstream of the DMA. Measuring the size distribution of sub-3 nm particles with conventional DMAs has been limited by the high diffusivities of these particles, which can easily cause diffusion loss and diffusion broadening of the DMA transfer functions.¹⁵⁷ In recent years, high resolution DMAs with significantly high sheath flow rates have been designed, making the measurement of sub-3 nm particles feasible.¹⁵⁸ Incipient molecular clusters and particles generated from aerosol reactors have been clearly observed, and aerosol formation pathways and chemical reaction rates have been predicted.^{157, 159} Hence, high resolution DMAs can serve as a powerful tool to study particle generation during silane pyrolysis.

In the present work, we used a high resolution DMA to measure (for the first time in our knowledge) the size of a silicon hydride stable cluster in a helium atmosphere in terms of their mobility diameters, which is however not behaving as a stable silicon nuclei.

5.3. Experimental methods

5.3.1. Experimental setup

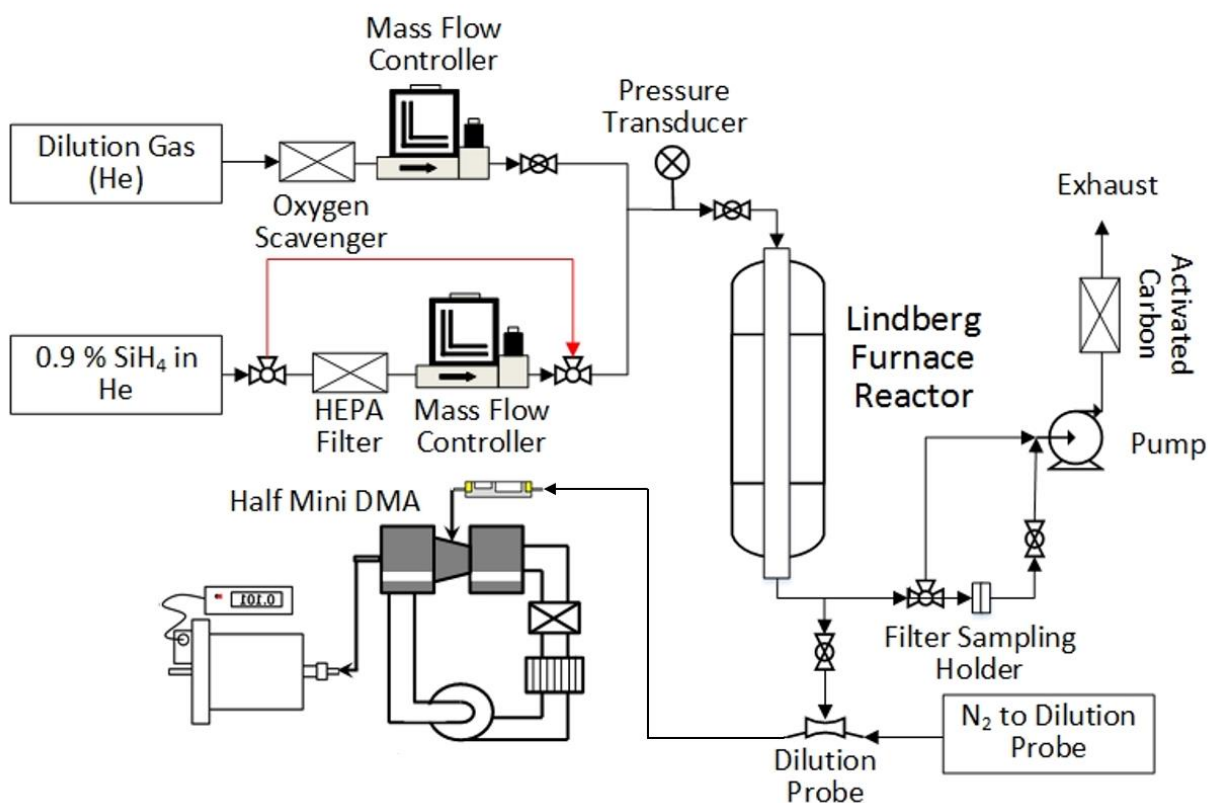


Figure 5-1 Silane reactor setup, including ancillary systems and connected online characterization instruments.

The setup used for this study is sketched in Figure 5-1. A 0.9% stream of silane in helium (Airgas Inc. PA, USA) is controlled using a mass flow controller (MFC) (MKS Instruments Inc., MA, USA) The second stream is ultra-high purity helium (99.999% Airgas Inc., PA, USA) passed

through an oxygen scavenger element (Cee Kay Supply, MO, USA) to eliminate trace amounts of oxygen. The streams were directed into a 1 inch stainless steel 316 tube heated by a Lindbergh Furnace (Thermo Fisher Scientific, MA, USA). The furnace temperature profile was measured using a K type thermocouple (McMaster-Carr, IL, USA). The pressure in the reactor was monitored using a pressure transducer (WIKA, Klingenberg am Main, Germany). The sampled stream was diverted from the main flow using a Y with branches at 45°. The primary flow was exhausted through a high capacity filtering medium, and the sample was diluted using a dilution probe composed of a 150 μm flow restrictor orifice in the suction section of a Venturi pump. This orifice diluted the aerosol sample by approximately 45 times. The sample was diluted in nitrogen (99.997% Airgas Inc., PA, USA) and 12.5 lpm of the diluted stream were then entered into the half mini DMA.

5.3.2. Characterization tools

This study used a high resolution half mini DMA to measure the size distribution of sub-3 nm particles generated during silane pyrolysis.^{158b} The DMA was operated in a closed loop, so that the aerosol inlet and outlet flow rates were equal. The sheath flow of the DMA was provided by a brushless blower (DOMEL Inc.), followed by an inline HEPA filter and a carbon trap to remove the remaining particles in the system. The voltage applied across the DMA electrodes was provided by a high voltage power supply (Bertan 205B, Spellman Inc.) controlled by a Labview® program. The voltage was scanned from 0 to 5 kV, with a step voltage of 5 V and a step time of 1 s. A homemade Faraday cup electrometer (FCE) was located downstream from the DMA to collect and count the classified particles. The actual particle concentration was calculated from the current monitored by the FCE and the aerosol flow rate controlled by the mass flow controller (MKS Inc.)

downstream the FCE. During the experiments, the aerosol flow rate was maintained at 10 lpm. Three measurements were made at each condition to reduce the effect of sample fluctuation. Before experiments, to establish a mobility standard, the half mini DMA was calibrated by the ions generated from an electrospray of tetraheptyl ammonium bromide (THAB)-methanol solution,^{157, 160} and the voltages corresponding to the monomer, dimer, and trimer of THAB clusters were recorded. Under the same DMA setting, the product of the mobility of a particle (Z) and the voltage at which the particle is classified (V) remains a constant. Hence, the mobility of particles classified at any DMA voltage can be calculated. The mobility size of a particle is further derived by $Z = Cne/3\pi\mu D_p$, where C is the Cunningham slip correction factor, n is the number of charges on the particle, e is the electronic charge, μ is the air viscosity, and D_p is the particle mobility size. For sub-3 nm particles, it is safe to assume that classified particles carry a single charge due to the difficulty to stabilize more than one charge in such small volume.¹⁶¹ Existing studies suggest that the volumetric diameter (D_v) of a sub-3 nm particle is approximately 0.3 nm smaller than D_p due to the effect of the gas molecule's effective diameter¹⁶². Further calculation is also needed to derive the exact value of the particle mobility diameter, since the influence of the ion-induced dipole potential on the particle mobility is not evaluated in the Stokes-Millikan equation for sub 3-nm particles¹⁶²⁻¹⁶³. However, for simplicity, the mobility diameter of the particle calculated by Eq. (1) was used to evaluate the particle size distributions. During the measurement with the half mini DMA, a Kr-85 radioactive neutralizer (TSI 3077A, TSI Inc.) was used to charge the particles that evolved from silane pyrolysis, since the silicon hydride stable clusters were not charged on their own and thus could not be measured without the neutralizer. This phenomenon indicated that silane pyrolysis in furnace aerosol reactors does not involve the

generation and exchange of ion species, or that they react too rapidly to be able to measure them, similar to the results obtained in a previous study.^{159b} It should also be noted that the strong ionization taking place in the neutralizer may also generate other species of stable charged clusters, which have been identified in previous studies.¹⁶⁴ The ions may serve as contaminant ions in the size distribution measurement, as introduced in the results section.

Copper grid samples for transmission electron microscopy (TEM) characterizations of aerosols formed at various temperatures were obtained using a thermophoretic sampler located on the outlet of the reactor. The samples were collected for 30 seconds and then analyzed using a Fei Spirit TEM (Fei, Hillsboro, OR, USA). The images were analyzed by converting the TEM images into binary files and executing pixel count software. Particle size distributions for conditions above the critical silane concentration were gained by manually counting the primary particles of a representative agglomerate with the aid of ImageJ[®] 1.48v software (Rasband W.S., ImageJ, U. S. National Institutes of Health, Bethesda, Maryland, USA, <http://imagej.nih.gov/ij/>, 1997-2015.). To assure representative sampling, more than 40 images were taken in at least 3 different sections of the TEM grid for each sample. The aerosols formed at various temperatures were collected using 47 mm quartz filters with a thickness of 0.38 mm and no binder. To collect a given sample, the filter was located in the interior of a homemade stainless steel filter holder.

5.4. Results and discussion

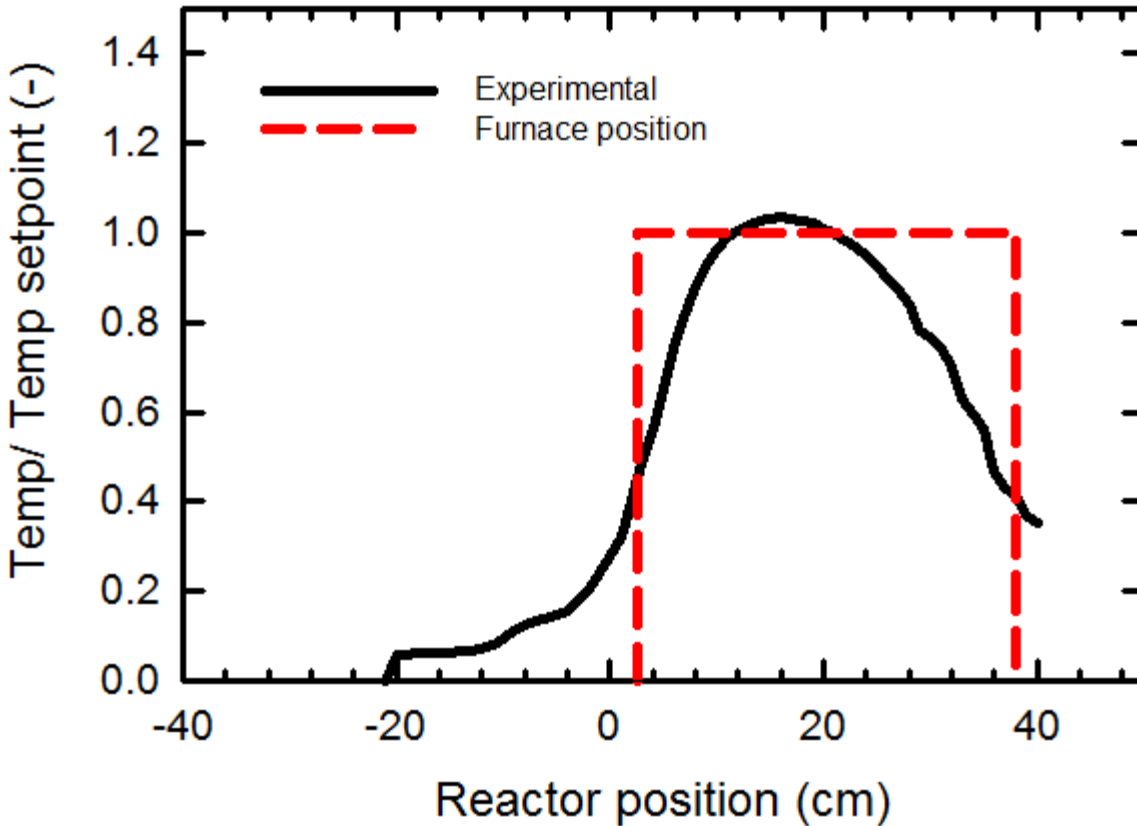


Figure 5-2 Temperature profile of flow reactor inside the Lindbergh furnace. The highest temperature is located at the end of the first third of the furnace. At this point maximum reaction rates are expected.

The temperature profile in the furnace is shown in Figure 5-2. It displays three different zones: (1) a rapidly heating inlet that reaches 80% of the temperature setpoint within about 5 cm, (2) an overshoot temperature region, where the temperature is about 5% higher than the setpoint, and (3) an outlet that gradually cools off. The thermocouple that controls the furnace heating elements is located at the central point, where the actual temperature matches the setpoint temperature. This behavior is typical for a vertically oriented furnace with a single thermocouple located in the center of the furnace and a single loop of heating elements connected to a PID controller. Despite having a cold inlet and outlet, the normalized temperature profile holds for a wide range of temperatures, which means that the bias caused by this intrinsic profile occurs for

all conditions in proportion to the setpoint temperature chosen. Thus the results presented here might differ from other geometries by a few degrees Celsius, but the trends discussed would still hold.

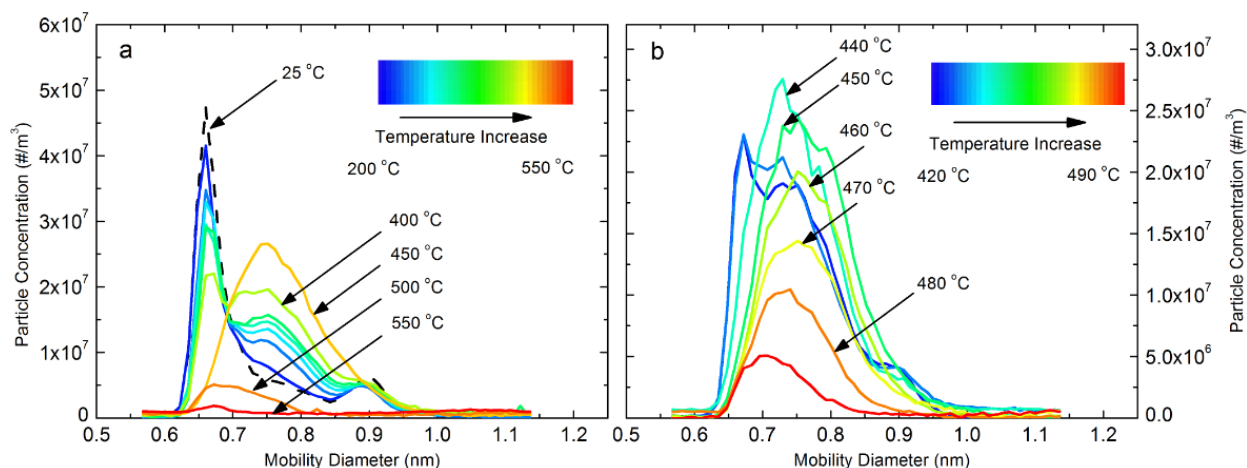


Figure 5-3 Negatively charged clusters measured by the DMA in the temperature range of a) 25 °C to 550 °C and b) 420 °C to 490 °C a) measurement including the nitrate ion with a peak around 0.65 nm and b) The nitrate ion has been subtracted using a Gaussian regression.

Figure 5-3 displays the size distribution of negatively charged particles generated during silane pyrolysis in temperature ranges of 25 °C to 500 °C (Figure. 5-3a) and 420 °C to 490 °C (Figure. 5-3b) at a feed rate of 600 standard cubic centimeters per minute (sccm) and 0.3% silane in helium. The size distribution measured at 25 °C (black line in Figure. 5-3a) shows the ion clusters generated from the Kr-85 radioactive neutralizer. A major peak at a mobility diameter of 0.67 nm was detected. Studies have shown that these ion species are closely related with nitric species, which have a high electron affinity.^{164a, 164b} As the furnace temperature increased, this major peak gradually decreased, while new charged species with sizes from 0.65 to 1.0 nm appeared. These intermediate species are produced by the pyrolysis of silane. Unlike the measurements conducted

in aerosol reactors with other precursor species, the newly formed species were not composed of molecular clusters with a specific mobility size, and did not display the highly resolved peaks observed in those scenarios.^{157, 159a, 159b} These intermediate species reached a maximum concentration at 440 °C, and their abundance at the outlet of the reactor decreased rapidly when the furnace temperature was raised to 550 °C. As shown elsewhere, the onset temperature for silicon nucleation in helium may lie between 450 and 550 °C, where the high nucleation rates quickly consume the molecular clusters through homogeneous and heterogeneous nucleation, forming large amounts of measurable particles.^{147a} Figure. 5-3b shows the detailed evolution of charged species as a function of the furnace temperature in the range of 420 to 490°C. The deconvolution of the originally detected contaminant ions was achieved by assuming a Gaussian shape of the size distribution at a size of 0.67 nm.

The size distributions of positively charged particles were also measured (Figure 5-7); however, as the furnace temperature increased, no new peaks were observed, and the intensity of the originally detected contaminant ion species decreased. The absence of species other than neutralizer ions suggested that the intermediate species generated from silane pyrolysis may have a high electron affinity, while the consumption of neutralizer ions was mainly caused by the collision between ions and newly formed silicon particles. It is important to mention that the outlet no signal could be detected when measuring the outlet of the reactor using the half mini DMA without a neutralizer.

At 400 °C the formation of the stable silicon hydride begins, at ~450 °C it reaches a maximum, and above that temperature the concentration of stable silicon hydride decreases as the particle dynamics consumes all the available clusters by means of condensation. The GCMS results in Figure 5-8 show an intensity peak at 207 m/z consistent with a Si₇H₁₁ polymer. As

mentioned, this silicon hydride cluster was measured using a concentration of 0.3% silane in helium. The nature of the process indicates that, as with the critical silane concentration, silicon hydride stable clusters might be of different sizes at different concentrations. In the numerous polymerization processes that occur in silane pyrolysis, the equilibrium and kinetic constants are modified as the temperature and concentration of precursor are changed. Thus the point at which a reaction becomes predominantly irreversible changes. Even though the effect of concentration may impact the silicon hydride cluster stability, its effect is not easy to measure below 0.3%, because the clusters formed become rapidly less abundant and the half mini DMA can no longer measure their concentration (See Figure 5-6).

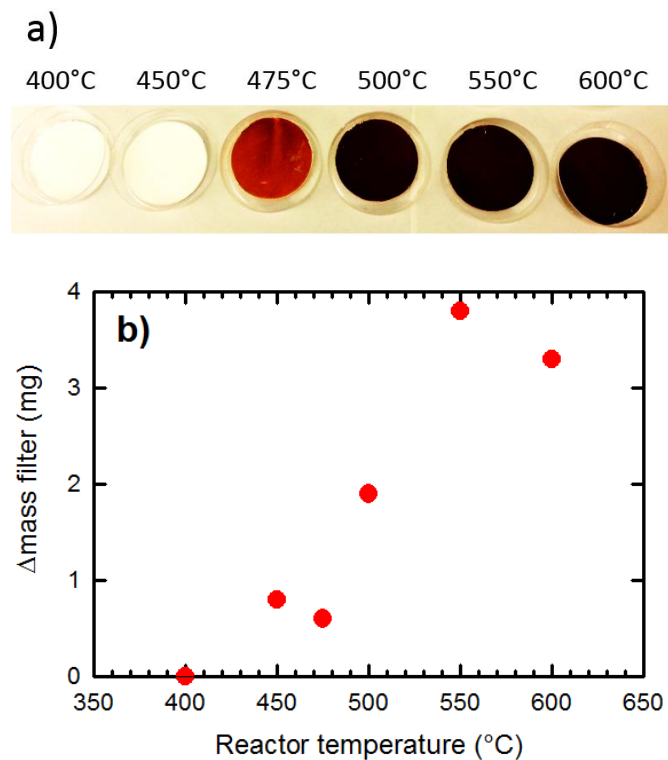


Figure 5-4 Aerosols collected for 5 min from running 0.3% silane through the reactor at temperatures between 400 -600 °C and b) Relative mass gain in the filter compared to the 400 °C case deviations in the linearity are attributed to filter handling and weighing

The onset of nucleation is evident in the color change of the filter, shown in Figure 5-4 a, as well as in the relative mass gain of the filter, shown in Figure 5-4b. Due to hydrogen and helium adsorption on the surface of the filters, the weight is displayed as relative weight gain compared to the 400 °C case, where no aerosols are expected at the given conditions. The onset of nucleation is also evident in TEM images in Figure 5-5 a. Above the critical silane concentration, as the temperature increases, the size distribution of the primary particles within the aerosol agglomerates increases as well, as can be seen in Figure 5-5 b. The mean of the primary particle size distribution is 10nm at 450 °C, 20 nm at 475 °C, and 40nm at 500 °C, showing a consistent increase in the particle size as the temperature rises. The total aerosol concentration also increases with increasing temperature. A projected area analysis, provided in Figure 5-5c, is consistent with an increase in the total mass concentration of aerosols. These results support the explanation of silicon cluster disappearance above 450 °C: The clusters are scavenged by the aerosols formed. This also explains the nitrate ions being depleted, because more aerosols are available to scavenge the ion charges for both negative (Figure 5-3a) and positive ions (Figure 5-7), in agreement with previous studies.¹⁵⁷ Interestingly, the ions generated by the neutralizer that are negatively charged are more easily depleted at the same temperature compared to the positive ions (See 500 °C and 550 °C peaks in Figure 5-3a and Figure 5-7 for negative and positive ions respectively). This suggests that the silicon nanoparticles are slightly positively charged and therefore can more easily accept a negative charge than a positive charge from the neutralizer ions.

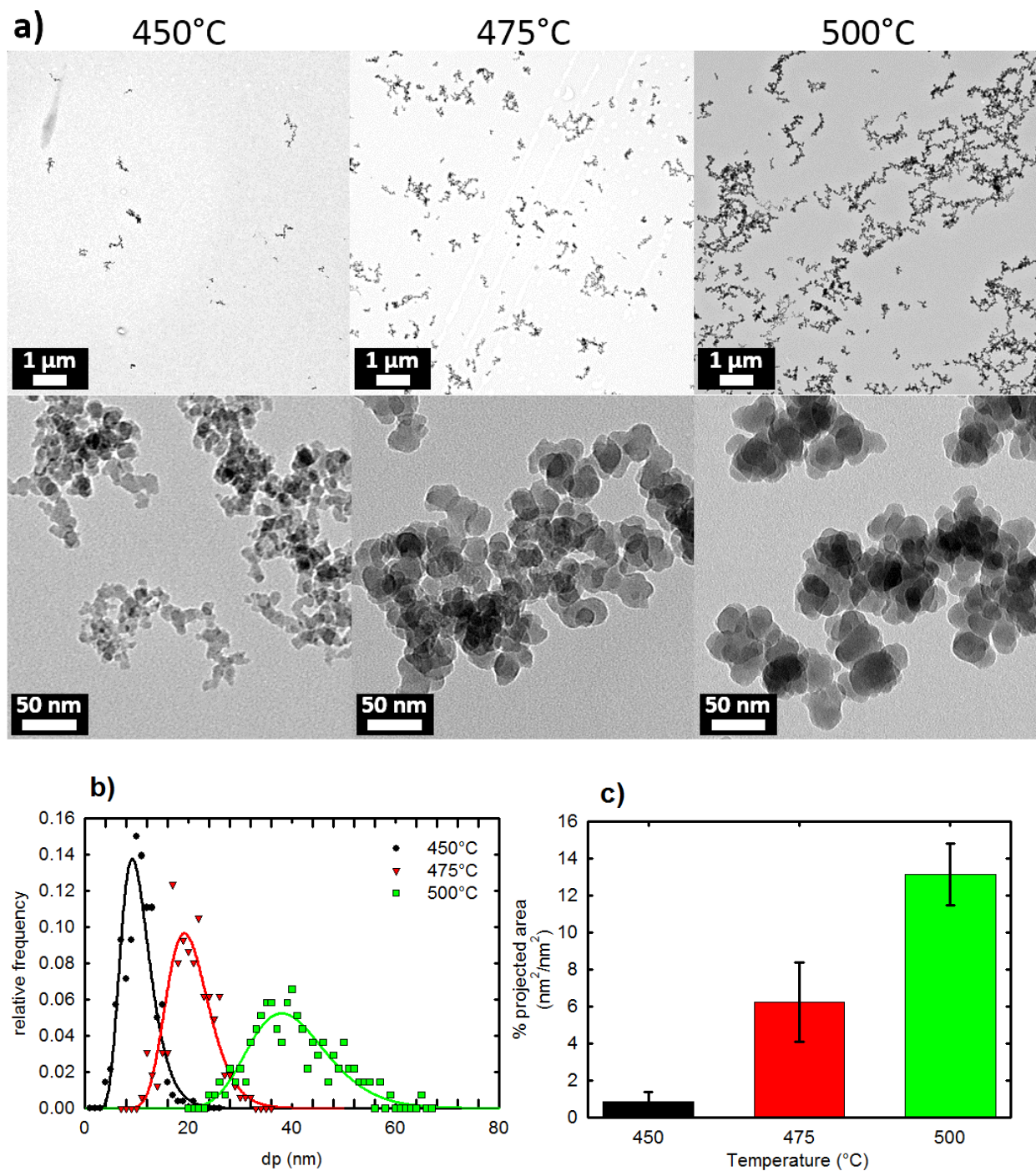


Figure 5-5 a) TEM silicon nanoparticles synthesized at different temperatures b) Primary particle size distributions for various temperatures and c) Relative abundance of silicon aerosols based on the projected area from representative TEM images. It provides the same trend as the filter weight gain from Figure 5-4 but with more resolution and accuracy.

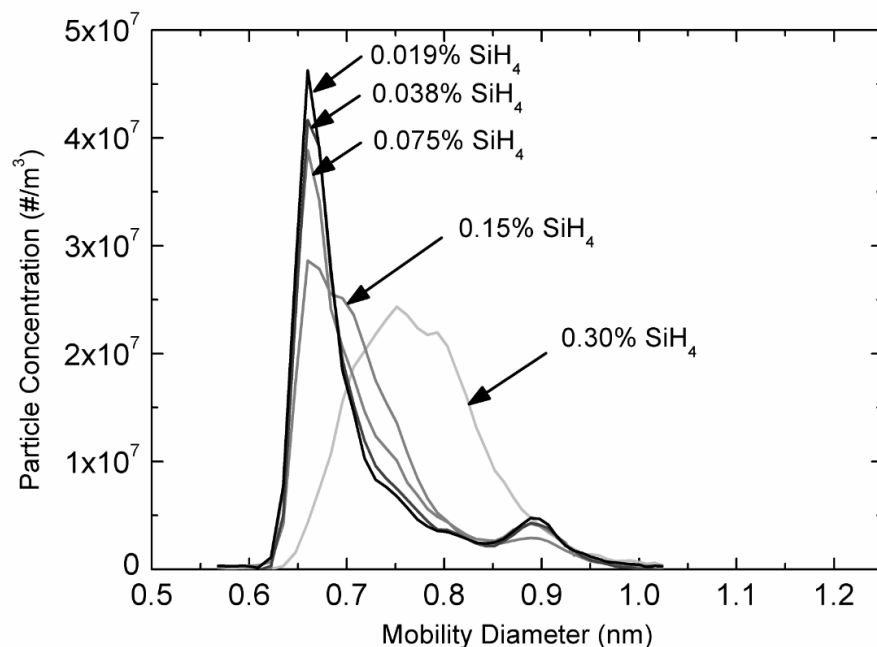


Figure 5-6 Sub-3 nm particle size distributions measured under different SiH_4 concentrations at 450 °C. The peak at 0.67 nm is generated by the neutralizer whereas the peak at around 0.75nm is attributed to the silicon hydride stable cluster. Detection of this cluster below 0.075% SiH_4 was not possible.

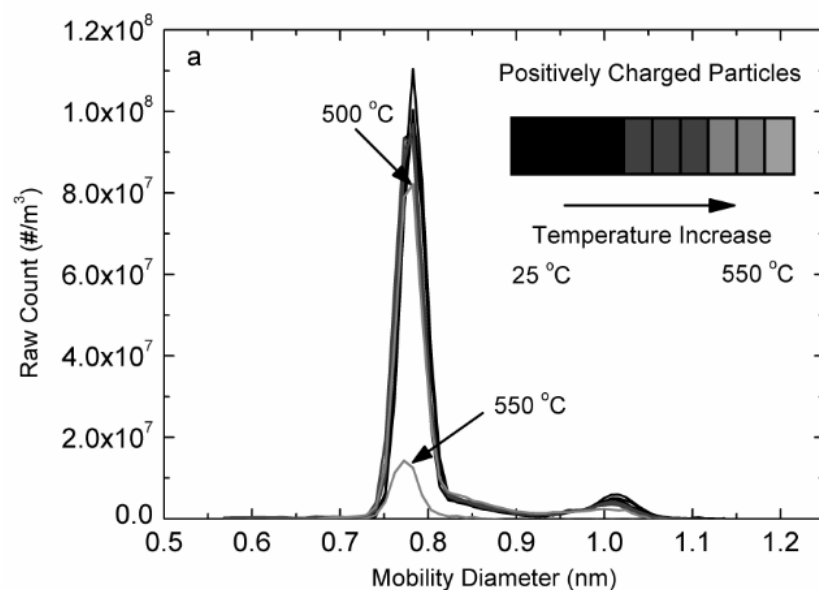


Figure 5-7 Neutralizer-generated positive ions measured in the temperature range of 25 °C to 550 °C. The decrease of the peak intensity at 550°C is attributed to ion scavenging by the large amount of aerosols formed at that temperature.

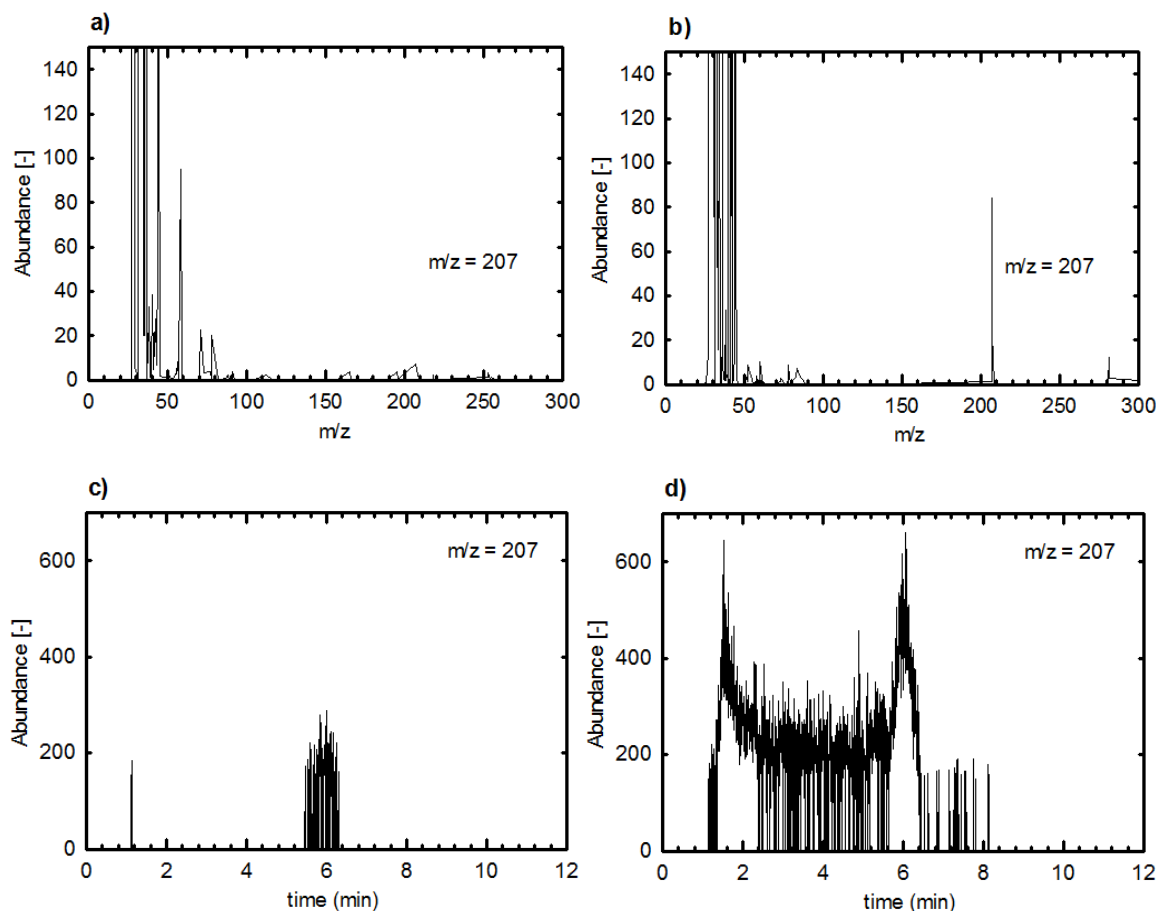


Figure 5-8 m/z spectra obtained via GCMS from an aliquot extracted manually from the reactor a) without silane and b) with 0.3% silane at 450 °C c) The spectra for the ion extraction plot for m/z 207 is displayed in c) for the blank reactor, and d) for the reactor with silane at 450°C. In the case of the blank reactor (c), a noisy signal at a time of around 6 min. is observed. It is attributed to traces of the cluster of interest from the reactor. In the case of the reactor with silane at 450°C (d), the plot indicates that the GC column used was not optimized for separating this compound. However, the presence of broad peaks is in agreement with a realistic signal and not to random noise. The signal suggests the presence of the 207 m/z ion is real. Thus it is the best and most realistic candidate for assigning the identity of the 0.75 nm cluster measured using the half mini DMA.

5.4.1. Interpretation of stable silicon hydride cluster as a condensable species and not as a stable nuclei

The interpretation of the cluster detected in the process of nucleation can be twofold: as a nuclei or as a condensable species. For the first case, the species measured is stable enough as to pass through the reactor, the dilution probe and the half mini DMA before being detected, which

is in agreement with previous definitions of the requirement for being a stable nuclei. On the other hand, by definition a stable nuclei should be capable of growing by receiving condensation on its surface so a wider and continuous distribution of particles larger than the detected cluster should be observable. However, at all tested conditions (See Figure 5-3), there is not a continuous distribution that goes above sub-nanometer sizes, but only a static peak around 0.75 nm. This suggests that the particle being detected is a condensable species and that is why the peak displays the same breadth regardless of the condition where it was measured. If the stable particles measured were stable nuclei, they would be able of receiving condensable species and would therefore grow larger. At 500°C (See Figure 5-5 a), the primary particle size of 40nm observed by TEM contrast with the measured cluster at 0.75 nm. Such a significant amount of condensation being possible in the primary particle and none in the observed cluster (As its size does not change compared to lower temperatures, See Figure 5-3 b)) suggests that this last it is not behaving as a stable nuclei but rather as a condensable species. A more plausible explanation for explaining why the concentration of this cluster decreases at higher temperatures is because because more aerosol surface is available to scavenge it as a condensable species.

The present observation casts doubt on the previous assumption that any stable silicon hydride Si_nH_m with n larger than 6 would behave as a stable silicon nuclei. More importantly, it suggests the need to revise the concept of thermodynamic stability of large silicon hydride clusters as a synonym of a cluster behaving as a silicon stable nuclei.

5.5. Conclusion and summary

Stable high molecular weight clusters formed during silane pyrolysis were measured for the first time, using a half mini DMA. The determined mobility size is 0.75 nm. A GCMS scan at

450 °C shows a peak at 207 m/z, which is consistent with a molecular identity of Si_7H_{11} . The measurement of this cluster provides insights into the nucleation process for silane pyrolysis in helium and is helpful for calibrating mechanistic modeling of the silane pyrolysis, aiding in the prediction of reaction rates for the nucleation process. This information is useful in optimizing processes to use the highest deposition rate without risking nucleation, as in the electronic industry. It also provides a better understanding of the fines formation, which is useful in the silicon refining industry, where a high mass yield demands regimes of high fine formation in the reactor internals.

The progressive formation of aerosols as temperature rises beyond the onset of critical silane concentration is evidenced by silicon nanoparticle collection in filters, TEM images and negative neutralizer-generated ions disappear after 500 °C, positive generated ions become less abundant as well as temperature increases in the reactor but at a slower rate. This observation suggests that the silicon nanoparticles are slightly positively charged or at least are capable of better stabilizing a negatively charged ion on their surface than a positive one.

The high molecular weight silicon hydride cluster signal is not measurable below ~400 °C for 0.3% SiH_4 in He. The signal peaks at 440 °C and then disappears gradually as temperature rises. This disappearance can be explained by the presence of more available aerosols which scavenge the mass of the silicon hydride clusters or are intermediates for the formation of the stable nuclei. Hence, these high molecular weight silicon hydrides may react more readily at high temperatures to form a stable nuclei. Both mechanisms compete actively and condensation becomes more dominant as the concentration of aerosols increases.

Finally, this study provides evidence that suggests that being a high molecular weight stable molecule, formed during silane pyrolysis is not a synonym of being a stable nuclei. The concept of thermodynamic stability of an incipient particle, borrowed from classical nucleation, as

sufficient for producing stable nuclei does not seem to be enough for reactive silane systems. Furthermore, we propose a new definition for silicon stable nuclei. This definition includes the previous requirement of the cluster being thermodynamically stable so that it does not degrade rapidly before growing. But in addition, a real stable nuclei should now demonstrate the capacity of receiving smaller molecules (Condensable species) and effectively capturing them with high efficiency, causing particle growth.

CHAPTER 6: DETERMINATION OF RELATIVE RATES OF CONDENSATION AND NUCLEATION IN SILICON NANOPARTICLE SYNTHESIS FROM SILANE PYROLYSIS

Results of this chapter are intended for publication in a peer reviewed journal

Vazquez-Pufleau, M., Yamane M., Biswas P., Thimsen E. Kinetics of nucleation and condensation of silicon nanoparticles from silane in helium atmosphere (2016), Chemical Engineering Science, to be submitted

6.1. Abstract

Polysilicon is a key commodity required for the manufacture of most commercial solar panels and computer chips. This material is traditionally produced in the well-established, but energy intensive, Siemens process by means of chemical vapor deposition (CVD) of SiHCl_3 . A significantly less energy demanding alternative is the SiH_4 fluidized bed reactor (FBR), which operates in a regime where aerosols are formed, a process which is not very well understood and is responsible for product losses and operating instability for industrial FBRs. In order to lower costs for FBR design and implementation, it is important to better understand the reaction mechanism and kinetics of silane pyrolysis. In this study, we present a systematic and parametric determination of the ratio of relative condensation and nucleation rates in the aerosol process of silane pyrolysis, based on primary particle analysis from transmission electron microscopy (TEM) and supported on X-Ray diffraction (XRD). These results are also compared with an online aerosol characterization from scanning mobility particle sizer (SMPS). The methodology described here is also proposed as a tool to help elucidate the kinetics and morphology of rapidly evolving aerosols in a regime where primary particles can be identified and their size is independent of residence time in the reactor. Such understanding can also help engineer silicon nanoparticles for a whole range of applications that require sharp control of primary particle size such as battery anodes and biomaterials.

6.2. Introduction

Silicon is the second most abundant element in the earth's crust, after oxygen,¹⁶⁵ but refining it to the purity required to meet electronics and photovoltaic standards is expensive due to energy intensive processing.¹⁵¹ The full silicon refining and purification process is summarized elsewhere⁴. In order to make silicon solar panels a competitive technology, it is critical to improve the process yield and decrease the energy cost for high purity silicon refining. Although several efforts have already been made to improve the yield and reduce the cost,^{38, 88} still more research on process improvement and optimization is required. This involves understanding fundamental aspects of the unit operations.

Among the various unit operations for refining silicon, one of the most energy intensive is the gas-to-solid conversion process by means of chemical vapor deposition (CVD) from silane, or trichlorosilane, to produce polysilicon. The energy intensity depends on the type of chemical reactor used. Chlorosilane CVD is traditionally performed in a Siemens reactor, which is a well-established technology. This batch process requires a large temperature gradient between the growing silicon and the reactor walls, which in combination with chlorosilane chemistry, limits aerosol formation and deposition on the polysilicon rods. An alternative to the Siemens reactor is the fluidized bed reactor (FBR), which is continuous, has low energy usage, operates at high throughput and has low labor requirements.²⁰ The FBR operates by feeding silane into a fluidized bed of millimeter-sized silicon beads, which grow in size and are eventually extracted from the reactor. Several challenges still hinder the successful implementation of the FBR. One of the main challenges is understanding the formation of fines, which are aerosol particles much smaller than the beads.²⁰

At high temperature $T > 600\text{ }^{\circ}\text{C}$, the mechanism, by which silicon mass is transferred from gaseous silane molecules to the millimeter-sized beads in the fluidized bed, is believed to primarily proceed through an aerosol intermediate state^{1, 166}. In other words, silane reacts predominantly to form aerosol particles, which are subsequently captured by, and incorporated into the beads in the fluidized bed. Hsu, et al.¹ grouped all the reactions that cause fine aerosol particles to nucleate and grow as one homogenous reaction. It was found that at typical reactor conditions, depending on the temperature, 50 to 90% of the silane was consumed by the homogenous reaction^{1, 166}. For the case where 90% of the silane formed fine aerosol particles, approximately 90% of the mass in that aerosol was collected in the fluidized bed. From the mass balance, at these conditions approximately 10% of the silicon mass fed into the reactor was elutriated as fine particles, which were not captured by the large beads. Clearly the aerosol processes occurring in the reactor are important to understand. To minimize elutriation and maximize mass yield of the process, one must understand 1) the molecular mechanism of silane decomposition, 2) how the aerosol growth mechanism affects the properties of the agglomerates, and 3) how the agglomerate properties affect capture by the beads in the reactor.

The majority of previous research has focused on understanding the molecular mechanism of silane decomposition. Decades on, there is still controversy about the reaction mechanism for silane pyrolysis⁴⁰. Proposed reaction mechanisms have been developed using simulation and theoretical techniques, such as those by Filtvedt et al.⁴⁶, Hashimoto et al.⁴⁴ Jasinski and Gates⁴¹, Purnell and Walsh⁴⁵, Ring and O'Neal⁴³, White et al.⁴² Swihart et al.¹⁶⁷ among others. These mechanisms range from five to ten reactions¹⁵² to about four hundred reactions⁴⁸. Other authors propose intermediates that may not always be physically plausible, such as Si atom formation in the gas phase⁴⁹.

Silicon aerosol formation during silane pyrolysis has mainly been studied at low pressures, which is quite different from the industrial process that operates above atmospheric pressure. For example, Qian et al.⁵² studied silane CVD homogeneous nucleation just above the critical silane concentration. Nijhawan et al.⁵³ provided experimental data on particle nucleation and growth of silicon at pressure lower than 2.5 torr. Van Den Brekel et al.⁵⁴ found the critical silane pressure for Si_2H_2 to be 0.1 torr silane at 725 °C. Other authors have studied Si aerosol formation using inert gases^{3, 168}, Wiggers et al.⁵⁵ investigated the formation of silicon powder by pyrolysis of 10 and 40% silane volume in argon. Giunta et al.⁵⁶ used N_2 . Morrison et al.¹⁶⁹ studied silane pyrolysis in a piston reactor. Finally, high pressure homogeneous nucleation has been studied by Odden et al.⁵⁷ who used monosilane at temperatures from 690 to 830 °C and pressures from 0.1 to 6.6 MPa in a free space reactor. They determined reaction rate to be a weak function of pressure.

Several aerosol models have been developed to compare to experimental results. Alam et al.¹⁷⁰ observed the surface growth on injected seed particles. They used an Arrhenius expression from Newman et al.¹⁷¹ and assumed sylylene (SiH_2) formation to be the rate limiting step and all subsequent reactions to be fast. Onischuk, et al.¹⁷² experimentally studied the formation of aggregates by decomposition of silane in Ar at low temperatures $T < 610$ °C for residence times that resulted in incomplete conversion, and proposed a model to describe this regime.

Gaps in understanding of the fundamental chemical mechanism of silane pyrolysis to cause nucleation and growth of silicon aerosol particles, propagate into errors in the models for predicting size distribution. The size distribution affects the capture of aerosol particles by the beads, and therefore affects the mass yield. Accurately predicting aerosol evolution as a function of residence time is made difficult because, to the best of our knowledge, experimental measurements of nucleation and condensation rates at relevant pressures have not been performed.

A comprehensive analysis of the available literature, some of which has been discussed here, leads us to the conclusion that the mechanism and kinetics for silane pyrolysis resulting in aerosol nucleation and growth are still uncertain. Experimental rates for the aerosol processes of nucleation and condensation from silane pyrolysis have not been reported, to our knowledge.

The objective of this work is to provide experimental information about nucleation and condensation rates for silane pyrolysis at atmospheric pressure. The study was executed in a bench scale flow reactor system equipped with instrumentation to precisely and accurately control process parameters. Various aerosols generated at different residence times, silane partial pressures, and temperatures, were characterized online by SMPS to obtain the agglomerate size distribution, and offline by TEM and XRD to ascertain the primary particle size distribution. From this information, we infer relative rates of nucleation and condensation, as well as estimate the relative orders of these reactions in silane concentration.

6.3. Experimental methods

6.3.1. Experimental setup

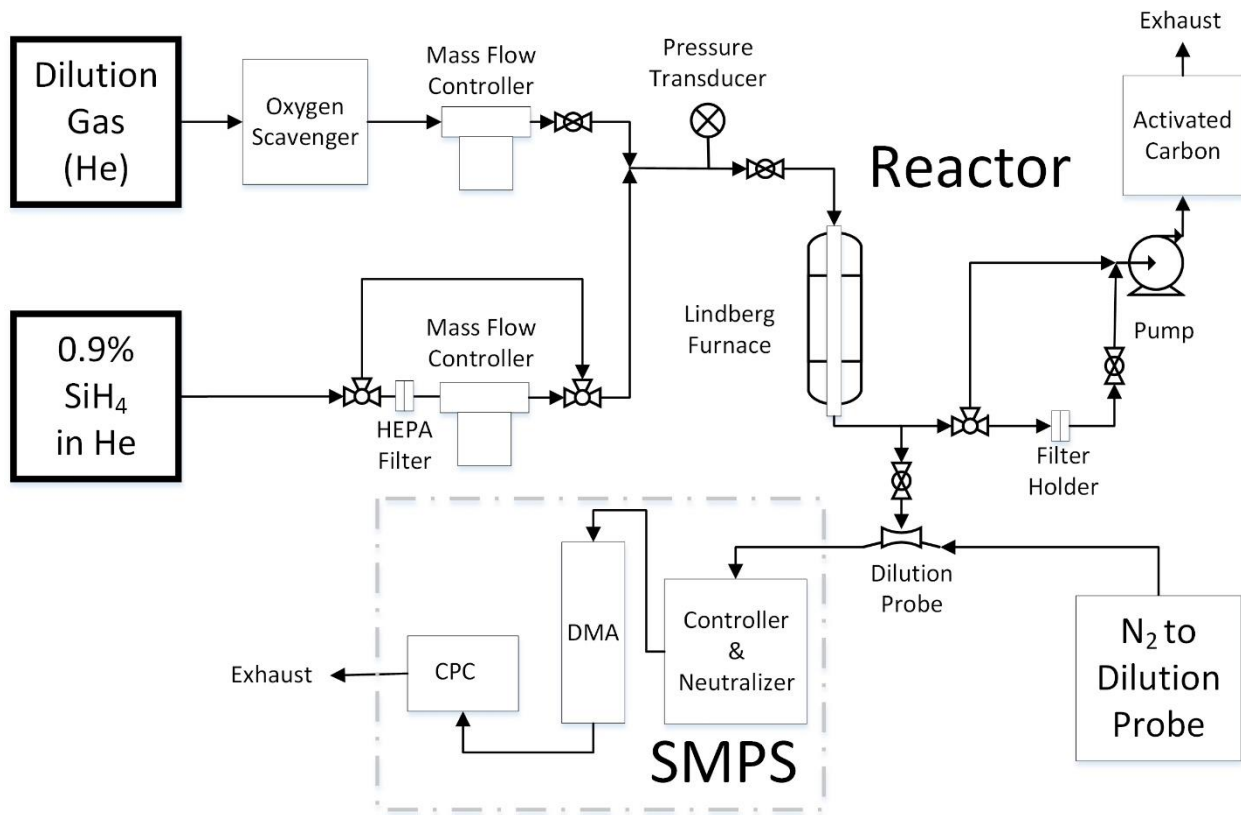


Figure 6-1 Experimental setup for silane pyrolysis and formation of silicon aerosols

The experimental apparatus is illustrated in Figure. 6-1. The reactor consists of a 2.54 cm diameter and 50 cm long stainless steel tube contained within a Lindberg Furnace whose temperature can be controlled from room temperature to 1100 °C. The furnace is fed by two gas streams. The first stream is silane reagent 0.9 volume % in helium (Airgas Inc., PA, USA), and the second stream is dilution gas, ultra-high purity helium (99.999% Airgas Inc., PA, USA). The helium is passed through an oxygen scavenger (Cee Kay Supply, MO, USA) to remove any trace O₂ before the stream reaches the reactor. Both streams are controlled by mass flow controllers (MFC) (MKS Instruments, Inc., MA, USA) The silane stream is passed through a high efficiency

particulate arrestance (HEPA) filter before entering the flow controller. The silane concentrations used for this work ranged from 0.0025% to 0.9%. The reactor pressure was measured using a pressure transducer (PT) (WIKA, Klingenberg am Main, Germany). After the reactor, the outlet stream was partially diverted through a ball valve to a dilution probe that was used to quench the aerosol evolution and reduce the total number concentration to one that could be measured by the scanning mobility particle sizer (SMPS) (TSI Inc., Shoreview, MN, USA) for online characterization. The main product stream of the reactor flowed through a quartz collection filter to a vacuum pump. At the outlet of the pump, an activated carbon filter was used to remove particulates and any unconverted silane before exhausting to the interior of the fume hood.

6.3.2. Characterization tools

Transmission electron microscopy (TEM) was employed to visualize the samples that were prepared by cutting a small wedge from the quartz filters with collected sample, sonicating it for few seconds in deionized water, and pipetting 20-40 μ l of the suspension onto a TEM copper grid. The grid was then allowed to air dry and observed in a FEI Spirit TEM (Fei, Hillsboro, OR, USA). To obtain statistically valid data, three different sections of the TEM grid were used. Each section was photographed at successive magnifications. The images were then analyzed by using the ImageJ® 1.48v software (Rasband W.S., ImageJ, U. S. National Institutes of Health, Bethesda, Maryland, USA, <http://imagej.nih.gov/ij/>, 1997-2015.). The size for each primary particle was determined by taking the diameter of non-necked particles; for necked agglomerates the smallest diameter was used. To obtain the primary particle size distribution for a given condition, typically 200-600 measurements were used from at least 1 TEM image.

6.3.3. Model description

The experimental rates of nucleation and condensation are assumed to be a function of silane concentration in power law form:

$$r_{cond} = k_{cond} * [SiH_4]^p = \frac{d[m]_{cond}}{dt} \quad (6-1)$$

$$[m]_{cond} = \int_0^t r_{cond} dt = k_{cond} \int_0^t [SiH_4]^p dt \quad (6-2)$$

$$r_{nucl} = k_{nucl} * [SiH_4]^q = \frac{d[m]_{nucl}}{dt} \quad (6-3)$$

$$[m]_{nucl} = \int_0^t r_{nucl} dt = k_{nucl} \int_0^t [SiH_4]^q dt. \quad (6-4)$$

the relative rates of both become

$$\frac{m_{cond}}{m_{nucl}} = \frac{\int_0^t r_{cond} dt}{\int_0^t r_{nucl} dt} = \frac{k_{cond} \int_0^t [SiH_4]^p dt}{k_{nucl} \int_0^t [SiH_4]^q dt}. \quad (6-5)$$

here, m is the mass, r is the rate, the subscript cond stands for condensation, nucl stands for nucleation, p and q are the orders of reaction for condensation and nucleation respectively, k is the reaction constant, [] indicates concentration and t is the time.

So if the relative amounts of condensed mass to nucleated mass are obtained for various precursor concentrations, the experimental ratio of orders of reaction can be extracted by comparison with various hypothetically computed ratios.

Based on mass balance, for a given control volume, the total mass can be extracted from

$$m_{total} = m_{cond} + m_{nucl} \quad (6-6)$$

$$m_{cond} = \sum_{i=1}^N (V_{final} - V_{nucl}) = \frac{\rho\pi}{6} \sum_{i=1}^N (d_{p,final}^3 - d_{p,nucl}^3) \quad (6-7)$$

$$m_{nucl} = \frac{\rho\pi}{6} \sum_{i=1}^N (d_{p,nucl}^3) = \frac{\rho\pi}{6} * N * d_{p,nucl}^3 \quad (6-8)$$

Substituting Eq. 7 and 8 in Eq 5, we get

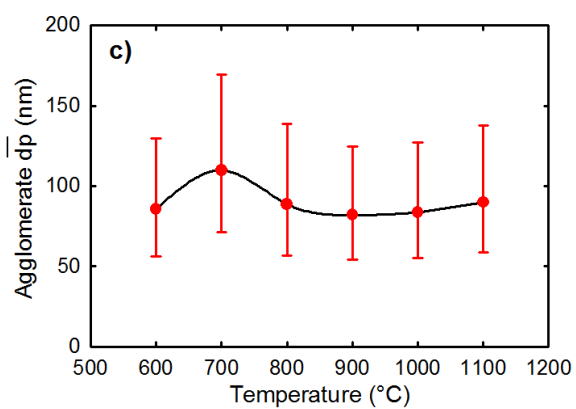
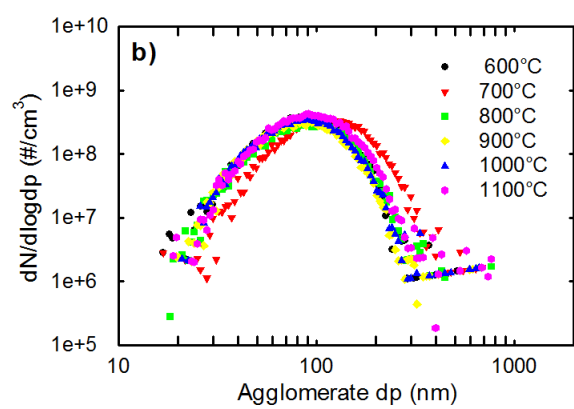
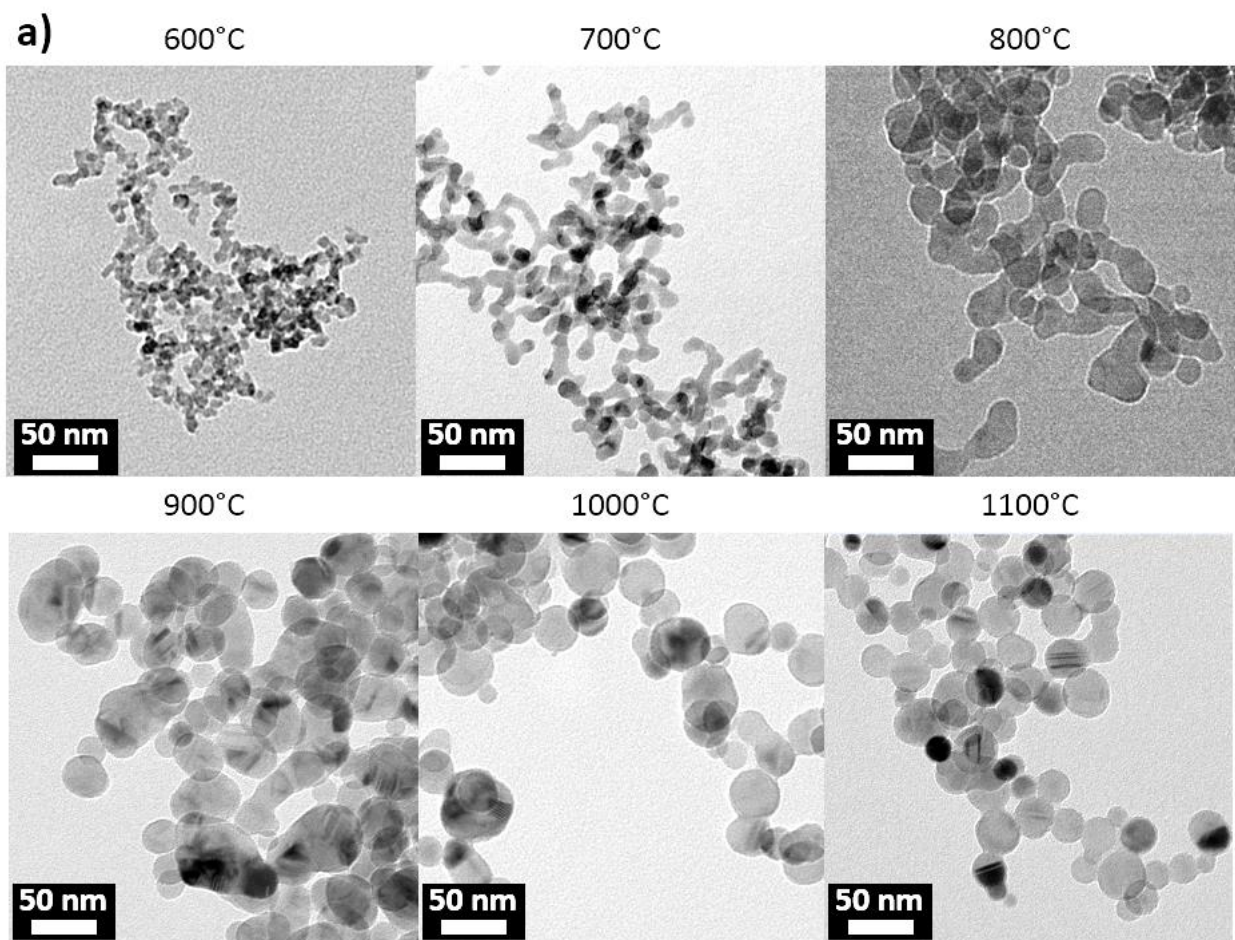
$$\frac{\sum_{i=1}^N (d_{p,final}^3 - d_{p,nucl}^3)}{N * d_{p,nucl}^3} = \frac{m_{cond}}{m_{nucl}} = \frac{\int_0^t r_{cond} dt}{\int_0^t r_{nucl} dt} = \frac{k_{cond} \int_0^t [SiH_4]^p dt}{k_{nucl} \int_0^t [SiH_4]^q dt}, \quad (6-9)$$

where N is the total number concentration of the primary particles, d_p is the particle diameter, and V stands for volume.

The equations presented before are based on the assumption that particle sintering is negligible after the quick reaction phase of aerosol nucleation and condensation occurs. Their results are valid only for such circumstances. Therefore, the first step was to find a temperature regime where different residence times in the reactor did not cause particle sintering. For our system this was proven for the 700 °C condition.

6.4. Results

In this section we start with a description of the dichotomy of the behavior of primary particle and agglomerate size distributions as a function of temperature. Then we discuss the effect of sintering at different temperatures and finally we describe the role that concentration has on both primary particle and agglomerate size distribution for a condition where no sintering is observed.



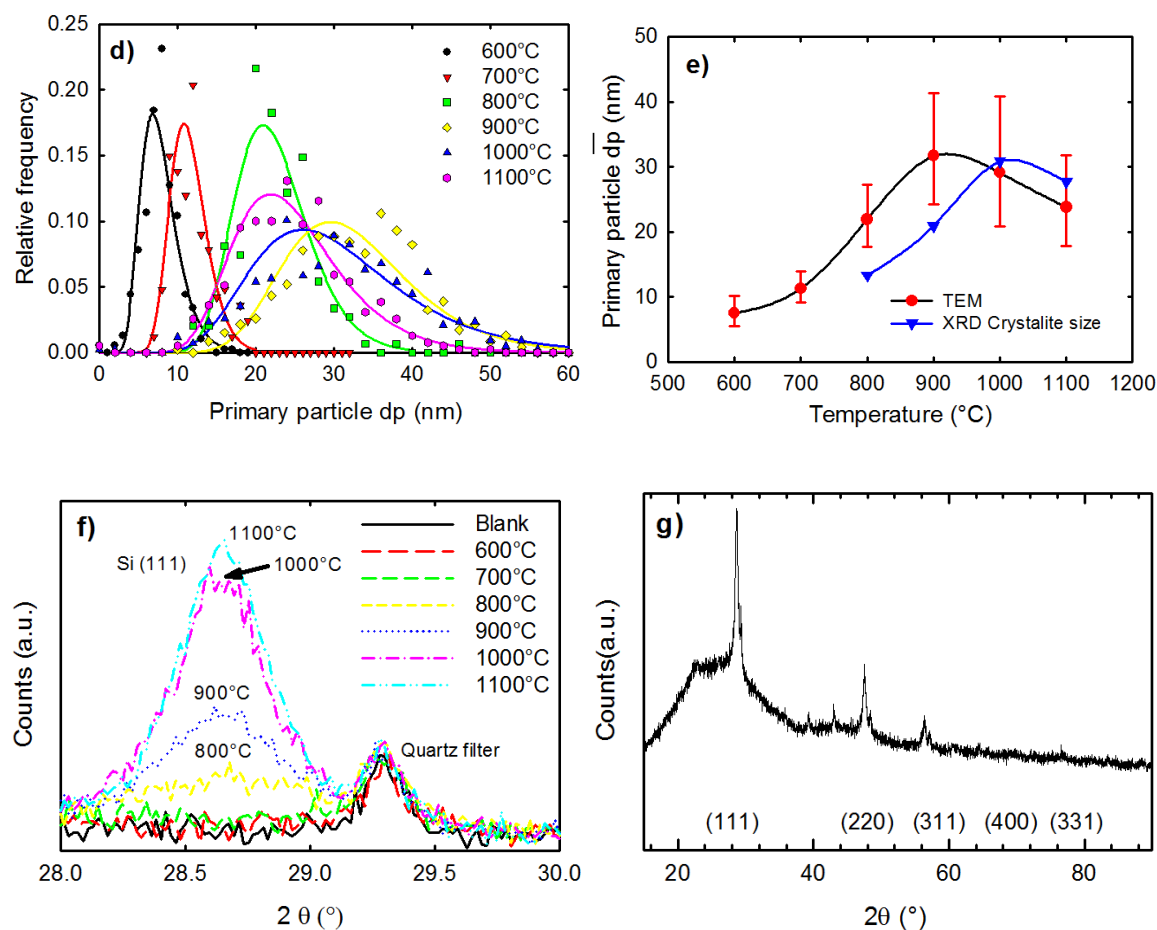
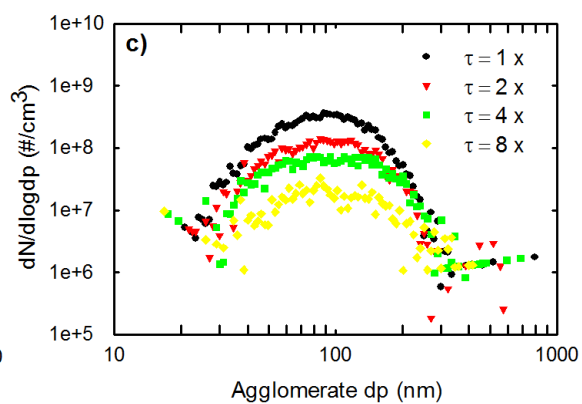
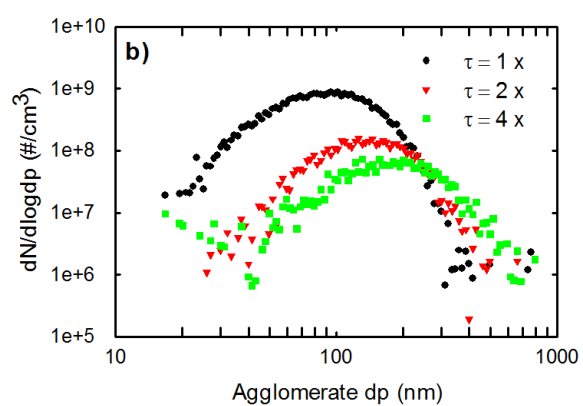
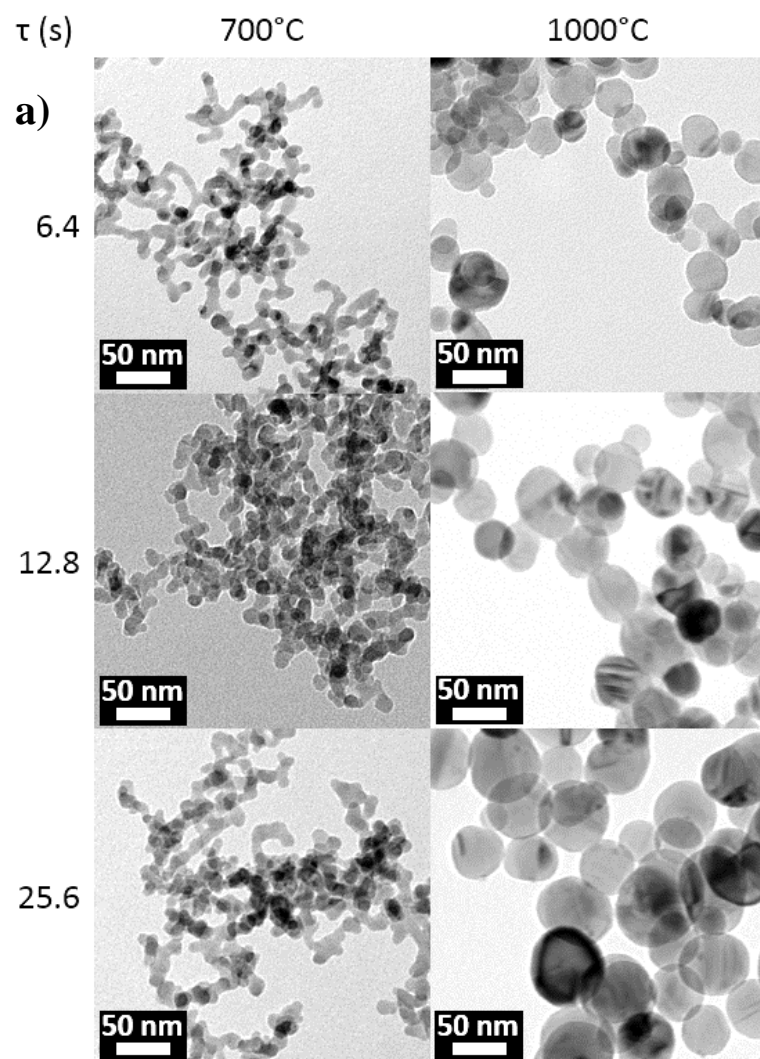


Figure 6-2 a) TEM results showing temperature's effect on primary particle size distribution, b) Agglomerate size by SMPS where dp stands for particle diameter, c) Summary of agglomerate mean size and lognormal standard deviation, d) Primary particle size distribution, e) Summary of primary particle size distribution compared to crystallite size f) XRD pattern for silicon nanoparticles synthesized at various temperatures, g) Unfiltered silicon pattern from a crystalline silicon nanoparticle sample.

The effect of temperature on agglomerate mobility is small, but primary particle size and morphology differ substantially at the various temperatures (Figure 6-2). Figure 6-2 (a) shows a clear difference for primary particle size. Figure 6-2 (b) shows the agglomerate size distribution determined by SMPS at the outlet of the reactor. The size distribution means and their lognormal standard deviation are summarized in Figure 6-2 (c). Little difference is observed for similar fluid dynamics in a single stage aerosol reactor under similar conditions regardless of the synthesis

temperature, in agreement with Nguyen et al.¹⁵⁵. However as Figure 6-2 (d) shows, the primary particle size is a significant function of temperature. Primary particle size distributions are summarized in Figure 6-2 (e) and compared to the crystallinity of the nanoparticles based on XRD and the Scherrer equation. Below 800 °C no significant crystallinity was observed. Above that temperature both primary particle and crystallite mean size follow the same trend, but the latter displays smaller size up to ~1000 °C. Figure 6-2 (a) provides an explanation. There, at 900 °C particles are not completely sintered but rather display a lumpy spheroid shape, suggesting that their structure is not made of a single crystal but rather includes polycrystalline constituents. The X-ray diffraction patterns for the silicon 111 plane for all the temperatures tested are shown in Figure 6-2 (f). The 1100 °C unfiltered XRD pattern for the crystalline silicon nanoparticles is presented in Figure 6-2 g.



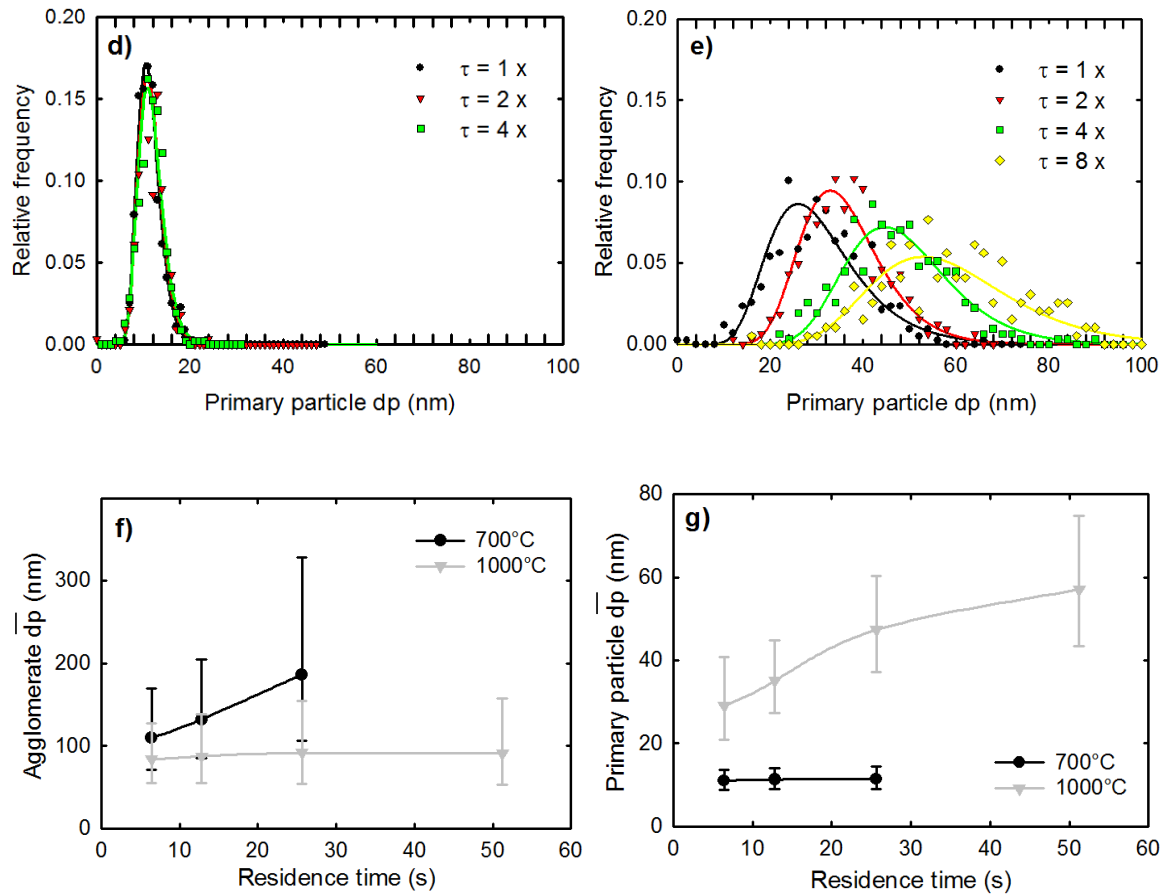


Figure 6-3 a) TEM images comparing the effect of residence time at 2 different temperatures b) agglomerate size distribution at 700 °C c) at 1000 °C d) primary particle size distribution at 700 °C and e) at 1000 °C f) summary of the agglomerate size distribution for both conditions where error bars represent the lognormal standard deviation and g) summary of the primary particle sizes for both temperatures.

The evolution of primary particle size as a function of residence time depends on temperature. At 700 °C different residence times did not change the primary particle size distribution. However at 1000 °C every increase in residence time materialized into larger primary particles. This confirms that the assumption of negligible sintering is consistent with the experimental conditions, both temperature runs (700 °C and 1000 °C) were executed using the same 0.02% silane concentration. The results, presented in Figure 6-3 (a) show the TEM images

for both conditions. Figure 6-3 (b) and 6-3 (c) display the agglomerate sizes for 700 and 1000 °C respectively. Figure 6-3 (d) and 6-3 (e) show the primary particle sizes for 700 and 1000 °C respectively. Figure 6-3 (f) shows a summary of agglomerate mean sizes and lognormal standard deviations for both conditions. Finally, Figure 6-3 (g) shows the mean primary particle size as a function of residence time where error bars represent the lognormal standard deviation. Based on the evidence presented, at 700 °C the primary particle size distribution remains essentially the same, despite higher residence times, indicating that agglomeration occurs without sintering. At 1000 °C the primary particle changes copiously at larger residence times compared to low residence times providing evidence that the sintering time is lower than all residence times used at such temperature.

a) → Increasing concentration →



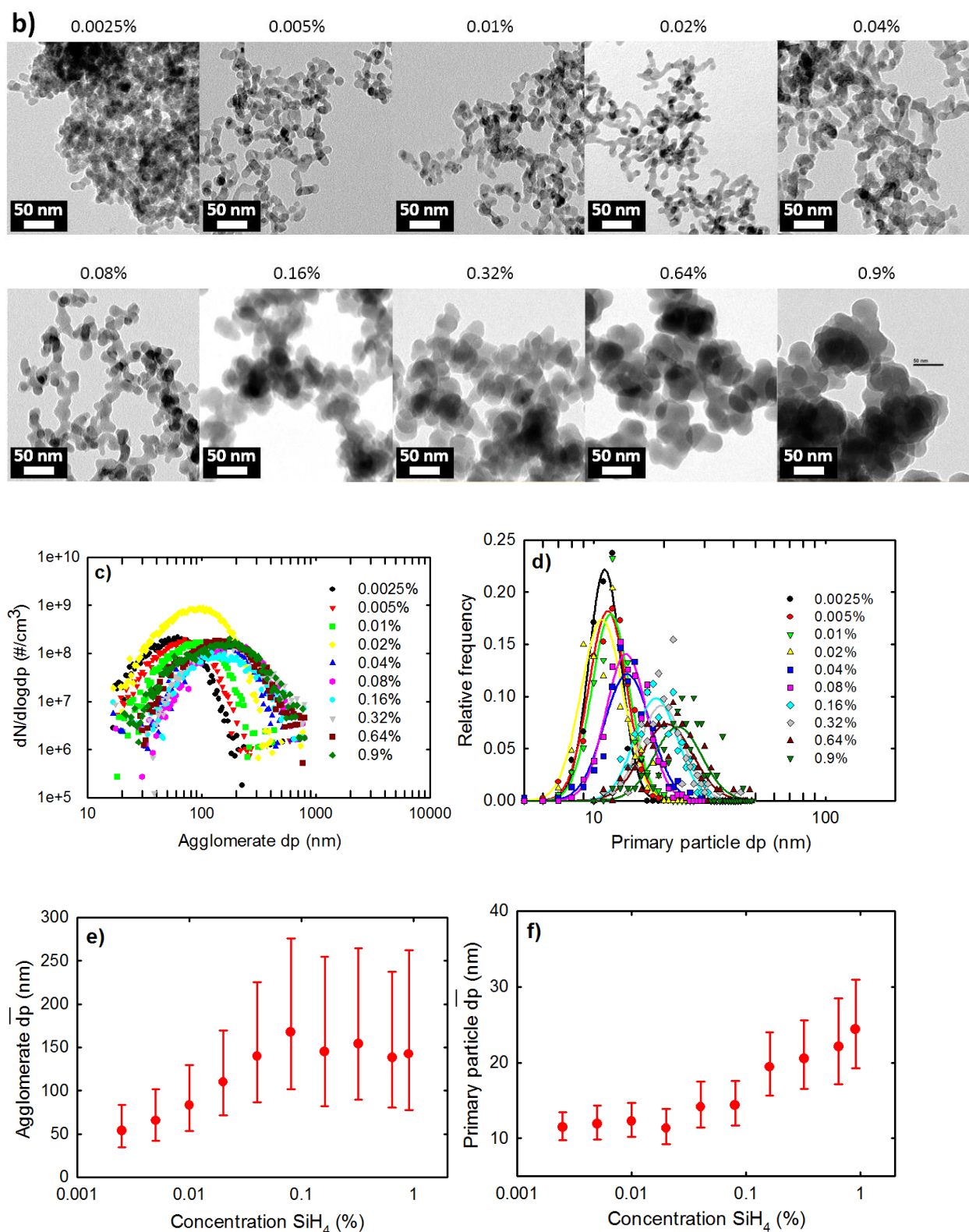


Figure 6-4 Run at 700 °C using different concentrations of silane in helium. a) Picture of the filters after collection of silicon nanoparticles, filters are arranged at progressively increasing

concentrations where the lowest concentration is in the left side and the highest concentration in the right hand b) TEM images of silicon nanoparticles synthesized at different silane concentrations c) Agglomerate size distribution for various concentrations d) Primary particle size distribution for the different concentrations e) summary of agglomerate size. The dots represent the mean and the error bars are the lognormal standard deviation f) summary of primary particle size

Mean primary particle size increases progressively as a function of concentration for the concentration run using the same residence time and temperature. The effect of silane concentration on the aerosols primary particle size distribution can be seen in Figure 6-4. Figure 6-4 (a) shows how the color of the silicon nanoparticle cake collected in the filters change dramatically as the agglomerate size changes. Figure 6-4 (b) shows TEM images of samples from 0.0025% to 0.9% silane. The primary particle size is constant at low concentrations, but increases progressively for concentrations above 0.02% SiH_4 . Figure 6-4 (c) shows the SMPS agglomerate size distribution for different concentrations of SiH_4 at the outlet of the reactor. Figure 6-4 (d) presents the primary particle size distribution of the silicon nanoparticles. Figures 6-4 (e) and 6-4 (f) summarize the agglomerate and the primary particle size distributions respectively. The reason why the agglomerate size distribution does not continue to grow above 0.1% SiH_4 is because the residence time needed to be decreased to reach this and higher concentrations. See Table 6-2 for further details. Higher residence times are expected to produce larger agglomerate losses, however they are not expected to cause Finally, Table 1 displays the condensed mass/ nucleation mass and relative $k_{\text{cond}}/k_{\text{nucl}}$ for various temperatures for 0.02% SiH_4 at around 2 seconds residence time.

Table 6-1 Relative condensed/nucleated mass effect of temperature.

Temperature (°C)	m_{cond}/m_{nucl} (Mass/mass)	k_{cond}/k_{nucl}
600	1745	40000
700	5152	117500
800	38193	870000

Table 6-2 Summary of conditions and synthesized aerosols characteristics. Residence time has been calculated based on the set point temperature

Run	Temp	Residence time	Concentration silane	Primary particles		Agglomerate		
				Geometric mean	Geometric stdev	Geometric mean	Geometric stdev	Total number concentration
	(°C)	s	%	nm	nm	nm	nm	No/cm3
Temperature	600	2.14	0.02	7.51	1.36	85.52	1.52	1.7E+08
	700	1.92	0.02	11.30	1.23	109.90	1.54	1.6E+08
	800	1.74	0.02	21.95	1.24	88.77	1.56	1.5E+08
	900	1.59	0.02	31.70	1.31	82.10	1.52	1.4E+08
	1000	1.47	0.02	29.14	1.40	83.64	1.52	1.6E+08
	1100	1.36	0.02	23.84	1.34	89.94	1.53	1.9E+08
Residence time	700	1.92	0.02	11.03	1.24	109.90	1.54	1.6E+08
	700	3.84	0.02	11.33	1.25	131.91	1.55	7.0E+07
	700	7.69	0.02	11.43	1.26	186.23	1.76	3.5E+07
	700	15.38	0.02	7.31	2.06	200.03	2.11	7.6E+06
Residence time	1000	1.47	0.02	29.14	1.40	83.64	1.52	1.6E+08
	1000	2.94	0.02	35.03	1.28	87.41	1.58	6.7E+07
	1000	5.88	0.02	47.37	1.27	91.48	1.68	4.2E+07
	1000	11.76	0.02	57.02	1.31	91.04	1.72	1.2E+07
Concentration	700	1.92	0.0025	11.43	1.17	53.77	1.55	9.3E+07
	700	1.92	0.005	11.88	1.21	65.50	1.55	8.5E+07
	700	1.92	0.01	12.22	1.20	83.18	1.56	7.8E+07
	700	1.92	0.02	11.30	1.23	109.90	1.54	1.6E+08
	700	1.96	0.04	14.13	1.24	140.01	1.61	7.1E+07
	700	1.96	0.08	14.33	1.22	167.57	1.65	7.9E+07
	700	8.03	0.16	19.41	1.24	144.90	1.76	5.2E+07
	700	8.03	0.32	20.55	1.24	154.36	1.72	8.9E+07
	700	16.06	0.64	22.09	1.29	138.21	1.72	1.0E+08
	700	22.58	0.9	24.40	1.27	142.37	1.84	1.0E+08

6.5. Discussion

In this section, we start with an examination of why this approach is useful to measure aerosol formation kinetics in a silane pyrolysis system. Next, we provide the assumptions of our approach and how they lead into equations to obtain the relative rates of reaction for nucleation

and condensation. Then, we discuss which reported experimental conditions are suitable for using the developed kinetic analysis. Finally we report an expression for the relative rates for the 700 °C condition.

Determining the order of reaction is one of the most important steps in understanding any kinetic system. The simplest system is one that evolves at moderate temperatures and displays measurable concentration changes at easily measurable time intervals. The conversion or concentration as a function of time can then be observed and fitted into a model that best describes the reactive behavior. While this is valid for one step reactions, a different approach is necessary for the more complicated case of silane pyrolysis at elevated temperatures, where not only a large amount of parallel and consecutive reactions take place, but also the reactants change phase from gas to solid. Additionally, full conversion is achieved within milliseconds at industrially relevant conditions⁶⁸. Furthermore, aerosol dynamics can significantly and irreversibly modify the primary particles generated in the subsequent milliseconds after their synthesis. These system properties make it challenging to implement traditional kinetic approaches for the determination of silane reaction rates for relevant aerosol processes. This work attempts to obtain kinetic information that summarizes all reactions and intermediates into aerosol relevant processes– Nucleation and condensation – by using the following assumptions.

The first assumption is that the nuclei are 0.7 nm in diameter. This value is based on previous modeling efforts by Talukdar and Swihart,^{147a} who consider a polymer of 10 or more silicon atoms to be a stable nucleus. Although the value is a bit arbitrary, Girschick et al.⁴⁸ also used 10 atoms as a stable cluster for their aerosol dynamics calculations. Based on ab initio calculations, Swihart and Girschick^{147b} also showed that cyclic or polycyclic structures containing 11 Si atoms are rather stable and mainly result from irreversible reactions that would need

significant energy to go backwards. Wong et al.¹⁴⁸ used an automated reaction mechanism generation and determined the critical nucleus size to be larger than 7 Si atoms. Si-Si bond lengths are typically about 0.235 nm and Si-H bonds are about 0.15 nm¹⁶⁷. So the assumed nuclei of 0.7 nm would be about 3 – 4 Si atoms in diameter. Even if this assumption were partially mistaken, the results would still be accurate because condensation mass is at least three orders of magnitude higher than nucleation mass for all primary particles observed in this study.

Another assumption made in this study is that only one nucleus is present in each primary particle. This is supported by the fact that no significant sintering of agglomerates occurs below a transition temperature around 800-900 °C. Regardless of the residence time, the primary particles remained the same size for all tests as verified by TEM. This is in agreement with observations made by Lunden et al.¹⁷³ On the other hand, agglomerate size changes significantly as a function of residence time, as aerosol dynamics predict. This proves that, at least after the first milliseconds of reaction, the primary particles formed during the reaction do not sinter or grow significantly.

The last assumption is that losses through surface reactions on the reactor wall by CVD are negligible and comprise a small fraction of the non-recoverable material. Most of the product losses are believed to occur via diffusion of already formed aerosols downstream of the reactive zone of the reactor. Thus the wall CVD is assumed to have no effect on the rate at which bulk aerosols are formed. This is supported in the speed of the reaction for silane pyrolysis, which for full conversion at the temperatures studied is on the order of milliseconds according to Hogness et al.⁶⁸ The calculations consider full conversion from precursor into aerosols for the mass balance.

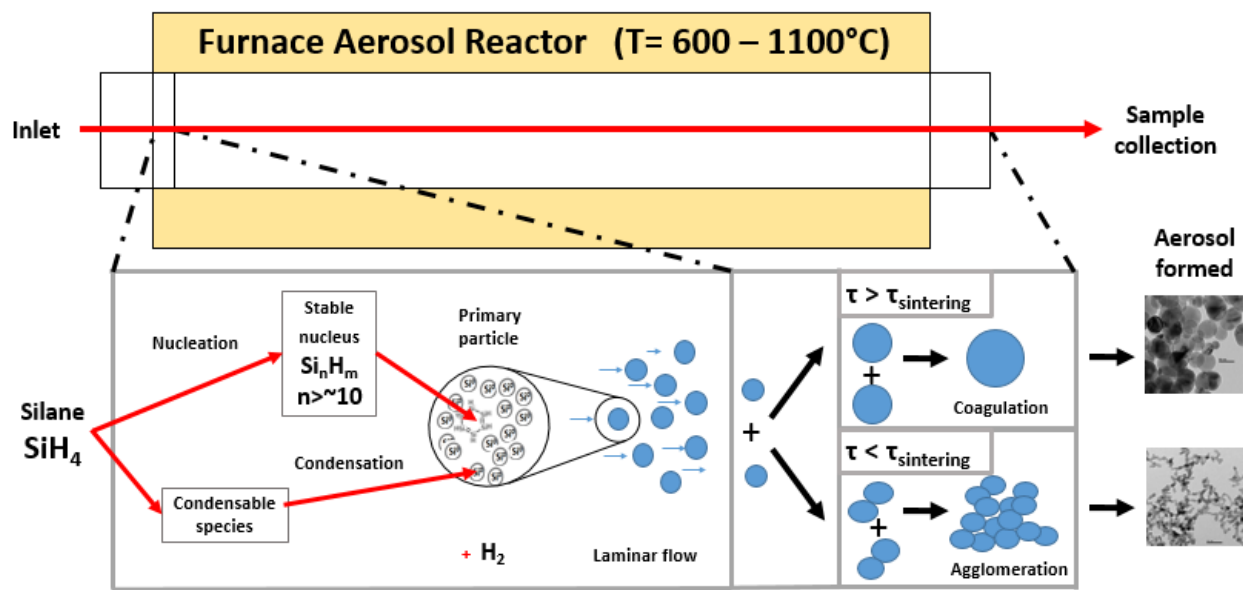


Figure 6-5 Schematic mechanism for silane pyrolysis and particle evolution in a flow reactor

The difference between the mass of the primary particle and the mass of the nucleus is considered to be condensed material. A summarized reaction pathway and aerosol evolution is shown in Figure 6-5. According to Becerra et al.¹⁷⁴, the most stable species for deposition (condensable species) for a 0.1% SiH_4 in He between 900 – 1300 K are Si_2H_4 and Si_2H_2 .

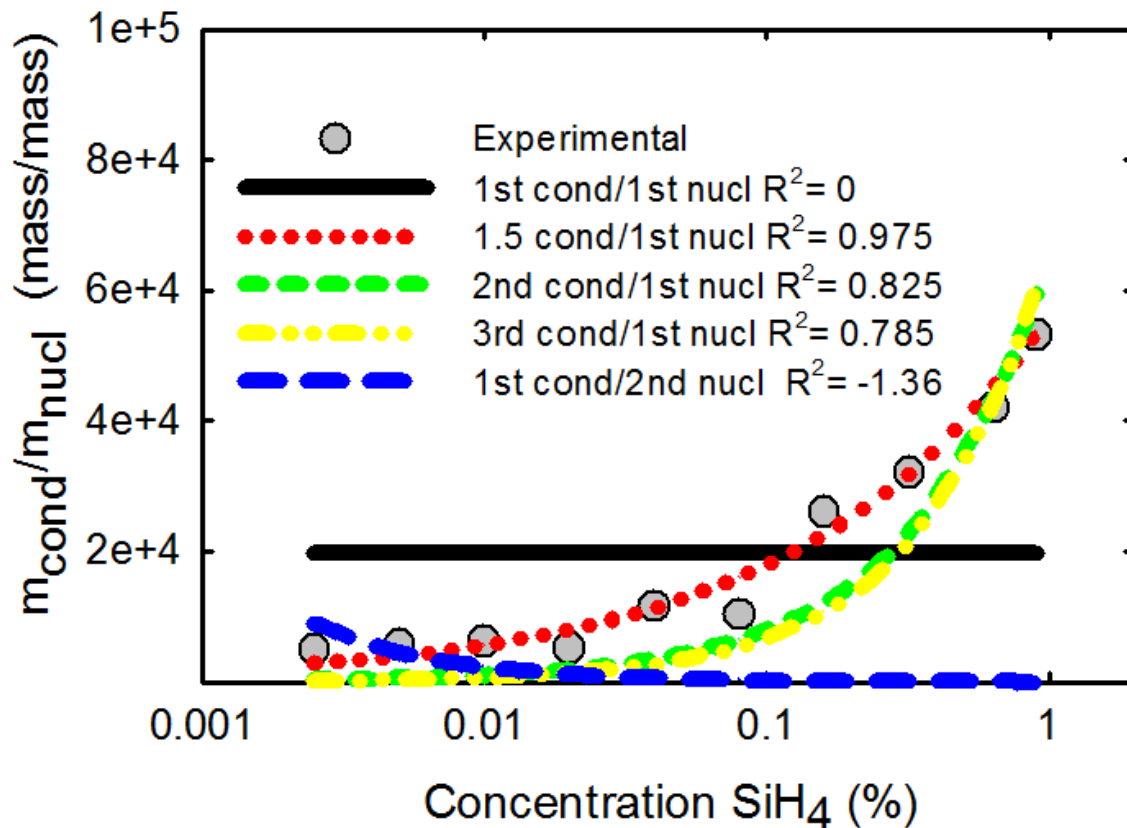
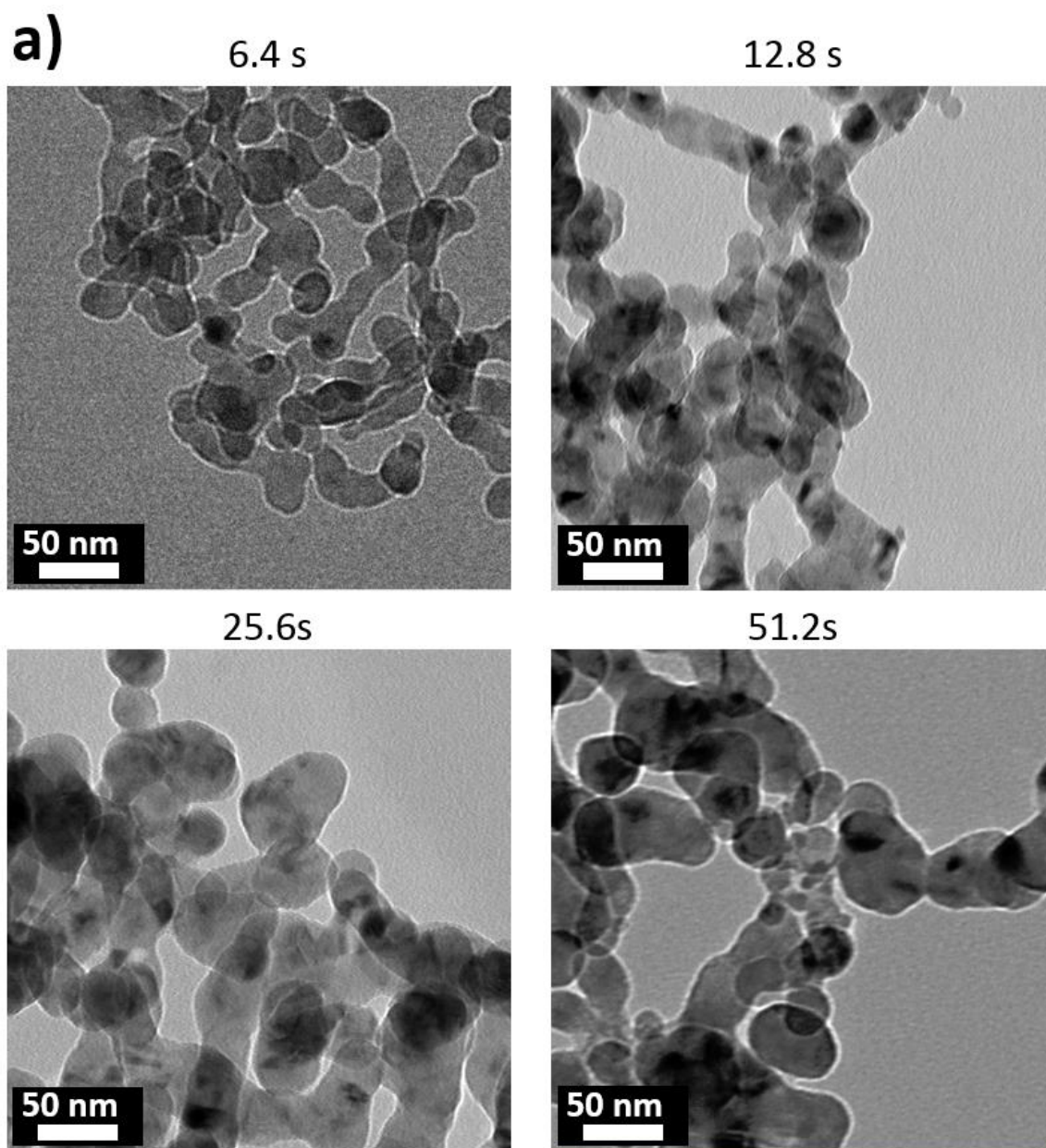


Figure 6-6 Condensed mass over nucleated mass for various concentrations

Regarding the experimentally determined orders of reaction, Figure 6-6 summarizes the relative condensed / nucleated masses for all concentrations studied in this work. Since the orders are different, p and q are also dissimilar. The integrals of eq. 5 do not cancel out and need to be solved starting at the concentrations tested. This approach yields the ratios of the reaction orders for both processes. The best fit is obtained for a case of condensation order of 1.5 with a nucleation order of 1.

The temperature at which sintering occurs is roughly linked to the degree of crystallinity of the nanoparticles. Below $\sim 800^\circ\text{C}$ the silicon nanoparticles are amorphous. 800°C is the highest temperature at which, the primary particle size distribution does not significantly change with

larger residence times in the reactor (Figure 6-7). On the other hand, the crystallite mean size agrees within reasonable limits, with the primary particle size distribution determined by Scherrer's equation from XRD data. Below 1000 °C, the crystallite size is lower than the primary particle size. This idea is supported by the TEM images in Figure 6-2, at 900 °C that show partially sintered primary particles, which most likely contain more than a single crystal.



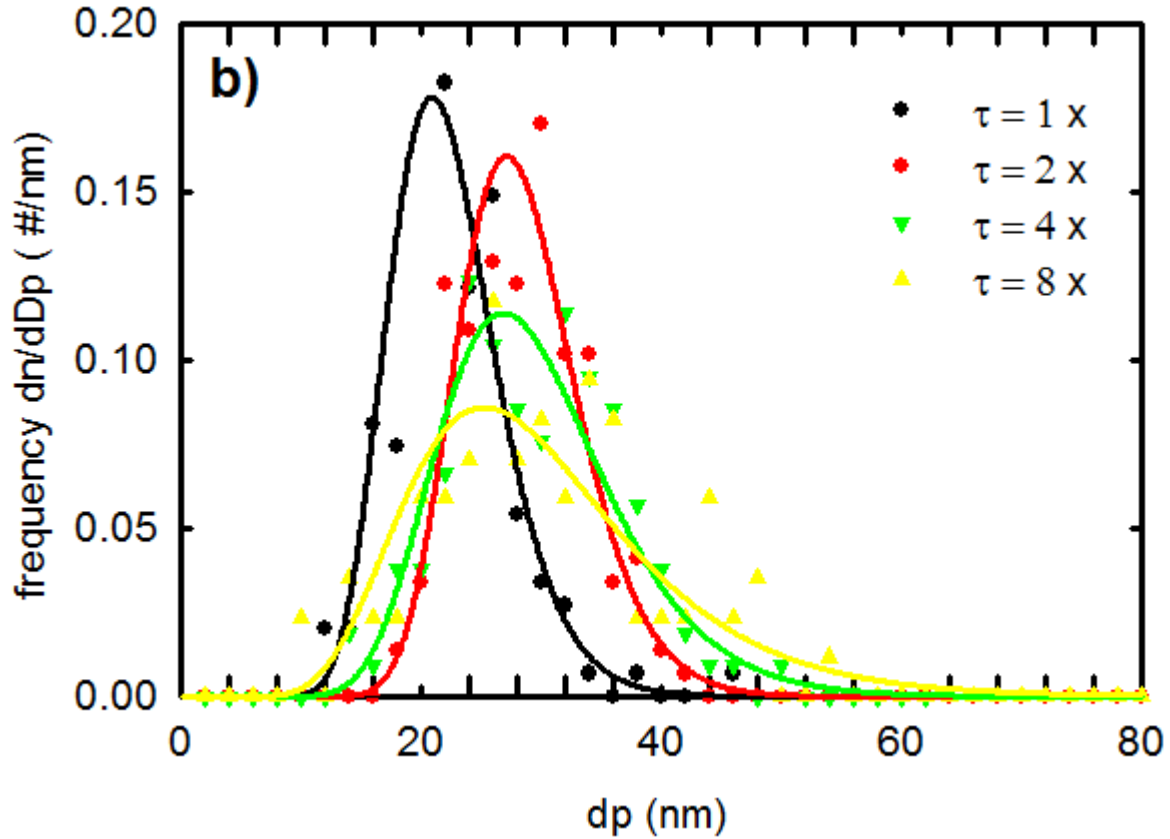


Figure 6-7 a) TEM images of four different residence times for the temperature of 800 °C. b) The summary of primary particle size distributions for the four residence times. The effect of size distribution broadening starts to take place suggesting that sintering becomes important above this temperature.

Figure 6-3 clearly shows that there are two regimes for sintering. At 700 °C the “no primary particle sintering” assumption holds. As the residence time increases, no change is observed in the primary particle size distribution, but the agglomerate size observed by SMPS grows dramatically. At 1000 °C, the primary particles grow as residence time increases, but the agglomerate size does not grow as dramatically as in the 700 °C case. The agglomerates at 1000 °C undergo sintering and densification, rather than forming a porous extended agglomerate as in the case of 700 °C. In

the cold zone of the reactor before quenching, further agglomeration occurs for both conditions but without sintering.

The fact that the apparent orders of reaction are different for condensation than for nucleation could be due to transport limitations. A comprehensive determination of collision frequency as a function of all discrete sizes during primary particle formation is beyond the scope of this study. However, if calculations of the collision frequency did not show that transport can be responsible for the effect, the implications would cast doubt on the previously used assumption that the reaction forming syllylene is the sole step-limiting reaction.¹⁷⁰

The ratio of (ks) required for the 1.5 order condensation / nucleation is 117500 in terms of mass:

$$\frac{r_{cond}}{r_{nucl}} = 117500 \frac{[SiH_4]^{1.5}}{[SiH_4]^1} \quad (6-10)$$

where the number reported for the ratio of ks has units of (%^{-1/2}). K_{nucl} has units of (%⁻¹) and kcond has units of (%^{-1.5})

6.5.1. Evidence that supports the no sintering assumption

This section presents some additional information on the no sintering assumption below the primary particle size range. Figure 6-8 shows a) the TEM data and b) primary particle size distribution for the longest residence time at 700°C where due to the long residence time in the reactor, buoyancy is believed to occur and cause some turbulence in a section of the reaction zone, in which agglomerates that have already formed are momentarily transported back into the reaction zone due to turbulence and the agglomerates capture some particles that are growing in the reaction region. Thus, providing a window for observing the reaction zone. A picture of the nucleation process frozen and separated from condensation as the agglomerate itself scavenges a good amount

of the available condensable species (See increase of mean for the primary particle size in Figure 6-8 (b) for $\tau = 8x$ compared to the other residence times), This phenomena allows the nuclei to stay relatively untouched as it is transported by the “carrier agglomerate”. While all of this internal turbulence is hard to measure and validate experimentally, the fact is that after the turbulent zone, the particles remain in the hot zone of the reactor a good fraction of the total residence time (51s) before reaching the outlet. In addition, it is a fact that we have silicon nanoparticles that are smaller than our reported primary particles. These small nanoparticles are next to each other and do not show signs of sintering. This no sintering observation provides evidence for the following: At 700°C the temperature effect is not enough to cause sintering of the nanoparticles larger than 2 nm and sintering (two spheres touching each other becoming a larger sphere) may occur only if condensable species deposit on the surface of the separate nanoparticles.

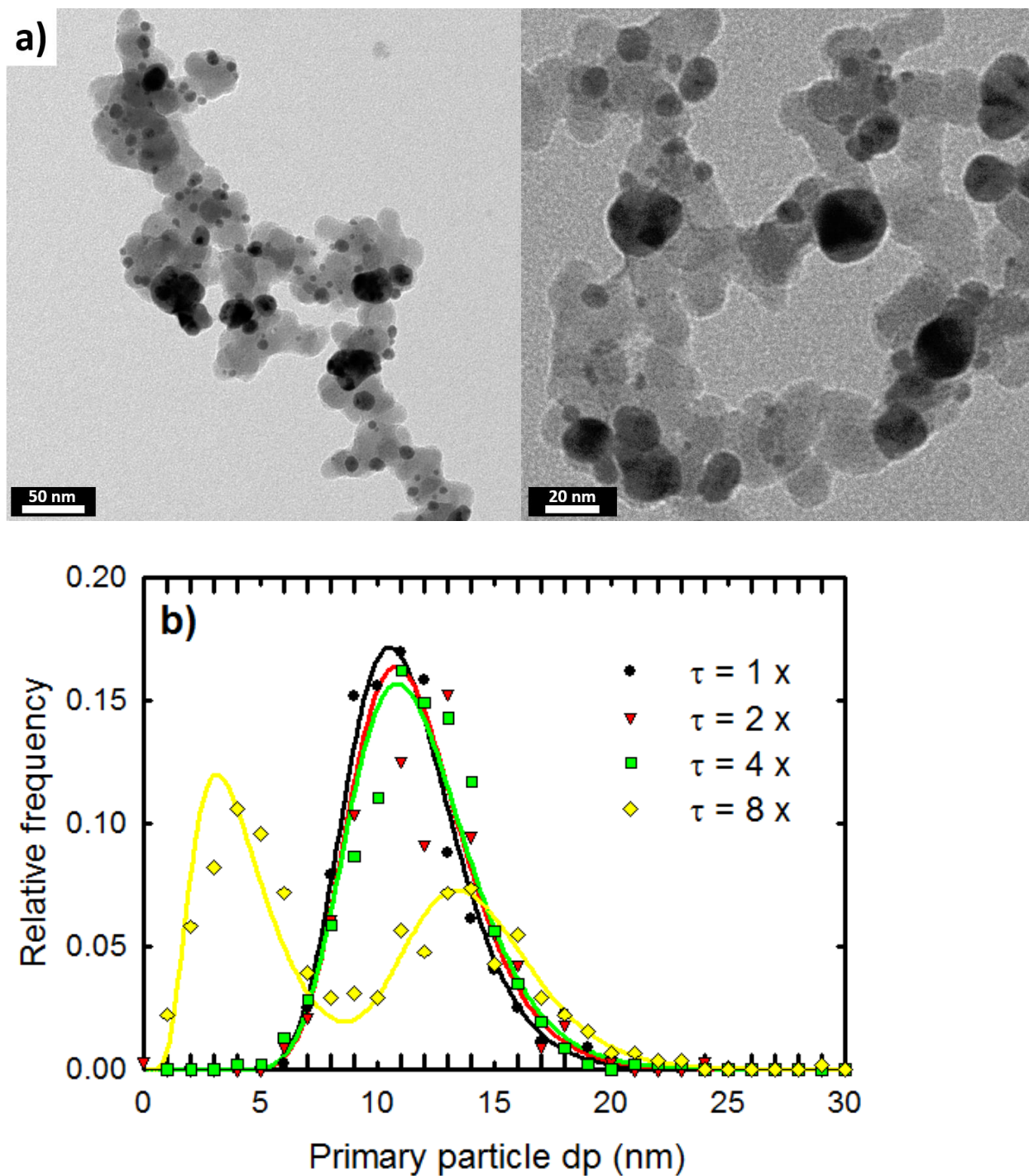


Figure 6-8 a) Two TEM images of silicon nanoparticles synthesized from silane pyrolysis in helium with a residence time of 51.2 s, and a concentration of 0.02% SiH_4 . Nanoparticles as small as 2-3 nm are abundant and visible in contact with each other, yet they do not sinter. This is consistent with the assumption of no thermal sintering occurring at this temperature. b) Primary particle size distributions for a residence time run at 700°C. $\tau = 8 \times$ corresponds to the TEM images on a). The peak at around 14nm is larger than the other 3 peaks with lower residence times and is attributed to further condensation in the window that the aerosol passes through the reaction zone.

6.5.2. Discussion on assumption of 1 nucleus per primary particle

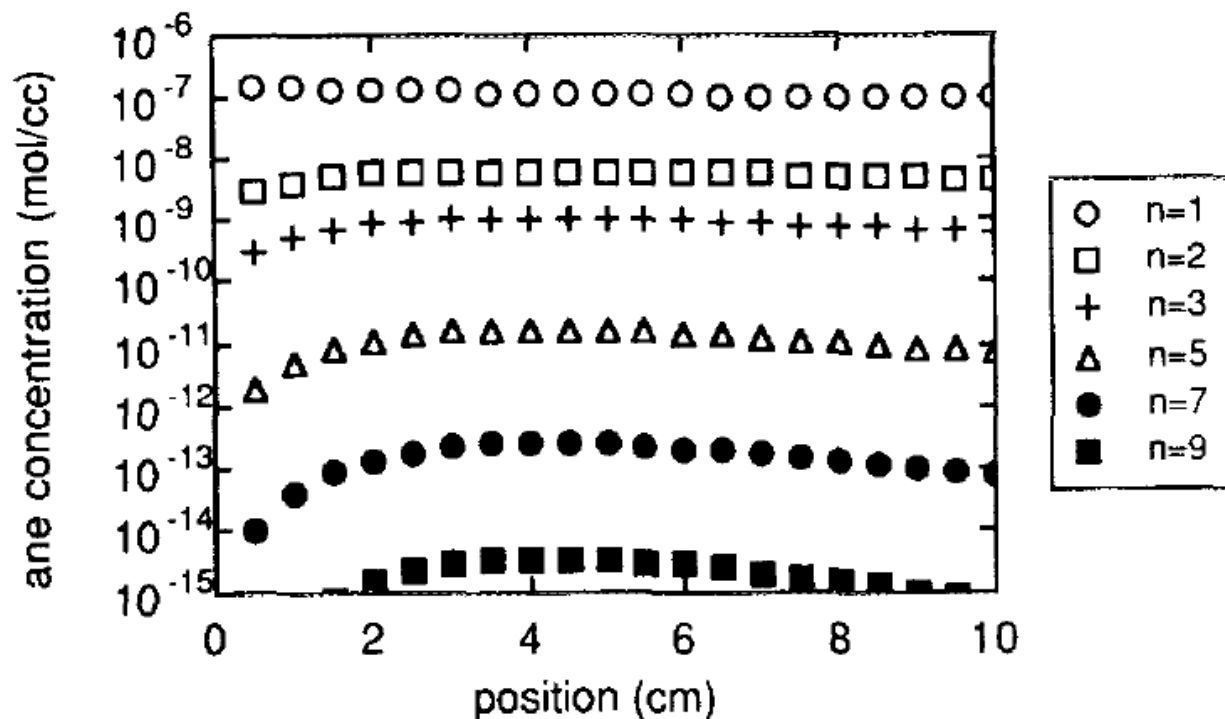


Figure 6-9 Simulated concentration profiles of ane from 1% silane in nitrogen at 890K Giunta et al.⁵⁶ Reproduced with permission. n represents the number of silicon atoms within the polymeric unit.

According to Giunta et al.⁵⁶, based on simulation more than 80% of surface deposition growth is attributable to disilene for 1% silane in nitrogen at 890K. The trends of higher order silanes occurring in very low concentrations reported by Giunta et al.⁵⁶ are also supported by observations of Purnell et al.⁴⁵

In addition, based on Figure 6-9 according to simulations by Giunta, if we compare the concentrations for n=2 and n= 7 we obtain 5 orders of magnitude. If we do it between n=2 and n=9, it becomes 7 orders of magnitude.

Based on a quadrupole gas analyzer (XT300, Extorr Inc.), the concentration of disilene for a 0.3% silane system at 475°C is 0.0152%. For the same conditions using half mini DMA measurements, the measured concentration of stable nuclei is $1.82 \times 10^{-13}\%$. To know the actual concentration of the nuclei the charging efficiency needs to be estimated. This is not an easy task and in general charging efficiencies below 2 nm are material dependent. If we extrapolate the value for 2nm reported by Hoppel et al.¹⁶¹ into 0.7nm, the charging efficiency fraction turns to be $\sim 10^{-4}$ (N/z). Thus the concentration of nuclei becomes $1.82 \times 10^{-9}\%$. This is 7 orders of magnitude between the concentration of condensable species and nuclei.

The ratio of condensed/nucleated mass at 0.3% at 700°C based on Figure 6-4 is only 32000 or ~ 4 orders of magnitude. Consequently, these calculations show that it is feasible to have only one nucleus per primary particle due to the fact that the concentration of species that have been reported to be stable nuclei is more than 5 orders of magnitude lower than the concentration of species reported to act as condensable species.

6.5.3. Discussion of collision frequency effect

The monodisperse model simplified after Kruis et al.¹⁷⁵ can be used to show the behavior particles would have if all the precursor reacted immediately to form monomers and these monomers would collide to form particles, growing by coagulation. The derivation follows:

$$\frac{dN}{dt} = -\frac{1}{2}\beta N^2 \quad (6-11)$$

Where β is the collision kernel and N the particle number concentration.

$$\beta = \beta(V_1, V_2) = \left(\frac{3}{4\pi}\right)^{1/6} \left[\frac{6k_b T}{\rho_p} \left(\frac{1}{V_1} + \frac{1}{V_2} \right) \right]^{1/2} \left(V_1^{1/3} + V_2^{1/3} \right)^2 \quad (6-12)$$

Where k_b is the Boltzmann constant, T is the absolute temperature, ρ_p is the particle density, V_1 is the volume of particle 1 colliding with particle 2 with volume V_2 . For monodisperse case $V_1=V_2$

$$\beta = KV^{1/6} \quad (6-13)$$

Where

$$K = 4 \left(\frac{3}{4\pi}\right)^{1/6} \left[\frac{12k_b T}{\rho_p} \right]^{1/2} \quad (6-14)$$

$$V = \frac{N_0 v_0}{N} \quad (6-15)$$

Where N_0 is the initial concentration of monomers and v_0 is the initial monomer volume.

Combining 6-13, 6-14 and 6-15 gives

$$\frac{dN}{dt} = -\frac{K}{2} (N_0 V_0)^{1/6} N^{11/6} \quad (6-16)$$

$$\int \frac{dN}{N^{11/6}} = -\int \frac{K}{2} (N_0 V_0)^{1/6} dt \quad (6-17)$$

$$\frac{6}{5N^{5/6}} = -\frac{K}{2} (N_0 V_0)^{1/6} t - \frac{6}{5} \frac{1}{N_0^{5/6}} \quad (6-18)$$

The right hand expression is obtained after evaluating the integration constant at $N=N_0$ and $t=0$.

The final analytical expression becomes:

$$N = \left[-\frac{6}{5} \left(\frac{1}{\frac{K}{2} (N_0 V_0)^{1/6} t - \frac{6}{5} \frac{1}{N_0^{5/6}}} \right) \right]^{6/5} \quad (6-19)$$

Where K is given by equation 6-14

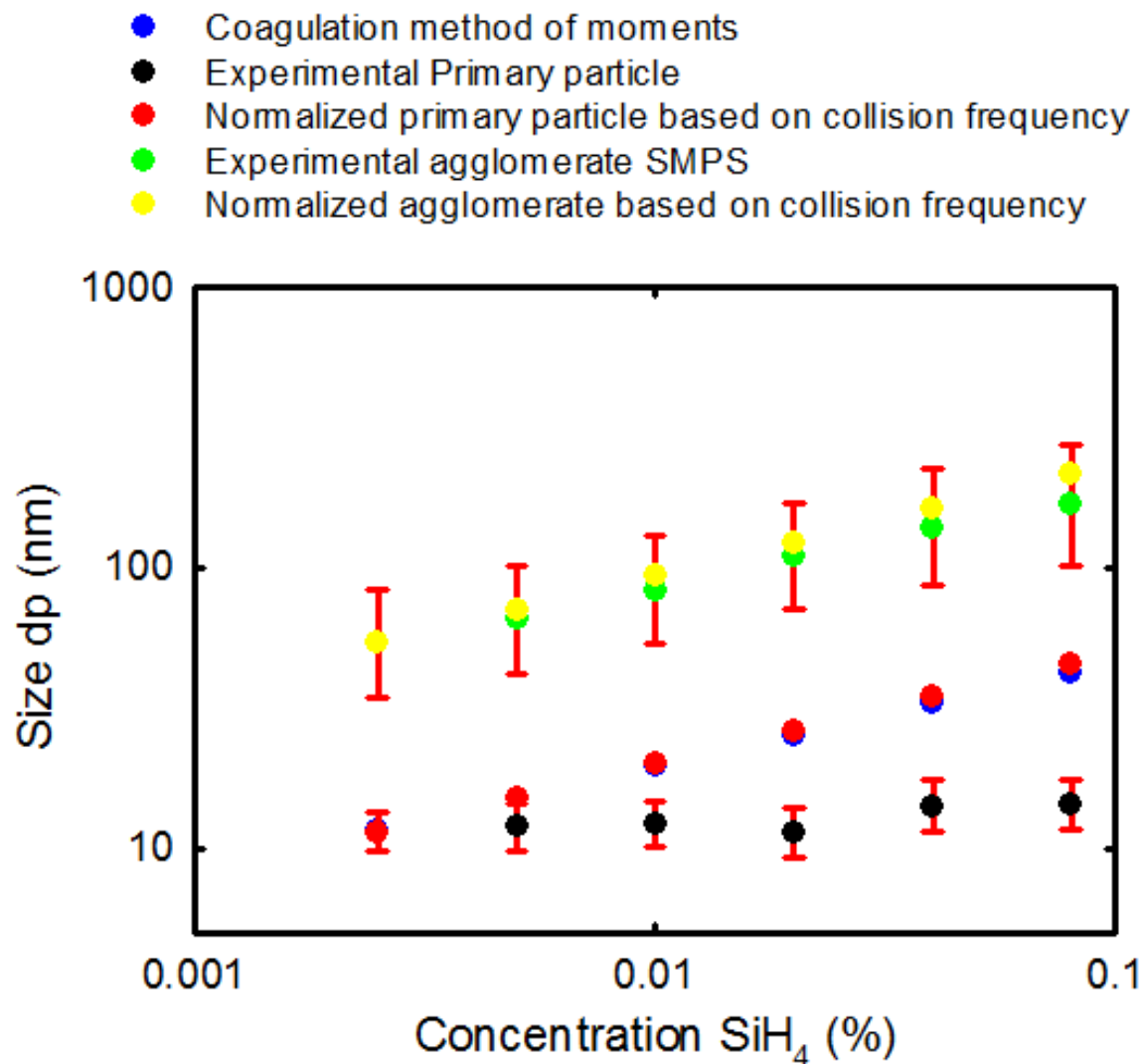


Figure 6-10 Observed agglomerate mean size (green) and predicted based on the monodisperse model (yellow) and measured primary particle size distribution (black) compared to predicted using the monodisperse model (red) and coagulation from the method of moments (blue) . The agglomerate behavior as a function of concentration is fairly well described by the model. On the other hand the mean primary particle size is not well described by either of the models. The predictions from the polydisperse and monodisperse models are close to each other but far from the experimental data, suggesting that the dominant mechanism for the formation of the primary particles is not dominated by collision of aerosols.

Figure 6-10 provided the comparison of the expected primary particle size if the dominant mechanism was the formation of nuclei that would then evolve through collision and coagulation. The fact that the model does match the mean size distribution for agglomerates, but it deviates for primary particles suggests that the reaction is not dominated by collision of aerosols. This conclusion is also obtained using a more accurate polydisperse model for coagulation: the method of moments.¹⁷⁶

According to Hinds et al.¹⁷⁷ the geometric standard deviation of the self preserving size distribution due to coagulation are 1.32- 1.36. Geometric standard deviations lower than that value can be attributed to condensation. Körner et al.¹⁷⁸ attributed condensation as well to be one of the primary mechanisms for the formation of silicon nanoparticles in their studies, although they used diluted streams with low total pressures.

6.5.4. Interpretation of 1.5 / 1 order for nucleation / condensation

Explanation based on reaction order for the chemical decomposition of silane

The 1.5 order here observed for condensation/nucleation has also been reported for initial disilane formation by Purnell and Walsh.⁴⁵ They suggest 3 possibilities:

- a) Heterogeneous steps
- b) Unimolecular reaction that is not first order
- c) Bimolecular propagation by reaction between radical and reactant

Purnell and Walsh report that the initial formation rate of disilane shows experimentally a reaction order of 1.5 with respect to silane or:

$$\frac{d[Si_2H_6]}{dt} = k'[SiH_4]^{3/2} \quad (6-20)$$

They propose the reactions



Becerra et Walsh¹⁷⁹ found that it is more likely that the 3rd reaction of Purnell is actually:



And Purnell et. Walsh⁴⁵ report that SiH_3SiH formation rate is enhanced by chemically activated Si_2H_6 produced through the insertion of SiH_2 into SiH_4 . Becerra et. Walsh¹⁷⁹ reported that the experimental study including the solid deposition proved independent of reaction surface area to volume ratio. This suggests that there is not a single rate determining step in the surface. However it is still possible to have both surface initiation and termination steps.

According to Odden et al. the reaction rate of 1.5 orders with respect to silane is due to the hydrogen elimination of silylene:



This is in agreement with White et al.⁴² Becerra does not seem to support this idea but says that it is due to the third reaction:



The condensable species is Si_3H_8 according to Becerra et al.¹⁷⁹ They also report that at the time they executed their study (1992) there were no available kinetics for the formation of $\text{H}_2\text{Si}=\text{SiH}_2$ (disilene).

According to Friedlander⁵¹, for aerosol phase reaction limited growth, the rate of reaction per unit volume is independent of droplet size. In our system we can describe the reaction mechanism as displayed in Figure 6-11.

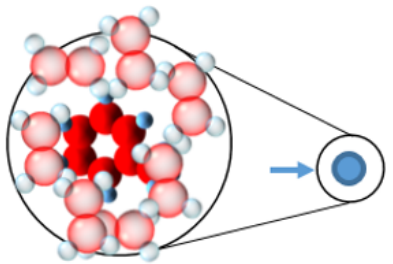
Chemical process	Aerosol process
Consecutive reactions Condensable species \rightarrow Stable nuclei	Consecutive processes Nucleation then Condensation
$\text{SiH}_4 \rightarrow \text{SiH}_2 + \text{H}_2$ $\text{SiH}_2 + \text{SiH}_4 \rightarrow \text{Si}_2\text{H}_6$ $\text{Si}_2\text{H}_6 \rightarrow \text{SiH}_4 + \text{H}_2$ $\text{Si}_2\text{H}_6 + \text{SiH}_4 \rightarrow \text{Si}_3\text{H}_8 + \text{H}_2$ $\text{Si}_n\text{H}_m + \text{SiH}_4 \rightarrow \text{Si}_{n+1}\text{H}_{m+2} + \text{H}_2$ stable nuclei $n > 7$ or $n > 10$	

Figure 6-11 Sequence of chemical reactions and aerosol processes

Explanation based on collision frequency and silane molecule distance

Some variables can be thought of as being a link between nucleation rate and silane concentration. Collision frequency is one of them. It is described by the following expression:

$$Z_{AB} = N_A N_B (r_A + r_B)^2 \sqrt{\frac{8\pi K_B T}{\mu_{AB}}} \quad (6-27)$$

Where Z_{AB} is the collision frequency between species A and B, N_A and N_B are the concentrations of species A and B respectively, r stands for radius, K_B is the Boltzmann constant and μ_{AB} is the reduced mass of the system defined as $\mu_{AB} = (m_A m_B) / (m_A + m_B)$. For the experimental system composed of helium and silane at a given temperature, the expression for collision frequency can be rewritten as:

$$Z_{AB} = \text{constant} [SiH_4] \quad (6-28)$$

This expression indicates that the amount of collisions between silane molecules and helium molecules is a monotonic function of silane concentration at low concentrations of silane such as the experimental data (<1% silane). On the other hand the distance between silane molecules can be expressed as a function of concentration using the following expression:

$$d_{SiH_4} = \frac{\text{Constant}}{[SiH_4]^{1/3}} \quad (6-29)$$

Where d_{SiH_4} is the distance between silane molecules. It is well known that hydrogen has an inhibitor effect in nucleation from silane pyrolysis³ mainly because it drives the reaction of silane polymerization backwards. Thus, it is expected that hydrogen produced by pyrolysis of silane will be proportional to the concentration of silane, in a similar manner the distance between formed molecules of hydrogen will be proportional to the distance between silane molecules. As nucleation starts and finishes at very low conversion, silane number of nuclei can then be related to the initial conditions by the following expression.

$$N_{Nuclei} = f(Z_{AB}, d_{SiH_4}, T) \quad (6-30)$$

Where N_{Nuclei} is the number concentration of nuclei in number/m³ and T is the temperature. If we substitute Eq. 6-28 and Eq. 6-29 into equation 6-30 for a given temperature we can express the number concentration of nuclei as:

$$N_{Nuclei} = Constant[SiH_4]^{2/3} \quad (6-30)$$

From the experimental section in this chapter, the number concentration of nuclei can be plotted as a function of silane concentration. The number concentration of nuclei is obtained as being the same as the number concentration of primary particles for each condition, which is obtained from the size distribution of primary particle and mass balance from the inlet silane concentration. Evidence for these assumptions is provided in the previous section. The plot of number concentration of nuclei as a function of silane concentration is shown in Figure 6-12.

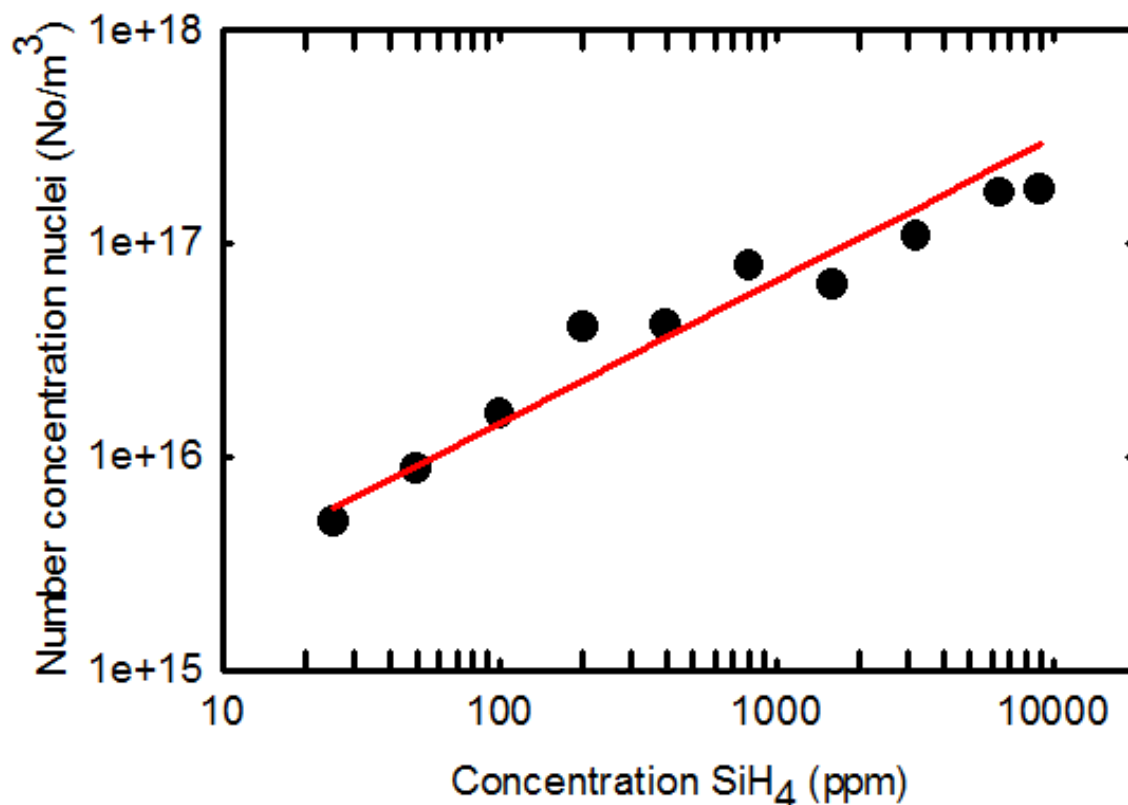


Figure 6-12 Number concentration of nuclei in number/m³ as a function of concentration. Black dots represent the data calculated from experimental results. The red line represents the fit provided in Eq. 6-31.

The representation of Figure 6-12 data can be expressed as a function of silane concentration in parts per million (ppm) as:

$$N_{Nuclei} = 6.7 * 10^{14} [SiH_4]^{2/3} \quad (6-31)$$

The problem of the explanation based on the observed initial order of reaction of Purnell and Walsh is that both processes of nucleation and condensation are not parallel for the whole extent of reaction, but the nucleation process seems to be inhibited and stop at some point through the process. This suggests that at that point, the order or reaction for condensation does not longer play a role in the overall process and the relative rates for both processes are become an indication

of nucleation itself. Therefore, the explanation of the limitation of nucleation based on collision frequency and the distance between silane molecules is a more plausible explanation for the $2/3$ order of reaction for the nucleation process as a function of silane concentration.

The observations suggest that there is a brief nuclei burst after which nucleation inhibition occurs and particle growth proceeds by surface reaction and condensation. The schematic of this proposed nucleation quenching mechanism is illustrated in Figure 6-13. A suggested mechanism for the process is based on an acquired property of the stable nuclei, where hydrogen atoms are capable of adsorbing on the surface of the nuclei, this causes a stable nuclei to form and its charge to form a dipole. As the silicon atom is less electronegative than the hydrogen atom, the second effectively attracts electrons closer and forms a dipole where the center of the nuclei made of silicon atoms is positive (lacks electrons) and the surface with adsorbed hydrogen becomes negative (surplus electrons) Thus even though the molecule is overall electrically neutral, the dipole formed is capable of attracting the reactive species, especially sylylene and thus quench further nucleation once enough nuclei have been formed. Then the rest of the reaction proceeds primarily by surface reaction for radicals and by condensation by capture of stable molecules that were formed by radical polymerization and the radical was then stabilized by a hydrogen atom collision.

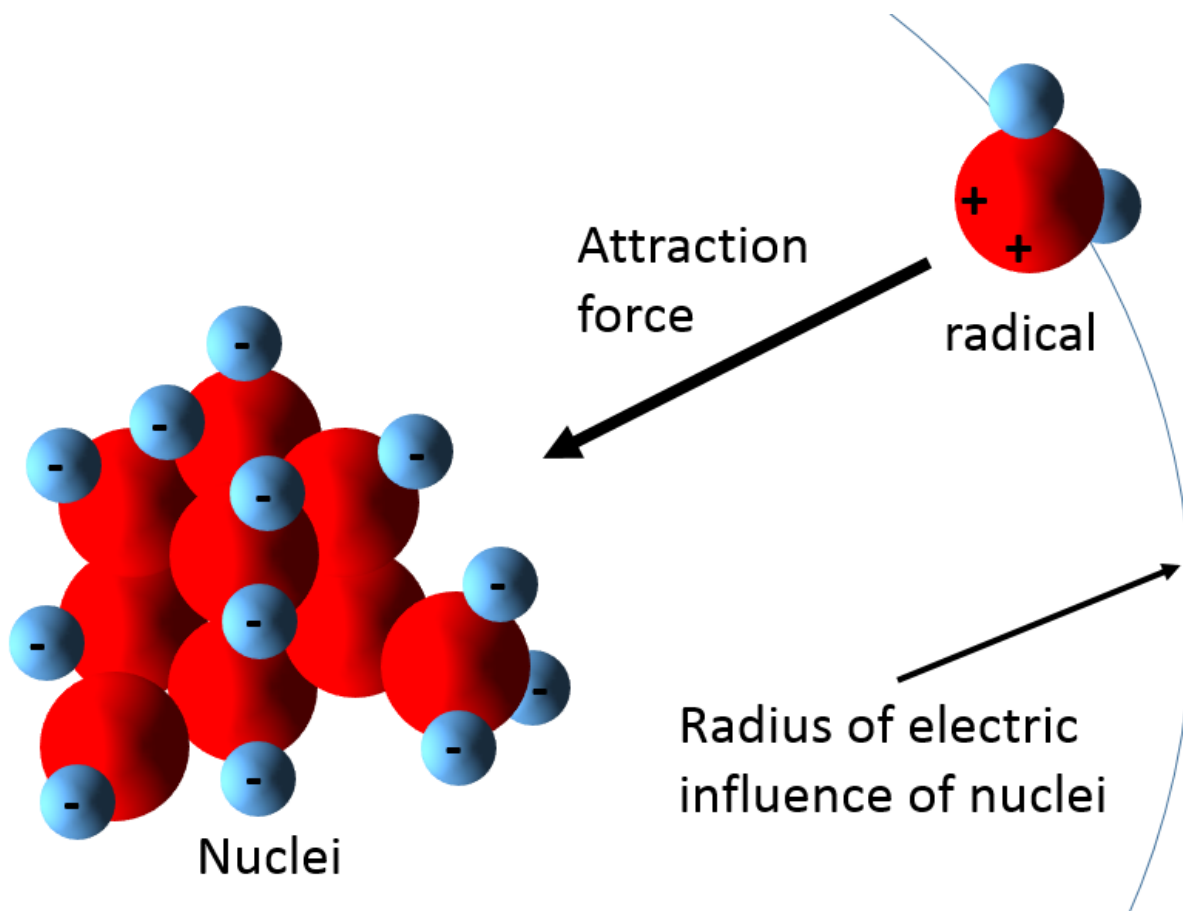
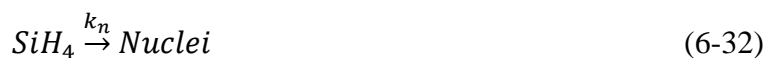


Figure 6-13 Proposed mechanism for nucleation quenching. Newly formed radicals are attracted by electrostatic forces between the dipoles of the formed radical and the charged surface of nuclei. In this way the radical undergoes surface reaction before it gets a chance to react with silane molecules and form new nuclei.

Based on the nucleation quenching mechanism, a reaction pathway is proposed to explain the size distribution of primary particles based on the following kinetic scheme:



The following differential equations describe the reactive system and a nuclei inhibition term is added to account for the phenomena using the expression in equation 6-31.

$$\frac{d[SiH_4]}{dt} = k_c[SiH_4]^{1.5} - k_n[SiH_4] \left(\frac{N_{Nuclei,f} - N_{Nuclei,t}}{N_{Nuclei,f}} \right) \quad (6-34)$$

$$\frac{d[Condensation]}{dt} = k_c[SiH_4]^{1.5} \quad (6-35)$$

$$\frac{d[Nucleation]}{dt} = k_n[SiH_4] \left(\frac{N_{Nuclei,f} - N_{Nuclei,t}}{N_{Nuclei,f}} \right) \quad (6-36)$$

Where $N_{Nuclei,f}$ is the final number concentration of nuclei and is given by the expression in equation 6-31. $N_{Nuclei,f}$ is obtained from integrating Equation 6-36 up to time t . To obtain a size distribution for a given concentration it is necessary to solve the system of differential equations. The process is considered to be limited by the chemical reaction so the condensed material produced at any step is added immediately to the total number of nuclei present at a given time step. To obtain number concentration of nuclei at a given point the total amount of nucleated mass concentration is divided by the size of a nuclei. The results from solving these differential equations and assigning the condensed mass to the nucleated mass at each time step is presented in Figure 6-14. Good agreement between the simulated size distribution for various initial silane concentrations is observed by comparing to the best fit of the experimental data, represented by symbols in Figure 6-14.

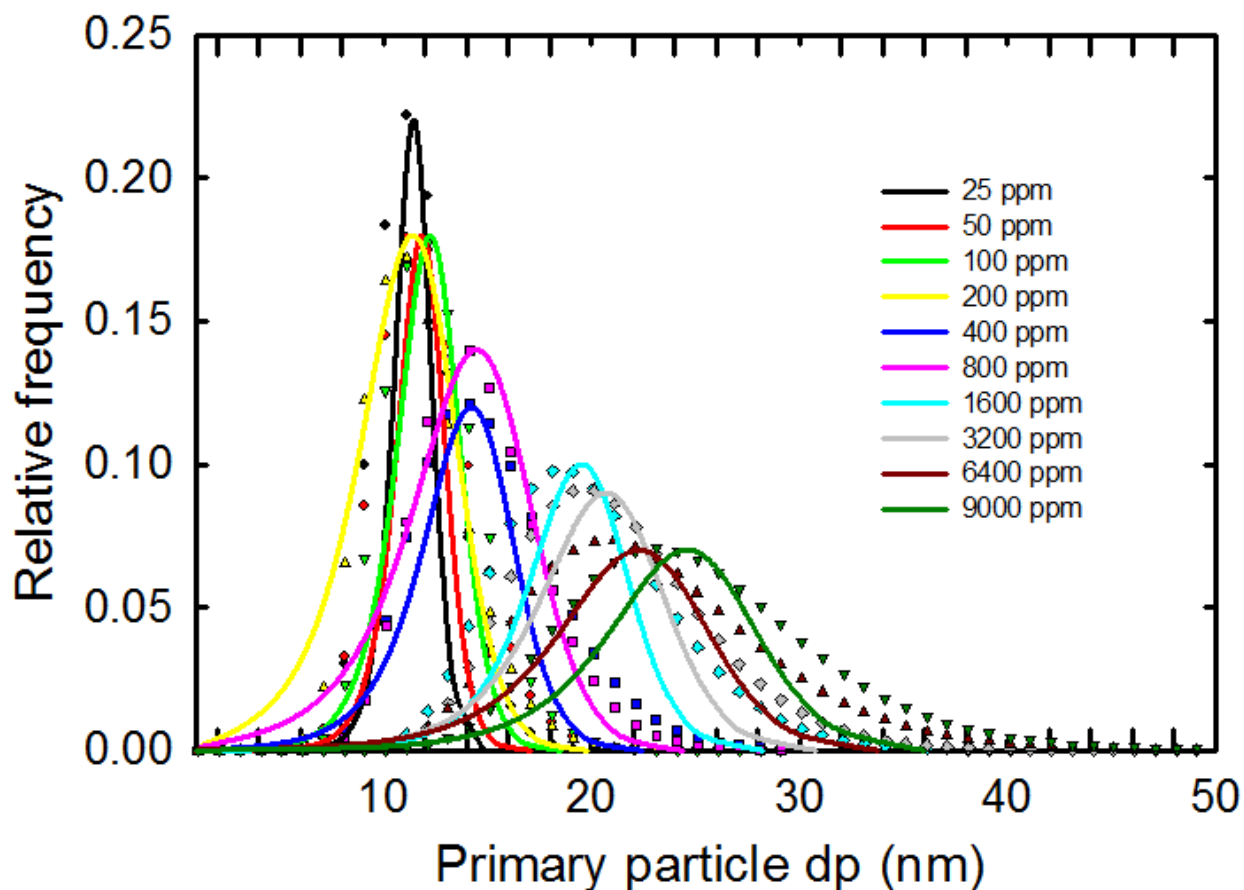


Figure 6-14 Color lines are the simulated size distributions for using equations 6-34 to 6-36. Symbols of the same color represent the lognormal fit of the experimental data presented in Figure 6-4d. The condensation constant used was $1.51 \times 10^{12} \text{ L}^{0.5}/(\text{mol}^{0.5}\text{s})$ and the nucleation rate was $1.2 \times 10^6 \text{ 1/s}$. These values are based on silylene formation and the relative rate expression developed previously in this chapter. The nucleation rate was corrected by a factor of 2.5 to account for the quenching effect.

6.5.5. Comparison of various methods for determining aerosol size distributions

Table 6-3 summarizes the different assumptions that are typically done in aerosol simulations and displays a schematic of different aerosol processes occurring: nucleation, condensation, agglomeration (Occurs in real life but is hard to account for in models) and

coagulation (Simultaneous agglomeration and coalescence) and a qualitative occurrence with respect to each other as a function of process time. (See figure 6-5 for a graphic description of these aerosol processes).

Table 6-3 Comparison of different models to describe aerosol dynamics for aerosol formation via chemical reaction. A sketch of dominant processes with qualitative times are shown. Also the assumption each model does is presented.

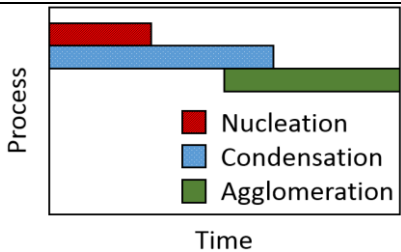
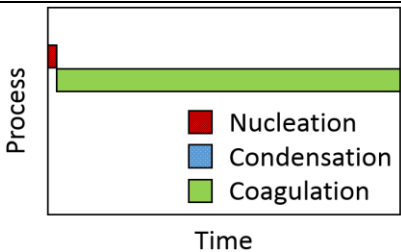
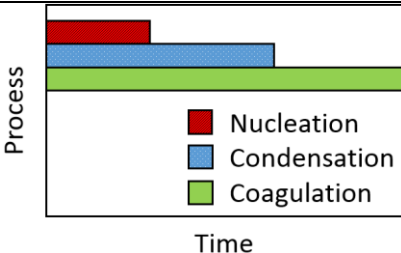
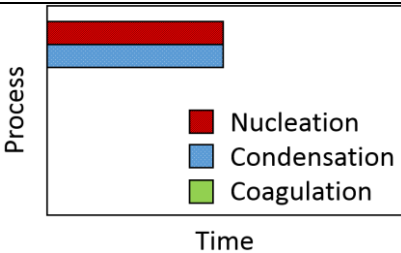
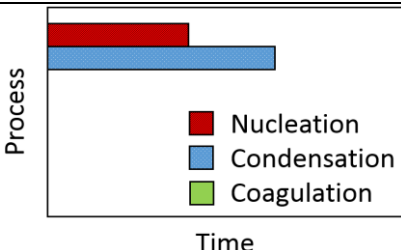
Sketch		Assumptions
Real process outline		
 <p>Process</p> <p>Time</p> <p> ■ Nucleation ■ Condensation ■ Agglomeration </p>		No assumptions
Immediate full reaction followed by coagulation		
 <p>Process</p> <p>Time</p> <p> ■ Nucleation ■ Condensation ■ Coagulation </p>		Reaction proceeds to completion at time=0 Condensation is not considered Coalescence of aerosols is assumed to occur instantaneously upon collision Progress of aerosol dynamics exclusively by coagulation
Nucleation/condensation/coagulation		
 <p>Process</p> <p>Time</p> <p> ■ Nucleation ■ Condensation ■ Coagulation </p>		Classical nucleation is believed to hold The reaction kinetics and the timing for each process of aerosol dynamics are believed to be accurate
Nucleation and condensation equal time for both processes		
 <p>Process</p> <p>Time</p> <p> ■ Nucleation ■ Condensation ■ Coagulation </p>		Coagulation is neglected The time required for both nucleation and condensation are considered to be identical
Inhibited nucleation at higher conversion and condensation		
 <p>Process</p> <p>Time</p> <p> ■ Nucleation ■ Condensation ■ Coagulation </p>		Coagulation is neglected Nucleation stops at some point at higher conversion

Table 6-4 Comparison of pros and cons of the various methods available for describing aerosol dynamics

Input	Pros	Cons
Immediate full reaction followed by coagulation		
<ul style="list-style-type: none"> Monomer number concentration 	<ul style="list-style-type: none"> Relatively simple For long times (when coagulation becomes dominant) it provides reasonable results 	<ul style="list-style-type: none"> It fails to provide primary particle size distribution It does not reproduce narrow size distribution particles that are formed mainly by condensation
Nucleation/condensation/coagulation		
<ul style="list-style-type: none"> Monomer flux Saturation Collision frequency and coagulation coefficient 	<ul style="list-style-type: none"> It takes into account most aerosol processes 	<ul style="list-style-type: none"> The concept of saturation is rather physical and not optimal for describing chemical processes. Classical nucleation theory was developed for liquids, its calculation shows errors in the range of various orders of magnitude for chemical nucleation The model is not capable of providing primary particle size distribution because it assumes immediate coalescence
Nucleation and condensation equal time for both processes		
<ul style="list-style-type: none"> Nucleation rate Condensation rate 	<ul style="list-style-type: none"> Difficult to measure times are not needed as both the time for nucleation and condensation are assumed to be the same 	<ul style="list-style-type: none"> Because nucleation does not end, broad size distributions may be obtained if calculated using differential approaches
Inhibited nucleation at higher conversion and condensation		
<ul style="list-style-type: none"> Nucleation rate Condensation rate Intermediate formation/decomposition rates 	<ul style="list-style-type: none"> It provides more realistic size distributions using the differential method compared to the equal time case 	<ul style="list-style-type: none"> An additional term for considering the nucleation inhibition is necessary Determination of kinetic constants is more difficult because nucleation rate becomes a function of 2 kinetic parameters that compensate each other

6.5.6. Obtaining a size distribution from chemical reaction

The reaction of silane can be summarized based on important processes as:



Where nuclei will be any species that is both thermodynamically stable and also capable of supporting condensation on its surface and condensable species is any species that after collision with a stable nuclei or another surface will stick (adsorb/chemisorb/react) with great efficiency causing particle/surface growth and allowing subsequent layers to be formed as well.

Each process is determined by a kinetic rate that for a power law form can be defined as:

$$\frac{d[\text{Nuclei}]}{dt} = \frac{k_{nuc}[\text{SiH}_4]^q}{n_{\text{Si},nuc}} \quad (6-39)$$

$$\frac{d[\text{Condensable_species}]}{dt} = \frac{k_{cond}[\text{SiH}_4]^p}{n_{\text{Si},cond}} \quad (6-40)$$

Where $n_{\text{Si},nuc}$ is the number of silicon atoms in the nuclei chemical formula and $n_{\text{Si},cond}$ is the number of silicon atoms in the predominant condensable species, q is the order of reaction for nucleation and p is the order of reaction for condensation.

If collisions of nuclei are neglected, which as discussed before is a reasonable assumption in some circumstances (Section 6.5.2), the total number of primary particles N at a given time t as the conversion of silane proceeds can be defined by:

$$N_t = \frac{[\text{Nuclei}]_t}{\text{mass_nucleus}} \quad (6-41)$$

For obtaining the size distribution of the primary particles it is important to include the effect of condensation on particle size by distributing the mass gained at each time step between the bin sizes of particles already formed in the system.

So for any given time step $t=i+1$

$$\Delta mass_{part,t=i+1} = \frac{[Condensable\ species]_{t=i+1} - [Condensable\ species]_{t=i}}{N_{t=i+1}} \quad (6-42)$$

Where $\Delta mass_{part}$ is the mass each particle gains per time step. A similar analysis can be done to distribute the condensed mass at each time step based on surface area of the particle, which is the typically used dependence for physical condensation. Then by knowing the number of particles present at each time step, and the mass gained by each particle at a given time step. Finally, the particle diameter can be obtained assuming the particles are spherical and the size distribution can be plotted by accounting for all the particles.

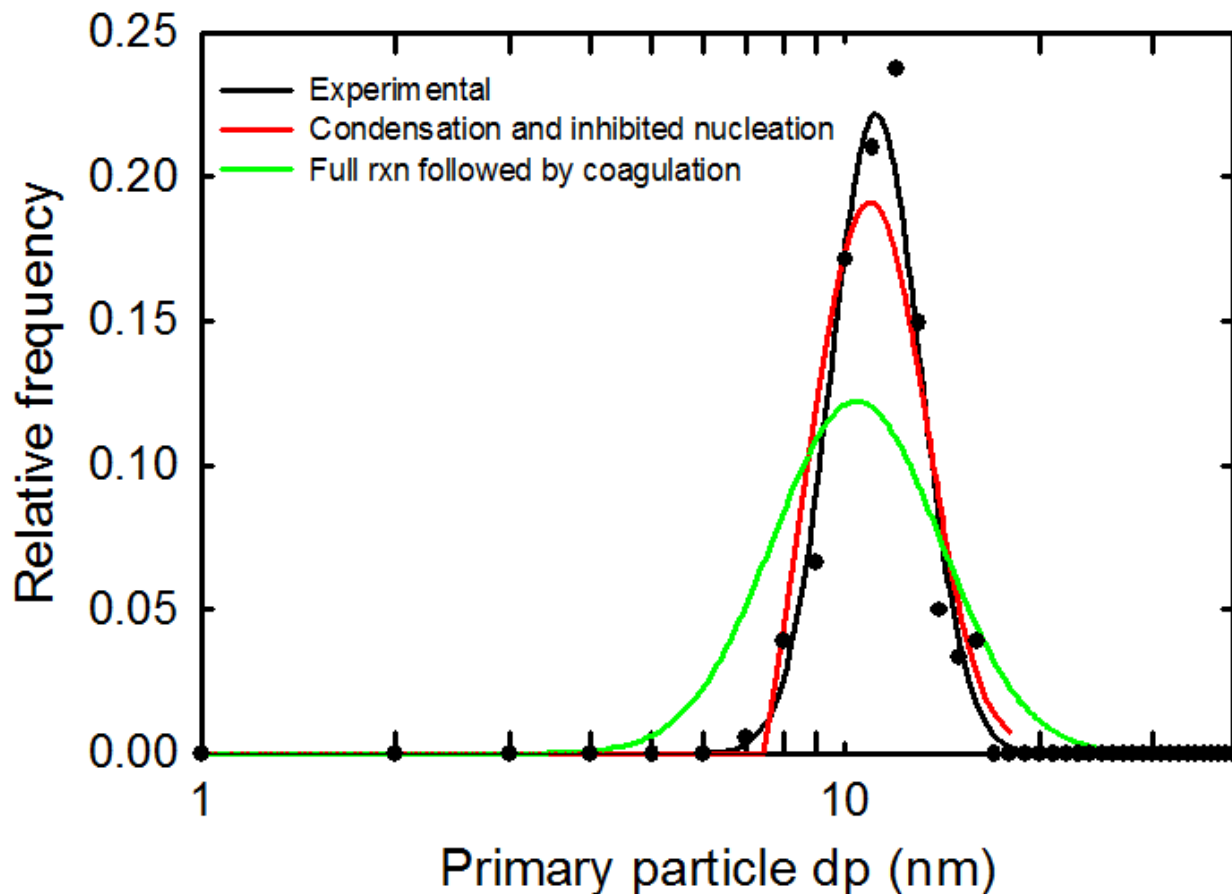


Figure 6-15 Comparison of the experimental primary particle size distribution from the pyrolysis of 25 ppm silane in helium at 700°C. vs. selected models for predicting the primary particle size distribution. The condensation with inhibited nucleation at higher conversion is capable of fitting the experimental size distribution well. On the other hand, the full reaction followed by coagulation model shows a broader geometric standard deviation (1.35), which is much higher than the experimental (1.17). Furthermore the time used to stop coagulation is rather arbitrary so accurately predicting the mean size of primary particles from this model is virtually impossible.

Figure 6-12 shows a comparison of selected models for predicting the size distribution of the primary particles. The best match is obtained from inhibited nucleation. The mean of that distribution is determined by kinetic parameters and the model is capable of reproducing the geometric standard deviation of 1.17. Since the growth of the particle is determined solely by kinetic parameters according to this model, choosing a right time to stop the simulation and report the primary particle size distribution is not a concern as conversion will not go beyond one. For

this scenario, the critical parameters are to determine the relative kinetics of nucleation/condensation and nucleation inhibition as the reaction progresses.

On the other hand, the model of full reaction followed by coagulation is intrinsically inappropriate for describing the size distribution of primary particles due to the assumption of immediate coagulation in the model. This model works well for predicting aerosol size distributions when studying aerosols that have been dominated by agglomeration/coagulation for a long time but not at the initial stages of aerosol formation. At this advanced point in aerosol evolution, the primary particle size distribution does not longer play a significant role in the agglomerated aerosol size distribution, but it does on the aerosol properties of industrial relevance (See Appendix A). However, for the primary particle size distribution itself this model would require to stop the simulation at a known time to be able to predict the mean of the distribution. This time would typically be in the order of milliseconds or microseconds and thus very difficult to measure or validate experimentally. Therefore the model of full reaction followed by coagulation is not appropriate for determining the primary particle size distribution and also, the high geometric standard deviation predicted suggests that the process for primary particle formation is not dominated by coagulation and supports the condensation assumption.

6.6. Conclusion and summary

The primary particle and agglomerate size distributions for silane pyrolysis in helium were obtained for various temperatures, concentrations, and residence times. Based on the results we concluded that sintering within the range of residence times tested in the reactor (6 to 60 seconds) is negligible for silicon nanoparticles synthesized below ~900 °C but becomes important above this temperature. Crystallinity of particles is not observed below 800 °C (see Figure 6-2 f, detection

limits of the instrument is $\sim 1\%$), and above this temperature crystallinity follows the same trend as the primary particle mean size, determined by TEM. For silane in a helium atmosphere, crystallinity seems to be linked to the degree of sintering.

A novel technique to gain insights into the relative reaction orders for parallel processes occurring in the aerosol phase based on TEM measurements was developed and is implemented in this study. The relative condensation / nucleation rates were determined and are provided as a ratio of k 's and reaction orders, which are 1.5/1 for condensation/nucleation processes respectively as a function of the inlet silane concentration. If despite the evidence presented, the assumption of 1 nucleus per primary particle did not hold, this estimation would provide a low bound on the rate of nucleation.

If the same concentrations and residence times are used, the agglomerate size distribution does not seem to be a strong function of temperature in the reactor. However the primary particle size distribution significantly depends on temperature. This feature has been reported previously and proves that for flow reactors under similar fluid dynamics conditions the rates of nucleation and condensation do not significantly change the agglomerate final size. So measuring agglomerate size distribution at the outlet of an aerosol reactor provides little information on the primary particle properties. Nevertheless, for systems where more dynamic conditions are present such as FBR, the knowledge of nucleation and condensation rates, orders of reaction, and reaction mechanisms that this work provides are relevant for correct reactor design and operation.

This methodology is recommended for future studies of the kinetics of relative rates in aerosol systems where it can be proved that the primary particles agglomerate without sintering, regardless of the residence time (no sintering regime). If this is proved, a run for different concentrations will yield relative orders of reaction, giving mechanistic information that can be

used to validate both chemical and transport mechanisms for nucleation and condensation processes of particular materials.

A novel process mechanism for the chemical nucleation of silane pyrolysis is developed and proposed as the backbone of the actual aerosol nucleation phenomena via chemical reaction. The mechanism includes a quick polymerization process which is a function of collision frequency between silane and helium. There is a quenching mechanism based on the distance of formed hydrogen molecules. The order of nucleation is determined to be $2/3$ as a function of initial silane concentration. Finally after enough nuclei have been formed new nuclei are inhibited as electrostatic forces cause newly formed radicals to deposit onto the growing particles due to dipole formation and electrostatic interaction before the radicals have a chance to react enough to form a new nuclei.

CHAPTER 7:SUMMARY AND RECOMMENDATIONS

7.1. Summary

In summary, this work was divided into two sections. In the first section, a kinetic and mechanistic study of both carbon elimination from kerf and the oxidation of silicon kerf was conducted, and a proof of concept demonstrated the feasibility of a furnace aerosol reactor for eliminating carbon from kerf and minimizing oxidation. In the second section, a better understanding of silane pyrolysis was presented with a focus on the initial aerosol dynamics. It included the measurement of a stable silicon hydride cluster that does not behave as stable nuclei formed from 0.3% silane and the synthesis of silicon aerosols with controlled morphology based on reactor operating parameters such as temperature, residence time, and concentration. Based on the results, a relative rate of condensation/nucleation was proposed in agreement with experimental results.

Chapter 1 was dedicated to an overview of silicon refining technologies, including persistent challenges associated with its refining. Critical points for improvement were identified, including the waste of more than 40% of ultra-high purity silicon through wafering, and the excessive energy consumption of the Siemens reactor (250 KWhr/kg of refined material). Chapter 1 reviews the silicon processing and market, the kinetic relations, and processes involving aerosol technologies that lower the energy footprint and final cost of refined silicon, in particular kerf recycling and fluidized bed reactors for polysilicon synthesis.

Chapter 2 approached the conceptual development and implementation of a furnace aerosol reactor for purifying kerf from its second most abundant impurity (carbon), which is perhaps the most challenging to remove. Carbon contamination comes from the lubricant used during ingot slicing, epoxy from the beam, and coagulant used to recover the coolant. The furnace aerosol reactor was run in air and nitrogen atmospheres up to various temperatures to observe the thermal

elimination of carbon. A decrease of carbon content was observed to occur gradually as temperature increased in both atmospheres. A reduction to below instrumental detection limits was achieved only in the air atmosphere (up to 900 °C). In the nitrogen atmosphere, carbon could not be fully eliminated. A kinetic phenomenological expression was determined from thermogravimetric analysis for each atmosphere, and the kinetics described by TGA predicted well the observed carbon elimination in the bench scale furnace aerosol reactor.

Chapter 3 was devoted to a mechanistic understanding of the process that occurs during thermal elimination of carbon in kerf. The source of carbon is a proprietary formulated lubricant based on polyethylene glycol and other additives. The elimination mechanism is composed of two differentiated stages for both air and nitrogen and was elucidated using GCMS, FTIR, TGA, SEM, and TC. The first stage is similar for both atmospheres: A depolymerization process by C-C and C-O bond scission yields volatiles at the same time as further polymerization of the oligomers yields a higher molecular weight residue. In the case of air, for the first stage, the dominant mechanism is the formation of volatiles, whereas in the case of nitrogen, the formation of a high molecular weight polymer dominates. The second stage of the reaction is different for each atmosphere. In the case of air, the high molecular weight residue completely undergoes depolymerization by C-C and C-O bond scission and becomes volatile. For nitrogen on the other hand, the mechanism is analogous to the first stage. Depolymerization still occurs in competition with formation of a high molecular weight residue that does not evolve into volatiles. For kerf heated up to 900 °C in nitrogen, 12% total carbon remains in the sample. In addition, the activation energy for the process for both atmospheres was determined based on TGA data using the OFW, KAS, and Kissinger methods.

Chapter 4 focused on predicting, with more accuracy, the oxidation kinetics of silicon samples that are made of agglomerates with various surface areas and crystallite sizes. It was proved that, in agreement with previous research, the experimental kinetics for the oxidation of polycrystalline powder are not properly described by the classical models for monocrystalline silicon wafer oxidation, partly due to the ill-defined morphology of agglomerates. The activation energy for the oxidation of silicon agglomerates was measured using the OFW and KAS methods, and it was observed to be correlated to the crystallite size rather than to the surface area. In addition, an expression for the parabolic constant was found to be related to both surface area and crystallite size, and a roughness factor was added to account for non-smooth powders such as kerf.

The second section of this work focused on silane pyrolysis and understanding the initial phenomena of silicon aerosol formation.

Chapter 5 focused on the measurement of a stable silicon hydride cluster using a half mini differential mobility analyzer. The mobility size determined was 0.75 nm, and TEM, Image J analysis and filters explained why the highest concentration of the silicon hydride cluster occurs at 440 °C and then decreases as the silicon hydride behaves as a condensable species and gets consumed by the formation of larger amounts of bigger aerosols as temperature increases. GCMS from the reactor outlet near the measured peak of the half mini DMA showed a peak at 207 m/z. This is consistent with a chemical identity of Si_7H_{11} , which is also in agreement with simulation results from the literature for stable molecules. Experimentally this stable cluster does not seem to behave as a stable nuclei, but rather appears to behave as a condensable species and the fact that it can be measured in the presence of a large amount of aerosols suggests that it is not capable of behaving as a stable nucleus as previously assumed. This is because if it was a nucleus, due to the

large fraction of condensable species concentration compared to nuclei, the likelihood of it colliding with condensable species and being depleted of the gas stream would be virtually 100%.

Chapter 6 was dedicated to studying the synthesis of aerosols and the control of their morphology based on operating reactor parameters such as temperature, residence time, and concentration of the silane precursor. Characterization techniques included TEM, XRD, and SMPS. It was found that below ~ 900 °C the synthesized nanoparticles did not undergo significant sintering for the achievable residence times in the reactor. Above that, temperature sintering of the nanoparticles was observed. Crystallinity as determined by XRD was not observed below 800 °C. and as temperature rose above that value, the crystallite size approached the size of the TEM-determined primary particle size. A novel approach to calculate the relative rate of condensation/nucleation was presented, where the ratio of kinetic constants was also determined for 700 °C silicon aerosol in helium. The relative rate that best fitted the experimental data was 1.5/1 condensation/nucleation. Finally, an out of the box mechanism for the chemical nucleation process of silane pyrolysis was presented on which nucleation occurs in a burst and is latter inhibited by proposed electrostatic interactions between the formed nuclei and radicals. This interaction causes radicals to be attracted and captured onto the surface of silicon incipient particles, causing them to grow and preventing nucleation of newer particles.

7.2. Future work recommendations

By focusing on removal of carbon, this work takes a new step towards the purification of kerf. More research is necessary to accomplish the full recyclability of kerf back into the refining steps of silicon in the form of polysilicon. An integrated approach that uses this recent advance in

kerf processing, combined with other recent developments, is desirable to achieve the end target of recycling kerf. Furthermore, work on the concentration limits for given contaminants is highly relevant to establish the bounds required for kerf recycle. Recycled kerf may not meet the stringent needs of electronic chip manufacture, but it might be usable in the photovoltaic industry.

A further idea to test for kerf purification is the use of plasma purification, which has been demonstrated to be very effective in removing small amounts of C and O from Si in upgraded metallurgical grade (UMG), silicon technologies. In addition, traces of C and O could be removed after FuAR directly in a crucible.

The initial stages of silicon oxidation remains a difficult problem for both the semiconductor and the photovoltaic industries. This step is of primary importance for processing non-ideal silicon nanoparticle agglomerates. The initial regime of oxidation and its dependence on core-shell differences are a little explored field that promises a better understanding of the interaction of nanoparticles with their environment. Such knowledge would not only improve prediction of reaction rates for oxidation or decomposition, but would also illuminate the reactions which may be of interest for toxicity studies¹⁸⁰ or medical applications.¹⁸¹

A better understanding of the initial stages of aerosol formation that integrates both the aerosol and chemistry processes is highly desired to predict with more accuracy the properties and processes of nanoparticle synthesis. Some ideas were developed and evidence was provided that suggests the process is chemically driven and electrostatic interactions play a prime role in the initial stages of nanoparticle nucleation and growth. Further work to continue, provide more evidence and more details of this approach are desirable for better understanding this transition

regime that is currently not well understood for most gas-solid reactions, including the silane-silicon system.

The interaction between silicon nanoparticle agglomerates and the silicon beads in a fluidized bed reactor needs to be better elucidated. Parameters including filtration efficiency, attrition, and CVD gluing capabilities need to be considered to improve the predictive model for fluidized bed reactors that operate continuously.

Fine and accurate control of morphology and particle properties is one of the remaining challenges of nanotechnology. Various kinetic measurements of kinetic competing rates have been discussed in Chapter 6. It remains an open question to predict such behavior based on first principles.

Silicon is a fabulous material. As more accurate and precise control of the morphology of nanoparticles is acquired, a whole range of applications including anode batteries, nanopharmaceuticals, and electronic components will open for exploration and optimization. The opportunities are significant and the impact new developments can have on the current technology market are also substantial. Therefore, more research should be dedicated to this wonderful material and the enhanced properties that can be acquired by the nano-aerosol synthesis.

7.3. Safety considerations

Silane is a pyrophoric gas that reacts with water and air above 1.4%.¹⁸² It forms dangerous metastable mixtures that might explode violently above 4% silane in air. Between 1.4 and 4% it burns smoothly in contact with air, and below 1.4% it does not burn. Silane forms nonflammable mixtures with air if the concentration is below 1.4%.¹⁸³ The numerous deaths and injuries from

silane handling and researching in the past decades have caused an increase in the regulations for transporting, handling, and are particularly stringent for indoor use and university research. Safety operations using silane can be found on Fthenakis et al.¹⁸³ Minimum requirements for handling silane include an extensive compliance list. It includes an exhaust line exclusive for silane, working exclusively on isolated environments with waterfall failure analysis, a training requirement for all people in the lab about silane usage, extreme safety measures to transport, store, and discard silane tanks, etc. Furthermore, the maximum concentration permissible for the vendors to supply local universities is 1.9%. Additional to its pyrophoricity, silane is highly toxic. It is well known that even below the pyrophoric concentrations, it reacts with moisture and forms SiO_2 producing silicosis in the lungs and reacting with the moisture in the eyes producing extreme irritation and corneal damage if the threshold limit value of 5ppm is exceeded. For handling silane below those concentrations, select eye protection in accordance with OSHA 29 CFR 1910.133. **EYE PROTECTION:** Wear safety glasses when handling cylinders.

Due to these reasons, it is important to build a system that complies with the most stringent regulations for safe operation. And to guarantee operator integrity and lab staff health. Key components to comply with this include a system that is air tight and capable of being fully purged with inert gas (VCR fittings) Routine tests are designed and need to be executed on a daily basis that prove air tightness is functional before each experimental run, and a portable silane detector with an alarm sounds if SiH_4 concentration reaches or exceeds 5ppm on the working place.

The dilution gas that will be employed with SiH_4 can be hydrogen or an inert gas. The first generates explosive mixtures with air if it is in the range of 4 to 77.4% and in chlorine if it is in the range of 5 to 95% requiring some additional safety measures and equipment. Inert gases as Ar or N_2 on the other hand do not pose a significant risk unless they decrease the oxygen concentration

of the room below 20%. Using these inert gases would limit the safety concerns to the silane factor, but with the disadvantage of obtaining idealized results as the industrial reactors use H_2 and not inert gases in normal operations.

List of safety equipment and proposed safety tests

Safety equipment includes sealed goggles, PVC safety mask, ear protection, leather gloves, anti fire apron, and silane portable sensor. Additionally, the silane gas tank should be stored exclusively in a gas cabinet with an approved independent exhaust. The experiments should be performed in a hood with correct use and in agreement with regulation of the local safety organization. The silane portable detector is located in the interior of the lab next to the operator. A calibration tank is provided so regular tests and calibrations can be executed by the operator (according to the manufacturer recommended frequency). The silane line should be purged for 3 times after finishing the experiments each day and then should be pressurized with inert gas. On a daily basis, a 5 min pressure test should be executed in the silane line using inert gas before proceeding to open the SiH_4 gas line.

APPENDIX .

A: Capture of aerosols by silicon beads and their saturation in an FBR

Abstract

Polysilicon is a key commodity required for both electronics and solar photovoltaic modules. The traditional route to produce polysilicon involves the Siemens reactor. More recent advances in fluidized bed reactor (FBR) technology are making the transition to polysilicon synthesis via FBR more attractive. Nevertheless more work is still required to better understand this type of reactor. In particular the fines formation and scavenging by the beads are of particular relevance, because to keep the production rate high, the reactor needs to be operated in a regime where the kinetics of silane pyrolysis favor the formation of aerosols, which are later to a large extent integrated into the beads via scavenging. This work provides insights into silicon aerosol filtration and retention over wide ranges of operating conditions such as temperature, time, aerosol morphology, and crystallinity.

Introduction

Silicon background

Currently, silicon (Si) is the material most commonly used for computer chips and solar photovoltaic modules. Si is abundant as a raw material in the Earth's crust in the form of silicon dioxide (SiO₂) but needs to be refined above 99.999% (5N) or even up to 9N purity for current photovoltaic (PV) usage. 9N or higher is also required for modern electronic applications.⁴ One of the most expensive steps in silicon refining is polysilicon synthesis, which requires chemical vapor deposition of silane or trichlorosilane from gas into a solid, which is later extracted as refined product. This process permits achieving the required Si purity but at the cost of significant energy consumption, which translates into elevated cost for the material.¹⁸⁴

Siemens vs. fluidized bed reactor (FBR) for polysilicon synthesis

Historically, polysilicon has been primarily refined using the Siemens reactor¹⁸⁵. Because more polysilicon is currently utilized for solar modules than for electronic chips, a cheaper methodology to produce polysilicon (poly Si) has emerged, the fluidized bed reactor (FBR). The FBR can significantly reduce both the cost and energy demand of the polysilicon refining process, mainly due to its more efficient thermal behavior and lower thermal gradients than the Siemens reactor.¹⁸⁴ Comparing the products from both reactors shows that FBR poly Si has a fracture toughness about 20% lower than Siemens poly Si, mainly due to solute hydrogen trapped within the beads. A simple thermal annealing removes the hydrogen and makes the properties of FBR poly Si similar to those of conventionally processed Siemens poly Si.¹⁸⁶

FBR disadvantages

Despite its intrinsic energy efficiency, FBR's complexity still prevents its widespread implementation for polysilicon production. To date, mainly due to silicon aerosols formation (fines) inside the FBR, long-term efficient continuous operation is still challenging²⁰. This issue can be subdivided into three significant problems that need to be understood. First, the chemical mechanism for the reaction of silane to form solid Si needs to be elucidated. This problem has received significant attention,^{43, 167, 187} yet there is still disagreement on the detailed mechanism. Second, the determination of the kinetics of aerosol formation relevant mechanisms, such as nucleation, condensation, sintering, and agglomeration, needs to be quantitatively determined. Finally, understanding the fate of aerosols formed inside the reactor as they rise with the fluidization gas is critical. This phenomenon is not only problematic, because material losses occur as fines get elutriated, and it also negatively affects reactor performance.²¹ Additionally, as new

particles are formed and grow inside the bed, the fluidization regime could change from empirical Geldart group B into a combination of groups B, C, and A, modifying the fluidization properties of the original bed ² and the mass and heat transport rates. The purpose of this work is to correlate the capture efficiency and retention of the aerosols based on their properties, providing insights into this last question. A brief discussion is presented on fluidized bed dynamics and filtration to provide perspective for the experimental work.

Current perceptions of fines in Si FBR

Several authors have considered fines formation as a problem that needs to be avoided at all costs in FBR. Nevertheless Hsu et al.¹ proved that fine scavenging is actually a very important step for bead growth. At industrial relevant conditions it even contributes more significantly to bead growth than CVD itself. Some authors have implemented the concept of scavenging as an adjustable parameter in their modeling¹⁸⁸ and others have assigned it to be proportional to the total surface area of silicon beads and to the concentration of silicon formed by homogeneous reaction.¹⁸⁵

It is critical to better understand the delicate balance between bead growth by fine scavenging and fine release by attrition, since small changes in this balance could have long-term effects on the stable operation of the reactor.¹⁸⁹ Figure A-1 displays our understanding of the various CVD and aerosol processes occurring inside the fluidized bed reactor.

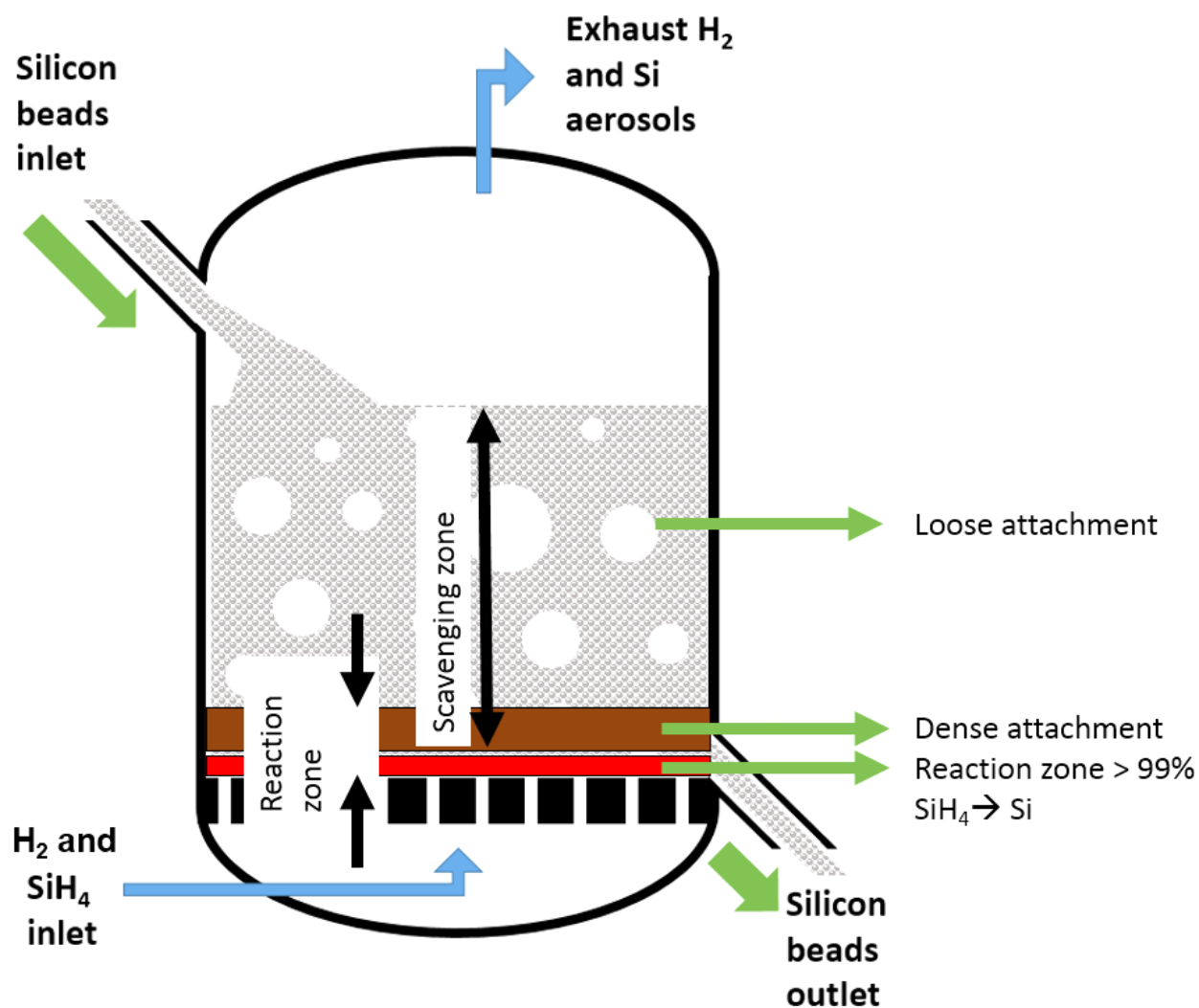


Figure A-1 Schematic of proposed mechanism for silicon bead growth in FBR

Historical challenges of FBR

The most attractive characteristic of fluidized bed reactors is the potential for relatively high efficiency of heat and mass transfer between solid particles and gas, an optimum that FBR reactor designers try to achieve.¹⁹⁰ However, FBRs have historically proven challenging to scale up, mainly because typically pilot plants operate in the slugging fluidization regime whereas industrial reactors operate in the bubbling fluidization regime.¹⁹¹ This has been learned the hard

way.¹⁹¹ Some efforts to improve our understanding on FBR scale up have been reported by authors like Constantineau et al., who developed a single model to predict the behavior of a fluidized bed reactor for both slugging and bubbling behavior.

Types of fluidization:

As the fluidization velocity increases, a fluidized bed passes from a fixed bed, to a bubbling bed, into a slugging bed at high flow velocities. As this progresses, the bed height changes as well. Bed height fluctuations are rather periodic and can be correlated with pressure fluctuations.¹⁹² Depending on the diffuser design, a fluidized bed can also allow for channeling of the fluid through the bed.

Slugging

In an FBR, according to Liu et al.¹⁸⁸, slugging occurs when the bubble diameter is greater than 0.6 times the bed diameter. Most lab scale reactors operate in the slugging regime, whereas their industrial counterparts tend to operate in the bubbling regime because the ratio bed diameter to particle diameter is larger. Slugging behavior of fluidized beds has been described by de Luca et al.¹⁹³ They describe how slugging occurs based on the bed diameter and also provide an expression to calculate the slug frequency. It has been reported based on simulation by Liu et al.¹⁸⁸ that reactors as large as 2 inch ID show a slugging flow pattern.

Fines elutriation

Elutriation of fines from classifications A and C from a group B particle bed displays a maximum at a critical powder diameter, which confirms that changes in elutriation rate may be attributed to inter-particle adhesion forces. Ma et al.¹⁹⁴ studied the powder cohesiveness or inter-particle adhesion forces in mixed B-C-A fluidized beds. They found that smaller particles for group C, even though they have a smaller gravitational pull compared to their drag, which would make them more likely to exhibit high elutriation rates, actually display a decrease in elutriation due to powder cohesiveness. The same behavior was observed by Briens et al.¹⁹⁵, who also studied how electrostatics affect the size distribution of elutriated particles.

Choi et al.¹⁹⁶ studied how increasing the proportion of fine particles in a mixed bed with coarse particles increased the elutriation rate of the coarse particles. The same effect was observed with increasing gas velocity.

FBR filtration

Different agglomerates and granules were used by Quevedo et al.¹⁹⁷ to study their performance as filtering media for submicron particles. They used a cumulative collection efficiency because the single channel efficiency is very noisy. Quevedo et al. also observed that fluidized beds release particles. They studied both fixed and fluidized beds for many different beads against small particulate and oil aerosols.

Computational Fluid Dynamics of FBR SiH₄

For filtration modeling in a fluidized bed reactor, the Eulerian-Eulerian model is typically used. The term for collector saturation that causes a reduction in filtration efficiency over time due

to saturation of the single collector is not generally included in the simulations. Yamamoto et al.¹⁹⁸ presented a comparison of their model that does not include adhesion and then presented a series of equations to add that term so that efficiency drops over time. Their experimental values were obtained from their previous work. Yamamoto et al. also report that, based on their simulation, the collection is nearly uniform on the entire bed particle phase.

Ushiki et Tien¹⁹⁹ proposed a model to calculate aerosol collection in fluidized filter beds that consists of breaking the bed in compartments, each of which is comprised of two or three phases. For each they present different cases and existing theories of particle deposition.

Principle of particle release in FBR due to collision

Fines can get scavenged by the silicon beads in the FBR. However their retention of the aerosols is limited by the saturation value of aerosols in the particle.²⁰⁰ Some techniques used in filtration application involve adding a liquid retention aid on the collector surface. Ghadiri et al.²⁰⁰ also mentioned that dust collection in the bubble phase is negligible, but gas exchange between the two different phases can cause particulate collection. They also distinguish two different collection zones: a gas entry zone and a bubbling bed zone. Ghadiri et al. clearly show the need to report both collection efficiency and retention efficiency. These two properties are a function of Van der Waals forces, electrostatic attractive forces, and capillary forces and humidity. Additionally, plastic deformable dust can be retained more easily than non-plastic dust.

The silicon FBR

Hsu et al.¹ studied the fines formation in a fluidized bed silane pyrolysis system. They used kinetics for homogeneous reaction from Hogness et al.⁶⁸ and heterogeneous reaction kinetics from Iya et al.⁶⁹ Hsu et al. by comparing the kinetics vs. their experimental measurements, came to the conclusion that most of the deposition of material in the beads is due to aerosol scavenging through the bed.¹

Different configurations of the fluidized bed reactor have been proposed, such as changing the fluidization regime from Group B to group D to eliminate bubble formation.²⁰¹ However this might cause improper bed mixing, resulting in problems such as particle segregation, non-uniform bead heating, and large inadvertent temperature gradients inside the bed.

Formation and accumulation of fines near the reactor walls and on the top of the reactor has been observed experimentally,¹⁶⁶ and its existence has also been predicted based on modeling by Liu et al.²⁰² The formation and accumulation of particles from a different Geldart group in a silicon FBR can affect the fluidization dynamics of the reactor, hindering its continuous operation.

Elutriation from fluidized beds

Several attempts have been made to understand elutriation from fluidized beds. Pemberton et al.²⁰³ attempted to model elutriation from bubbling fluidized beds. They found conditions such as downflowing of material in the bed, bubble coalescence due to the reactor distributor, and particle segregation are not always easy to predict and can significantly change elutriation. Parker et al.²⁰⁴ report that a screen mesh distributor creates a bubbling bed that leads to high conversion of silane, but nozzles minimize clogging in the reactor. Parker also reports the effect of mesh vs. nozzles on mixing, using a CFD model. The results indicate that both provide adequate mixing.

Balaji et al.¹⁸⁵ performed a comprehensive modeling using CFD, a reaction module, and population balance. One of the main assumptions is that the rate of powder scavenging follows a proportional trend with respect to the concentration of silicon powder produced and the total surface area of silicon particles. They also assume that particle phase is well mixed.

In the 70s and 80s, some effort was invested in understanding fluidized bed filtration,²⁰⁵ mainly for applications such as integrated gasification combined cycle technology and to capture pollutant gases and particulates. However, studies such as the one by Liu et al.²⁰⁶ showed that different materials of the same size have significantly different collection efficiencies, based on the bed material and the inter-particle forces between it and the nanoparticles to be captured. Due in part to its mathematical simplicity and higher efficiency, research has focused more on fixed beds than fluidized beds.²⁰⁷ Despite being less efficient in removing small particles, fluidized bed filters have the advantage of being continuous and intrinsically capable of operation at high temperatures.²⁰⁸

Contrary to the operation of a Siemens reactor, where most of the growth comes from chemical vapor deposition (CVD), the primary mechanism for product growth in the FBR is by aerosol scavenging by the bed. It is therefore paramount to understand the filtration efficiency in a silicon FBR. This is difficult to study in an FBR, where CVD occurs in parallel to scavenging, because the CVD process that occurs in the lower section of the reactor causes a gluing effect that bounds the effect of both phenomena in an inextricable way. Yet it is important to assess and quantify this effect to maximize product capture and retention, otherwise, to study the effect of aerosol capture and retention without gluing it demands a decoupling of both processes. We have done so in our reactor. In the first section we exclusively form aerosols and then we feed them into the fluidized bed. The objective of this work is to observe the effect aerosol morphology has on

the capture and retention efficiency in a silicon fluidized bed. The effect of various parameters was studied: aerosol release due to attrition of beads at several fluidization conditions, the time for bead saturation, and the effect of fluidized bed temperature and the incoming aerosol morphology on its capture.

Materials and methods

The experimental setup can be seen in Figure A-2. The setup consists of three main areas: The silane reactor section, the fluidized bed region, and the online characterization part. The silane reactor starts with two primary streams of gas: The first is 0.9% silane (SiH_4) diluted in helium (Airgas Inc., PA, USA) that passes through a mass flow controller (MFC) (MKS Instruments, Inc. MA, USA), and the second is a high purity helium (99.999% Airgas Inc., PA, USA) stream that passes through an oxygen scavenger and is also controlled using a MFC. Both streams are controlled using a modular analog data acquisition system using software and hardware from NI (National Instruments Corporation, TX, USA). Both streams are then passed through a pressure transducer (WIKA, Klingenberg am Main, Germany) and then into the aerosol flow reactor, which consists of a nominal 1 in. stainless steel 316 tube inside a Lindbergh furnace (Thermo Fisher Scientific, NC, USA). The aerosol is then passed into the fluidized bed region. The fluidized bed consist of a nominal 1 in. quartz tube with an ID of 2cm. The fluidization gas used is nitrogen from a liquid nitrogen source (99.998% Airgas Inc., PA, USA). The inlet and outlet of the fluidized bed are connected using ball valves to a 3080 Scanning Mobility particle sizer (SMPS) instrument (TSI Inc, Shoreview, MN), which measures size distribution and number concentration on real time.

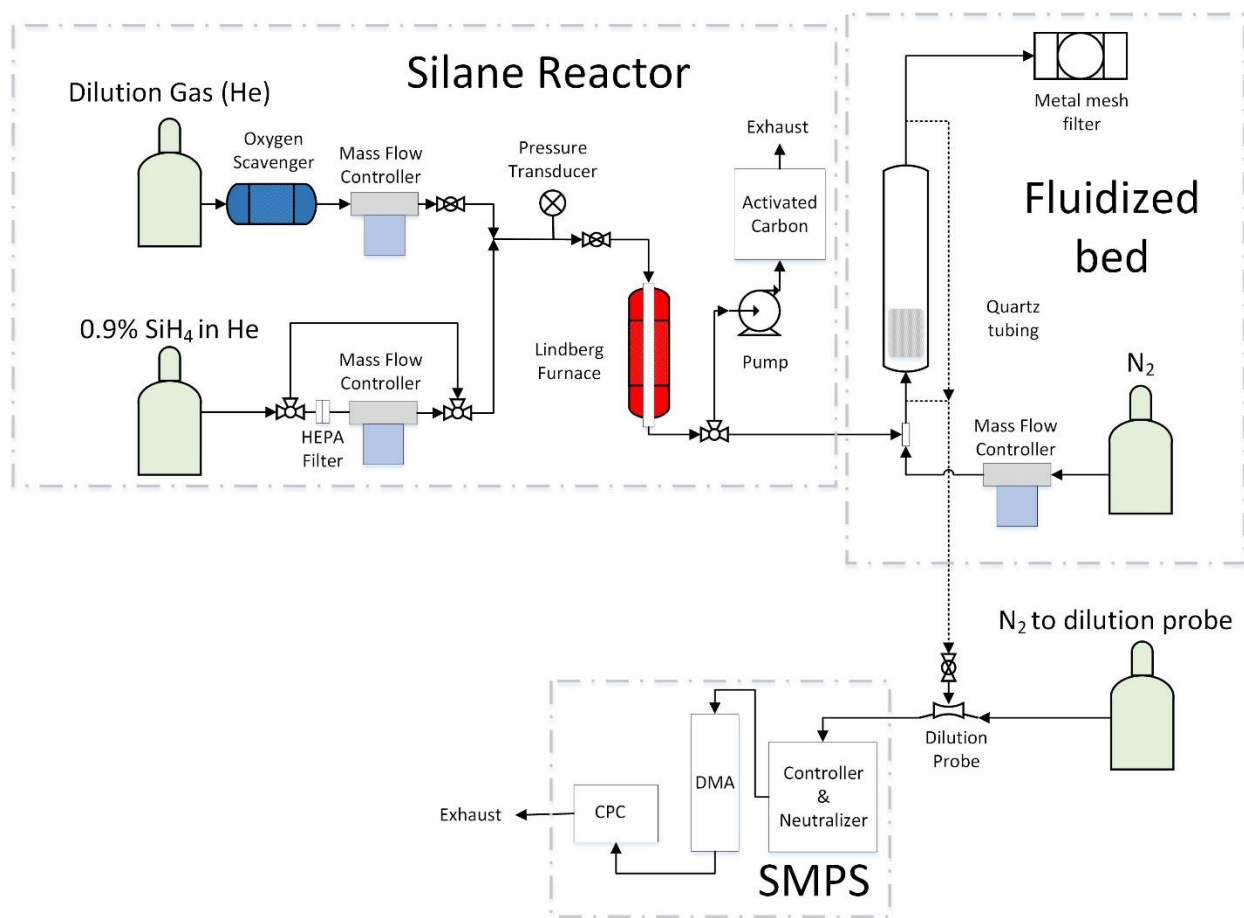


Figure A-2 Experimental setup

The silicon beads used in this study were provided by Sun Edison Inc. from their industrial scale FBRs. The beads were characterized before and after selected runs using SEM in a FEI Nova 2300 SEM (FEI, Hillsboro, OR). For the fluidized bed, a 20 x 20 mesh stainless steel disk in combination with a 1/8" perforated plate were used as the diffuser.

Results

The characterization of silicon beads is shown in Figure A-3. Part a) shows the size distribution of the silicon beads provided by Sun Edison. They display a mean diameter around

1.2 mm. SEM shows that the surface of the raw untreated beads is rough and porous, indicating that dust scavenging is one of the primary mechanisms for bead growth.

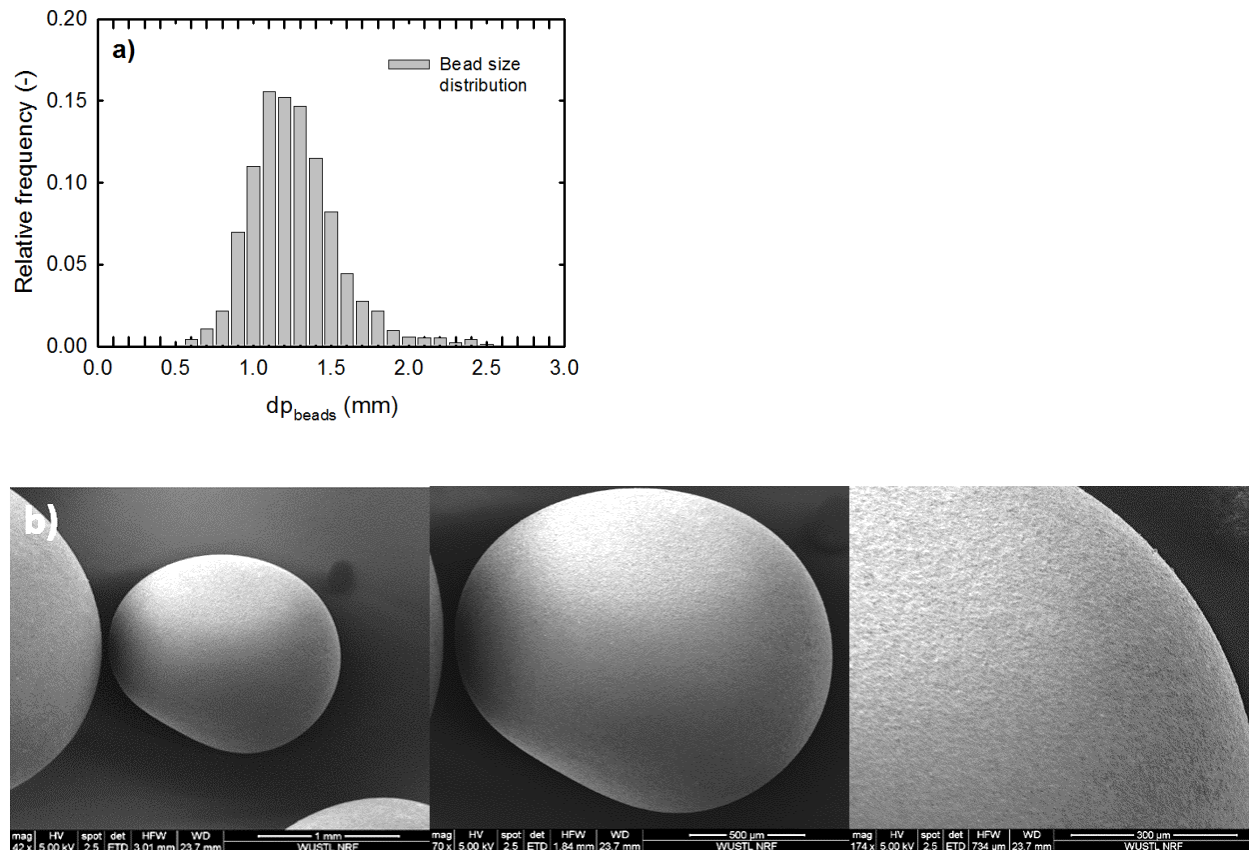
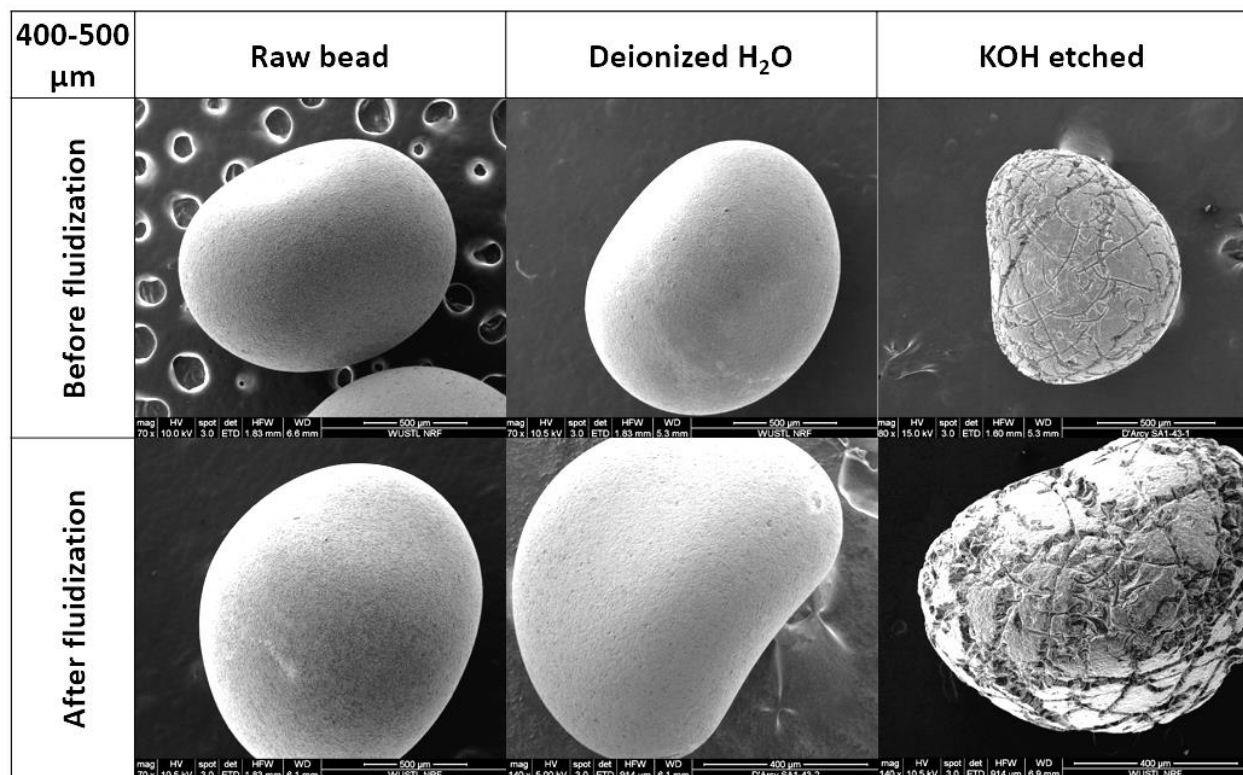


Figure A-3 a) The size distribution of the silicon beads b) A silicon bead at different levels of magnification under SEM, from 1 mm to 300 μm.



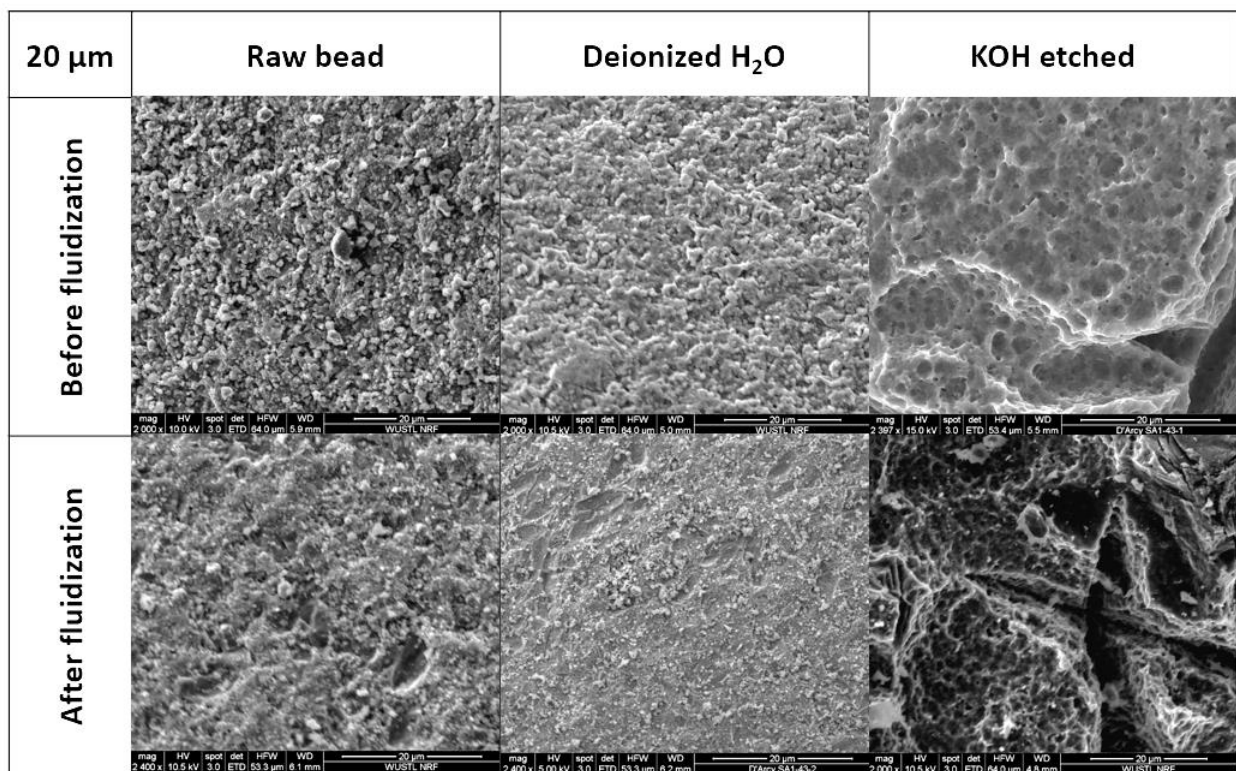


Figure A-4 SEM images of various cleaning procedures before and after fluidization. The beads etched with 20% mass KOH for 1 min show significant fissures in the surface. The remaining material is still subject to abrasion through fluidization.

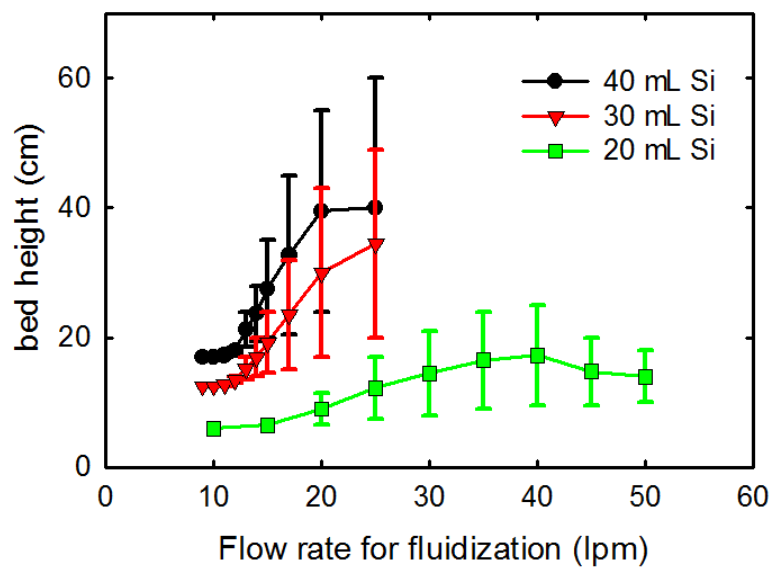


Figure A-5 Shows the bed expansion as a function of fluidization velocity. The error bars indicate the minimum and maximum height observed at the given flow rate conditions.

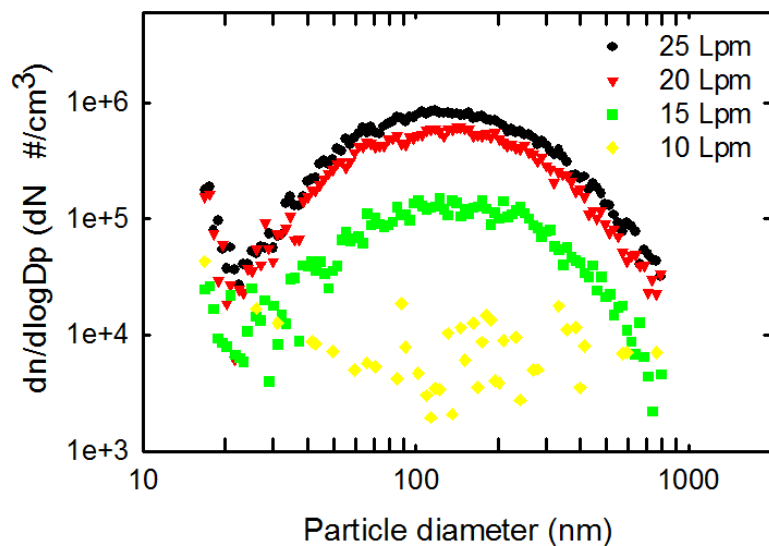


Figure A-6 Effect of different fluidization flow rates for a 30 mL bed of raw silicon beads

Discussion

Selection of the gas distributor

The gas distributor is a critical component in the fluidized bed²⁰⁹. While some distributors may be perfect in certain systems, the same distributors might perform poorly in other conditions. Based on the report of Rohatgi et al.⁷¹ at the Jet Propulsion Laboratory (JPL), using a combination of a 325 stainless steel mesh supported in a 1/20 in. thick plate with 1/8 in. circular perforations provided good performance in fluidization. By comparing it with other diffusers such as porous carbon and a multilayer screen, they found that all were satisfactory for good quality fluidization. More elaborate fluidization meshes that yield good hydrodynamics for some systems such as the punched plate²⁰⁹, can cause large aerosol losses. Similarly, fused brass beads would not only get clogged more rapidly, but would also cause large aerosol losses, directly interfering with aerosol capture by the fluidized bed, which is the objective of this research. Therefore we used the same

perforated plate as in the JPL report together with a mesh, in our case a 20 x 20 SS316, to limit aerosol losses.

Deionized water provide the most effective cleaning and was therefore used in this study. We found 20% KOH produced a quick reaction that significantly damaged the beads, producing a clear eroded pattern on their surface, as shown in Figure A-4.

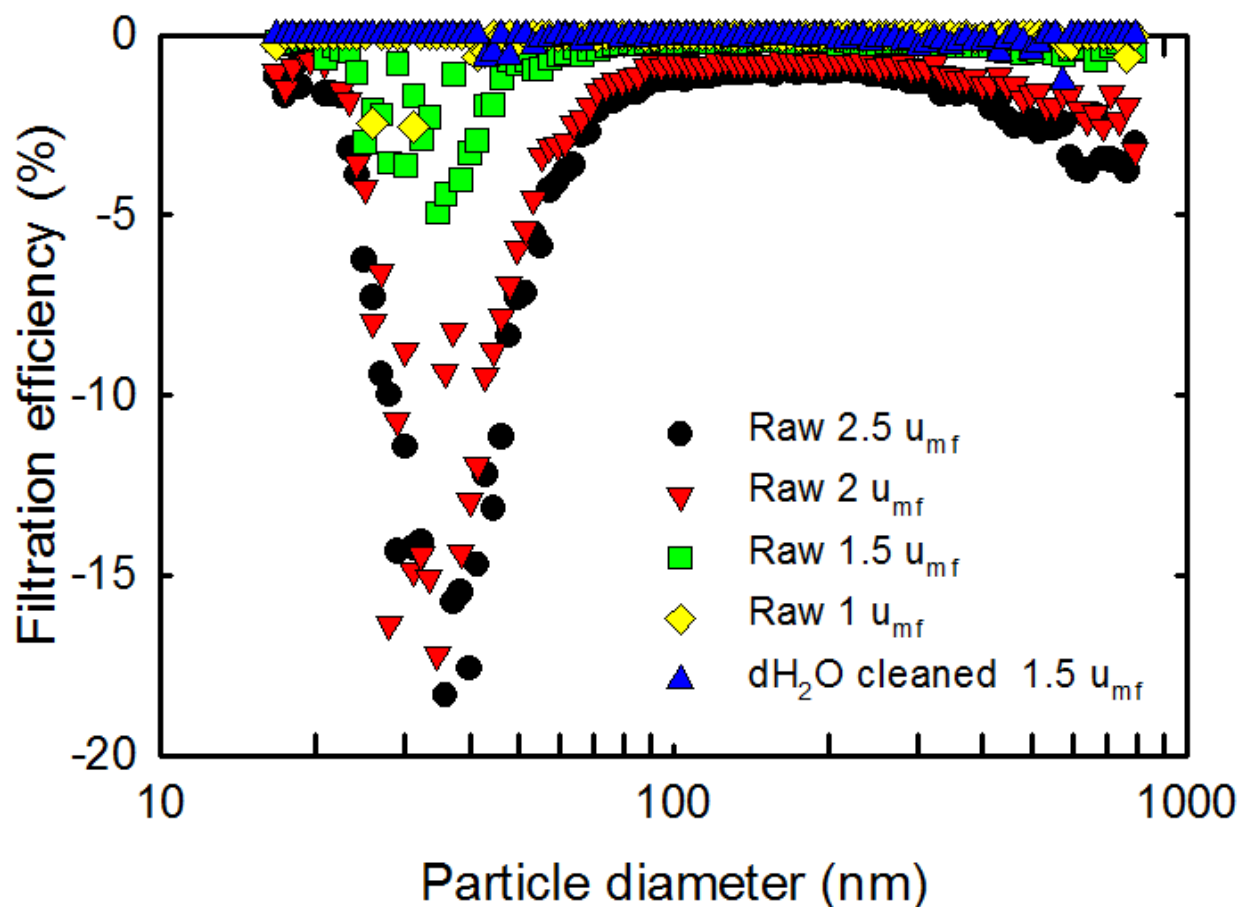


Figure A-7 Filtration efficiency (negative because it is produced by attrition) for various fluidization conditions without introducing aerosols in the inlet of the bed for raw (not-cleaned beads) and clean beads at 1.5 minimum fluidization velocity (u_{mf}). The cleaned beads had low attrition at the given conditions. The bed consisted on 30mL of silicon beads, with a bed height of 13 cm. The minimum fluidization velocity for the beads was 10 lpm. The experiment was carried out at room temperature.

Table A-1 Fluidized bed filtration efficiencies for various collection mechanisms, from Xiao et al.²⁰⁸

Mechanism	Efficiency	Dimensionless parameter
Interception	$E_R = \left(\frac{3}{\bar{\varepsilon}}\right) \bar{R}$	$\bar{R} = \frac{d_p}{d_c}$
Inertial impaction	$E_I = (1 + 0.04Re)[St + f(\bar{R})]$ *	$St = \frac{\rho_p u_f d_p^2 C_c}{9\mu d_c}$ **
Gravitational settling	$E_G = (Ga)(St)$	$Ga = \frac{d_c g}{2\mu_f^2}$
Diffusion	$E_D = \frac{4.52}{(\bar{\varepsilon}Pe)^{1/2}}$	$Pe = \frac{d_c u_f}{D_p}, D_p = \frac{k_b T}{3\pi\mu d_p} C_c$
Electrostatic attraction	$E_{EI} = 4K_c$	$K_c = \frac{C_c d_p Q_c Q_p}{3\varepsilon_f \mu \mu_f}$
<p>* $f(\bar{R}) = 0.48 \left(4 - \frac{4}{d_{tube}} \bar{R} - \frac{\bar{R}^2}{d_{tube}^2}\right)^{0.5} \left(\frac{\bar{R}^{1.041}}{d_{tube}}\right)$</p> <p>** $C_c = 1 + \frac{2\lambda}{d_p} \left[1.257 + 0.4 \exp\left(-0.55 \frac{d_p}{\lambda}\right)\right]$</p>		

Table A-1 shows the filtration efficiency from different mechanisms and the dimensionless parameters associated with them. According to Xiao et al.²⁰⁸ $\bar{\varepsilon}$ is the bed porosity, \bar{R} is the interception parameter, d_c is a parameter given by the bed material, d_p is a parameter for the particles to be removed, d_{tube} is the dimensionless diameter of the tube, Re is the Reynolds number, St is the Stokes number, Pe corresponds to the Péclet number and Ga to the Galileo number k_b is the Boltzmann constant, g is the gravitational acceleration, T is the absolute temperature ρ_p is the density of the particles, μ is the dynamic viscosity of the gas and λ is the mean free path of gas molecules, μ_f is the superficial gas velocity, Q_c is the electrical charge density on the bed material,

Q_p is the electrical charge density of the particles, K_c is a dimensionless electrical constant, ε_f is the dielectric constant of the fluid. E_R is the collection efficiency due to interception, E_I the filtration efficiency due to impaction, E_D the filtration efficiency due to diffusion, E_G the collection efficiency due to gravitational settling and finally E_{EI} the collection efficiency due to electrostatic attraction.

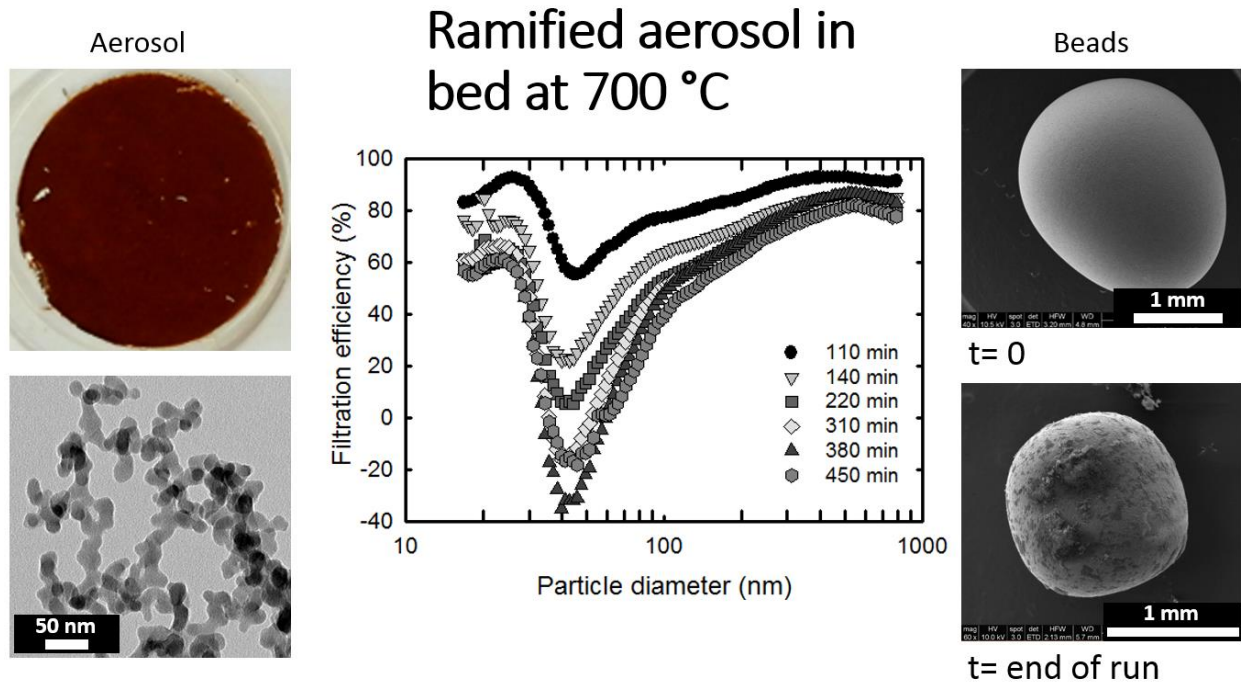


Figure A-8 Saturation of a fluidized bed at 700 °C with an aerosol synthesized at 700 °C from a 0.072% silane in He in a total flow of 2.5lpm. The flow was merged then with 7 lpm of nitrogen. Moving clockwise from the upper left, we see the aerosol collected in a filter, the filtration efficiency as a function of time, a clean bead in the initial condition, a saturated bead at the end of the run, and finally a TEM micrograph of the silicon introduced in the bottom of the fluidized bed.

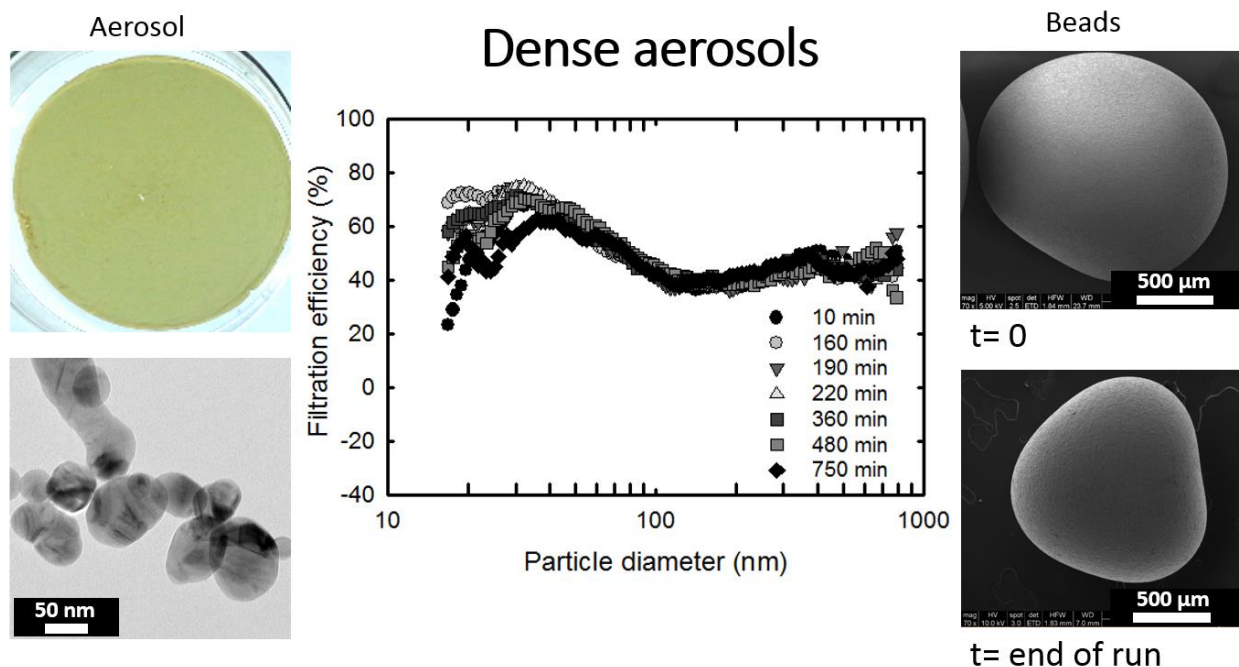


Figure A-9 Saturation of fluidized bed at room temperature for an aerosol synthesized at 1000 °C 0.072% silane in He in a total flow of 2.5lpm. The bed was fluidized using 13 lpm of nitrogen, which provides for a total flow equivalent to 1.5 the minimum fluidization velocity (μ_{mf}). As before we see the aerosol collected in a filter, the filtration efficiency as a function of time, a clean bead at the initial condition, a saturated bead at the end of the run, and finally a TEM micrograph of the silicon produced.

The aerosol synthesized at 700 °C displays a ramified structure that allows it to entangle more easily and build a surface layer more resistant to attrition. This resistance is the result of a higher filtration efficiency and saturation after a specific amount of aerosols has deposited into the surface of the beads. In the case of the 1000 °C aerosol, denser and less ramified than the 700 °C case, the initial filtration efficiency is much lower than the 700 °C counterpart. In addition, the saturation effect is negligible, in agreement with the SEM micrograph of the silicon bead after the run, where no saturation layer is observed.

The scavenging factor, first conceptually introduced by Hsu et al.¹⁶⁶, has been implemented in modeling work, where it is related to the scavenging rate by the following relationship^{185, 188}:

$$R_{sc} = k_{sc} C_{cluster} \quad (A-1)$$

where R_{sc} is the aerosol scavenging rate in g/s, k_{sc} is the rate constant for aerosol scavenging in m³/s, and $C_{cluster}$ is the concentration of aerosols in g/m³. The scavenging rate constant is given by

$$k_{sc} = \frac{R_{sc}}{C_{cluster}} = \frac{(C_{cluster})(\dot{Q})(\eta_{overall})}{(\dot{C}_{cluster})} = \eta_{overall} \dot{Q} \quad (A-2)$$

where the overall filtration efficiency is

$$\eta_{overall} = \frac{\sum_{i=1}^N \eta_i n(dp)_i M_i}{\sum_{i=1}^N n(dp)_i M_i} \quad (A-3)$$

the mass of the agglomerate is given by

$$M_i = k_{fm} \left(\frac{d_m}{d} \right)^{D_{fm}} \quad (A-4)$$

Here, k_{sc} is the scavenging rate constant given in m³/s, $C_{cluster}$ is the concentration of aerosols given in g/m³, η is the filtration efficiency in dimensionless units, \dot{Q} is the flow rate in m³/s, $n(dp)$ is the size distribution function given in #/cm³nm, M is the aggregate mass in g, k_{fm} is the aggregate mass-mobility prefactor in dimensionless units, D_{fm} is the aggregate mass-mobility exponent in dimensionless units, d_m is the aggregate mobility diameter in nm, and d is the monomer diameter in nm.

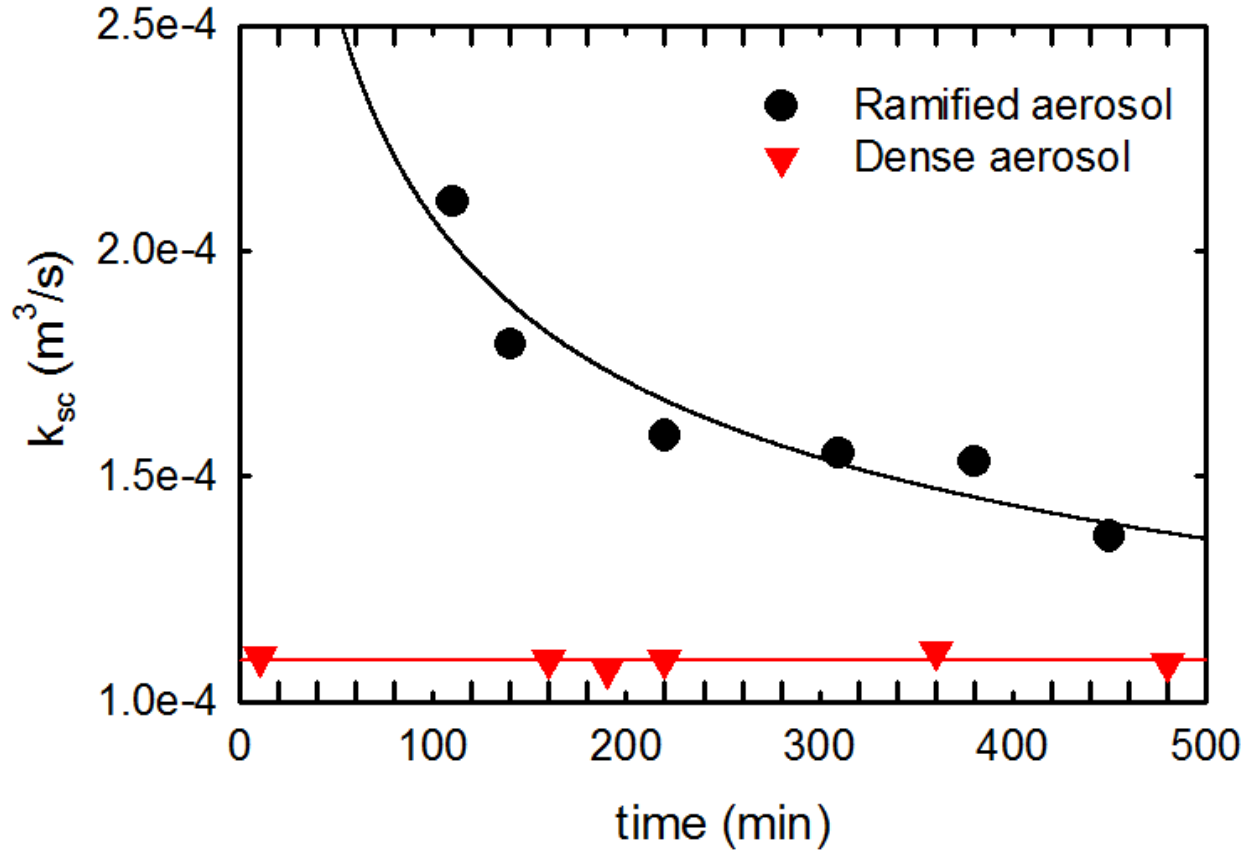


Figure A-10 The scavenging rate k_{sc} experimental results for a fluidized bed at 700 °C receiving aerosols synthesized at 700 °C based on SMPS data. k_{sc} is not constant because as the bed gets saturated with aerosols, the filtration efficiency decreases.

It is important to mention that the scavenging factor is reactor-specific and depends on the thickness of the fluidized bed. To normalize data and make it possible to compare experimental determinations, the filtration parameter penetration is introduced:

$$P_i = \frac{N_{out,i}}{N_{in,i}} = (1 - \eta_i) \quad (A-5)$$

$$P_i = e^{-\gamma_i \theta} \quad (A-6)$$

where P is penetration, η is efficiency, N_{out} is the number concentration leaving the bed, N_{in} is the number concentration entering the bed, θ is the thickness of the filtering media, and γ is the

fractional capture per unit thickness for a differentially thin layer $d\theta$. The subindex i indicates that the parameter is for a given particle size within a polydisperse aerosol. Equation 5 can be used only for monodisperse aerosols or for a particular size of a polydisperse size distribution, but it does not hold for the overall penetration of a polydisperse aerosol.¹⁷⁷ The values for γ are plotted in Figure A-11 as a function of particle diameter (d_p) for initial fresh beads and also for saturated beads at the end of the run. For comparability with other reactors, the mass ratios of aerosol to beads are shown.

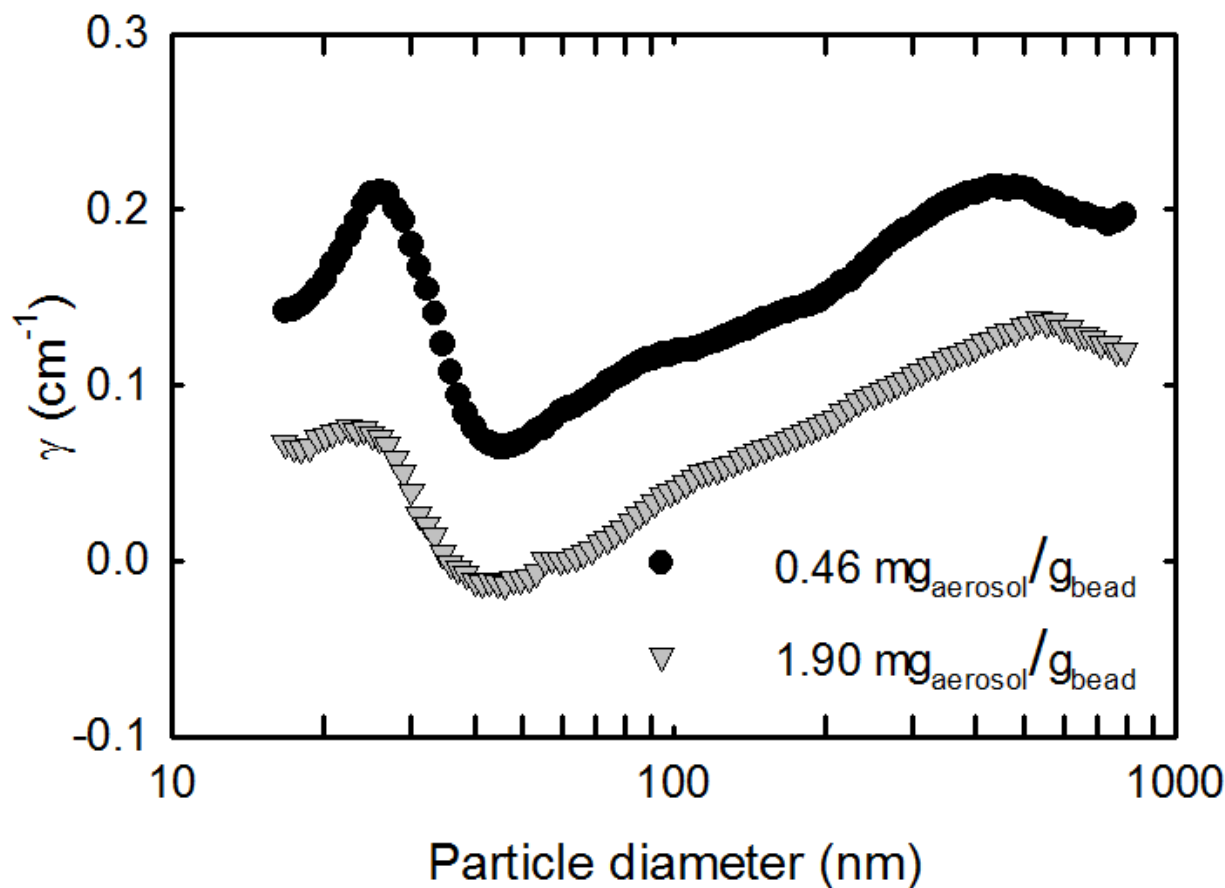


Figure A-11 Gamma as a function of total silicon aerosol mass feed to the fluidized bed per unit of mass for beads. As the beads get saturated, their gamma decreases, indicating a lower capacity to filter/retain aerosols per unit of filtering media or silicon beads

Based on the observations, the filtration efficiency drops continuously as a function of saturation and time. This drop implies that there must be a sticking zone at the base of the reactor where the beads saturated with aerosols are regenerated and the aerosols become incorporated into the beads in a more solid manner. This process is schematically shown in Figure A-12.

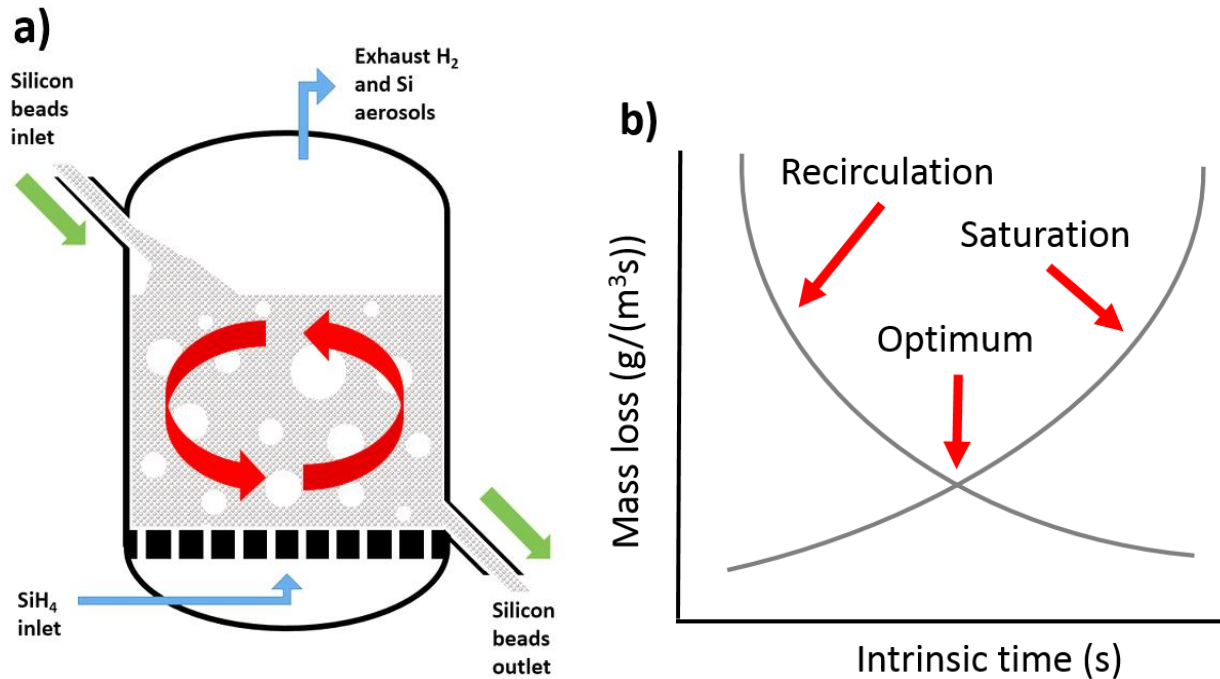


Figure A-12 a) Sketch of the natural recirculation that occurs inside the FBR. Recirculation is a function of fluidization gas velocity, which also impacts the elutriation of fines and bead attrition. For that reason a compromise between both effects should be found and the reactor should be operated at such a condition, as sketched in b)

Conclusion

The fluidization velocity runs done in the current work provided evidence that lower fluidization velocities promote lower elutriation of particles entrained on the bed and also cause less abrasion of the bead surface. But this comes at the cost of less mixing in the bed. Higher

fluidization velocities provide more thorough mixing, but at the cost of more particulate release. Nozzles can improve mixing in the lower regions without increasing the overall reactor gas fluidization velocity used, and they are suggested for industrial reactors. The saturation of the beads and their filtration efficiency, are both functions of fluidization velocity, aerosol size, bed height, and bed temperature.

A new and different approach to understand silicon fluidized bed reactors is proposed, in which the reactor operation is analogous to a filtration process. The focus is shifted from seeing aerosols as something to avoid, towards trying to maximize their capture and retention in the beads through filtration principles.

B: Silane pyrolysis literature review

Silane properties

Yaws et al. published a feasibility study up to 1981 including properties and of silane in a 450 page NASA report.²¹⁰ Adamczyk et al.²¹¹ estimated the thermochemical properties of H-Si clusters.

Silane pyrolysis mechanism:

Jasinski et al.⁴¹ studied chemical vapor deposition of silicon hydrides. White et al.⁴² studied the effect of hydrogen on silane pyrolysis. Ring et al.⁴³ reviewed the mechanism of thermal decomposition of silane. Hashimoto et al.⁴⁴ studied the growth kinetics of polycrystalline silicon from silane by CVD. Purnell et al.⁴⁵ study reaction kinetics for silane pyrolysis. Filtvedt et al.⁴⁶ reported basic concepts on CVD growth. Kleijin et al.⁴⁷ report 5 intermediate species for silane pyrolysis. Girschick et al.⁴⁸ report 400 reactions for silane pyrolysis. Ho et al.⁴⁹ propose silicon atoms in the gas phase as intermediates for condensation. Claasen et al.⁵⁰ work on CVD in cold wall. Friedlander et al.⁵¹ report that CVD is not a well understood phenomena. Newman et al.¹⁷¹ studied kinetics of silane pyrolysis in a shock tube. Giunta et al.⁵⁶ model the concentration for different silane polymers in the gas phase. Martin et al.¹⁸⁷ Used GC for separating polysilanes. Körner et al.^{178, 212} mention that the rate limiting reaction for silane is silylane formation (Si_2H_2) disilane, trisilane and analyzing reaction kinetics. Diaz et al.²¹³ employed XRD in situ for determining crystallinity on the outlet of the reactor. Swihart et al.^{167, 214} study the vibrational frequencies, energies and structures of silanes as well as chlorinated silanes. Sprung et al.²¹⁵ used a hot wire filament to study Si-H reactivity, elemental analysis of reaction and nanopowder formed by laser granulometry. Adamczyk et al.²¹⁶ calculated SiH_4 pyrolysis kinetics using statistical

thermodynamics, TST and quantum calculations. Holm et al.²¹⁷ study how different radiofrequency parameters change nanoparticle surface Si-H ratio composition. Moffat et al.²¹⁸ used nonlinear regression analysis for estimating Arrhenius parameters for SiH₄ to SiH₂. Matsumoto et al.²¹⁹ Propose a novel transition state model for disilane thermal decomposition.

Filtvedt, Holt Ramachandran and Melaaen.⁴⁰ report that silane kinetics are complex, are not well understood and are still under debate. Jasinski et al.^{41, 220} mention that more work is needed to understand Si CVD, particularly nucleation, surface structure, defects, adsorption and formation of particles.

Studies of aerosol formation

Slootman et al.³ defined the critical silane concentration at which silane particles start to form. Eversteijn et al.^{168a} report critical silane concentration an APCVD. Nijhawan et al.⁵³ did some experiments on particle nucleation and growth. Van Den Brekel et al.⁵⁴ found critical silane concentration for Si₂H₂. Wiggers et al.⁵⁵ studied Si aerosol formation for silane in Ar. Giunta et al.⁵⁶ did the same in nitrogen. Odden et al.⁵⁷ studied the effect of pressure on aerosol formation and found little effect. Yuuki et al.²²¹ propose a mechanism from silane to aerosol nuclei based on polymers with 5 atoms. Kremer et al.²²² propose a mechanism based on a series of dehydrogenation steps for aerosol formation. Whitby et al.²²³ use a similar approach of aerosol population balance. Veprek et al.²²⁴ studied fine formation mechanisms based on silicon hydrides and complex cyclic structure in a plasma reactor. Groschel et al.²²⁵ study control mechanisms for narrow size distribution of si nanoparticles. Onischuk et al.^{150, 153} observed the phenomena of aerosol formation in a quartz flow reactor. Swihart et al.^{147b} present a thorough chemical kinetic

mechanism for silicon hydride cluster formation. Wong et al.¹⁴⁸ studied Nanoparticle formation chemistry via automated reaction mechanisms including linear energy relationships and group additivity approach. Li et al.²²⁶ performed kinetic montecarlo simulations to predict homogeneous nucleation of hydrogenated silicon particles. Bhandarkar et al.²²⁷ did some modeling on silicon hydride clustering in low pressure silane plasma. Girschick et al.⁴⁸ executed numerical modeling of gas phase nucleation for Si CVD up to 10 Si atoms. Hulser et al.²²⁸ proposed a pilot plant for Si nanoparticle synthesis for solar applications based on their results

Modeling of size distribution:

The authors that report aerosol parameters such as nucleation and condensation are:

Tulukdar and Swihart^{147a} compare 3 modeling methods using cyclic clusters kinetics and couple them with aerosol dynamic models to obtain values for nucleation condensation and then try to predict nanoparticle evolution but not always being accurate. Schmid et al.²²⁹ developed some models to understand simultaneous coagulation and sintering but report coupling it with CVD is complex and mention interest to attempt including condensation in a future model. Dang et al.²³⁰ proposed a computational model of silicon nanoparticle synthesis. For nucleation they employ the kinetics of silane derivatives that are bigger than certain threshold proposed by Swihart and Girshick (1999)¹⁶⁷ and for condensation they consider the formation of silicon atoms. Kommu et al.²³¹ use the same approach for their GDE-CVD model.

Studied nucleation (mathematically):

Some laboratory heads have worked substantially on nucleation processes, such as Richard Flagan, who studied nucleation and coagulation in the continuum and free molecular regime for water.²³² the effect of aerosols in the rate of homogeneous nucleation (HN) for dibutyl phthalate.²³³ He also studies the theory of aerosols formation and growth in laminar flow using classical and Lothe Pound theories of HN.²³⁴ He compares several classical nucleation vs phenomenological models for cloud formation.²³⁵ He describes the explosive tendency of how in the transition region only 17% change of reactant concentration changes 4 orders of magnitude the aerosol number concentration.²³⁶ He and another 30 authors studied the effect of charge on nucleation.²³⁷ he does also sulfuric acid nucleation.²³⁸ nucleation in clouds.²³⁹ He proposed a levitation system based on an electric field to study nucleation.²⁴⁰ , studied nucleation of marine aerosols based on a iodine proposed reaction pathway.²⁴¹ cloud nucleation on ship tracks.²⁴² nucleation of mercury particles.²⁴³ calculate nucleation rates based on thermodynamic properties for 4 different gases.²⁴⁴ They also studied nucleation of dibutylphthalate (DBP) and compare it with classical nucleation theory which matched after applying a multiplicative factor.²⁴⁵ They have also studied homogeneous nucleation of dibutylphthalate on aerosols containing foreign seed aerosols ZnCl_2 .²⁴⁶ They also study the effect of spatial inhomogeneities in the gas phase for homogeneous nucleation and find these effects as minor for total number concentration.²⁴⁷ Sitarski studied nucleation of phthalate droplets with Monte Carlo simulations²⁴⁸. Seinfeld et al. analytically solved the Zeldovich-Frenkel-Becker-Döring equation for homogeneous nucleation²⁴⁹. McCoy et al. studied classical vs experimental nucleation and described the large temperature discrepancy among them.²⁵⁰ Higuchi et al. study the Becker-Doering nucleation theory using DBP.²⁵¹ Stauffer et al. discuss the Fisher theory for nucleation vs classical theory.²⁵²

Studied condensation:

Flagan et al. present the discrete sectional solution for the aerosol dynamic equation and employ saturation as the precept for calculating condensation.²⁵³ Marek et al.²⁴⁸ use Monte Carlo simulations for calculation condensation of dioctyl phthalate droplets in nitrogen. Watanabe et al.²⁵⁴ studied growth process by condensation of silane in plasmas at high frequency (3.5-28MHz). Seon Kim et al.²⁵⁵ and DJ Kim et al.²⁵⁶ study modeling of particle growth coagulation in silane plasmas. Pratsinis et al.^{176, 257} and Warren et al.^{246, 258} studied simultaneous condensation, nucleation and coagulation in models

Most of silicon condensation studies have been focused on epitaxial growth. Henderson et al.²⁵⁹ studied coagulation in silicon homoepitaxial films at low pressures (0.15 torr) using auger electron microscopy. Farrow et al.²⁶⁰ studied condensation in a 111 surface at low pressures (0.4 torr)

Particle capture by beads

Hsu et al.¹⁶⁶ 3 years after their first paper improved their model by implementing a scavenging model using Levenspiel⁸⁵ 1979. Tardos et al.²⁶¹ calculate filtration efficiencies. Gutfinger et al.²⁶² use inertia diffusion and interception for their filtration efficiency calculation. Peters et al.^{205a} report their results by using more complicated FBR mechanics. Furusawa et al.²⁶³ did some calculations approximating the FBR from Hsu et al. as a fixed bed and improved the original predictions from Hsu et al.¹

Fluidized bed reactors

According to Perez, Sanchez and Kinkel et al. This is challenging because it combines both CVD and FBRs.⁵⁸ Lai, Dudukovic and Ramachandran⁶⁶ used the Kato and Wen⁶⁷ models and a kinetic law from Hogness et al.⁶⁸ and Iya et al.⁶⁹ The main approach of using fluidized bed reactors is by employing fluid dynamics. Reuge et al.⁶⁰ use a multifluid Eulerian model Filtvedt et al.²⁰ Review different FBRs that can be used for SiCVD. Zbib et al.⁶¹ characterized Si granules from FBRs. Dahl et al.⁶² studied porosity of polycrystalline Si from FBRs., Caussat et al. studied FBRs experimentally⁶³ and they also employed computational fluid dynamics for modelling.⁶⁴ Geldart² provides an empirical classification for beads for fluidization. Pina et al.⁷⁰ report that the main challenges of implementing CVD FBRs is that a pilot plant is needed and that is expensive. Hsu et al.¹ studied experimentally an FBR and they used kinetic modeling for nucleation and got unsatisfactory predictions. Tejero-Ezpeleta et al.²⁶⁴ did some experimental work on silane FBR reporting 25 μ m/hr using 1-10% silane. Rohatgi et al.^{71, 265} Show a feasibility report for JPL using FBRs Li et al.²¹ report technical challenges and progress in FBRs. Song et al.²⁶⁶ propose microwaves in FBRs. Flitvedt et al.²⁶⁷ also show developments in fluidization bed technology. Lord et al.²⁶⁸ propose pulsing silane to optimize mixing. Hwang et al.²⁶⁹ suggest to etch at the same time of deposition to improve FBR. Kim et al.²⁷⁰ report that SunEdison reactor designs consist mainly on standard bubbling FBR's. Rohatgi et al.²⁶⁵ have observed good fluidization conditions and no agglomeration in their FBRs. Kojima et al.²⁷¹ have found aerosol generation from 1 to 25% depending on the operation. Ritter et al.²⁷² recommend using THERM software for estimating properties in the gas phase radical molecules. Si et al.¹⁸⁸ used an Eulerian-Eulerian model CFD model coupled with a PBM using the same homogeneous and heterogeneous kinetic parameters as Lai and Dudukovic on their 1986 paper.

Different reactors:

Flagan et al. studied formation of 10 μ m particles in a 2 stage reactor.¹⁷⁰ they also propose a turbulent mixing aerosol reactor for oxide coated silicon nanoparticles.²⁷³ Flagan also reports using two stage reactors one for silicon seed growth and the second for chemical vapor deposition as they argue coagulation can become an issue to study CVD.¹⁵⁵ Belmonte et al. used a microwave plasma for studying SiO₂ deposition.²⁷⁴ Frencklach et al.^{168b} used a shock tube and found 15% hydrogen in synthesized Si. Morrison et al.¹⁶⁹ and Donovan et al.²⁷⁵ studied silane pyrolysis conversion in a piston reactor. Pozdnyakov et al.¹⁵⁶ employed an adiabatic reactor for silane pyrolysis. Knipping et al.²⁷⁶ studied silane pyrolysis in a microwave reactor. Rao et al.²⁷⁷ used a plasma expansion reactor. Siegmann et al.²⁷⁸ and Watanabe et al.^{254, 279} propose plasma reactors for Si pyrolysis.

Other uses for a silane pyrolysis reactor

Körner et al.¹⁷⁸ synthesized silicon nanoparticles with narrow size distribution for optical or electrical applications using a hot wall reactor. Flagan et al. synthesized Si aerosols with narrow size distribution for luminescence applications.²⁸⁰ More recently he has focused silane nanoparticle formation to applications such as aerosol nanocrystal floating gate devices.^{131, 281} Ultrapure silicon particles for novel memory devices.²⁸² Silicon quantum dots for solid state devices.²⁸³ Erogbogbo et al.²⁸⁴ propose using silicon nanoparticles for water splitting applications. Okamoto . Although they propose to form silicon nanotubes, single layer sheets and ribbons using vapor liquid solid deposition, an aerosol route could be possible.²⁸⁵ Kummer et al.²⁸⁶ use Si

nanoparticles as anode materials for Lithium anode batteries. Petermann et al.²⁸⁷ used a plasma synthesis method for Si nanoparticles with improved thermoelectric properties. Goller et al.²⁸⁸ discuss how different Si nanoparticles are capable of emitting tunable light. Cabarrocas et al.²⁸⁹ and Mangolini et al.^{133a} propose Si nanoparticles for nanoelectronic components.

C: Appendix silane setup diagram

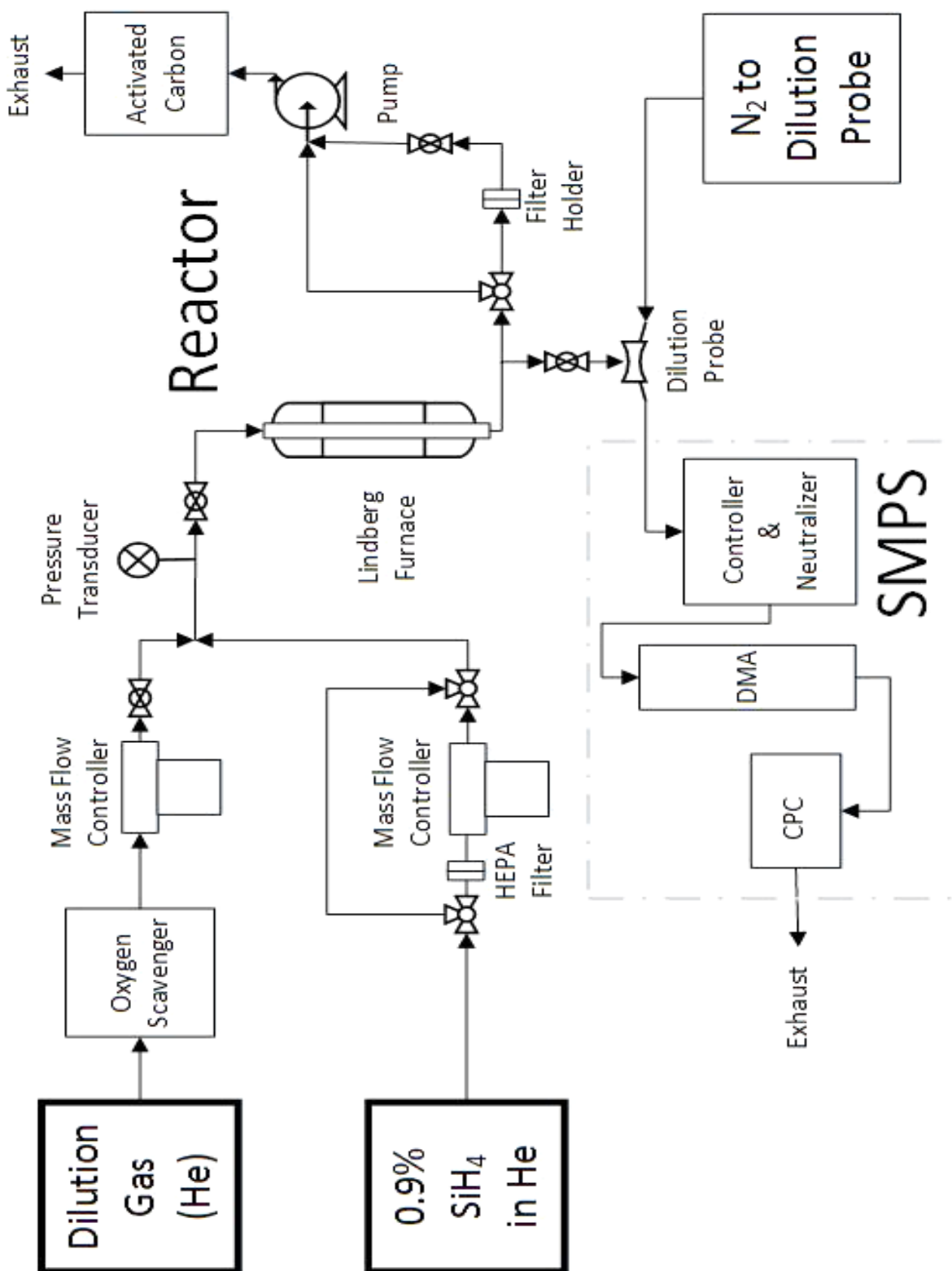


Figure C-1. Silane setup and reactor diagram

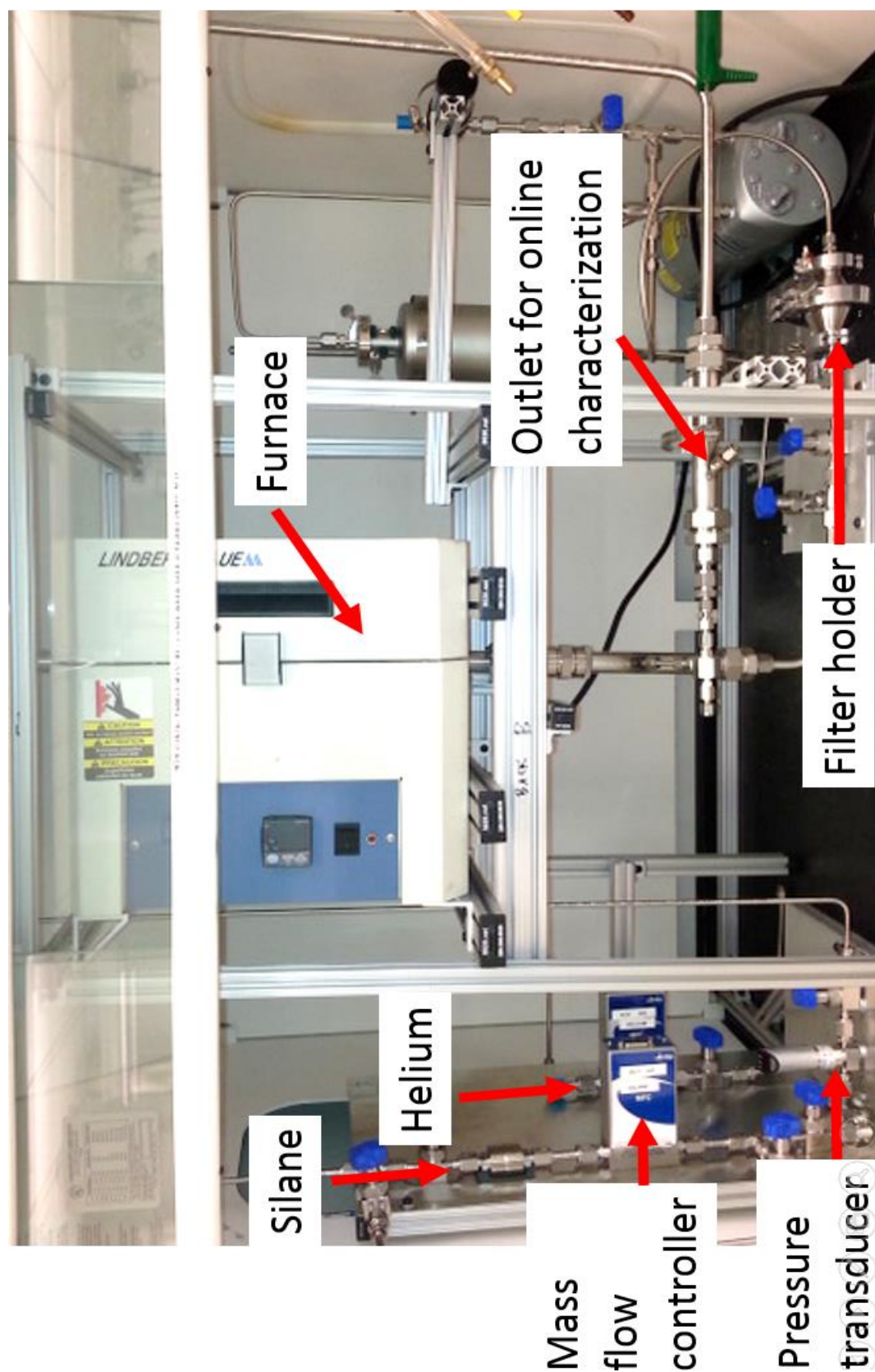


Figure C-2. Picture of silane setup and reactor

D: References

1. Hsu, G.; Hogle, R.; Rohatgi, N.; Morrison, A., Fines in fluidized bed silane pyrolysis. *J. Electrochem. Soc.* **1984**, *131* (3), 660-663.
2. Geldart, D., Types of gas fluidization. *Powder Technol.* **1973**, *7* (5), 285-292.
3. Sloodman, F.; Parent, J.-C., Homogeneous gas-phase nucleation in silane pyrolysis. *J. Aerosol Sci* **1994**, *25* (1), 15-21.
4. Ranjan, S.; Balaji, S.; Panella, R. A.; Ydstie, B. E., Silicon solar cell production. *Comput. Chem. Eng.* **2011**, *35* (8), 1439-1453.
5. Bruno Burger, K. K., Christoph Kost, Sebastian Nold, Simon Philipps, Ralf Preu, Roland Schindler, Thomas Schlegl, Gerhard Stryi, Gerhald Willeke, Harry Wirth, Ingo Brucker, Andreas Häberle, Volker Schacht, Werner Warmuth *Photovoltaics Report*; Fraunhofer ISE: 79119 Freiburg, Germany, 20 October 2014, 2014; p 4.
6. (a) Sarti, D.; Einhaus, R., Silicon feedstock for the multi-crystalline photovoltaic industry. *Sol. Energy Mater. Sol. Cells* **2002**, *72* (1), 27-40; (b) Green, M. A., *Solar cells. Operating principles, technology, and systems applications*. 1982; p xiv+274 pp-xiv+274 pp.
7. Van Sark, W. G. J. H. M.; Brandsen, G. W.; Fleuster, M.; Hekkert, M. P., Analysis of the silicon market: Will thin films profit? *Energy Policy* **2007**, *35* (6), 3121-3125.
8. Hahn, G.; Schonecker, A., New crystalline silicon ribbon materials for photovoltaics. *Journal of Physics-Condensed Matter* **2004**, *16* (50), R1615-R1648.
9. De Gramont, A., The most sensitive rays of the metalloids, tellurium, phosphorus, arsenic, antimony, carbon, silicon and bonn. *Comptes Rendus Hebdomadaires des Seances de l'Academie des Sciences* **1908**, *146*, 1260-1263.
10. Lombi, E.; Holm, P. E., Metalloids, Soil Chemistry and the Environment. In *Mips and Their Role in the Exchange of Metalloids*, Jahn, T. P.; Bienert, G. P., Eds. **2010**; Vol. 679, pp 33-44.
11. Lodders, K.; Fegley Jr, B., An Oxygen Isotope Model for the Composition of Mars. *Icar* **1997**, *126* (2), 373-394.
12. Guillet, L., Constitution and properties of silicon steels. *Comptes Rendus Hebdomadaires des Seances de l'Academie des Sciences* **1903**, *137*, 1052-1054.
13. Fracnel, W., Silicon-aluminium alloys. *Zeitschrift fur Anorganische Chemie* **1908**, *58* (2), 154-158.
14. Kline, G. M., Advances in plastics during 1943. *Modern Plastics* **1944**, 123-126, 178.
15. (a) Katz, R. N., Recent developments in high performance ceramics. *AIP Conference Proceedings* **1976**, (32), 236-52; (b) Weaver, G. Q.; Olson, B. A., High strength silicon carbide for use in severe environments. *International Conference on Silicon Carbide (abstracts only received)* **1973**, 1 pp.-1 pp.
16. Anon *Silicon and Ferrosilicon: Global Industry Markets and Outlook, 13th edition*; 978 0 86214 573 6; Roskill: London, **2011**.
17. Castells, M., *The rise of the network society: The information age: Economy, society, and culture*. John Wiley & Sons: **2011**; Vol. 1.
18. Glendinning, W. B., Silicon integrated circuits. *Institute of Radio Engineers Transactions on Military Electronics* **1960**, *MIL-4* (4), 459-468.
19. Rothwarf, A.; Böer, K. W., Direct conversion of solar energy through photovoltaic cells. *Prog. Solid State Chem.* **1975**, *10*, Part 2 (0), 71-102.

20. Filtvedt, W.; Javidi, M.; Holt, A.; Melaaen, M.; Marstein, E.; Tathgar, H.; Ramachandran, P., Development of fluidized bed reactors for silicon production. *Sol. Energy Mater. Sol. Cells* **2010**, *94* (12), 1980-1995.
21. Li, J.; Chen, G.; Zhang, P.; Wang, W.; Duan, J., Technical challenges and progress in fluidized bed chemical vapor deposition of polysilicon. *Chin. J. Chem. Eng.* **2011**, *19* (5), 747-753.
22. Green, M. A., Photovoltaics: technology overview. *Energy Policy* **2000**, *28* (14), 989-998.
23. (a) Castellano, R., *Solar Panel Processing*. Archives contemporaines: 2010; (b) Van Zant, P., *Microchip fabrication*. McGraw-Hill, Inc.: 2004.
24. Johnston, M. D.; Khajavi, L. T.; Li, M.; Sokhanvaran, S.; Barati, M., High-Temperature Refining of Metallurgical-Grade Silicon: A Review. *JOM* **2012**, *64* (8), 935-945.
25. Wang, T. Y.; Lin, Y. C.; Tai, C. Y.; Sivakumar, R.; Rai, D. K.; Lan, C. W., A novel approach for recycling of kerf loss silicon from cutting slurry waste for solar cell applications. *J. Cryst. Growth* **2008**, *310* (15), 3403-3406.
26. Green, M. A.; Ho-Baillie, A.; Snaith, H. J., The emergence of perovskite solar cells. *Nature Photonics* **2014**, *8* (7), 506-514.
27. Fulop, G.; Doty, M.; Meyers, P.; Betz, J.; Liu, C., High-efficiency electrodeposited cadmium telluride solar cells. *Appl. Phys. Lett.* **1982**, *40* (4), 327-328.
28. Kazmerski, L. L., Photovoltaics: a review of cell and module technologies. *Renewable and sustainable energy reviews* **1997**, *1* (1), 71-170.
29. Hahn, G.; Seren, S.; Kaes, M.; Schonecker, A.; Kalejs, J. P.; Dube, C.; Grenko, A.; Belouet, C., Review on ribbon silicon techniques for cost reduction in PV. *Photovoltaic Energy Convers., Conf. Rec. IEEE 4th World Conf.* **2006**, *1*, 972-975.
30. Green, M. A., Crystalline and thin-film silicon solar cells: state of the art and future potential. *Sol. Energy* **2003**, *74* (3), 181-192.
31. Sarti, D.; Einhaus, R., Silicon feedstock for the multi-crystalline photovoltaic industry. *Sol. Energy Mater. Sol. Cells* **2002**, *72* (1-4), 27-40.
32. Hao, W.; Melkote, S. N.; Danyluk, S., Mechanical strength of silicon wafers cut by loose abrasive slurry and fixed abrasive diamond wire sawing. *Adv. Eng. Mater.* **2012**, *14* (5), 342-8.
33. Drouiche, N.; Cuellar, P.; Kerkar, F.; Medjahed, S.; Boutouchent-Guerfi, N.; Hamou, M. O., Recovery of solar grade silicon from kerf loss slurry waste. *Renewable Sustainable Energy Rev.* **2014**, *32*, 936-943.
34. (a) Wang, T. Y.; Lin, Y. C.; Tai, C. Y.; Fei, C. C.; Tseng, M. Y.; Lan, C. W., Recovery of silicon from kerf loss slurry waste for photovoltaic applications. *Prog. Photovoltaics* **2009**, *17* (3), 155-163; (b) Tsai, T. H.; Shih, Y. P.; Wu, Y. F., Recycling silicon wire-saw slurries: Separation of silicon and silicon carbide in a ramp settling tank under an applied electrical field. *J. Air Waste Manag. Assoc.* **2013**, *63* (5), 521-527; (c) Park, K. Y.; Park, H. K.; Ko, B. W.; Kang, T. W.; Jang, H. D., Recycling of SiC-Si sludge to silicon tetrachloride and porous carbon via chlorination. *Ind. Eng. Chem. Res.* **2013**, *52* (10), 3943-3946.
35. Chao, C. L.; Ma, K. J.; Liu, D. S.; Bai, C. Y.; Shy, T. L., Ductile behaviour in single-point diamond-turning of single-crystal silicon. *J. Mater. Process. Technol.* **2002**, *127* (2), 187-190.
36. A. Bidiville, K. W., R. Kraft, C. Ballif, Diamond wire-sawn silicon wafers – from the lab to the cell production. *24th Eur. Photovoltaic Sol. Energy Conf. Exhib.* **2009**, 1400-1405.
37. Maeda, M.; Imamura, K.; Matsumoto, T.; Kobayashi, H., Fabrication of Si nanoparticles from Si swarf and application to solar cells. *Appl. Surf. Sci.* **2014**, *312*, 39-42.
38. Tomono, K.; Miyamoto, S.; Ogawa, T.; Furuya, H.; Okamura, Y.; Yoshimoto, M.; Komatsu, R.; Nakayama, M., Recycling of kerf loss silicon derived from diamond-wire saw cutting process by chemical approach. *Sep. Purif. Technol.* **2013**, *120*, 304-309.
39. Dhamrin, M.; Saitoh, T.; Kamisako, K., Recycling of silicon powder retrieved from diamond wire slicing kerf. *25th Eur. Photovoltaic Sol. Energy Conf. Exhib.* **2010**, 1600-1603.

40. Filtvedt, W. O.; Holt, A.; Ramachandran, P. A.; Melaaen, M. C., Chemical vapor deposition of silicon from silane: Review of growth mechanisms and modeling/scaleup of fluidized bed reactors. *Sol. Energy Mater. Sol. Cells* **2012**, *107*, 188-200.
41. Jasinski, J. M.; Gates, S. M., Silicon chemical vapor deposition one step at a time: fundamental studies of silicon hydride chemistry. *Acc. Chem. Res.* **1991**, *24* (1), 9-15.
42. White, R.; Espino-Rios, R.; Rogers, D.; Ring, M.; O'neal, H., Mechanism of the silane decomposition. I. Silane loss kinetics and rate inhibition by hydrogen. II. Modeling of the silane decomposition (all stages of reaction). *Int. J. Chem. Kinet.* **1985**, *17* (10), 1029-1065.
43. Ring, M. A.; O'Neal, H. E., Mechanism of the thermally induced gas-phase decomposition of silane: a revisitation. *The Journal of Physical Chemistry* **1992**, *96* (26), 10848-10855.
44. Hashimoto, K.; Miura, K.; Masuda, T.; Toma, M.; Sawai, H.; Kawase, M., Growth kinetics of polycrystalline silicon from silane by thermal chemical vapor deposition method. *J. Electrochem. Soc.* **1990**, *137* (3), 1000-1007.
45. Purnell, J.-H.; Walsh, R., The pyrolysis of monosilane. *Proceedings of the Royal Society of London. Series A. Mathematical and Physical Sciences* **1966**, *293* (1435), 543-561.
46. Filtvedt, W. O.; Holt, A., *Silane based CVD growth, governing mechanisms, material and concepts*. 2012; p 1039-41.
47. Kremer, D. M.; Davis, R. W.; Moore, E. F.; Ehrman, S. H., A numerical investigation of the effects of gas-phase particle formation on silicon film deposition from silane. *J. Cryst. Growth* **2003**, *247* (3-4), 333-356.
48. Girshick, S. L.; Swihart, M. T.; Suh, S. M.; Mahajan, M. R.; Nijhawan, S., Numerical modeling of gas-phase nucleation and particle growth during chemical vapor deposition of silicon. *J. Electrochem. Soc.* **2000**, *147* (6), 2303-2311.
49. Ho, P.; Coltrin, M. E.; Breiland, W. G., Laser-induced fluorescence measurements and kinetic analysis of Si atom formation in a rotating disk chemical vapor deposition reactor. *The Journal of Physical Chemistry* **1994**, *98* (40), 10138-10147.
50. Claassen, W., The growth of silicon from silane in cold wall CVD systems. *Philips Journal of Research* **1981**, *36* (2), 122-137.
51. Friedlander, S. K., *Smoke, dust, and haze*. Oxford University Press New York: 2000; Vol. 198.
52. Qian, Z. M.; Michiel, H.; Vanammel, A.; Nijs, J.; Mertens, R., Homogeneous Gas-Phase Nucleation of Silane in Low-Pressure Chemical Vapor Deposition (LPCVD). *J. Electrochem. Soc.* **1988**, *135* (9), 2378-2379.
53. Nijhawan, S.; McMurry, P. H.; Swihart, M. T.; Suh, S. M.; Girshick, S. L.; Campbell, S. A.; Brockmann, J. E., An experimental and numerical study of particle nucleation and growth during low-pressure thermal decomposition of silane. *J. Aerosol Sci* **2003**, *34* (6), 691-711.
54. Van Den Brekel, C.; Bollen, L., Low pressure deposition of polycrystalline silicon from silane. *J. Cryst. Growth* **1981**, *54* (2), 310-322.
55. Wiggers, H.; Starke, R.; Roth, P., Silicon particle formation by pyrolysis of silane in a hot wall gasphase reactor. *Chemical engineering & technology* **2001**, *24* (3), 261-264.
56. Giunta, C. J.; McCurdy, R. J.; Chapplesokol, J. D.; Gordon, R. G., Gas-Phase Kinetics in the Atmospheric Pressure Chemical Vapor Deposition of Silicon from Silane and Disilane. *J. Appl. Phys.* **1990**, *67* (2), 1062-1075.
57. (a) Odden, J. O.; Egeberg, P.; Kjekshus, A., From monosilane to crystalline silicon, Part I: Decomposition of monosilane at 690–830K and initial pressures 0.1–6.6 MPa in a free-space reactor. *Sol. Energy Mater. Sol. Cells* **2005**, *86* (2), 165-176; (b) Odden, J. O.; Egeberg, P. K.; Kjekshus, A., From monosilane to crystalline silicon, part II: Kinetic considerations on thermal decomposition of pressurized monosilane. *Int. J. Chem. Kinet.* **2006**, *38* (5), 309-321; (c) Odden, J. O.; Egeberg, P. K.; Kjekshus, A., From

monosilane to crystalline silicon. Part III. Characterization of amorphous, hydrogen-containing silicon products. *J. Non-Cryst. Solids* **2005**, *351* (14), 1317-1327.

58. (a) Perez, F. J.; Hierro, M. P.; Pedraza, F.; Gomez, C.; Carpintero, M. C., Aluminizing and chromizing bed treatment by CVD in a fluidized bed reactor on austenitic stainless steels. *Surface & Coatings Technology* **1999**, *120*, 151-157; (b) Sanchez, L.; Bolivar, F. J.; Hierro, M. d. P.; Trilleros, J. A.; Perez, F. J., CVD in a fluidized bed reactor: a method of developing coatings at temperatures below 600 degrees C. *Chem. Vap. Deposition* **2007**, *13* (9), 465-473; (c) Kinkel, S.; Angelopoulos, G. N.; Papamantellos, D. C.; Dahl, W., Feasibility of fluidized bed CVD for the formation of protective coatings. *Steel research* **1995**, *66* (7), 318-324.
59. Taghipour, F.; Ellis, N.; Wong, C., Experimental and computational study of gas-solid fluidized bed hydrodynamics. *Chem. Eng. Sci.* **2005**, *60* (24), 6857-6867.
60. Reuge, N.; Cadoret, L.; Caussat, B., Multifluid Eulerian modelling of a silicon Fluidized Bed Chemical Vapor Deposition process: Analysis of various kinetic models. *Chem. Eng. J.* **2009**, *148* (2-3), 506-516.
61. Zbib, M.; Dahl, M.; Sahaym, U.; Norton, M.; Osborne, E.; Bahr, D., Characterization of granular silicon, powders, and agglomerates from a fluidized bed reactor. *JMats* **2012**, *47* (6), 2583-2590.
62. Dahl, M. M.; Bellou, A.; Bahr, D. F.; Norton, M. G.; Osborne, E. W., Microstructure and grain growth of polycrystalline silicon grown in fluidized bed reactors. *J. Cryst. Growth* **2009**, *311* (6), 1496-1500.
63. Caussat, B.; Hemati, M.; Couderc, J. P., Silicon deposition from silane or disilane in a fluidized bed—Part I: Experimental study. *Chem. Eng. Sci.* **1995**, *50* (22), 3615-3624.
64. Caussat, B.; Hemati, M.; Couderc, J. P., Silicon Deposition from Silane or Disilane in a Fluidized Bed.2. Theoretical -Analysis and Modeling *Chem. Eng. Sci.* **1995**, *50* (22), 3625-3635.
65. Cadoret, L.; Reuge, N.; Pannala, S.; Syamlal, M.; Rossignol, C.; Dexpert-Ghys, J.; Coufort, C.; Caussat, B., Silicon chemical vapor deposition on macro and submicron powders in a fluidized bed. *Powder Technol.* **2009**, *190* (1), 185-191.
66. Lai, S.; Dudukovic, M. P.; Ramachandran, P. A., Chemical vapor deposition and homogeneous nucleation in fluidized bed reactors: silicon from silane. *Chem. Eng. Sci.* **1986**, *41* (4), 633-641.
67. Kato, K.; Wen, C., Bubble assemblage model for fluidized bed catalytic reactors. *Chem. Eng. Sci.* **1969**, *24* (8), 1351-1369.
68. Hogness, T. R.; Wilson, T. L.; Johnson, W. C., The thermal decomposition of silane. *J. Am. Chem. Soc.* **1936**, *58* (1), 108-112.
69. Iya, S.; Flagella, R.; DiPaolo, F., Heterogeneous decomposition of silane in a fixed bed reactor. *J. Electrochem. Soc.* **1982**, *129* (7), 1531-1535.
70. Pina, J.; Bucala, V.; Schbib, N.; Ege, P.; de Lasa, H. I., Modeling a silicon CVD spouted bed pilot plant reactor. *International Journal of Chemical Reactor Engineering* **2006**, *4*.
71. Rohatgi, N. K. *Silicon production in a fluidized bed reactor: Final report*; Jet Propulsion Lab., Pasadena, CA (USA): 1986.
72. Okada, R.; Iijima, S., Oxidation property of silicon small particles. *Appl. Phys. Lett.* **1991**, *58* (15), 1662-1663.
73. Smil, V., *Making the Modern World: Materials and Dematerialization*. John Wiley & Sons: 2013.
74. Khlyap, H.; Tsmots, V.; Pankiv, L.; Labovka, D., Depletion of charge carriers in electronic polycrystalline silicon. *Mater. Sci. Semicond. Process.* **2004**, *7* (4-6), 443-445.
75. Quina, M. J.; Bordado, J. C.; Quinta-Ferreira, R. M., Treatment and use of air pollution control residues from MSW incineration: An overview. *Waste Manage. (Oxford)* **2008**, *28* (11), 2097-2121.
76. Linak, W. P.; Kilgroe, J. D.; McSorley, J. A.; Wendt, J. O.; Dunn, J. E., On the occurrence of transient puffs in a rotary kiln incinerator simulator I. Prototype solid plastic wastes. *JAPCA* **1987**, *37* (1), 54-65.

77. Lenoir, D.; Kaune, A.; Hutzinger, O.; Mützenich, G.; Horch, K., Influence of operating parameters and fuel type on PCDD/F emissions from a fluidized bed incinerator. *Chemosphere* **1991**, *23* (8–10), 1491-1500.
78. Deal, B. E.; Grove, A. S., General relationship for the thermal oxidation of silicon. *J. Appl. Phys.* **1965**, *36* (12), 3770-3778.
79. (a) White, J. E.; Catallo, W. J.; Legendre, B. L., Biomass pyrolysis kinetics: A comparative critical review with relevant agricultural residue case studies. *J. Anal. Appl. Pyrolysis* **2011**, *91* (1), 1-33; (b) Fang, J.; Leavey, A.; Biswas, P., Controlled studies on aerosol formation during biomass pyrolysis in a flat flame reactor. *Fuel* **2014**, *116* (0), 350-357.
80. Cao, Y. C.; Harjanto, S.; Shibayama, A.; Naitoh, I.; Nanami, T.; Kasahara, K.; Okumura, Y.; Fujita, T., Kinetic study on the leaching of Pt, Pd and Rh from automotive catalyst residue by using chloride solutions. *Materials Transactions* **2006**, *47* (8), 2015-2024.
81. Vazquez-Pufleau, M., Ph.D. proposal Determination of kinetics for carbon elimination in kerf under air and nitrogen atmospheres. Washington University in St. Louis: St. Louis, MO, **2014 Feb**.
82. Vyazovkin, S.; Burnham, A. K.; Criado, J. M.; Perez-Maqueda, L. A.; Popescu, C.; Sbirrazzuoli, N., ICTAC Kinetics Committee recommendations for performing kinetic computations on thermal analysis data. *Thermochim. Acta* **2011**, *520* (1-2), 1-19.
83. Zhou, D.; Biswas, P.; Oostens, J.; Boolchand, P., Superconducting Properties of Aerosol-Generated YBa₂Cu₃O₇₋₈ Powders. *J. Am. Ceram. Soc.* **1993**, *76* (3), 678-682.
84. Raider, S. I.; Gdula, R. A.; Petrak, J. R., Nitrogen reaction at a silicon-silicon dioxide interface. *Appl. Phys. Lett.* **1975**, *27* (3), 150-152.
85. Levenspiel, O., *The chemical reactor omnibook*. OSU book stores Corvallis, Or.: 1996.
86. Peterson, J. D.; Vyazovkin, S.; Wight, C. A., Kinetics of the thermal and thermo-oxidative degradation of polystyrene, polyethylene and poly(propylene). *Macromol. Chem. Phys.* **2001**, *202* (6), 775-784.
87. Zhang, Z.; Guo, D.; Wang, B.; Kang, R.; Zhang, B., A novel approach of high speed scratching on silicon wafers at nanoscale depths of cut. *Sci. Rep.* **2015**, *5*, 16395.
88. Vazquez-Pufleau, M.; Chadha, T. S.; Yablonsky, G. S.; Erk, H. F.; Biswas, P., Elimination of carbon contamination from silicon kerf using a furnace aerosol reactor methodology. *Ind. Eng. Chem. Res.* **2015**, *54* (22), 5914-5920.
89. Vyazovkin, S.; Linert, W., Thermally induced reactions of solids: Isokinetic relationships of non-isothermal systems. *Int. Rev. Phys. Chem.* **1995**, *14* (2), 355-369.
90. Arisawa, H.; Brill, T. B., Flash pyrolysis of polyethyleneglycol II: Kinetics determined by T-jump/FTIR spectroscopy. *Combust. Flame* **1997**, *109* (1-2), 105-112.
91. (a) Barton, Z.; Kemp, T. J.; Buzy, A.; Jennings, K. R., Mass spectral characterization of the thermal degradation of poly(propylene oxide) by electrospray and matrix-assisted laser desorption ionization. *Polymer* **1995**, *36* (26), 4927-4933; (b) Pielichowski, K.; Flejtuch, K., Non-oxidative thermal degradation of poly(ethylene oxide): kinetic and thermoanalytical study. *J. Anal. Appl. Pyrolysis* **2005**, *73* (1), 131-138; (c) Voorhees, K. J.; Baugh, S. F.; Stevenson, D. N., An investigation of the thermal degradation of poly(ethylene glycol). *J. Anal. Appl. Pyrolysis* **1994**, *30* (1), 47-57; (d) P Lattimer, R., Mass spectral analysis of low-temperature pyrolysis products from poly (ethylene glycol). *J. Anal. Appl. Pyrolysis* **2000**, *56* (1), 61-78; (e) Arisawa, H.; Brill, T. B., Flash pyrolysis of polyethyleneglycol .1. Chemometric resolution of FTIR spectra of the volatile products at 370-550 degrees C. *Combust. Flame* **1997**, *109* (1-2), 87-104; (f) Kitahara, Y.; Takahashi, S.; Fujii, T., Thermal analysis of polyethylene glycol: Evolved gas analysis with ion attachment mass spectrometry. *Chemosphere* **2012**, *88* (5), 663-669.
92. de Sainte Claire, P., Degradation of PEO in the solid state: A theoretical kinetic model. *Macromolecules* **2009**, *42* (10), 3469-3482.

93. Lin, Z.; Han, X.; Wang, T.; Li, S., Effects of adding nano metal powders on thermooxidative degradation of poly(ethylene glycol). *J. Therm. Anal. Calorim.* **2008**, *91* (3), 709-714.
94. Han, S.; Kim, C.; Kwon, D., Thermal/oxidative degradation and stabilization of polyethylene glycol. *Polymer* **1997**, *38* (2), 317-323.
95. Fares, M. M.; Hacaloglu, J.; Suzer, S., Characterization of degradation products of polyethylene oxide by pyrolysis mass spectrometry. *Eur. Polym. J.* **1994**, *30* (7), 845-850.
96. Smallwood, I., *Handbook of organic solvent properties*. Butterworth-Heinemann: 2012; p 109-111.
97. Doyle, C. D., Estimating isothermal life from thermogravimetric data. *J. Appl. Polym. Sci.* **1962**, *6* (24), 639-642.
98. Starink, M. J., The determination of activation energy from linear heating rate experiments: a comparison of the accuracy of isoconversion methods. *Thermochim. Acta* **2003**, *404* (1-2), 163-176.
99. Mansour, N.; Momeni, A.; Karimzadeh, R.; Amini, M., Surface effects on the luminescence properties of colloidal silicon nanocrystals in water. *Phys. Scr.* **2013**, *87* (3), 035701.
100. Martinet, C.; Devine, R. A. B., Analysis of the vibrational mode spectra of amorphous SiO₂ films. *J. Appl. Phys.* **1995**, *77* (9), 4343-4348.
101. Asuha, H. K.; Maida, O.; Takahashi, M.; Iwasa, H., Nitric acid oxidation of Si to form ultrathin silicon dioxide layers with a low leakage current density. *J. Appl. Phys.* **2003**, *94* (11), 7328-7335.
102. Queeney, K. T.; Weldon, M. K.; Chang, J. P.; Chabal, Y. J.; Gurevich, A. B.; Sapjeta, J.; Opila, R. L., Infrared spectroscopic analysis of the Si/SiO₂ interface structure of thermally oxidized silicon. *J. Appl. Phys.* **2000**, *87* (3), 1322-1330.
103. Devine, R. A. B., Structural nature of the Si/SiO₂ interface through infrared spectroscopy. *Appl. Phys. Lett.* **1996**, *68* (22), 3108-3110.
104. Sun, M.; Ma, X.-X.; Yao, Q.-X.; Wang, R.-C.; Ma, Y.-X.; Feng, G.; Shang, J.-X.; Xu, L.; Yang, Y.-H., GC-MS and TG-FTIR study of petroleum ether extract and residue from low temperature coal tar. *Energy Fuels* **2011**, *25* (3), 1140-1145.
105. Maroni, V. A.; Epperson, S. J., An in situ infrared spectroscopic investigation of the pyrolysis of ethylene glycol encapsulated in silica sodalite. *Vib. Spectrosc.* **2001**, *27* (1), 43-51.
106. Zaki, M. I.; Hasan, M. A.; Al-Sagheer, F. A.; Pasupulety, L., In situ FTIR spectra of pyridine adsorbed on SiO₂-Al₂O₃, TiO₂, ZrO₂ and CeO₂: general considerations for the identification of acid sites on surfaces of finely divided metal oxides. *Colloids Surf., A* **2001**, *190* (3), 261-274.
107. Matsuura, H.; Miyazawa, T.; Machida, K., Infrared spectra of poly (ethylene glycol) dimethyl ethers in the crystalline state. *Spectrochim. Acta, Part A* **1973**, *29* (5), 771-779.
108. Pospisil, J., Aromatic and heterocyclic amines in polymer stabilization. *Polysoaps/Stabilizers/Nitrogen-15 Nmr* **1995**, *124*, 87-189.
109. (a) Bligaard, T.; Nørskov, J.; Dahl, S.; Matthiesen, J.; Christensen, C.; Sehested, J., The Brønsted–Evans–Polanyi relation and the volcano curve in heterogeneous catalysis. *J. Catal.* **2004**, *224* (1), 206-217; (b) Yablonskii, G. v.; Bykov, V.; Elovkin, V.; Gorban, A., *Kinetic models of catalytic reactions*. Elsevier: Amsterdam-New York, 1991; Vol. 32, p 396; (c) Marin, G.; Yablonsky, G. S., *Kinetics of chemical reactions*. John Wiley & Sons: 2011.
110. Bigger, S.; Scheirs, J.; Delatycki, O.; Billingham, N., Effects of frequency, molecular weight and thermal oxidation on the dynamic mechanical response of poly (ethylene oxide). *Polym. Int.* **1991**, *26* (3), 181-186.
111. Van Santen, R. A.; Neurock, M., *Molecular heterogeneous catalysis: a conceptual and computational approach*. John Wiley & Sons: 2009; p 474.
112. Sofield, C. J.; Stoneham, A. M., Oxidation of silicon - The VLSI gate dielectric. *Semicond. Sci. Technol.* **1995**, *10* (3), 215-244.

113. Doremus, R. H., Oxidation of silicon: strain and linear kinetics. *Thin Solid Films* **1984**, 122 (3), 191-196.
114. Pieraggi, B., Calculations of parabolic reaction-rate constants. *Oxid. Met.* **1987**, 27 (3-4), 177-185.
115. Irene, E., Silicon oxidation studies: some aspects of the initial oxidation regime. *J. Electrochem. Soc.* **1978**, 125 (10), 1708-1714.
116. Marcus, R. B.; Sheng, T. T., The oxidation of shaped silicon surfaces *J. Electrochem. Soc.* **1982**, 129 (6), 1278-1282.
117. Fargeix, A.; Ghibaudo, G.; Kamarinos, G., A revised analysis of dry oxidation of silicon. *J. Appl. Phys.* **1983**, 54 (5), 2878-2880.
118. EerNisse, E. P., Stress in thermal SiO₂ during growth. *Appl. Phys. Lett.* **1979**, 35 (1), 8-10.
119. EerNisse, E. P., Viscous flow of thermal SiO₂ *Appl. Phys. Lett.* **1977**, 30 (6), 290-293.
120. Jimin, W.; Yu, L.; Ruiwei, L., An improved silicon-oxidation-kinetics and accurate analytic model of oxidation. *Solid-State Electronics* **2003**, 47 (10), 1699-1705.
121. Fargeix, A.; Ghibaudo, G., Dry oxidation of silicon: A new model of growth including relaxation of stress by viscous flow. *J. Appl. Phys.* **1983**, 54 (12), 7153-7158.
122. Irene, E. A., Silicon oxidation studies: A revised model for thermal oxidation. *J. Appl. Phys.* **1983**, 54 (9), 5416-5420.
123. Marcus, R.; Sheng, T.; Lin, P., Polysilicon/SiO₂ interface microtexture and dielectric breakdown. *J. Electrochem. Soc.* **1982**, 129 (6), 1282-1289.
124. Kim, B. H.; Pamungkas, M.; Park, M.; Kim, G.; Lee, K. R.; Chung, Y. C., Stress evolution during the oxidation of silicon nanowires in the sub-10 nm diameter regime. *Appl. Phys. Lett.* **2011**, 99 (14).
125. Liao, Y.-C.; Nienow, A. M.; Roberts, J. T., Surface chemistry of aerosolized nanoparticles: thermal oxidation of silicon. *The Journal of Physical Chemistry B* **2006**, 110 (12), 6190-6197.
126. Das, D.; Farjas, J.; Roura, P.; Viera, G.; Bertran, E., Enhancement of oxidation rate of a-Si nanoparticles during dehydrogenation. *Appl. Phys. Lett.* **2001**, 79 (22), 3705-3707.
127. Winters, B. J.; Holm, J.; Roberts, J. T., Thermal processing and native oxidation of silicon nanoparticles. *J. Nanopart. Res.* **2011**, 13 (10), 5473-5484.
128. Yang, D. Q.; Meunier, M.; Sacher, E., Room temperature air oxidation of nanostructured Si thin films with varying porosities as studied by x-ray photoelectron spectroscopy. *J. Appl. Phys.* **2006**, 99 (8).
129. Pereira, R. N.; Rowe, D. J.; Anthony, R. J.; Kortshagen, U., Oxidation of freestanding silicon nanocrystals probed with electron spin resonance of interfacial dangling bonds. *PhRvB* **2011**, 83 (15), 9.
130. Yang, D. Q.; Gillet, J. N.; Meunier, M.; Sacher, E., Room temperature oxidation kinetics of Si nanoparticles in air, determined by x-ray photoelectron spectroscopy. *J. Appl. Phys.* **2005**, 97 (2).
131. Ostraat, M. L.; Brongersma, M.; Atwater, H. A.; Flagan, R. C., Nanoengineered silicon/silicon dioxide nanoparticle heterostructures. *Solid State Sciences* **2005**, 7 (7), 882-890.
132. Agnello, S.; Di Francesca, D.; Alessi, A.; Iovino, G.; Cannas, M.; Girard, S.; Boukenter, A.; Ouerdane, Y., Interstitial O₂ distribution in amorphous SiO₂ nanoparticles determined by Raman and photoluminescence spectroscopy. *J. Appl. Phys.* **2013**, 114 (10), 104305.
133. (a) Mangolini, L., Synthesis, properties, and applications of silicon nanocrystals. *Journal of Vacuum Science & Technology B* **2013**, 31 (2); (b) Yoo, B.; Ma, K.; Zhang, L.; Burns, A.; Sequeira, S.; Mellinghoff, I.; Brennan, C.; Wiesner, U.; Bradbury, M. S., Ultrasmall dual-modality silica nanoparticle drug conjugates: Design, synthesis, and characterization. *Biorg. Med. Chem.* **2015**, 23 (22), 7119-7130.
134. Holm, J.; Roberts, J. T., Sintering, coalescence, and compositional changes of hydrogen-terminated silicon nanoparticles as a function of temperature. *The Journal of Physical Chemistry C* **2009**, 113 (36), 15955-15963.
135. Yu, D. K.; Zhang, R. Q.; Lee, S. T., Structural properties of hydrogenated silicon nanocrystals and nanoclusters. *J. Appl. Phys.* **2002**, 92 (12), 7453-7458.

136. Holm, J.; Roberts, J. T., Thermal Oxidation of 6 nm Aerosolized Silicon Nanoparticles: Size and Surface Chemistry Changes. *Langmuir* **2007**, *23* (22), 11217-11224.
137. Fritzsche, H., Chapter 9 Electronic Properties of Surfaces in a-Si: H. In *Semiconductors and Semimetals*, Jacques, I. P., Ed. Elsevier: 1984; Vol. Volume 21, Part C, pp 309-345.
138. Mills, R. L.; Dhandapani, B.; He, J., Highly stable amorphous silicon hydride. *Sol. Energy Mater. Sol. Cells* **2003**, *80* (1), 1-20.
139. Lu, Z. H.; Sacher, E.; Yelon, A., Kinetics of the room-temperature air oxidation of hydrogenated amorphous-silicon and crystalline silicon. *Philosophical Magazine B-Physics of Condensed Matter Statistical Mechanics Electronic Optical and Magnetic Properties* **1988**, *58* (4), 385-388.
140. Vazquez-Pufleau, M.; Chadha, T. S.; Yablonsky, G.; Erk, H. F.; Biswas, P., Elimination of Carbon Contamination from Silicon Kerf Using a Furnace Aerosol Reactor Methodology. *Ind. Eng. Chem. Res.* **2015**, *54* (22), 5914-5920.
141. Licciardello, A.; Puglisi, O.; Pignataro, S., Effect of Organic Contaminants on the Oxidation-Kinetics of Silicon at Room-Temperature. *Appl. Phys. Lett.* **1986**, *48* (1), 41-43.
142. Chuanqiang, Y.; Xiuqin, W.; Yuhua, X.; Panbing, Z.; Genxiang, Z.; Lang, Z., Oxidation behaviors of dusts generated in different cutting processes of silicon ingots. *Advanced Materials Research* **2012**, *463-464*, 669-673.
143. Filipovic, L., Topography Simulation of Novel Processing Techniques. **2012**.
144. Pap, A. E.; Kordas, K.; George, T. F.; Leppavuori, S., Thermal oxidation of porous silicon: Study on reaction kinetics. *J. Phys. Chem. B* **2004**, *108* (34), 12744-12747.
145. Bohling, C.; Sigmund, W., Self-Limitation of Native Oxides Explained. *Silicon* **2016**, *8* (3), 339-343.
146. Sofield, C.; Stoneham, A., Oxidation of silicon: the VLSI gate dielectric. *Semicond. Sci. Technol.* **1995**, *10* (3), 215.
147. (a) Talukdar, S. S.; Swihart, M. T., Aerosol dynamics modeling of silicon nanoparticle formation during silane pyrolysis: a comparison of three solution methods. *J. Aerosol Sci* **2004**, *35* (7), 889-908; (b) Swihart, M. T.; Girshick, S. L., Thermochemistry and kinetics of silicon hydride cluster formation during thermal decomposition of silane. *J. Phys. Chem. B* **1999**, *103* (1), 64-76.
148. Wong, H. W.; Li, X. G.; Swihart, M. T.; Broadbelt, L. J., Detailed kinetic modeling of silicon nanoparticle formation chemistry via automated mechanism generation. *J. Phys. Chem. A* **2004**, *108* (46), 10122-10132.
149. Goodrich, A.; Hacke, P.; Wang, Q.; Sopori, B.; Margolis, R.; James, T. L.; Woodhouse, M., A wafer-based monocrystalline silicon photovoltaics road map: Utilizing known technology improvement opportunities for further reductions in manufacturing costs. *Sol. Energy Mater. Sol. Cells* **2013**, *114*, 110-135.
150. Onischuk, A. A.; Levykin, A. I.; Strunin, V. P.; Sabelfeld, K. K.; Panfilov, V. N., Aggregate formation under silane pyrolysis. *J. Aerosol Sci* **1999**, *30*, Supplement 1 (0), S425-S426.
151. Williams, E. D.; Ayres, R. U.; Heller, M., The 1.7 kilogram microchip: Energy and material use in the production of semiconductor devices. *Environ. Sci. Technol.* **2002**, *36* (24), 5504-5510.
152. Kleijn, C., A Mathematical Model of the Hydrodynamics and Gas-Phase Reactions in Silicon LPCVD in a Single-Wafer Reactor. *J. Electrochem. Soc.* **1991**, *138* (7), 2190-2200.
153. Onischuk, A. A.; Strunin, V. P.; Ushakova, M. A.; Panfilov, V. N., On the pathways of aerosol formation by thermal decomposition of silane. *J. Aerosol Sci* **1997**, *28* (2), 207-222.
154. Ho, P.; Coltrin, M. E.; Breiland, W. G., LASER-INDUCED FLUORESCENCE MEASUREMENTS AND KINETIC-ANALYSIS OF SI ATOM FORMATION IN A ROTATING-DISK CHEMICAL-VAPOR-DEPOSITION REACTOR. *J. Phys. Chem.* **1994**, *98* (40), 10138-10147.
155. Nguyen, H. V.; Flagan, R. C., Particle Formation and Growth in Single-Stage Aerosol Reactors. *Langmuir* **1991**, *7* (8), 1807-1814.

156. Pozdnyakov, G. A.; Yakovlev, V. N.; Saprykin, A. I., Production of Nanosized Silicon Powders by Monosilane Decomposition in an Adiabatic Process. *DokPC* **2014**, *456*, 67-70.
157. Wang, Y.; Fang, J.; Attoui, M.; Chadha, T. S.; Wang, W.-N.; Biswas, P., Application of Half Mini DMA for sub 2 nm particle size distribution measurement in an electrospray and a flame aerosol reactor. *J. Aerosol Sci.* **2014**, *71* (0), 52-64.
158. (a) Fernandez de la Mora, J., Electrical Classification and Condensation Detection of Sub-3-nm Aerosols. *Aerosol Measurement: Principles, Techniques, and Applications, Third Edition* **2011**, 697-721; (b) Fernández de la Mora, J.; Kozlowski, J., Hand-held differential mobility analyzers of high resolution for 1-30nm particles: Design and fabrication considerations. *J. Aerosol Sci.* **2013**, *57*, 45-53.
159. (a) Fang, J.; Wang, Y.; Attoui, M.; Chadha, T. S.; Ray, J. R.; Wang, W.-N.; Jun, Y.-S.; Biswas, P., Measurement of sub-2 nm clusters of pristine and composite metal oxides during nanomaterial synthesis in flame aerosol reactors. *Anal. Chem.* **2014**, *86* (15), 7523-7529; (b) Wang, Y.; Liu, P.; Fang, J.; Wang, W.-N.; Biswas, P., Kinetics of sub-2 nm TiO₂ particle formation in an aerosol reactor during thermal decomposition of titanium tetraisopropoxide. *J. Nanopart. Res.* **2015**, *17* (3), 1-13; (c) Wang, Y.; Kangasluoma, J.; Attoui, M.; Fang, J.; Junninen, H.; Kulmala, M.; Petäjä, T.; Biswas, P., Observation of incipient particle formation during flame synthesis by tandem differential mobility analysis-mass spectrometry (DMA-MS). *Proceedings of the Combustion Institute* **2016**.
160. Ude, S.; Fernandez de la Mora, J.; Thomson, B., Charge-induced unfolding of multiply charged polyethylene glycol ions. *J. Am. Chem. Soc.* **2004**, *126* (38), 12184-12190.
161. Hoppel, W.; Frick, G. *Aerosol charge distributions produced by radioactive ionizers*; DTIC Document: 1988.
162. Larriba, C.; Hogan Jr, C. J.; Attoui, M.; Borrajo, R.; Garcia, J. F.; de la Mora, J. F., The mobility-volume relationship below 3.0 nm examined by tandem mobility-mass measurement. *Aerosol Sci. Technol.* **2011**, *45* (4), 453-467.
163. Ku, B. K.; de la Mora, J. F., Relation between electrical mobility, mass, and size for nanodrops 1-6.5 nm in diameter in air. *Aerosol Science and Technology* **2009**, *43* (3), 241-249.
164. (a) Maißer, A.; Thomas, J. M.; Larriba-Andaluz, C.; He, S.; Hogan, C. J., The mass-mobility distributions of ions produced by a Po-210 source in air. *J. Aerosol Sci.* **2015**, *90*, 36-50; (b) Steiner, G.; Jokinen, T.; Junninen, H.; Sipilä, M.; Petäjä, T.; Worsnop, D.; Reischl, G. P.; Kulmala, M., High-Resolution Mobility and Mass Spectrometry of Negative Ions Produced in a 241Am Aerosol Charger. *Aerosol Sci. Technol.* **2014**, *48* (3), 261-270; (c) Steiner, G.; Reischl, G. P., The effect of carrier gas contaminants on the charging probability of aerosols under bipolar charging conditions. *J. Aerosol Sci.* **2012**, *54*, 21-31.
165. Clarke, F. W.; Washington, H. S., *The composition of the earth's crust*. US Government Printing Office: 1924; Vol. 127.
166. Hsu, G.; Rohatgi, N.; Houseman, J., Silicon particle growth in a fluidized-bed reactor. *AIChE J.* **1987**, *33* (5), 784-791.
167. Swihart, M. T.; Girshick, S. L., Ab initio structures and energetics of selected hydrogenated silicon clusters containing six to ten silicon atoms. *Chem. Phys. Lett.* **1999**, *307* (5-6), 527-532.
168. (a) Eversteijn, F., Gas-phase decomposition of silane in a horizontal epitaxial reactor. *PHILIPS RESEARCH REP* **1971**, *26* (2), 134-144; (b) Frenklach, M.; Ting, L.; Wang, H.; Rabinowitz, M. J., Silicon particle formation in pyrolysis of silane and disilane. *Isr. J. Chem.* **1996**, *36* (3), 293-303.
169. Morrison, P. W.; Reimer, J. A., Silane pyrolysis in a piston reactor. *AIChE J.* **1989**, *35* (5), 793-802.
170. Alam, M. K.; Flagan, R. C., Controlled Nucleation Aerosol Reactors: Production of Bulk Silicon. *Aerosol Sci. Technol.* **1986**, *5* (2), 237-248.
171. Newman, C.; O'neal, H.; Ring, M.; Leska, F.; Shipley, N., Kinetics and mechanism of the silane decomposition. *Int. J. Chem. Kinet.* **1979**, *11* (11), 1167-1182.
172. Onischuk, A.; Levykin, A.; Strunin, V.; Sabelfeld, K.; Panfilov, V., Aggregate formation under homogeneous silane thermal decomposition. *J. Aerosol Sci.* **2000**, *31* (11), 1263-1281.

173. Lunden, M. M. Sintering of aerosol agglomerates. California Institute of Technology, 1995.
174. Becerra, R.; Frey, H. M.; Mason, B. P.; Walsh, R.; Gordon, M. S., PROTOTYPE SI-H INSERTION REACTION OF SILYLENE WITH SILANE - ABSOLUTE RATE CONSTANTS, TEMPERATURE-DEPENDENCE, RRKM MODELING AND THE POTENTIAL-ENERGY SURFACE. *Journal of the Chemical Society-Faraday Transactions* **1995**, 91 (17), 2723-2732.
175. Kruis, F. E.; Kusters, K. A.; Pratsinis, S. E.; Scarlett, B., A simple model for the evolution of the characteristics of aggregate particles undergoing coagulation and sintering. *Aerosol Sci. Technol.* **1993**, 19 (4), 514-526.
176. Pratsinis, S. E., SIMULTANEOUS NUCLEATION, CONDENSATION, AND COAGULATION IN AEROSOL REACTORS. *J. Colloid Interface Sci.* **1988**, 124 (2), 416-427.
177. Hinds, W. C., *Aerosol technology: properties, behavior, and measurement of airborne particles*. John Wiley & Sons: 2012.
178. (a) Körmer, R.; Schmid, H. J.; Peukert, W., Aerosol synthesis of silicon nanoparticles with narrow size distribution—Part 2: Theoretical analysis of the formation mechanism. *J. Aerosol Sci* **2010**, 41 (11), 1008-1019; (b) Körmer, R.; Jank, M. P. M.; Ryssel, H.; Schmid, H. J.; Peukert, W., Aerosol synthesis of silicon nanoparticles with narrow size distribution—Part 1: Experimental investigations. *J. Aerosol Sci* **2010**, 41 (11), 998-1007.
179. Becerra, R.; Walsh, R., Some mechanistic problems in the kinetic modeling of monosilane pyrolysis. *The Journal of Physical Chemistry* **1992**, 96 (26), 10856-10862.
180. (a) Warheit, D. B., How meaningful are the results of nanotoxicity studies in the absence of adequate material characterization? *Toxicol. Sci.* **2008**, 101 (2), 183-185; (b) Fischer, H. C.; Chan, W. C., Nanotoxicity: the growing need for in vivo study. *Curr. Opin. Biotechnol.* **2007**, 18 (6), 565-571.
181. Chen, F.; Nayak, T. R.; Goel, S.; Valdovinos, H. F.; Hong, H.; Theuer, C. P.; Barnhart, T. E.; Cai, W., In Vivo Tumor Vasculature Targeted PET/NIRF Imaging with TRC105(Fab)-Conjugated, Dual-Labeled Mesoporous Silica Nanoparticles. *Mol. Pharm.* **2014**, 11 (11), 4007-4014.
182. Corbin, B.; Pierce, A.; Bailey, C. In *Rethinking the approach to higher 450mm process gas flows: A case study*, Advanced Semiconductor Manufacturing Conference (ASMC), 2014 25th Annual SEMI, 19-21 May 2014; 2014; pp 208-212.
183. Fthenakis, V.; Carlisle, C.; Chan, W. In *Silane Safety in amorphous silicon and silicon nitride operations*, Proceedings 21st European Photovoltaic Solar Energy Conference, Dresden, Germany, 2006; pp 4-8.
184. Ramos, A.; Filtvedt, W. O.; Lindholm, D.; Ramachandran, P. A.; Rodríguez, A.; del Cañizo, C., Deposition reactors for solar grade silicon: A comparative thermal analysis of a Siemens reactor and a fluidized bed reactor. *J. Cryst. Growth* **2015**, 431, 1-9.
185. Balaji, S.; Du, J.; White, C.; Ydstie, B. E., Multi-scale modeling and control of fluidized beds for the production of solar grade silicon. *Powder Technol.* **2010**, 199 (1), 23-31.
186. Zbib, M.; Tarun, M.; Norton, M.; Bahr, D.; Nair, R.; Randall, N.; Osborne, E., Mechanical properties of polycrystalline silicon solar cell feed stock grown via fluidized bed reactors. *JMatS* **2010**, 45 (6), 1560-1566.
187. Martin, J. G.; Oneal, H. E.; Ring, M. A., THERMAL-DECOMPOSITION KINETICS OF POLYSILANES - DISILANE, TRISILANE, AND TETRASILANE. *Int. J. Chem. Kinet.* **1990**, 22 (6), 613-632.
188. Liu, S. S.; Xiao, W. D., Numerical simulations of particle growth in a silicon-CVD fluidized bed reactor via a CFD-PBM coupled model. *Chem. Eng. Sci.* **2014**, 111, 112-125.
189. White, C. M.; Ege, P.; Ydstie, B. E., Size distribution modeling for fluidized bed solar-grade silicon production. *Powder Technol.* **2006**, 163 (1), 51-58.
190. Wang, H.; Yang, W.; Dyakowski, T.; Liu, S., Study of bubbling and slugging fluidized beds by simulation and ECT. *AIChE J.* **2006**, 52 (9), 3078-3087.

191. Constantineau, J.; Grace, J.; Lim, C.; Richards, G., Generalized bubbling–slugging fluidized bed reactor model. *Chem. Eng. Sci.* **2007**, *62* (1), 70-81.
192. Kang, W.; Sutherland, J.; Osberg, G., Pressure fluctuations in a fluidized bed with and without screen cylindrical packings. *Industrial & Engineering Chemistry Fundamentals* **1967**, *6* (4), 499-504.
193. De Luca, L.; Di Felice, R.; Foscolo, P. U.; Boattini, P. P., Slugging behaviour of fluidized beds of large particles. *Powder Technol.* **1992**, *69* (2), 171-175.
194. Ma, X.; Kato, K., Effect of interparticle adhesion forces on elutriation of fine powders from a fluidized bed of a binary particle mixture. *Powder Technol.* **1998**, *95* (2), 93-101.
195. Briens, C.; Bergougnou, M.; Incullet, I.; Baron, T.; Hazlett, J., Size distribution of particles entrained from fluidized beds: electrostatic effects. *Powder Technol.* **1992**, *70* (1), 57-62.
196. Choi, J.-H.; Suh, J.-M.; Chang, I.-Y.; Shun, D.-W.; Yi, C.-K.; Son, J.-E.; Kim, S.-D., The effect of fine particles on elutriation of coarse particles in a gas fluidized bed. *Powder Technol.* **2001**, *121* (2–3), 190-194.
197. Quevedo, J.; Patel, G.; Pfeffer, R.; Dave, R., Agglomerates and granules of nanoparticles as filter media for submicron particles. *Powder Technol.* **2008**, *183* (3), 480-500.
198. Yamamoto, T.; Tsuboi, T.; Tatebayashi, J., A numerical simulation of PM adhesion characteristics in a fluidized bed type PM removal device by a finite volume Eulerian–Eulerian method. *Powder Technol.* **2016**, *288*, 26-34.
199. Ushiki, K.; Tien, C., Calculation of aerosol collection in fluidized filter beds. *AIChE J.* **1984**, *30* (1), 156-168.
200. Ghadiri, M.; Seville, J.; Clift, R., Fluidised bed filtration of gases at high temperatures: Particle processing. *Chemical engineering research & design* **1993**, *71* (4), 371-381.
201. Gidaspow, D.; Chaiwang, P., Bubble free fluidization of a binary mixture of large particles. *Chem. Eng. Sci.* **2013**, *97*, 152-161.
202. Liu, S.-S.; Xiao, W.-D., Evaluation of the Flow Behavior in a Large-Scale Polydisperse Particle Fluidized System by an Energy Minimization Multiscale-Eulerian Combined Model. *Ind. Eng. Chem. Res.* **2014**, *53* (36), 14113-14126.
203. Pemberton, S. T.; Davidson, J. F., Elutriation from fluidized beds—I. Particle ejection from the dense phase into the freeboard. *Chem. Eng. Sci.* **1986**, *41* (2), 243-251.
204. Parker, J. M., Validation of CFD model for polysilicon deposition and production of silicon fines in a silane deposition FBR. *International Journal of Chemical Reactor Engineering* **2011**, *9* (1).
205. (a) Peters, M. H.; Fan, L.-S.; Sweeney, T. L., Simulation of particulate removal in gas-solid fluidized beds. *AIChE J.* **1982**, *28* (1), 39-49; (b) Lim, K. S.; Hadley, T. D.; Nikolov, J., Understanding capture efficiency in fluidized beds. **2010**; (c) Henneke, M. R.; Ellzey, J. L., Modeling of filtration combustion in a packed bed. *Combust. Flame* **1999**, *117* (4), 832-840.
206. Liu, K.-Y.; Wey, M.-Y., Filtration of nano-particles by a gas–solid fluidized bed. *J. Hazard. Mater.* **2007**, *147* (1–2), 618-624.
207. Knettig, P.; Beeckmans, J., Capture of monodispersed aerosol particles in a fixed and in a fluidized bed. *The Canadian Journal of Chemical Engineering* **1974**, *52* (6), 703-706.
208. Xiao, G.; Wang, X.; Zhang, J.; Ni, M.; Gao, X.; Luo, Z.; Cen, K., Granular bed filter: A promising technology for hot gas clean-up. *Powder Technol.* **2013**, *244*, 93-99.
209. Wormsbecker, M.; Pugsley, T. S.; Tanfara, H., The influence of distributor design on fluidized bed dryer hydrodynamics. **2007**.
210. Yaws, C. L.; Li, K.; Hopper, J.; Fang, C.; Hansen, K., Process feasibility study in support of silicon material task 1. **1981**.
211. Adamczyk, A. J.; Broadbelt, L. J., Thermochemical Property Estimation of Hydrogenated Silicon Clusters. *J. Phys. Chem. A* **2011**, *115* (32), 8969-8982.

212. Kormer, R.; Butz, B.; Spiecker, E.; Peukert, W., Crystal Shape Engineering of Silicon Nanoparticles in a Thermal Aerosol Reactor. *Crystal Growth & Design* **2012**, *12* (3), 1330-1336.
213. Diaz, J. M. A.; Kambara, M.; Yoshida, T., Detection of Si nanoclusters by x-ray scattering during silicon film deposition by mesoplasma chemical vapor deposition. *J. Appl. Phys.* **2008**, *104* (1).
214. (a) Swihart, M. T.; Carr, R. W., Ab initio molecular orbital study of the thermochemistry and reactions of the chlorinated disilenes and their isomers ($\text{Si}_2\text{H}_n\text{Cl}_{4-n}$). *J. Phys. Chem. A* **1998**, *102* (4), 785-792; (b) Swihart, M. T.; Carr, R. W., Thermochemistry and thermal decomposition of the chlorinated disilanes $\text{Si}_2\text{H}_n\text{Cl}_{6-n}$, $n=0-6$ studied in ab initio molecular orbital methods. *J. Phys. Chem. A* **1997**, *101* (40), 7434-7445.
215. Sprung, C.; Heimfarth, J.; Erler, J.; Ziegenbalg, G.; Patzold, C.; Singliar, U.; Frohlich, P.; Muller, A.; Schubert, C.; Roewer, G.; Bohmhammel, K.; Mertens, F.; Seidel, J.; Bertau, M.; Kroke, E., Hydrogen Terminated Silicon Nanopowders: Gas Phase Synthesis, Oxidation Behaviour, and Si-H Reactivity. *Silicon* **2015**, *7* (1), 31-42.
216. (a) Adamczyk, A. J.; Broadbelt, L. J., The Role of Multifunctional Kinetics during Early-Stage Silicon Hydride Pyrolysis: Reactivity of Si_2H_2 Isomers with SiH_4 and Si_2H_6 . *J. Phys. Chem. A* **2011**, *115* (11), 2409-2422; (b) Adamczyk, A. J.; Reyniers, M. F.; Marin, G. B.; Broadbelt, L. J., Hydrogenated amorphous silicon nanostructures: novel structure-reactivity relationships for cyclization and ring opening in the gas phase. *Theor. Chem. Acc.* **2011**, *128* (1), 91-113; (c) Adamczyk, A. J.; Reyniers, M. F.; Marin, G. B.; Broadbelt, L. J., Kinetics of Substituted Silylene Addition and Elimination in Silicon Nanocluster Growth Captured by Group Additivity. *Chemphyschem* **2010**, *11* (9), 1978-1994.
217. Holm, J.; Roberts, J. T., Modifying the composition of hydrogen-terminated silicon nanoparticles synthesized in a nonthermal rf plasma. *Journal of Vacuum Science & Technology A* **2010**, *28* (2), 161-169.
218. (a) Moffat, H. K.; Jensen, K. F.; Carr, R. W., DETERMINATION OF THE ARRHENIUS PARAMETERS FOR Si_2H_6 REVERSIBLE-ARROW $\text{SiH}_4 + \text{SiH}_2$ AND $\Delta\text{-H-CIRCLE-F}(\text{SiH}_2)$ BY RRKM ANALYSIS OF FORWARD AND REVERSE REACTION-RATE DATA. *J. Phys. Chem.* **1992**, *96* (19), 7683-7695; (b) Moffat, H. K.; Jensen, K. F.; Carr, R. W., ESTIMATION OF ARRHENIUS PARAMETERS FOR THE 1,1 ELIMINATION OF H-2 FROM Si_2H_6 AND THE ROLE OF CHEMICALLY ACTIVATED DISILANE IN SILANE PYROLYSIS. *J. Phys. Chem.* **1992**, *96* (19), 7695-7703; (c) Moffat, H. K.; Jensen, K. F.; Carr, R. W., ESTIMATION OF THE ARRHENIUS PARAMETERS FOR SiH_4 REVERSIBLE SiH_2+H_2 AND $\Delta\text{-HFO}(\text{SiH}_2)$ BY A NONLINEAR-REGRESSION ANALYSIS OF THE FORWARD AND REVERSE REACTION-RATE DATA. *J. Phys. Chem.* **1991**, *95* (1), 145-154.
219. (a) Matsumoto, K.; Klippenstein, S. J.; Tonokura, K.; Koshi, M., Channel specific rate constants relevant to the thermal decomposition of disilane. *J. Phys. Chem. A* **2005**, *109* (22), 4911-4920; (b) Yoshida, K.; Matsumoto, K.; Oguchi, T.; Tonokura, K.; Koshi, M., Thermal decomposition mechanism of disilane. *J. Phys. Chem. A* **2006**, *110* (14), 4726-4731.
220. Jasinski, J. M.; Becerra, R.; Walsh, R., DIRECT KINETIC-STUDIES OF SILICON HYDRIDE RADICALS IN THE GAS-PHASE. *Chem. Rev.* **1995**, *95* (5), 1203-1228.
221. Yuuki, A.; Matsui, Y.; Tachibana, K., A numerical study on gaseous reactions in silane pyrolysis. *Jpn. J. Appl. Phys.* **1987**, *26* (5R), 747.
222. Kremer, D.; Davis, R.; Moore, E. F.; Maslar, J. E.; Burgess, D.; Ehrman, S., An investigation of particle dynamics in a rotating disk chemical vapor deposition reactor. *J. Electrochem. Soc.* **2003**, *150* (2), G127-G139.
223. Whitby, E. R.; McMurry, P. H.; Shankar, U.; Binkowski, F. S. *Modal aerosol dynamics modeling*; Computer Sciences Corp., Research Triangle Park, NC (USA): 1991.
224. Vepřek, S.; Schopper, K.; Ambacher, O.; Rieger, W.; Vepřek-Heijman, M., Mechanism of cluster formation in a clean silane discharge. *J. Electrochem. Soc.* **1993**, *140* (7), 1935-1942.
225. Groschel, M.; Kormer, R.; Walther, M.; Leugering, G.; Peukert, W., Process control strategies for the gas phase synthesis of silicon nanoparticles. *Chem. Eng. Sci.* **2012**, *73*, 181-194.

226. Li, X.; Swihart, M., Kinetic Monte Carlo simulation of homogeneous nucleation of hydrogenated silicon particles during silane decomposition. *Electrochemical Society Proceedings Volume, PV* **2001**, 13, 455.
227. Bhandarkar, U. V.; Swihart, M. T.; Girshick, S. L.; Kortshagen, U. R., Modelling of silicon hydride clustering in a low-pressure silane plasma. *Journal of Physics D-Applied Physics* **2000**, 33 (21), 2731-2746.
228. Hulser, T.; Schnurre, S. M.; Wiggers, H.; Schulz, C., Gas-Phase Synthesis of Nanoscale Silicon as an Economical Route Towards Sustainable Energy Technology. *Kona Powder and Particle Journal* **2011**, (29), 191-207.
229. (a) Schmid, H.-J.; Al-Zaitone, B.; Artelt, C.; Peukert, W., Evolution of the fractal dimension for simultaneous coagulation and sintering. *Chem. Eng. Sci.* **2006**, 61 (1), 293-305; (b) Schmid, H.-J.; Tejwani, S.; Artelt, C.; Peukert, W., Monte Carlo simulation of aggregate morphology for simultaneous coagulation and sintering. *J. Nanopart. Res.* **2004**, 6 (6), 613-626.
230. Dang, H. Y.; Swihart, M. T., Computational Modeling of Silicon Nanoparticle Synthesis: I. A General Two-Dimensional Model. *Aerosol Sci. Technol.* **2009**, 43 (3), 250-263.
231. Kommu, S.; Khomami, B.; Biswas, P., Simulation of aerosol dynamics and transport in chemically reacting particulate matter laden flows. Part II: Application to CVD reactors. *Chem. Eng. Sci.* **2004**, 59 (2), 359-371.
232. Khairul Alam, M.; Flagan, R. C., Simultaneous homogeneous nucleation and aerosol growth. *J. Colloid Interface Sci.* **1984**, 97 (1), 232-246.
233. Pesthy, A. J.; Flagan, R. C.; Seinfeld, J. H., The effect of a growing aerosol on the rate of homogeneous nucleation of a vapor. *J. Colloid Interface Sci.* **1981**, 82 (2), 465-479.
234. Pesthy, A. J.; Flagan, R. C.; Seinfeld, J. H., Theory of aerosol formation and growth in laminar flow. *J. Colloid Interface Sci.* **1983**, 91 (2), 525-545.
235. McClurg, R. B.; Flagan, R. C., Critical comparison of droplet models in homogeneous nucleation theory. *J. Colloid Interface Sci.* **1998**, 201 (2), 194-199.
236. Jin Jwang, W.; Flagan, R. C., Onset of runaway nucleation in aerosol reactors. *J. Appl. Phys.* **1987**, 61 (4), 1365-1371.
237. Bianchi, F.; Praplan, A. P.; Sarnela, N.; Dommen, J.; Kurten, A.; Ortega, I. K.; Schobesberger, S.; Junninen, H.; Simon, M.; Trostl, J.; Jokinen, T.; Sipila, M.; Adamov, A.; Amorim, A.; Almeida, J.; Breitenlechner, M.; Duplissy, J.; Ehrhart, S.; Flagan, R. C.; Franchin, A.; Hakala, J.; Hansel, A.; Heinritzi, M.; Kangasluoma, J.; Keskinen, H.; Kim, J.; Kirkby, J.; Laaksonen, A.; Lawler, M. J.; Lehtipalo, K.; Leiminger, M.; Makhmutov, V.; Mathot, S.; Onnela, A.; Petaja, T.; Riccobono, F.; Rissanen, M. P.; Rondo, L.; Tome, A.; Virtanen, A.; Viisanen, Y.; Williamson, C.; Wimmer, D.; Winkler, P. M.; Ye, P. L.; Curtius, J.; Kulmala, M.; Worsnop, D. R.; Donahue, N. M.; Baltensperger, U., Insight into Acid-Base Nucleation Experiments by Comparison of the Chemical Composition of Positive, Negative, and Neutral Clusters. *Environ. Sci. Technol.* **2014**, 48 (23), 13675-13684.
238. Almeida, J.; Schobesberger, S.; Kurten, A.; Ortega, I. K.; Kupiainen-Maatta, O.; Praplan, A. P.; Adamov, A.; Amorim, A.; Bianchi, F.; Breitenlechner, M.; David, A.; Dommen, J.; Donahue, N. M.; Downard, A.; Dunne, E.; Duplissy, J.; Ehrhart, S.; Flagan, R. C.; Franchin, A.; Guida, R.; Hakala, J.; Hansel, A.; Heinritzi, M.; Henschel, H.; Jokinen, T.; Junninen, H.; Kajos, M.; Kangasluoma, J.; Keskinen, H.; Kupc, A.; Kurten, T.; Kvashin, A. N.; Laaksonen, A.; Lehtipalo, K.; Leiminger, M.; Leppa, J.; Loukonen, V.; Makhmutov, V.; Mathot, S.; McGrath, M. J.; Nieminen, T.; Olenius, T.; Onnela, A.; Petaja, T.; Riccobono, F.; Riipinen, I.; Rissanen, M.; Rondo, L.; Ruuskanen, T.; Santos, F. D.; Sarnela, N.; Schallhart, S.; Schnitzhofer, R.; Seinfeld, J. H.; Simon, M.; Sipila, M.; Stozhkov, Y.; Stratmann, F.; Tome, A.; Trostl, J.; Tsagkogeorgas, G.; Vaattovaara, P.; Viisanen, Y.; Virtanen, A.; Vrtala, A.; Wagner, P. E.; Weingartner, E.; Wex, H.; Williamson, C.; Wimmer, D.; Ye, P. L.; Yli-Juuti, T.; Carslaw, K. S.; Kulmala, M.; Curtius, J.; Baltensperger, U.; Worsnop, D. R.; Vehkamäki, H.; Kirkby, J., Molecular understanding of sulphuric acid-amine particle nucleation in the atmosphere. *Nature* **2013**, 502 (7471), 359-+.

239. Russell, L. M.; Sorooshian, A.; Seinfeld, J. H.; Albrecht, B. A.; Nenes, A.; Leaitch, W. R.; Macdonald, A. M.; Ahlm, L.; Yi-Chun, C.; Coggon, M.; Corrigan, A.; Craven, J. S.; Flagan, R. C.; Frossard, A. A.; Hawkins, L. N.; Jonsson, H.; Eunsil, J.; Lin, J. J.; Metcalf, A. R.; Modini, R.; Mulmenstadt, J.; Roberts, G. C.; Shingler, T.; Siwon, S.; Zhen, W.; Wonaschutz, A., Observed aerosol effects on marine cloud nucleation and supersaturation. *AIChE Conference Proceedings* **2013**, 1527, 696-701.
240. Olsen, A. P.; Flagan, R. C.; Kornfield, J. A., Single-particle levitation system for automated study of homogeneous solute nucleation. *Rev. Sci. Instrum.* **2006**, 77 (7).
241. O'Dowd, C. D.; Jimenez, J. L.; Bahreini, R.; Flagan, R. C.; Seinfeld, J. H.; Hameri, K.; Pirjola, L.; Kulmala, M.; Jennings, S. G.; Hoffmann, T., Marine aerosol formation from biogenic iodine emissions. *Nature* **2002**, 417 (6889), 632-636.
242. Russell, L. M.; Seinfeld, J. H.; Flagan, R. C.; Ferek, R. J.; Hegg, D. A.; Hobbs, P. V.; Wobrock, W.; Flossmann, A. I.; O'Dowd, C. D.; Nielsen, K. E.; Durkee, P. A., Aerosol dynamics in ship tracks. *Journal of Geophysical Research-Atmospheres* **1999**, 104 (D24), 31077-31095.
243. McClurg, R. B.; Flagan, R. C.; Goddard, W. A., Influences of binding transitions on the homogeneous nucleation of mercury. *Nanostruct. Mater.* **1997**, 9 (1-8), 53-61.
244. McClurg, R. B.; Flagan, R. C.; Goddard, W. A., Thermodynamic properties and homogeneous nucleation for surface-melted physical clusters. *J. Chem. Phys.* **1996**, 105 (17), 7648-7663.
245. Nguyen, H. V.; Okuyama, K.; Mimura, T.; Kousaka, Y.; Flagan, R. C.; Seinfeld, J. H., HOMOGENEOUS AND HETEROGENEOUS NUCLEATION IN A LAMINAR-FLOW AEROSOL GENERATOR. *J. Colloid Interface Sci.* **1987**, 119 (2), 491-504.
246. Warren, D. R.; Okuyama, K.; Kousaka, Y.; Seinfeld, J. H.; Flagan, R. C., HOMOGENEOUS NUCLEATION IN SUPERSATURATED VAPOR CONTAINING FOREIGN SEED AEROSOL. *J. Colloid Interface Sci.* **1987**, 116 (2), 563-581.
247. Stern, J. E.; Wu, J. J.; Flagan, R. C.; Seinfeld, J. H., EFFECT OF SPATIAL INHOMOGENEITIES ON THE RATE OF HOMOGENEOUS NUCLEATION IN SYSTEMS WITH AEROSOL-PARTICLES. *J. Colloid Interface Sci.* **1986**, 110 (2), 533-543.
248. Sitarski, M., Condensation kinetics of trace vapor on submicron aerosols by Monte Carlo simulation. *J. Colloid Interface Sci.* **1980**, 73 (1), 152-161.
249. Shi, G.; Seinfeld, J. H., Homogeneous nucleation in the presence of an aerosol. *J. Colloid Interface Sci.* **1990**, 135 (1), 252-258.
250. McCoy, B. J., Vapor Nucleation and Droplet Growth: Cluster Distribution Kinetics for Open and Closed Systems. *J. Colloid Interface Sci.* **2000**, 228 (1), 64-72.
251. Higuchi, W. I.; O'Konski, C. T., A test of the becker-doering theory of nucleation kinetics. *J. Colloid Sci.* **1960**, 15 (1), 14-49.
252. Stauffer, D.; Kiang, C., Fisher's droplet model and nucleation theory. *Adv. Colloid Interface Sci.* **1977**, 7 (1), 103-130.
253. Wu, J. J.; Flagan, R. C., A discrete-sectional solution to the aerosol dynamic equation. *J. Colloid Interface Sci.* **1988**, 123 (2), 339-352.
254. Watanabe, Y.; Shiratani, M.; Kawasaki, H.; Singh, S.; Fukuzawa, T.; Ueda, Y.; Ohkura, H., Growth processes of particles in high frequency silane plasmas. *Journal of Vacuum Science & Technology A* **1996**, 14 (2), 540-545.
255. Kim, K.-S.; Kim, D.-J., Modeling of rapid particle growth by coagulation in silane plasma reactor. *J. Appl. Phys.* **2000**, 87 (6), 2691-2699.
256. Kim, D. J.; Kim, K. S., Analysis on nanoparticle growth by coagulation in silane plasma reactor. *AIChE J.* **2002**, 48 (11), 2499-2509.
257. (a) Phanse, G. M.; Pratsinis, S. E., THEORY FOR AEROSOL GENERATION IN LAMINAR-FLOW CONDENSERS. *Aerosol Sci. Technol.* **1989**, 11 (2), 100-119; (b) Pratsinis, S. E.; Kim, K. S., PARTICLE

- COAGULATION, DIFFUSION AND THERMOPHORESIS IN LAMINAR TUBE FLOWS. *J. Aerosol Sci* **1989**, 20 (1), 101-111.
258. (a) Warren, D. R.; Seinfeld, J. H., SIMULATION OF AEROSOL SIZE DISTRIBUTION EVOLUTION IN SYSTEMS WITH SIMULTANEOUS NUCLEATION, CONDENSATION, AND COAGULATION. *Aerosol Sci. Technol.* **1985**, 4 (1), 31-43; (b) Warren, D. R.; Seinfeld, J. H., NUCLEATION AND GROWTH OF AEROSOL FROM A CONTINUOUSLY REINFORCED VAPOR. *Aerosol Sci. Technol.* **1984**, 3 (2), 135-153.
259. Henderson, R.; Helm, R. F., Silicon homoepitaxial thin films via silane pyrolysis: a HEED and Auger electron spectroscopy study. *Surf. Sci.* **1972**, 30 (2), 310-334.
260. Farrow, R., The Kinetics of Silicon Deposition on Silicon by Pyrolysis of Silane A Mass Spectrometric Investigation by Molecular Beam Sampling. *J. Electrochem. Soc.* **1974**, 121 (7), 899-907.
261. Tardos, G.; Gutfinger, C.; Abuaf, N., DEPOSITION OF DUST PARTICLES IN A FLUIDIZED-BED FILTER. *IsJT* **1974**, 12 (3-4), 184-190.
262. Gutfinger, C.; Tardos, G. I., Theoretical and experimental investigation on granular bed dust filters. *Atmospheric Environment (1967)* **1979**, 13 (6), 853-867.
263. Furusawa, T.; Kojima, T.; Hiroha, H., CHEMICAL VAPOR-DEPOSITION AND HOMOGENEOUS NUCLEATION IN MONOSILANE PYROLYSIS WITHIN INTERPARTICLE SPACES - APPLICATION OF FINES FORMATION ANALYSIS TO FLUIDIZED-BED CVD. *Chem. Eng. Sci.* **1988**, 43 (8), 2037-2042.
264. Tejero-Ezpeleta, M. P.; Buchholz, S.; Mleczko, L., Optimization of reaction conditions in a fluidized-bed for silane pyrolysis. *Can. J. Chem. Eng.* **2004**, 82 (3), 520-529.
265. N Rohatgi, G. H., R Lutwach, Silane pyrolysis in a fluidized bed reactor In *Electrochemical Society*, Montreal, Canada, 1982.
266. Song, Y.; Yoon, P., Fluidized bed reactor with microwave heating system for preparing high-purity polycrystalline silicon. Google Patents: 1988.
267. Filtvedt, W. O.; Javidi, M.; Holt, A.; Melaaen, M. C.; Marstein, E.; Tathgar, H.; Ramachandran, P. A., Development of fluidized bed reactors for silicon production. *Sol. Energy Mater. Sol. Cells* **2010**, 94 (12), 1980-1995.
268. Lord, S. M., Method for improving the efficiency of a silicon purification process. Google Patents: 2002.
269. Hwang, N. M., Deposition and simultaneous etching of Si in the chemical vapor deposition (CVD) process: approach by the charged cluster model. *J. Cryst. Growth* **1999**, 205 (1), 59-63.
270. KIM, Y. H. Y., Verfahren zur herstellung von polysilizium unter verwendung von exothermer reaktionswärme. Google Patents: 2007.
271. Kojima, T. H., Hiroha, K. Iwata and T. Furusawa, Production of polycrystalline silicon from monosilane in a fluidized bed: Clogging, particle Growth and Formation of Fines in a SiH₄ Ar system. *Intern. Chem Eng.*, **1992**, 32, 739-749.
272. Ritter, E. R.; Bozzelli, J. W., THERM - THERMODYNAMIC PROPERTY ESTIMATION FOR GAS-PHASE RADICALS AND MOLECULES. *Int. J. Chem. Kinet.* **1991**, 23 (9), 767-778.
273. Holunga, D. M.; Flagan, R. C.; Atwater, H. A., A scalable turbulent mixing aerosol reactor for oxide-coated silicon nanoparticles. *Ind. Eng. Chem. Res.* **2005**, 44 (16), 6332-6341.
274. Belmonte, T.; Gries, T.; Cardoso, R. P.; Arnoult, G.; Kosior, F.; Henrion, G., Chemical vapour deposition enhanced by atmospheric microwave plasmas: a large-scale industrial process or the next nanomanufacturing tool? *Plasma Sources Science & Technology* **2011**, 20 (2).
275. Donovan, M. T.; He, X.; Zigler, B.; Palmer, T. R.; Walton, S. M.; Wooldridge, M. S., Experimental investigation of silane combustion and particle nucleation using a rapid-compression facility. *Combust. Flame* **2005**, 141 (4), 360-370.
276. Knipping, J.; Wiggers, H.; Rellinghaus, B.; Roth, P.; Konjhodzic, D.; Meier, C., Synthesis of high purity silicon nanoparticles in a low pressure microwave reactor. *Journal of Nanoscience and Nanotechnology* **2004**, 4 (8), 1039-1044.

277. Rao, N.; Girshick, S.; Heberlein, J.; McMurtry, P.; Jones, S.; Hansen, D.; Micheel, B., NANOPARTICLE FORMATION USING A PLASMA EXPANSION PROCESS. *Plasma Chem. Plasma Process.* **1995**, *15* (4), 581-606.
278. Siegmann, S.; Girshick, S.; Szepvolgyi, J.; Leparoux, M.; Shin, J. W.; Schreuders, C.; Rohr, L.; Ishigaki, T.; Jurewicz, J. W.; Habib, M.; Baroud, G.; Gitzhofer, F.; Kambara, M.; Diaz, J. M. A.; Yoshida, T., NANO POWDER SYNTHESIS BY PLASMAS Report of the Session held at the International Round Table on Thermal Plasma Fundamentals and Applications Held in Sharm el Sheikh Egypt - Jan. 14-18 2007. *High Temp. Mater. Processes (New York)* **2008**, *12* (3-4), 205-254.
279. Watanabe, Y., Formation and behaviour of nano/micro-particles in low pressure plasmas. *Journal of Physics D-Applied Physics* **2006**, *39* (19), R329-R361.
280. Sankaran, R. M.; Holunga, D.; Flagan, R. C.; Giapis, K. P., Synthesis of blue luminescent Si nanoparticles using atmospheric-pressure microdischarges. *Nano Lett.* **2005**, *5* (3), 537-541.
281. (a) De Blauwe, J.; Ostraat, M.; Green, M. L.; Weber, G.; Sorsch, T.; Kerber, A.; Klemens, F.; Cirelli, R.; Ferry, E.; Grazul, J. L.; Baumann, F.; Kim, Y.; Mansfield, W.; Bude, J.; Lee, J. T. C.; Hillenius, S. J.; Flagan, R. C.; Atwater, H. A. In *A novel, aerosol-nanocrystal floating-gate device for non-volatile memory applications*, Electron Devices Meeting, 2000. IEDM '00. Technical Digest. International, 10-13 Dec. 2000; 2000; pp 683-686; (b) Ostraat, M. L.; Atwater, H. A.; Flagan, R. C., The feasibility of inert colloidal processing of silicon nanoparticles. *J. Colloid Interface Sci.* **2005**, *283* (2), 414-421.
282. Ostraat, M. L.; De Blauwe, J. W.; Green, M. L.; Bell, L. D.; Atwater, H. A.; Flagan, R. C., Ultraclean two-stage aerosol reactor for production of oxide-passivated silicon nanoparticles for novel memory devices. *J. Electrochem. Soc.* **2001**, *148* (5), G265-G270.
283. Vahala, K. J.; Saunders, W. A.; Tsai, C. S.; Sercel, P. C.; Kuech, T.; Atwater, H. A.; Flagan, R. C., LOWER-DIMENSIONAL QUANTUM STRUCTURES BY SELECTIVE GROWTH AND GAS-PHASE NUCLEATION. *Journal of Vacuum Science & Technology B* **1993**, *11* (4), 1660-1666.
284. Erogbogbo, F.; Lin, T.; Tucciarone, P. M.; LaJoie, K. M.; Lai, L.; Patki, G. D.; Prasad, P. N.; Swihart, M. T., On-demand hydrogen generation using nanosilicon: splitting water without light, heat, or electricity. *Nano Lett.* **2013**, *13* (2), 451-456.
285. Okamoto, H.; Sugiyama, Y.; Nakano, H., Synthesis and Modification of Silicon Nanosheets and Other Silicon Nanomaterials. *Chemistry-a European Journal* **2011**, *17* (36), 9864-9887.
286. Kummer, M.; Badillo, J. P.; Schmitz, A.; Bremes, H. G.; Winter, M.; Schulz, C.; Wiggers, H., Silicon/Polyaniline Nanocomposites as Anode Material for Lithium Ion Batteries. *J. Electrochem. Soc.* **2014**, *161* (1), A40-A45.
287. Petermann, N.; Stein, N.; Schierning, G.; Theissmann, R.; Stoib, B.; Brandt, M. S.; Hecht, C.; Schulz, C.; Wiggers, H., Plasma synthesis of nanostructures for improved thermoelectric properties. *Journal of Physics D-Applied Physics* **2011**, *44* (17), 9.
288. Goller, B.; Polisski, S.; Wiggers, H.; Kovalev, D., Freestanding spherical silicon nanocrystals: A model system for studying confined excitons. *Appl. Phys. Lett.* **2010**, *97* (4), 3.
289. Cabarrocas, P. R. I.; Nguyen-Tran, T.; Djeridane, Y.; Abramov, A.; Johnson, E.; Patriarche, G., Synthesis of silicon nanocrystals in silane plasmas for nanoelectronics and large area electronic devices. *Journal of Physics D-Applied Physics* **2007**, *40* (8), 2258-2266.

E: Vita

VAZQUEZ PUFLEAU, MIGUEL

PhD Energy, Environmental and Chemical Engineering,

Washington University in St. Louis,

Aug.2012 – Sept.2016

MS Energy, Environmental and Chemical Engineering,

Washington University in St. Louis,

Aug.2012 – Aug.2015

BS Chemical Engineering,

University of Guadalajara,

Feb.2005 – July.2010

PUBLICATIONS

Vazquez-Pufleau, M., Chadha, T. Yablonsky G. Erk, H. and Biswas, P., Elimination of Carbon Contamination from Silicon Kerf using a Furnace Aerosol Reactor (FuAR) Methodology; *Ind. Eng. Chem. Res.*, **2015**, *54* (22), pp 5914–5920, DOI: 10.1021/acs.iecr.5b0057

Vazquez-Pufleau, M., Chadha, T. Yablonsky, G. and Biswas, P., Kinetics of Carbon elimination from Kerf by Thermogravimetric Analysis with mechanistic insights (**2016**), Nature Scientific Reports, submitted

Vazquez-Pufleau, M., Yamane M., Biswas P., Thimsen E. Kinetics of nucleation and condensation of silicon nanoparticles from silane in helium atmosphere (**2016**), Journal of Aerosol Science, to be submitted

Vazquez-Pufleau, M.[†], Wang, Y. [†], Thimsen, E., & Biswas, P. Measurement of stable silicon hydride clusters from silane pyrolysis in a helium atmosphere (**2016**), Journal of physical chemistry, To be submitted, [†]→ Equal contribution authors

Vazquez-Pufleau, M., Cui, J., Hayes, S. & Biswas, P. A simple model for the high temperature oxidation of non-ideal silicon agglomerates, (**2016**) Silicon journal, to be submitted

Vazquez-Pufleau, M., Biswas, P. & Thimsen, E, Capture of silicon agglomerates by beads in a fluidized bed reactor for the production of polysilicon (**2016**) AIChE Journal, in preparation
Diebolder P., **Vazquez-Pufleau, M.,** Thimsen, E, Biswas, P., and Rogers B. Case study of silicon nanoparticle biodistribution in mice with tumor, paving the road towards nanoparticles for cancer treatment, (**2016**) Journal of Cancer Research and Clinical Oncology, in preparation

CONFERENCE TALKS (T) AND POSTERS (P)

American Association for Aerosol Research (**AAAR**) Annual Conference Oct.2015

1. Selective Oxidation of Carbon on Silicon Kerf using Furnace Aerosol Reactor (FuAR) aided by TGA Kinetic Estimations. MIGUEL VAZQUEZ PUFLEAU, Tandeep Chadha, Gregory Yablonsky, Henry Erk, Pratim Biswas (T)
2. Silicon Particle Formation and Growth in Silane Pyrolysis Reactors. MIGUEL VAZQUEZ PUFLEAU, Martin Yamane, Shaline Kavadiya, Thimsen Elijah, Pratim Biswas (P)

American Institute of Chemical Engineers (**AIChE**) Annual Meeting Nov.2015

3. Kinetics of Carbon Elimination in Silicon Kerf Using Thermo-Gravimetric Analysis Estimations: MIGUEL VAZQUEZ PUFLEAU Tandeep S. Chadha, Gregory S. Yablonsky and Pratim Biswas (P)
4. Rates of Silicon Nucleation and Condensation during Silane Pyrolysis: MIGUEL VAZQUEZ PUFLEAU, Martin Yamane, Shaline Kavadiya, Elijah Thimsen and Pratim Biswas (P)

European Union Photovoltaic Solar Energy Conference and Exhibition (**EU PVSEC**) Jun.2016

5. Capture of silicon agglomerates in a model fluidized bed reactor for polysilicon production: MIGUEL VAZQUEZ PUFLEAU, Pratim Biswas, Martin Yamane and Elijah Thimsen (T)